SEARCH FOR CHARGED-LEPTON FLAVOR VIOLATION IN THE PRODUCTION AND DECAY OF TOP QUARKS AT $\sqrt{s} = 13$ TEV WITH THE CMS DETECTOR

JINGYAN LI
B.S. in Physics, Lanzhou University

A DISSERTATION SUBMITTED IN PARTIAL FULFILLMENT OF THE REQUIREMENTS FOR THE DEGREE OF DOCTOR OF PHILOSOPHY

DEPARTMENT OF PHYSICS
NORTHEASTERN UNIVERSITY

2023

Abstract

A search for charged-lepton flavor violation is performed in the top quark (t) sector through both top quark production and decay signal processes. The data were collected by the CMS experiment from proton-proton collisions at a center-of-mass energy of 13 TeV and correspond to an integrated luminosity of 138 fb^{-1}. The selected events are required to contain one opposite-sign electron-muon pair, a third charged lepton (electron or muon), and at least one jet of which at most one is associated with a bottom quark. The analysis utilizes boosted decision trees to distinguish background processes from a possible signal, exploiting differences in the kinematics of the final state particles. The data are found to be consistent with the standard model expectation. Upper limits at 95% confidence level are placed in the context of effective field theory on the Wilson coefficients, which range between 0.024–0.424TeV^{-2} depending on the flavor of the associated light quark and the Lorentz structure of the interaction. Upper limits on the Wilson coefficients are converted to upper limits on branching fractions involving up (charm) quarks, $t \to e\mu u$ ($t \to e\mu c$), of 0.032×10^{-6} (0.498×10^{-6}), 0.022×10^{-6} (0.369×10^{-6}), and 0.012×10^{-6} (0.216×10^{-6}) for tensor, vector, and scalar interactions, respectively.

Preliminary results from a second search for charged-lepton flavor violation is also presented in this thesis. Using the same 138 fb^{-1} dataset, this search extends the scope of the first search by introducing hadronic tau leptons. Events selected in this search contain exactly two charged leptons (electron or muon) and one hadronic tau lepton. This search simultaneously looks for all three charged-lepton flavor mixing modes (i.e. $e\mu$, $e\tau$, and $\mu\tau$) through top quark production and decay processes. The second search complements the results from the first search by providing strong sensitivity in $\mu\tau$ and $e\tau$ flavor mixing modes.

Dedication

This work is dedicated to tens of millions of fallen Chinese civilians and soldiers, who fought bravely and selflessly against the Axis powers.

Acknowledgments

Confucius says: "Is it not delightful to have friends coming from afar?" I am glad that I received a few visits from my brother during my graduate study. When we were not together, we spent a lot of time on the phone talking about all the happy and sad things that happened in the world. He is the "closest" person in my family and my best friend. I could not have made it this far without his moral support.

I am incredibly grateful to Louise who took me as her first student at a time when I was really unsure about the direction of my life. I imagined it would not be an obvious decision for most PIs given that I had no prior experience in the field. She always respected and supported the way I approach my research while deeply caring about my growth as a researcher. I am forever in her debt.

I would like to express my gratitude to members of the Northeastern HEP community, especially Ela and Toyoko. I learned about particle physics from Ela. Her enthusiastic and insightful lectures truly captured my heart and inspired me to pursue an adventure in particle physics. Toyoko reached out to me many times to offer me her encouragement. She was eager to hear about my life story and shared hers with me, which means a lot to me.

Special thanks go to my parents and grandparents, who never forgot to send me their words of care and love when I needed the most. Despite not receiving much formal education themselves, they value my education above all else and are always curious about everything I do. I love you!

With COVID-19 and constantly moving in foreign countries, it was hardly easy for me to have a "normal" graduate school experience. In this regard, I would like to thank Bingran who helped me in many ways when I relocated to CERN during the pandemic. I would also like to thank Amrutha, Meng, Nick, and Yixiao who were willing to get together for my rather random and sometimes silly initiatives/activities, which matter greatly to me. I regard them as both supportive colleagues and my friends during my stay at CERN.

Thank you to Emily who has made invaluable contributions to the analysis work presented in this thesis. I have always appreciated her dedication and bright ideas. The lack of in-person interaction and my ambiguous English language did not prevent a fruitful collaboration between us. I cherish my relatively short but wonderful experience working with her even though we have yet to meet in real life.

Table of Contents

List of Figures

List of Tables

List of Acronyms

Al-CF Carbon Fibre Reinforced Aluminium

ALICE A Large Ion Collider Experiment

AR Application Region

ATLAS A Toroidal LHC Apparatus

BDT Boosted Decision Tree

BRIL Beam Radiation, Instrumentation, and Luminosity

BSM Beyond the Standard Model

CBC CMS Binary Chip

CCC CERN Control Centre

CERN European Organization for Nuclear Research

CKM Cabibbo-Kobayashi-Maskawa

CL Confidence Level

CLFV Charged-Lepton Flavor Violation

CMS Compact Muon Solenoid

CMSSW CMS Software Components

CSC Cathode Strip Chambers

CTF Combinatorial Track Finder

DAQ Data Acquisition

DCS Detector Control System

DOC Detector On-Call

DQM Data Quality Monitoring

DSS Detector Safety System

DT Drift Tube

DY Drell-Yan

ECAL Electromagnetic Calorimeter

EFT Effective Field Theory

EW Electroweak

FF Fragmentation Function

FCCC Flavor-Changing Charged Current

FSM Finite State Machine

GEM Gas Electron Multiplier

GSF Gaussian Sum Filter

HCAL Hadron Calorimeter

HGCAL High-Granularity Calorimeter

HLT High Level Trigger

HL-LHC High Luminosity-LHC

HPS Hadron-Plus-Strips

ILC International Linear Collider

IP Interaction Point

IRC Infrared and Collinear

JES Jet Energy Scale

JER Jet Energy Resolution

KF Kalman Filter

LEFT Low-Energy Effective Field Theory

LEP Large Electron-Positron

LFUV Lepton Flavor Universality Violation

LHC Large Hadron Collider

LHCb Large Hadron Collider beauty

LO Leading Order

LS Long Shutdown

L1 Level-1

MC Monte-Carlo

ME Matrix-Element

MET Missing Transverse Momentum

MIP Minimum Ionizing Particles

MR Measurement Region

MTD Minimum Ionizing Particles (MIP) Timing Detector

MVA Multivariate Analysis

NLO Next-to-Leading Order

NN Neural Network

NNLO Next-to-Next-to-Leading Order

OS Opposite-Sign

OSDF Opposite-Sign and Different-Flavor

OSSF Opposite-Sign and Same-Flavor

PD Primary Dataset

PDF Parton Distribution Function

PDG Particle Data Group

PF Particle Flow

PMNS Pontecorvo-Maki-Nakagawa-Sakata

PPD Physics Performance & Dataset

PPS Precision Proton Spectrometer

PS Parton Shower

PU Pile-Up

PUPPI Pileup Per Particle Identification

PV Primary Vertex

QED Quantum Electrodynamics

QCD Quantum Chromodynamics

RFM Run Field Manager

ROC Receiver Operating Characteristic

RPC Resistive Plate Chambers

SL Shift Leader

SLIMOS Shift Leader In Matters Of Safety

SM Standard Model

SMEFT Standard Model Effective Field Theory

SPS Super Proton Synchrotron

SR Signal Region

SS Same-Sign

SSSF Same-Sign and Same-Flavor

SV Secondary Vertex

TCS Tracker Control System

TOTEM TOTal Elastic and diffractive cross section Measurement

UV Ultraviolet

VR Validation Region

WC Wilson Coefficient

YETS Year-End Technical Stop

Chapter 0

Introduction

The 20th century was not only dominated by unprecedented geopolitical events, but it also witnessed a giant leap in our understanding of nature. Among many great scientific achievements, a remarkable insight into the fundamental structure of matter was developed through the work of thousands of physicists worldwide, spanning several decades. At the most fundamental scale, everything in our universe is made up of indivisible building blocks known as fundamental particles. These point-like fundamental particles manifest in two kinds: fermions and bosons. Fermions comprise all the matter in our universe while bosons provide mechanisms to explain fundamental forces and and the origin of particle mass. Our best understandings of all the known fundamental particles and three of the four known fundamental forces (electromagnetism, weak, and strong interactions – excluding gravity) are encoded in the theory known as the Standard Model (SM) of particle physics.

The SM is a quantum field theory that obeys the principle of gauge invariance in which the dynamics of the full system are invariant under local gauge transformations. It comprises an Electroweak (EW) sector and a strong sector, where three fundamental forces emerge naturally. The EW sector provides a unified description of the electromagnetism and the weak interaction under the $SU(2)_L \bigotimes U(1)_Y$ gauge symmetry while the strong sector features the theory of Quantum Chromodynamics (QCD), which describes the strong interaction with the $SU(3)_C$ Lie group. Since its completion in the 1970s, the SM has been immensely successful in describing all the known fundamental particles in a self-consistent way. The properties of these fundamental particles predicted by the SM agree very well with the vast majority of the experimental data. However, the SM falls short of being the most fundamental description of nature as it does not incorporate any theory of gravity, provide any viable candidates for dark matter, or fully explain matter-antimatter asymmetry. Consequently, it is widely assumed that the SM is only one aspect of a more fundamental theory that we have yet to uncover.

One of the most mysterious aspects of the SM is the concept of fermion flavor, that is, fermions exist in three generations. With the exception of the masses, fermions of different generations can be viewed as identical copies of each other. The majority of the free parameters of the SM, such as the masses of fermions, belong to the flavor sector, and the SM remains completely silent on why these parameters are tuned to the values observed in experiments. A subset of

these free parameters that have yet to be measured precisely is related to the flavor mixings. When participating in the weak interactions, different-flavor fermions are characterized by distinct quantum states known as the flavor eigenstates, which might be different from the eigenstates of the free Hamiltonian (i.e. mass eigenstates). The mismatch of quark mass eigenstates and flavor eigenstates may occur, and it leads to flavor-changing interactions via the exchange of W bosons. In other words, quark flavor is not conserved in the SM, and the mixing of quark flavors is characterized by free parameters that can only be obtained through experimental measurements.

Unlike quark flavor, lepton flavor is conserved in the SM with massless neutrinos. However, the observation of neutrino oscillations [11, 36] confirms the existence and the mixing of massive neutrinos, and it also indicates that lepton flavor violation (LFV), meaning local interaction that alters lepton flavor, is expected to occur in the charged-lepton sector. The charged-lepton flavor violation (CLFV) processes can be divided into two main categories depending on the energy scale of the interactions. The CLFV processes that only involve light particles, such as $\mu \to e\gamma$ and $\mu \to eee$, generally carry low momentum transfers, thus extremely high sensitivity can be achieved at small but dedicated experiments [37, 38]. New physics can also manifest in CLFV processes involving heavy particles, such as the Z boson, Higgs boson, or top quark (t). In this case, the Large Hadron Collider (LHC) [39] built by the European Organization for Nuclear Research (CERN) could provide the highest sensitivity [40] as it is currently the only machine that is capable of producing all of them.

This thesis describes the research work I did in 2019-2023 on the Compact Muon Solenoid (CMS) experiment, including a brief description of the surrounding context and background knowledge. This thesis is organized into four parts, and Part I introduces the theoretical foundation of high energy particle physics, including the electroweak theory, QCD, and theories Beyond the Standard Model (BSM). Descriptions of the LHC and CMS experiment, including the operational and upgrade work that I made direct contributions to, are given in Part II. Part III describes a search for flavor-violating $e\mu qt$ interactions using data collected by the CMS detector in 2016-2018. The CLFV processes in the production and decay of top quarks are both considered in this search. The scope of this search is expanded to include $e\tau qt$ and $\mu\tau qt$ interactions in a second search, which is described in Part IV.

Part I

Theoretical Framework

Part I of this thesis gives a brief introduction of the theoretical framework behind the physics programs at the LHC, including both the SM of particle physics and extensions of the SM that partly motivate the physics searches discussed in Part III and Part IV. Part I is organized as follows. Chapter 1 introduces the field content of the standard model, including all known fermions and bosons. Chapter 2 discusses the theory of EW interaction developed initially by Glashow, Weinberg, and Salam. The theory of strong interaction and its application to hadron colliders are discussed in Chapter 3. Chapter 4 discusses a few fissures exposed in the SM in recent years along with models that aim to accommodate them. Finally, a model-independent framework called EFT is discussed in Chapter 5. Materials presented in Part I are borrowed liberally from various milestone papers and popular graduate physics textbooks, and thus shall not be considered original work of my own.

Chapter 1

Field Content of the Standard Model

The SM of particle physics is a quantum field theory that combines the concept of classic field theory with quantum mechanics and Einstein's special relativity. Different fundamental particles can be described as the excited states or quanta of distinct quantum fields, characterized by masses and various quantum numbers. A summary of the known fundamental particles and their properties is given in Figure 1.1.

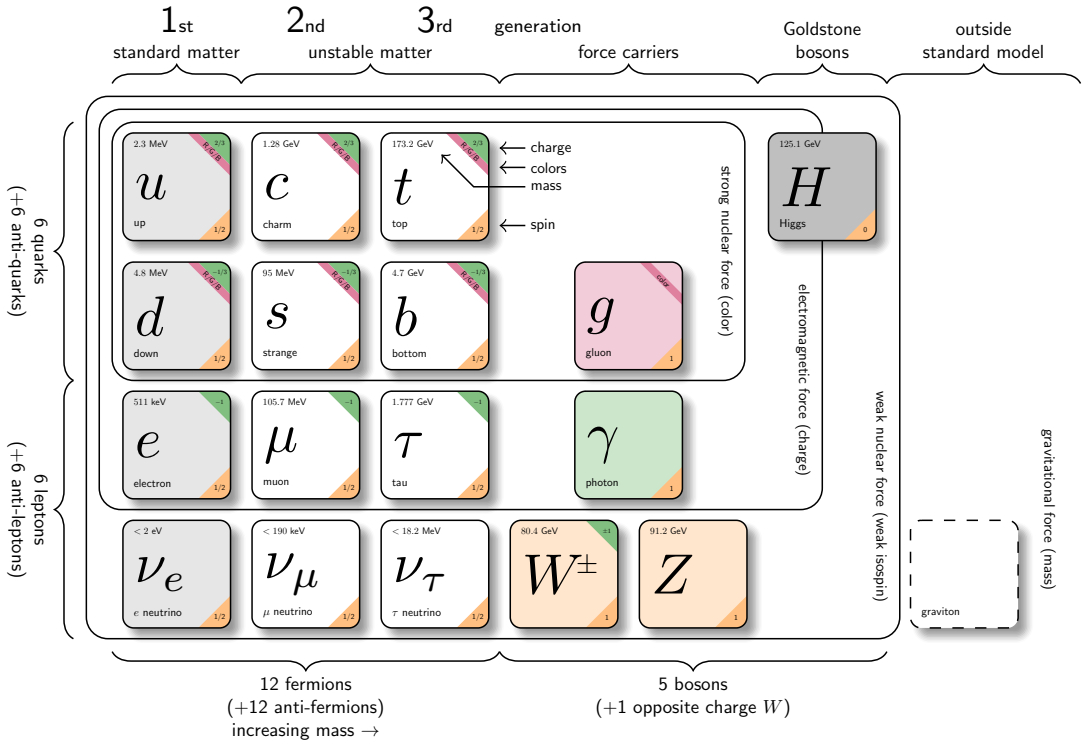

Figure 1.1: The field content of the SM, including all known fundamental particles. The three generations of fermions are shown in the first three columns. The gauge bosons that mediate the fundamental interactions are shown in the fourth and fifth columns. The sixth column shows the recently discovered Higgs boson. The hypothetical graviton that mediates gravitational force is also shown, which is outside of the realm of the SM. [1]

The effects described by special relativity apply to all fundamental particles. This requires the theory to be invariant under Lorentz transformations, which contain rotations and Lorentz boosts of the coordinate systems. The behaviors of fundamental particles under such transformations are characterized by their spin quantum numbers. This divides fundamental particles into two groups. Those with half-integer spins are known as "fermions". They are fundamental building blocks of matter that exist in the universe. Particles with integer spins are known as "bosons". They are either mediators of the fundamental forces or are required in the mechanism that generates mass for all fundamental particles. Properties of elementary fermions and bosons are discussed further in Section 1.1 and Section 1.2, respectively.

1.1 Fermions

Named after Italian physicist Enrico Fermi, fermions follow Fermi-Dirac statistics and obey the Pauli exclusion principle, which prohibits two or more fermions with the same quantum number from simultaneously occupying the same quantum state. The matter that exists in the universe is made up of spin-$\frac{1}{2}$ fermions that can be broken into two groups, quarks and leptons. They are represented by "spinors" under Lorentz transformations. For example, the free Lagrangian that encodes full information of a spinor field can be expressed as,

$$\mathcal{L} = i\psi_R^\dagger \sigma^\mu \partial_\mu \psi_R \tag{1.1}$$

or

$$\mathcal{L} = i\psi_L^\dagger \bar{\sigma}^\mu \partial_\mu \psi_L, \tag{1.2}$$

where σ^μ is the 2×2 Pauli matrix. The spinors in Equation (1.1)-(1.2) are known as Weyl spinors, which correspond to two-dimensional irreducible representations of the Lorentz group. Weyl spinors can be classified into left-handed spinors ψ_L or right-handed spinors ψ_R depending on the orientation of their spin relative to their momentum. More formally, ψ_R and ψ_L correspond to the $(\frac{1}{2},0)$ and $(0,\frac{1}{2})$ representation of the Lorentz group [41].

In addition to Lorentz invariance, the free Lagrangians should also be invariant under parity transformation. For Weyl spinors, however, this symmetry is violated as right-handed spinors transform into left-hand spinors under parity, and vice versa. To describe elementary fermions, the two irreducible representations must be stacked together, forming a four-dimensional reducible representation $(\frac{1}{2},0) \bigoplus (0,\frac{1}{2})$,

$$\mathcal{L} = i\psi_R^\dagger \sigma^\mu \partial_\mu \psi_R + i\psi_L^\dagger \bar{\sigma}^\mu \partial_\mu \psi_L. \tag{1.3}$$

It is also possible to introduce additional Lorentz- and parity-invariant terms $m(\psi_R^\dagger \psi_L + \psi_L^\dagger \psi_R)$ to Equation (1.3),

$$\mathcal{L}_{Dirac} = i\psi_R^\dagger \sigma^\mu \partial_\mu \psi_R + i\psi_L^\dagger \bar{\sigma}^\mu \partial_\mu \psi_L + m(\psi_R^\dagger \psi_L + \psi_L^\dagger \psi_R), \tag{1.4}$$

where m corresponds to the physical mass of the fermions. Equation (1.4) is known as the Dirac Lagrangian. Using the Euler-Lagrange equation that is based on the principle of least action,

$$\frac{\partial \mathcal{L}}{\partial \psi} - \partial_\mu \frac{\partial \mathcal{L}}{\partial(\partial_\mu \psi)} = 0, \tag{1.5}$$

the equation of motion for the Dirac Lagrangian can be written as,

$$i\sigma^\mu \partial_\mu \psi_R = m\psi_L \tag{1.6}$$

$$i\bar{\sigma}^\mu \partial_\mu \psi_L = m\psi_R \tag{1.7}$$

Defining the four-dimensional Dirac spinor as $\psi = \begin{pmatrix} \psi_R \\ \psi_L \end{pmatrix}$ and the 4×4 Dirac matrix as $\gamma^\mu = \begin{pmatrix} 0 & \bar{\sigma}^\mu \\ \sigma^\mu & 0 \end{pmatrix}$, Equation (1.6)-(1.7) can be rewritten as,

$$i\gamma^\mu \partial_\mu \psi - m\psi = 0, \tag{1.8}$$

which is the celebrated Dirac equation first derived by British physicist Paul Dirac [42]. Ironically, Dirac arrived at this equation with the simple goal of finding a relativistic equation with only one power of spacetime derivative and was puzzled by the negative-energy solutions to his equation. It was later understood these negative-energy solutions correspond to antiparticles that have the same mass but opposite signs of all quantum numbers. The existence of such particles was first confirmed by American physicist C. D. Anderson in 1932 [2], who used a cloud chamber to produce to first photographic evidence of positron, which is shown in Figure 1.2.

Quarks participate in all known fundamental interactions and they exist in two different types, up-type and down-type. Up-type and down-type quarks carry $+\frac{2}{3}$ and $-\frac{1}{3}$ electric charges, respectively, in units of the electron charge. For each type of quark, there exist three generations of quarks that are identical copies of each other, except their masses and flavor quantum numbers. For up-type quarks, the three generations are: i) up (u), ii) charm (c), and iii) top (t) quarks. The three generations of up-type quarks are illustrated in the first three columns of the first row in Figure 1.1. For down-type quarks, the three generations are: i) down (d), ii) strange (s), and iii) bottom (b) quarks. The three generations of down-type quarks are illustrated in the first three columns of the second row in Figure 1.1. Unlike leptons, which don't interact strongly, quarks carry three types of "color" charges: red, green, and blue, which allow them to participate in strong interactions. Strong interactions are discussed in more detail in Chapter 3.

With the exception of top quarks, which decay before forming bound states, quarks are only observed in bound states called "hadrons" as stable particles must be color neutral, and carry an

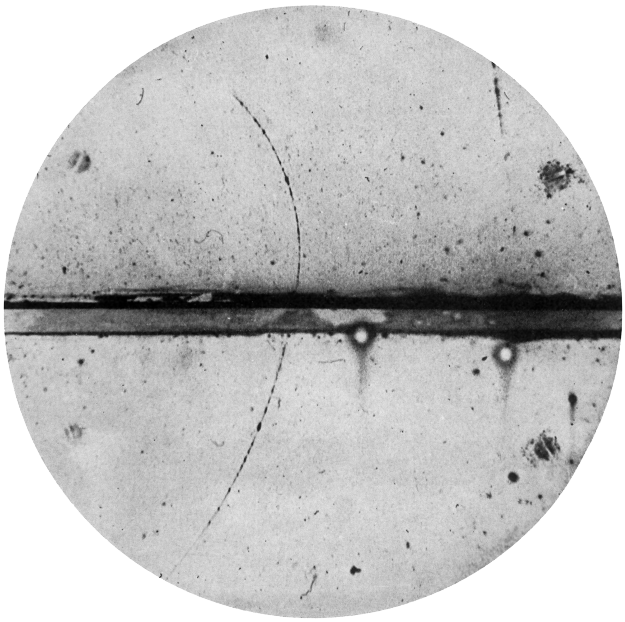

Figure 1.2: Cloud chamber photograph taken from Anderson's 1932 paper [2]. The upper chamber and the lower chamber are separated by a 6 mm lead plate. The deflection and direction of the particle's ion trail indicate that the particle is a positron.

integer electric charge. A quark can form two-particle bound states called "mesons" with another antiquark with opposite color charges. In addition to two-particle bound states, quarks can also form three- or more-particle bound states. The three-particle bound states, such as a proton (uud), are known as "baryons". Bound states with more than three quarks are extremely unstable with a short lifetime, such as the pentaquark recently discovered by the Large Hadron Collider beauty (LHCb) experiment [43]. Because isolated quarks do not exist in nature, their existence must be inferred from the decay products of high-energy collisions. Historically, lighter quarks were observed first as the production of heavier quarks requires higher energy. For example, the existence of charm quarks was confirmed in 1974 at Brookhaven [44] and SLAC [3] (illustrated in Figure 1.3) while top quarks were only observed in 1995 at the Tevatron [45, 46].

Leptons are divided into charged leptons and neutral leptons. Charged leptons carry -1 electric charge while neutral leptons, as the name suggests, do not carry any electric charge. Charged leptons participate in electromagnetism and weak interactions while neutral leptons only participate in weak interactions. Similar to quarks, charged- and neutral-leptons exist in three generations, also referred to as "flavors". For charged leptons, the three flavors are: i) electron (e), ii) muon (μ), and iii) tau (τ). The three flavors of charged leptons are illustrated in the first three columns of the third row in Figure 1.1. Neutral-leptons are known as "neutrinos", which are considered massless in the SM. The three flavors of neutrinos are: i) electron neutrino (ν_e), ii) muon neutrino (ν_μ), and iii) tau neutrino (ν_τ). The three flavors of neutral leptons are illustrated in

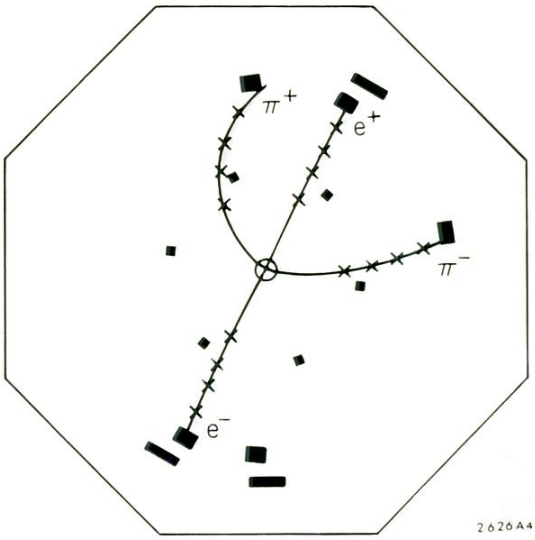

Figure 1.3: An example of the $\psi' \to \psi\pi^+\pi^-$ decay recorded by the Mark I detector in the discovery of ψ particle at SLAC [3]. A new resonance around 3.1 GeV was reported by this experiment which was later confirmed to be a two-particle bound state consisting of charm and anticharm quarks.

the first three columns of the fourth row in Figure 1.1.

Leptons shown in Figure 1.1 have definite masses created by the interaction with Higgs bosons. They are used to describe freely propagating particles of the same mass and quantum numbers, referred to as the "mass eigenstates". The three flavors of charged-leptons correspond exactly to their mass eigenstates, which means charged-lepton flavor is conserved in weak interactions. For neutrinos, however, their flavor eigenstates are not identical to their mass eigenstates, which allows neutrinos to oscillate between flavors as they propagate through space. The topic of fermion flavor is discussed further in Section 2.3.

The tau lepton is the only lepton that can decay into hadrons (through weak interactions), owing to its higher mass relative to other leptons. The higher mass also means more energy is needed to produce tau leptons. After a decade-long hunt, the tau lepton was eventually detected in 1974 at SLAC [47]. Neutrinos only interact weakly, making it virtually impossible to detect them using any general-purpose detectors. It wasn't until the detection of tau neutrinos in 2001 by a dedicated experiment at Fermilab [48] that all three flavors of neutrinos were experimentally confirmed.

1.2 Bosons

Bosons are named after Indian physicist Satyendra Bose, who along with Einstein, developed the foundations for Bose-Einstein statistics, which states that identical integer spin particles

may occupy the same quantum state simultaneously. Elementary bosons in the SM consist of spin-1 bosons, which behave like a vector under Lorentz transformation, and scalar bosons with a spin of 0. Vector bosons can be massive or massless and they are mediators of the fundamental forces. For example, photons are quanta of the massless vector boson field that mediates the electromagnetism between charged particles. The particle nature of photons was first demonstrated by American physicist Arthur Compton through the scattering of X-rays in 1923 [49].

The theory that describes the light-matter interaction is known as Quantum Electrodynamics (QED), which was first formulated by Dirac in the 1920s. QED introduces a photon field by adding two terms to the Dirac Lagrangian,

$$\mathcal{L}_{QED} = -\frac{1}{4}F_{\mu\nu}F^{\mu\nu} + i\bar{\psi}\gamma^{\mu}\partial_{\mu}\psi - m\bar{\psi}\psi - e\bar{\psi}\gamma^{\mu}A_{\mu}\psi, \tag{1.9}$$

where the first term in Equation (1.9) is known as the Electromagnetic tensor, which characterizes the spacetime properties, or more formally the curvature form of the photon field. The last term in Equation (1.9) describes the interaction between the fermion fields, mediated by the photon field.

However, it was soon realized that Dirac's theory was reliable only at a first order of perturbation theory. Attempts to compute high-order processes were often met with Ultraviolet (UV) divergence that were nonphysical. This problem remained unsolved for more than 20 years until the Second World War broke out, after which a procedure known as "renormalization" was developed independently by Japanese physicist Shinichiro Tomonaga [50], American physicists Julian Schwinger [51], and Richard Feynman [52]. Schwinger also provided in his paper a one-loop calculation of the electron anomalous magnetic moment which matched precisely with experiments. British physicist Freeman Dyson also made important contributions by providing mathematical insights into this new technique, most notably demonstrating the equivalence between the seemingly different approaches of Feynman, Schwinger, and Tomonaga [53]. Renormalization was initially designed to systematically remove infinities that appeared in QED. It was eventually accepted as a foundational element of quantum field theory as it ensures the validity of physics predictions at different scales. Another key feature of the QED, known as gauge invariance, is discussed in Section 2.1.

Discovered at DESY in 1979 [54], the gluon is the second elementary boson to be observed experimentally. Like photons, gluons arise from a massless boson field with spin 1. They mediate and participate in the strong interaction as they carry color charge themselves. This property enables the self-interaction of gluons which differentiates itself from the photon. This also means that isolated gluons do not exist in nature as stable particles need to be colorless. The theory of strong interaction is known as QCD, which is discussed further in Chapter 3.

Massive vector bosons exist in three types, W^+, W^-, and Z bosons. The Z boson has no electric

charge while the W^+ and W^- bosons carry the opposite electric charge and are antiparticles of each other. Together, they are also known as weak bosons as they mediate the weak interaction. Weak bosons are among the heaviest fundamental particles in the SM, behind only the top quark and the Higgs boson. The heavy mass limits the range of the weak interaction and also raises the threshold energy needed to produce them at high-energy experiments. The existence of these weak bosons was predicted by physicists in the 1960s and was confirmed nearly two decades later by experiments at CERN in 1983 [55, 56, 57, 58]. The theory developed by Weinberg that provided a unified description of electromagnetism and weak interaction is discussed further in Chapter 2.

The only known elementary boson with spin 0 is the Higgs boson, which was predicted in 1964 [59, 60, 61] by six physicists including Peter Higgs whose name was given to this massive scalar boson. The Higgs boson is the second heaviest fundamental particle, behind only the top quark. It has no electric charge and its associated Higgs field only interacts with other massive fields with the coupling strength proportional to the particle mass. The Higgs field provides a mechanism to generate mass for other massive fundamental particles, which is discussed further in Section 2.2. The high mass and lack of quantum charge make Higgs boson extremely difficult to produce. The search for this particle has been one of the longest in history, lasting over 40 years until its eventual observation in 2012 at the LHC [4, 5]. Evidence for Higgs to two photons presented by the ATLAS and CMS Collaborations in 2012 is shown in Figure 1.4.

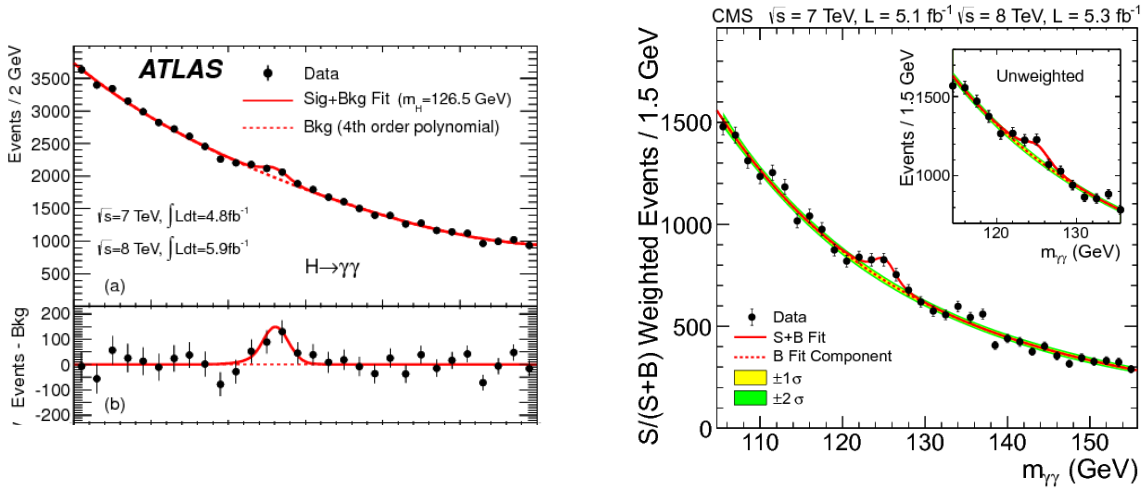

Figure 1.4: The diphoton invariant mass distributions reported by the ATLAS [4] (left) and CMS [5] (right) in their searches for the Higgs boson in 2012. The observed signal around the 125 GeV bump was consistent with the hypothesis of a new massive boson with spin 0, which was later confirmed to be the Higgs boson.

Chapter 2

Electroweak Theory

Developed in the 1960s, the Glashow–Weinberg–Salam theory of the EW interaction is regarded by many physicists as the cornerstone of the SM. It successfully unified the weak interaction with electromagnetism and postulated the existence of several new particles, all of which were later confirmed by experiments. One of the most important aspects of this theory is the $SU(2)_L \bigotimes U(1)_Y$ gauge symmetry, which is discussed in Section 2.1. The $SU(2)_L \bigotimes U(1)_Y$ symmetry is spontaneously broken through the Higgs mechanism, which is discussed in Section 2.2. Finally, flavor physics and its connection to the Yukawa interaction is discussed in Section 2.3.

2.1 Gauge Theory

Fundamental forces in the SM are formulated under a principle known as gauge invariance, where the Lagrangian is invariant under local transformations of gauge groups. Taking QED as an example, the local symmetry for a Dirac fermion is,

$$\psi \to e^{i\alpha(x)}\psi, \tag{2.1}$$

where $\alpha(x)$ is a phase angle defined at each spacetime point, hence the name "local transformation". The gauge group associated with this symmetry is $U(1)_{EM}$, where the subscript is a shorthand expression for "electromagnetism". Under a local $U(1)_{EM}$ rotation, Equation (1.8) can be written as:

$$\begin{aligned}\mathcal{L} &= -\frac{1}{4}F_{\mu\nu}F^{\mu\nu} + ie^{-i\alpha(x)}\bar{\psi}\gamma^\mu\partial_\mu e^{i\alpha(x)}\psi - m\bar{\psi}\psi - e\bar{\psi}\gamma^\mu(A_\mu + \delta A_\mu)\psi \\ &= \mathcal{L}_{Dirac} - \bar{\psi}\gamma^\mu\psi\partial_\mu\alpha(x) - e\bar{\psi}\gamma^\mu\delta A_\mu\psi.\end{aligned} \tag{2.2}$$

The gauge invariance requires $\delta A_\mu = -\frac{1}{e}\partial_\mu\alpha(x)$. This means the photon field transforms as:

$$A_\mu \to A_\mu - \frac{1}{e}\partial_\mu\alpha(x). \tag{2.3}$$

This behavior of the photon field under gauge transformation cancels out the gauge dependency of the free Dirac Lagrangian, which ensures the gauge invariance of the theory. Therefore, vector bosons such as photons also called gauge bosons, and the associated quantum fields are also known as gauge fields. The Dirac Lagrangian can be re-written as,

$$\mathcal{L} = -\frac{1}{4}F_{\mu\nu}F^{\mu\nu} + i\bar{\psi}\gamma^{\mu}D_{\mu}\psi - m\bar{\psi}\psi, \tag{2.4}$$

where $D_\mu = \partial_\mu + ieA_\mu$ is known as the gauge covariant derivative.

The mass term associated to the photon field $\frac{1}{2}m^2A_\mu A^\mu$ is however not gauge invariant as

$$[A_\mu - \frac{1}{e}\partial_\mu\alpha(x)][A^\mu - \frac{1}{e}\partial^\mu\alpha(x)] \neq A_\mu A^\mu. \tag{2.5}$$

Effectively, this means gauge bosons such as photons must be massless in a gauge invariant theory. As a consequence, a new mechanism, known as the Higgs mechanism, is needed to explain the origin of weak boson masses, which is discussed in the following chapter.

It should be pointed out that gauge symmetry is not a symmetry of nature. The Noether currents [62] associated with local gauge symmetry do not generally correspond to physical observables. Nevertheless, its existence is necessary to regulate the redundant degree of freedom in the Lagrangian using a procedure known as gauge fixing [63].

QED is also known as an abelian gauge theory as the $U(1)$ group operation is commutative, meaning the order of sequential group operations does not affect the final result. Chinese physicist Chen-Ning Yang and his American colleague Robert Mills at Brookhaven first generalized the concept of gauge invariance to the non-abelian Lie group, proposing what's now known as the Yang-Mills theory in 1954 [64]. Shortly after this work, Yang and his colleague Tsung-Dao Lee suggested parity might be violated in the weak interaction [65], which was later confirmed by the legendary Wu experiment led by Chien-Shiung Wu [66].

Not long after the Wu experiment, physicists understood that only left-handed fermions and right-handed antifermions are involved in weak charged-current interactions. Moreover, the very existence of weak charged-current forced physicists to consider the interaction between photons and weak mediators. This led to many problems in the weak theory, for example, the exchange of photons in s-channel $e^+e^- \to W^+W^-$ (shown in Figure 2.1) would lead to divergence at high energy unless there exists a neutral intermediate field that mediates the weak interaction. Hints of the weak neutral current and the interplay between electromagnetism and the weak interaction prompted the efforts by physicists to relate these two forces under the framework of Yang-Mills theory in the early 1960s.

Since fermions with different chiral structures were understood to be treated differently by the weak interaction, it was imperative to apply different gauge transformations to left-handed and

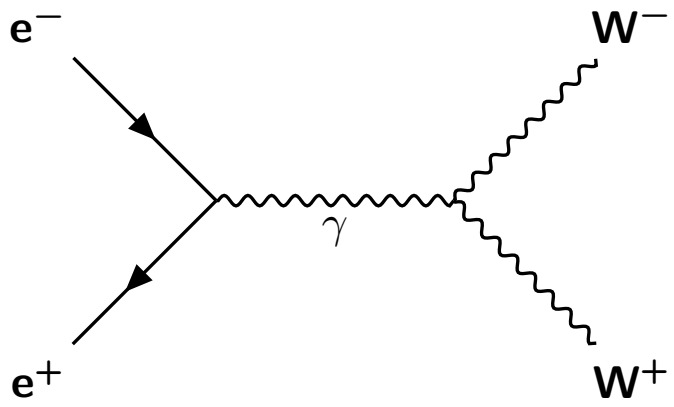

Figure 2.1: Representative *s* channel ee→WW diagram, mediated by a massless photon field. Without a heavy neutral mediator, such a process would lead to divergence at high energy scales.

right-handed fermionic fields. Initial work toward unification was done by American physicist Sheldon Glashow, who proposed the $SU(2)_L \bigotimes U(1)_Y$ symmetry in 1961 [67], where L denotes left-handed fields, and Y refers to the quantum number for hypercharge. Under this framework, left-handed components of the Dirac fields are organized into $SU(2)_L$ doublet,

$$L_L^j = \begin{pmatrix} \nu^j \\ e^j \end{pmatrix}_L, Q_L^j = \begin{pmatrix} u^j \\ d^j \end{pmatrix}_L, j = 1, 2, 3, \tag{2.6}$$

where ν^j, e^j, u^j, and d^j correspond to Dirac fields of neutrino, charged-lepton, up-type quark, and down-type quark, respectively. The right-handed components of the Dirac fields are treated as $SU(2)_L$ singlet: e_R^j, u_R^j, d_R^j, where neutrino terms are missing as only left-handed neutrinos have been observed in nature. The index j in both doublets and singlets runs over the fermion generations. The left-handed doublets carry $\frac{1}{2}$ weak isospin charge, denoted by T. The third component of T, denoted by T_3, is $\frac{1}{2}$ for neutrinos and up-type quarks, and -$\frac{1}{2}$ for charged-leptons and down-type quarks in the $SU(2)_L$ doublets. All right-handed singlets carry 0 weak isospin charge, which prevents them from participating in the weak interaction.

The $SU(2)_L \bigotimes U(1)_Y$ symmetry introduces the following local gauge transformations:

$$\begin{aligned} \psi_L &\to \exp[i\hat{T}^i\alpha^i(x) + i\frac{\hat{Y}}{2}\beta(x)]\,\psi_L, \\ \psi_R &\to \exp[i\frac{\hat{Y}}{2}\beta(x)]\,\psi_R, \end{aligned} \tag{2.7}$$

where $\Psi_L = \{L_L^j, Q_L^j\}$, and $\Psi_R = \{e_R^j, u_R^j, d_R^j\}$. $\hat{T}^i$ and $\hat{Y}$ denotes generators of the $SU(2)_L$ and $U(1)_Y$ group, respectively. To preserve gauge invariance, two massless gauge fields W_μ and B_μ are introduced. The corresponding gauge covariant derivative can be written as

$$D_\mu = \partial_\mu - ig\hat{T}^i W_\mu^i - ig'\frac{\hat{Y}}{2}B_\mu, \tag{2.8}$$

where g and g' correspond to coupling strengths of the $SU(2)$ and $U(1)$ gauge fields, respectively. The $SU(2)_L \bigotimes U(1)_Y$ gauge Lagrangian can therefore be written as:

$$\mathcal{L}_{gauge} = -\frac{1}{2}\mathrm{tr}W_{\mu\nu}W^{\mu\nu} - \frac{1}{4}B_{\mu\nu}B^{\mu\nu} + i\bar{\Psi}_L\gamma^\mu D_\mu \Psi_L + i\bar{\Psi}_R\gamma^\mu D_\mu \Psi_R \tag{2.9}$$

A linear combination of the first and second components of gauge field W_μ^i gives rise to the weak charge-current interactions observed in experiments:

$$W_\mu^\pm = \frac{1}{\sqrt{2}}(W_\mu^1 \mp W_\mu^2), \tag{2.10}$$

while neutral-current interactions can be constructed by the remaining fields:

$$\begin{pmatrix} B_\mu \\ W_\mu^3 \end{pmatrix} = \begin{pmatrix} \cos\theta_\omega & -\sin\theta_\omega \\ \sin\theta_\omega & \cos\theta_\omega \end{pmatrix} \begin{pmatrix} A_\mu \\ Z_\mu \end{pmatrix}, \tag{2.11}$$

where A_μ and Z_μ correspond to the photon and Z boson, respectively, and

$$g\sin\theta_\omega = g'\cos\theta_\omega = e. \tag{2.12}$$

The free parameter θ_ω is referred to as the weak mixing angle, or Weinberg angle, which can be measured experimentally.

The relation between electric charge, weak isospin, and hypercharge is given by the Gell-Mann-Nishijima formula [68, 69]:

$$Q = \frac{Y}{2} + T_3. \tag{2.13}$$

The preliminary version of the EW theory developed by Glashow did not garner a huge reception initially as all gauge fields in his theory were massless due to gauge invariance, resulting in long-range forces that matched with no experimental observations. Luckily, physicists did not have to wait long as the mechanism proposed by American physicist P. W. Anderson [70] in the context of non-relativistic field theory in the following year (1962) quickly gained attention.

Extending on Anderson's work, the theory of symmetry breaking and gauge boson mass generation was published by Higgs and others in 1964 [59, 60, 61], which led to the eventual completion of the EW theory in the following years by Salam and Weinberg [71, 72].

2.2 Higgs Mechanism

The Higgs mechanism provides a way to generate a mass term for gauge bosons without explicitly breaking the gauge symmetry. The core feature of this mechanism is a $SU(2)_L$ doublet of complex scalar fields $\phi = \begin{pmatrix} \phi^+ \\ \phi^0 \end{pmatrix}$, which is subject to the potential:

$$V(\phi) = -\mu^2(\phi^\dagger\phi) + \lambda(\phi^\dagger\phi)^2, \tag{2.14}$$

where λ is a real parameter that determines the Higgs quartic coupling and is required to be positive to ensure the stability of the EW vacuum [73]. The parameter μ^2 determines the minimum of the Higgs potential. The Lagrangian of this scalar field is written as

$$\mathcal{L}_{Scalar} = (D_\mu\phi)^\dagger(D^\mu\phi) - V(\phi), \tag{2.15}$$

where D_μ is same gauge covariant derivative shown in Equation (2.8). The $\mathcal{L}_{Scalar}$ is invariant under $SU(2)_L \bigotimes U(1)_Y$ gauge transformation when $\mu^2 < 0$, which corresponds to the early universe when temperature is very high, as illustrated in Figure 2.2.

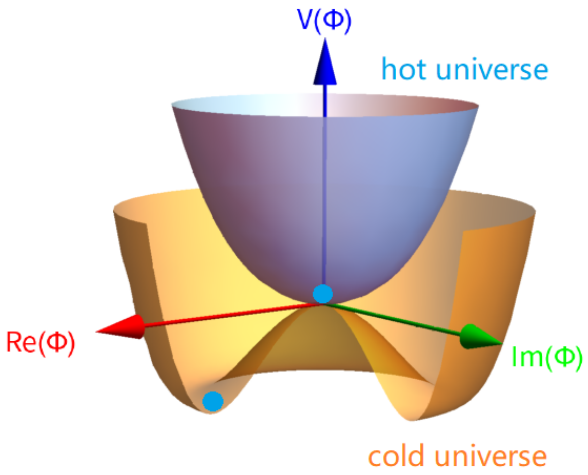

Figure 2.2: Possible shape of the Higgs potential before symmetry breaking in the hot universe (blue) and after symmetry breaking in the present universe (yellow). Adapted from [6].

Eventually, the universe cools down and μ^2 becomes positive. As a consequence, an infinite number of degenerate fields arise as ground states of the potential, which corresponds to

$$\phi_{min} = e^{i\varphi} \begin{pmatrix} 0 \\ \sqrt{\mu^2/2\lambda} \end{pmatrix} \equiv \frac{e^{i\varphi}}{\sqrt{2}} \begin{pmatrix} 0 \\ v \end{pmatrix}, \tag{2.16}$$

where φ is the phase angle that corresponds to the choice of the degenerate field, and $v = 246.22$ GeV [74] is the so-called vacuum expectation value that corresponds to the physical meaning of the minimum. The ground states in this case are not invariant under $SU(2)_L \bigotimes U(1)_Y$ symmetry. In other words, upon acquiring a vacuum expectation value by the scalar field ϕ, the EW symmetry will be spontaneously broken. Since the phase angle will eventually cancel out in $(\phi^\dagger\phi)$, it is free to expand the ground-state field around the arbitrarily selected minimum $\frac{1}{\sqrt{2}}\binom{0}{v}$:

$$\phi = \frac{e^{i\hat{T}^i\pi^i(x)/v}}{\sqrt{2}} \begin{pmatrix} 0 \\ v + h(x) \end{pmatrix}, \tag{2.17}$$

where $\hat{T}^i$ corresponds to the generators of the broken $SU(2)_L$ symmetry and $\pi^i(x)$ corresponds to three massless scalar bosons referred to as the Goldstone bosons [75]. The meaning of the field $h(x)$ will become clear later. The dependency on $\pi^i(x)$ can be removed by performing the following gauge transformation:

$$\phi \to \phi e^{-i\hat{T}^i\pi^i(x)/v}, \tag{2.18}$$

which corresponds to the so-called unitary gauge [76]. Expanding the kinetic term from $\mathcal{L}_{Scalar}$,

$$(D_\mu\phi)^\dagger(D^\mu\phi) = \frac{1}{2}\partial_\mu h(x)\partial^\mu h(x) + (v + h(x))^2\frac{g^2}{8}[(W_\mu^1)^2 + (W_\mu^1)^2 + (W_\mu^3 - \frac{g'}{g}B_\mu)^2]. \tag{2.19}$$

Using the relation specified in Equation (2.10)-(2.12), the v^2 terms in Equation (2.19) can be rewritten as

$$\begin{aligned} &m_W^2 W_\mu^\dagger W_\mu, \\ &\frac{1}{2}m_Z^2 Z_\mu Z^\mu, \end{aligned} \tag{2.20}$$

where $m_W = \frac{gv}{2}$, and $m_Z = \frac{gv}{2\cos\theta_\omega}$, which corresponds to the mass of the gauge bosons W and Z, respectively. The mass of the W and Z bosons can therefore be related by $m_Z/m_W = \cos\theta_\omega$, which can be used to test the self-consistency of the SM [77]. The linear combination of v^2 terms orthogonal to Z_μ cancels out and corresponds to the massless photon field:

$$A_\mu = \sin\theta_\omega W_\mu^3 + \cos\theta_\omega B_\mu. \tag{2.21}$$

Therefore, the Z boson and photon observed at experiments can be understood as different manifestations of the same fields in the EW theory.

The massless gauge fields before the symmetry breaking have 2 degrees of freedom, which correspond to the two transverse polarizations. The longitudinal polarization is left empty for these massless fields because they have no rest frame when propagating in space at the speed of light. After the symmetry breaking, the $W_\mu^\pm/Z_\mu$ gauge fields acquire masses, which also means that they acquire longitudinal polarizations. Therefore, it can be said that the three "would-be" Goldstone bosons are "eaten" by the three gauge bosons, becoming their longitudinal components.

The remaining scalar field $h(x)$ gives rise to the only elementary scalar boson in the SM, known as the Higgs boson. Except two mass terms for W and Z bosons, and a constant term

$$\frac{1}{2}\mu^2 v^2 - \frac{\lambda}{2}v^4 = \frac{1}{2}v^4 \tag{2.22}$$

coming from the potential, all terms in $\mathcal{L}_{Scalar}$ are related to the $h(x)$ field. They can be collected together as $\mathcal{L}_{Higgs}$:

$$\begin{aligned}\mathcal{L}_{Higgs} =& \frac{1}{2}\partial_\mu h(x)\partial^\mu h(x) - \frac{1}{2}m_H^2 h(x)^2 - \frac{1}{2v}m_H^2 h(x)^3 - \frac{1}{8v^2}m_H^2 h(x)^4 \\ &+ [\frac{2}{v}h(x) + \frac{1}{v^2}h(x)^2](m_W^2 W_\mu^\dagger W^\mu + \frac{1}{2}m_Z^2 Z_\mu Z^\mu),\end{aligned} \tag{2.23}$$

where $m_H = \sqrt{2\lambda}v$. The third and fourth terms on the first line of Equation (2.23) correspond to the Higgs triple and quartic couplings, respectively, and they come from the potential term in $\mathcal{L}_{Scalar}$. The terms on the second line of Equation (2.23) correspond to the Higgs-Gauge boson couplings, and they come from the kinetic terms in $\mathcal{L}_{Scalar}$. The strength of these coupling is proportional to the masses of the gauge bosons.

2.3 Yukawa Interaction and Flavor Sector

Adding Dirac mass terms $-m\bar{\psi}\psi = -m(\bar{\psi}_L\psi_R + \bar{\psi}_R\psi_L)$ to the EW theory directly will not be allowed, because they explicitly break the $SU(2)_L \bigotimes U(1)_Y$ symmetry. Instead, the origin of the fermion masses is explained by the interaction between fermionic fields and the scalar field introduced earlier, which was first pointed out by Weinberg in his famous 1967 paper [72]. This interaction is described by the $\mathcal{L}_{Yukawa}$ written as:

$$\mathcal{L}_{Yukawa} = -(Y_u)_{ij}\bar{Q}_L^i u_R^j \tilde{\phi} - (Y_d)_{ij}\bar{Q}_L^i d_R^j \phi - (Y_e)_{ij}\bar{L}_L^i e_R^j \phi + h.c., \tag{2.24}$$

where Y_f $(f = u, d, e)$ are complex 3×3 matrices, $\tilde{\phi} = i\sigma_2\phi^*$ with σ_2 being the second Pauli matrix. Indices i and j run over fermion generations. After the EW symmetry breaking, the $\mathcal{L}_{Yukawa}$ in unitary gauge becomes:

$$\mathcal{L}_{Yukawa} = -\frac{1}{\sqrt{2}}(v + h(x))[(Y_u)_{ij}\bar{u}_L^i u_R^j - (Y_d)_{ij}\bar{d}_L^i d_R^j - (Y_e)_{ij}\bar{e}_L^i e_R^j] + h.c., \tag{2.25}$$

which can be rewritten as:

$$\mathcal{L}_{Yukawa} = -(1 + \frac{h(x)}{v})[(m_u)_{ij}\bar{u}_L^i u_R^j + (m_d)_{ij}\bar{d}_L^i d_R^j + (m_e)_{ij}\bar{e}_L^i e_R^j] + h.c., \tag{2.26}$$

where $m_f = \frac{v}{\sqrt{2}}Y_f$ $(f = u, d, e)$ is known as the fermion mass matrices. The mass matrices can be diagonalized by unitary rotations:

$$m_f = V_f \hat{m}_f W_f^\dagger \ (f = u, d, e), \tag{2.27}$$

where $\hat{m}_f$ are the diagonalized mass matrices. The mass term becomes:

$$\mathcal{L}_{mass} = -(\bar{u}_L V_u \hat{m}_u W_u^\dagger u_R + \bar{d}_L V_d \hat{m}_d W_d^\dagger d_R + \bar{e}_L V_e \hat{m}_e W_e^\dagger e_R) + h.c. \tag{2.28}$$

Going to the so called "mass basis" with $u_L \to V_u u_L$, $u_R \to W_u u_R$, ...

$$\mathcal{L}_{mass} = -(\bar{u}_L \hat{m}_u u_R + \bar{d}_L \hat{m}_d d_R + \bar{e}_L \hat{m}_e e_R) + h.c., \tag{2.29}$$

where the diagonal elements of $\hat{m}_f$ $(f = u, d, e)$ corresponds to the Dirac mass observed in experiments.

On the other hand, these basis transformations will affect the charged-current interactions contained in the third term of $\mathcal{L}_{gauge}$ (Equation (2.9)):

$$\mathcal{L}_{cc} = -\frac{g}{\sqrt{2}}[\bar{u}_L\gamma^\mu(V_u^\dagger V_d)d_L + \bar{\nu}_L\gamma^\mu(V_\nu^\dagger V_e)e_L]W_\mu^+ + h.c, \tag{2.30}$$

where fermion flavor indices are suppressed, $V_u^\dagger V_d$ is known as the Cabibbo-Kobayashi-Maskawa (CKM) matrix [78, 79], and $V_\nu^\dagger V_e$ is known as the PMNS matrix [80, 81].

The CKM matrix is a 3×3 complex unitary matrix and is generally not diagonal as $V_u \neq V_d$. This enables quark flavor mixings in the charged-current interactions. For leptons, however, it is free to choose $V_\nu = V_e$ as there is no neutrino term in the $\mathcal{L}_{Yukawa}$. Therefore, the PMNS matrix only contains diagonal elements SM which imply the conservation of the lepton flavors.

Looking closely at the charged-current interactions in the lepton sector:

$$\begin{aligned}\mathcal{L}_{cc}^{lep} &= -\frac{g}{\sqrt{2}}[(\bar{\nu}_L^e, \bar{\nu}_L^\mu, \bar{\nu}_L^\tau)\gamma^\mu \begin{pmatrix} 1 & 0 & 0 \\ 0 & 1 & 0 \\ 0 & 0 & 1 \end{pmatrix} (e_L, \mu_L, \tau_L)^T]W_\mu^+ + h.c. \\ &= -\frac{g}{\sqrt{2}}(\bar{\nu}_L^e\gamma^\mu e_L + \bar{\nu}_L^\mu\gamma^\mu\mu_L + \bar{\nu}_L^\tau\gamma^\mu\tau_L)W_\mu^+ + h.c.\end{aligned} \tag{2.31}$$

The Lagrangian is invariant under three independent global $U(1)$ symmetry, namely $U(1)_e \bigotimes U(1)_\mu \bigotimes U(1)_\tau$, which correspond to the conserved charges: family numbers of three flavors. Moreover, since the coupling strength is the same across lepton generations in Equation (2.31), it implies that leptons of different flavors are treated equally by the weak interactions. This is the principle known as the lepton flavor universality.

It should be pointed out that the global $U(1)_e \bigotimes U(1)_\mu \bigotimes U(1)_\tau$ symmetry is accidental because it does not arrive by construction. Instead, it is driven by the field content of the SM, namely the absence of right-handed neutrinos.

Chapter 3

Quantum Chromodynamics

The strong interaction is the fundamental force responsible for binding quarks together into hadrons. It is described by QCD which is a gauge theory based on $SU(3)_C$ symmetry. One of the key features of QCD is the phenomenon known as asymptotic freedom, namely strong force weakens at shorter distances. This property differentiates the strong force from all three other fundamental forces. A brief description of the formulation of QCD is given in Section 3.1. Asymptotic freedom predicts that the strong coupling constant, denoted by α_S, is small at short distances, which allows for perturbative expansion of the probability amplitude. However, the expansion parameter α_S at long distances becomes too large and the predictions are therefore no longer reliable. Techniques developed to model QCD phenomenon in this regime are collectively known as nonperturbative-QCD, which is discussed in Section 3.2. Finally, the physics of hadron collisions is discussed in Section 3.3.

3.1 Formulation of QCD

The theory of strong interaction began taking its current form in 1964 when the quark model was independently proposed by American physicist George Zweig [82] and his Ph.D. advisor Murray Gell-Mann [83]. The original objective of this model was to explain the spectrum of new hadrons discovered at a rapid speed at the time. In this early version, mesons and baryons were viewed as composite objects formed by fractionally charged particles with a spin of $\frac{1}{2}$, named "quarks" by Gell-Mann and "aces" by Zweig. They came with several quantum charges and three different flavors: u, d, s. The strange quarks in this model had a higher mass, which explained the mass differences between different baryons and mesons.

This model was successful in explaining why protons of the same charge were bound together – they were bound states of more fundamental particles affected by the strong interactions. However, gaps still existed in this model, most notably the tension with Fermi-Dirac statistics. It was indicated by this model that the wave function for Ω^- (sss) should be symmetrical in the interchange of strange quarks. However, the wave function must be antisymmetric because quarks had half spins in this model. Gell-Mann and his collaborations were able to resolve this problem in the early 1970s by introducing color charges [84]. Under this updated framework, each flavor of quark should come with three colors, namely red, green, and blue. The wave

functions of hadrons were assumed to be singlets of the gauge group $SU(3)_C$. For example, the wave function for Ω^- baryon can be represented as,

$$(sss) \rightarrow (s_r s_g s_b - s_g s_r s_b + s_b s_r s_g - s_r s_b s_g + s_g s_b s_r - s_b s_g s_r), \tag{3.1}$$

which restored the Fermi-Dirac statistics.

The force mediators in this theory, known as "gluons", are massless vector bosons analogous to photons. They are electrically neutral but carry color charges, which enables the gluon-gluon self-interactions. The dynamics of gluon-gluon and quark-gluon interactions are described by the QCD Lagrangian in the following form:

$$\mathcal{L}_{QCD} = -\frac{1}{2}\mathrm{tr}G_{\mu\nu}G^{\mu\nu} + \bar{Q}(i\gamma^\mu D_\mu - m)Q, \tag{3.2}$$

where Q represents colour triplets quark fields $(Q_r, Q_g, Q_b)^T$ of the $SU(3)_C$ group that run over six different flavors, m corresponds to the mass of quarks. $G_{\mu\nu}$ is known as the gluon field strength tensor given by

$$G^a_{\mu\nu} = \partial_\mu A^a_\nu - \partial_\nu A^a_\mu + g_S f^{abc} A^b_\mu A^c_\nu, \tag{3.3}$$

where g_S corresponds to the strength of the gauge coupling. The strong coupling constant is also defined as $\alpha_S = \frac{g_S^2}{4\pi}$, which is analogous to the fine structure constant in QED. t_a are eight generators of the $SU(3)_C$ group, and A^a_μ represent eight gauge fields correspond to eight gluons. f^{abc} is the structure constant defined by $[t^a, t^b] = if^{abc}t^c$. D_μ is the $SU(3)_C$ gauge covariant derivative expresses as:

$$D_\mu = \partial_\mu - ig_S t_a A^a_\mu. \tag{3.4}$$

The non-abelian structure of the $SU(3)_C$ group implies that the third term in Equation (3.3) is nonzero as $SU(3)_C$ generators do not commute with each other. This leads to the trilinear and quartic gluon self-interactions when expanding the kinetic (first) term of the QCD Lagrangian. Feynman diagrams for these gluon self-interactions are shown in Figure 3.1.

In parallel to the development of the quark model, Feynman proposed a model to explain the behavior of deep inelastic scatterings [85]. In this model, Feynman postulated that protons are made of point-like constituents called "partons", and they behave like free particles at high momentum transfer. Since the de Broglie wavelength [86] is given by

$$\lambda = \frac{h}{p}, \tag{3.5}$$

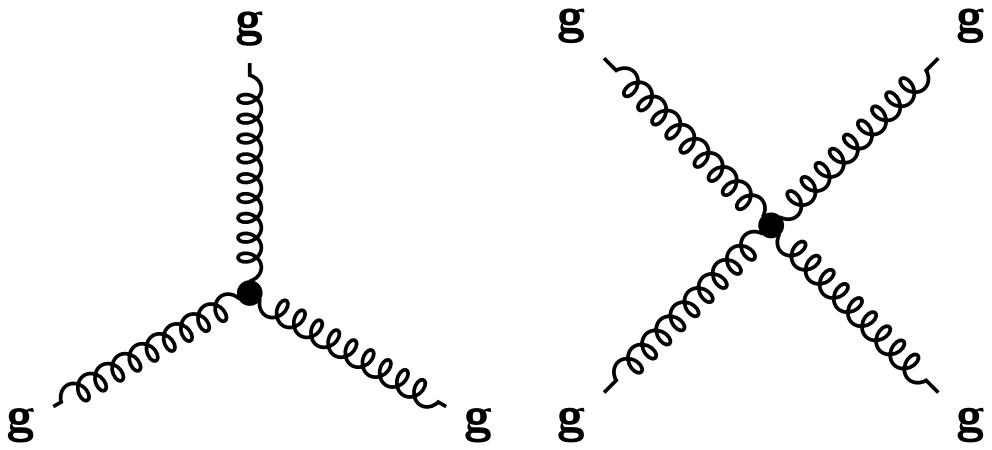

Figure 3.1: Feynman diagrams correspond to the trilinear (left) and quartic (right) gluon self-interactions.

a high momentum transfer corresponds to a smaller wavelength and consequently better experimental resolution at the distance scale. The parton model was an immediate success as it was able to predict the short distance "Bjorken scaling" effects of the strong interaction at a very good precision [87]. Despite the success at describing experimental data, the parton model was still viewed as a phenomenological approximation as Feynman provided no microscopic description of the strong interactions. It was later recognized that partons were matched to quarks, anti-quarks, and gluons within the nucleons.

Two years after Dutch physicist Gerard 't Hooft showed that non-abelian gauge theories were renormalizable [88], major breakthrough came in 1973 when American physicists H. D. Politzer, David Gross, and Frank Wilczek [89, 90] investigated the scale dependency of the strong coupling const α_S. 't Hooft also arrived at similar results himself sometime earlier but he didn't publish his work. At one-loop precision, the $\alpha_S(\mu^2)$ is given by:

$$\alpha_S(\mu^2) = \frac{\alpha_S(\mu_R^2)}{1 + \beta_0 \alpha_S(\mu_R^2) \ln(\frac{\mu^2}{\mu_R^2})} \tag{3.6}$$

where μ is the energy scale, μ_R is known as the renormalization scale, which corresponds to the initial energy scale at which α_S is evaluated. $\beta_0 = (33 - 2n_f)/12\pi$ is a constant that depends on the number of quark flavors that can be considered massless. Even though the strong coupling constant can not be predicted from first principles, Equation (3.6) allows physicists to predict its value at an energy scale μ using its measured value at a different scale μ_R.

Equation (3.6) also reveals that when $n_f < 16$, the strength of the strong coupling decreases as energy increases. In other words, quarks and gluons behave like free particles at very short

distances. The discovery of this property, known as "asymptotic freedom", by Politzer, Gross, and Wilczek brought the SM to its current formulation. Since then it has withstood the test of numerous measurements conducted at various experiments across a wide range of energy spectrum. A summary of recent measurements of α_S is given in Figure 3.2.

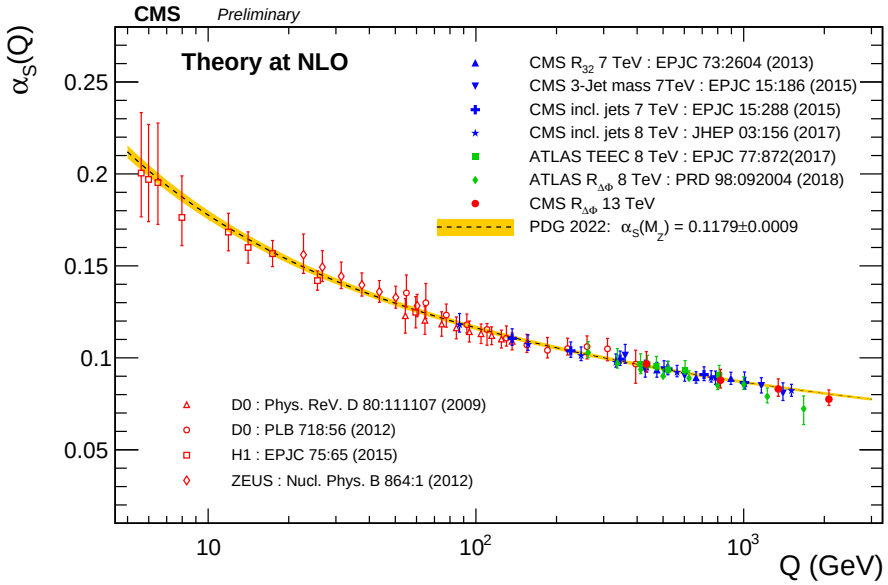

Figure 3.2: The strong coupling constant α_S as a function of energy scale Q, complied by CMS [7]. Measurements done by CMS, ATLAS, and other experiments are shown in points with uncertainty bars. Theoretical predictions based on the renormalization group equation are shown in the dashed line.

3.2 Nonperturbative QCD and Factorization

Perturbation theory is by far the best-developed tool for calculating scattering cross-sections from first principles. Despite being very successful, its predicting power becomes increasingly worse as the expansion parameter grows larger. As discussed earlier, the strong interaction grows stronger very rapidly at low energy which invalidates the perturbative expansions of parameter α_S. The transition from perturbative QCD regime to nonperturbative QCD regime is illustrated in Figure 3.3. The energy scales at which α_S diverges is known as Λ_{QCD}, which is roughly $\mathcal{O}$(300 MeV) [91].

The high-energy hadron collisions involve phenomena occurring on a wide range of distances or energy scales. The process that carries the highest momentum transfer in a collision event, referred to as "hard scattering", typically involves short-distance quark-gluon interactions where production cross-sections calculated by perturbative QCD are still valid. It is therefore critically important to separate the hard scattering from those long-distance effects in order to apply the perturbative QCD in any cross-section calculations. This is achieved through the so-called QCD

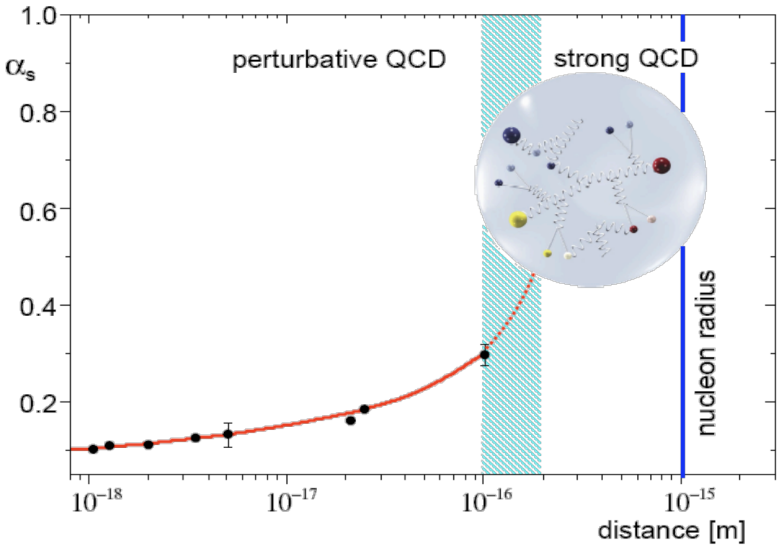

Figure 3.3: Illustration of the dependency of the strong coupling constant α_S on the distance scale, adapted from [8]. Experimental determinations are shown in filled points while theoretical predictions are shown in the red line. The dashed blue band separates the regime where the perturbative approach is still valid from the regime where the perturbative approach is no longer valid.

"factorization theorem" [92] whereby scattering cross-sections are decomposed as the product of several "factors". Each of these factors involves phenomena occurring on a single distance scale. An illustration of the factorization is shown in Figure 3.4.

Protons are made of two up quarks and one down quark, known as the "valence quarks". Since the total mass of the three valence quarks is much smaller than the mass of a proton, most of the proton mass manifests as strong interactions within the nucleons. The mediators of these interactions – the gluons can also spawn a pair of quark and anti-quark, forming part of the proton internal structure known as the "proton sea". Therefore, it is possible for strange, charm, or even bottom quarks to initiate a hard scattering, and the three-quark view of the proton is largely ineffective in the context of hadron collisions. Moreover, before the initial state of the hard scattering reveals itself, the quarks and gluons coming from different protons maintain a relatively large distance between each other, exchanging largely nonperturbative effects. This makes it virtually impossible to predict, from first principle, the structure of the proton before the hard scattering.

A phenomenological approach, inspired by Feynman's parton model, is used to describe the proton's internal structure. Under this approach, protons are seen as streams of quarks and gluons, collectively known as partons. These partons are considered collinear with the proton movement and each carries a fraction of the total proton momentum. The probability of a specific parton a that carries x fraction of the proton momentum is given by the PDF $F_a(x, \mu_F^2)$ where

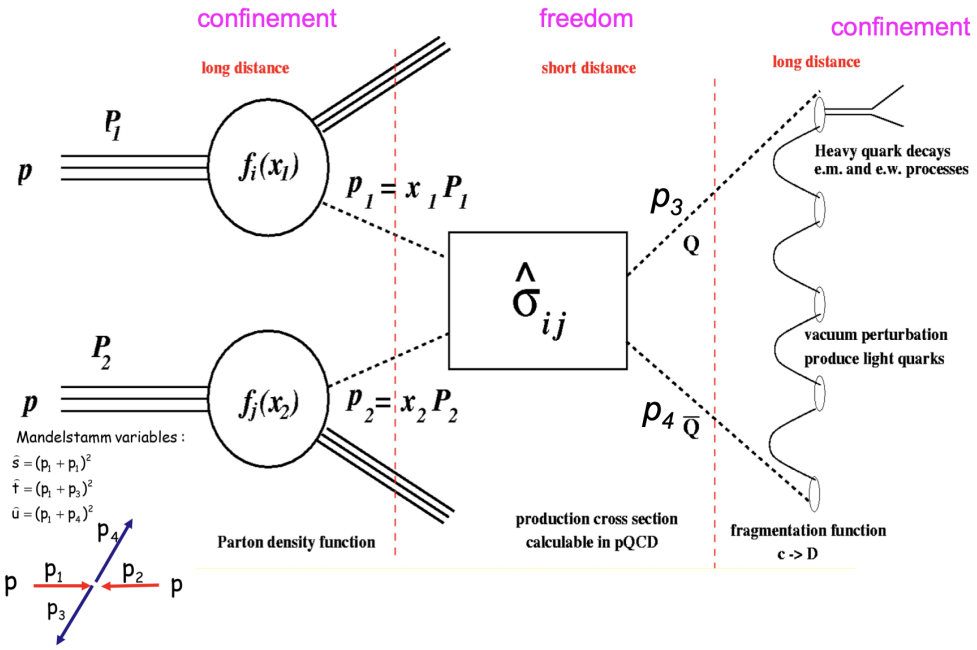

Figure 3.4: Illustration of the physics of proton-proton collisions, adapted from [9]. The two incoming protons are shown on the left. The PDF characterizes the properties of the two partons that participate in a hard interaction. The short-distance physics is handled by the perturbative QCD which is represented with the rectangular box. The outgoing partons fragment into hadrons which is described by the FF.

μ_F is the energy scale that defines the boundary between the short-distance and long-distance dynamics, known as the factorization scale. The cross-section for the inclusive production of a single hadron X from proton-proton collisions is given by the so-called "master formula":

$$\sigma_{pp\to X} = \sum_{a,b} \int_0^1 dx_1 dx_2 dz F_a(x_1, \mu_F^2) F_b(x_2, \mu_F^2) \hat{\sigma}_{ab\to k}(\mu_R^2, \mu_F^2) D_{k\to X}(z, \mu_F^2). \quad (3.7)$$

As PDFs only describe nonperturbative effects below the energy scale μ_F, they must be extracted by experimentalists from data [93, 10]. Analogous to the running of the strong coupling constant α_S, the exact details of PDFs depend on the energy scale at which it is evaluated. The PDFs extracted at one energy scale can be related to the PDFs at another scale energy scale by the so-called "DGLAP" equation [94, 95, 96], provided that $\mu_F \gg \Lambda_{\text{QCD}}$. A comparison of PDFs evaluated at different energy scales is shown in Figure 3.5. The solutions to the "DGLAP" equation are referred to as the renormalized PDFs, which can be used to describe the proton structures universally across experiments.

Descriptions of the short-distance physics are contained in the third factor of Equation (3.7), $\hat{\sigma}_{ab\to k}$, which is the partonic cross-section for the production of partonic final states k from

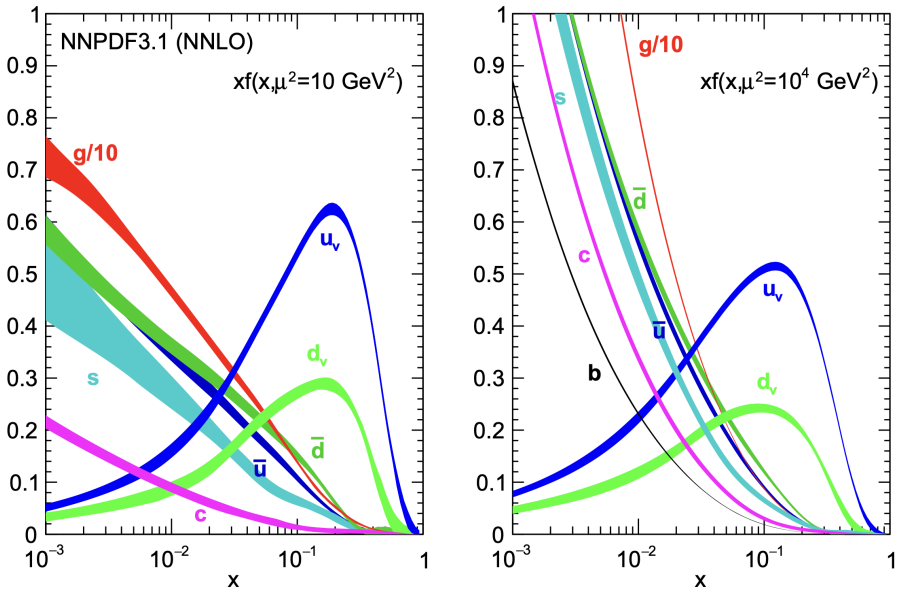

Figure 3.5: The NNPDF3.1 PDFs multiplied by the proton momentum fraction x calculated at at NNLO accuracy in perturbation theory for $\mu^2 = 10$ GeV^2 (left) and $\mu^2 = 10^4$ GeV^2 (right) [10]. The gluon PDFs in both plots are scaled down by a factor of 10 for improved visualization.

initial partons i and j. The initial partons i and j can be quarks, anti-quarks, or gluons, and all possible initial states to produce k are summed over and weighted by the probabilities given by the PDFs. The partonic cross-section is given by:

$$\hat{\sigma}_{ab\to k} = \frac{1}{2s}\int [\prod_{i=1}^{n} \frac{d^3 q_i}{(2\pi)^3 E_i}][(2\pi)^4 \delta^4(\sum_{i=1}^{n} q_i^\mu - (p_a + p_b)^\mu)]|\mathcal{M}_{ab\to k}(\mu_R^2, \mu_F^2)|^2, \tag{3.8}$$

where $\frac{1}{2s}$ is the flux factor with s being the squared center of mass energy of the collision. E_i, q_i and q_i^μ are the energy, three-, and four-momentum of the parton i in partonic final state k, respectively. p_a^μ and p_b^μ are the four momenta of the initial state partons a and b, respectively. $\mathcal{M}_{ab\to k}(\mu_R^2, \mu_F^2)$ is the ME that characterizes the transition rate of the partonic process $ab \to k$.

The partonic cross-section is calculated with the perturbative expansions in powers of the strong coupling constant:

$$\hat{\sigma}_{ab\to k} = \hat{\sigma}_0 + \alpha_s(\mu_R^2)\hat{\sigma}_1 + \alpha_s^2(\mu_R^2)\hat{\sigma}_2 + ..., \tag{3.9}$$

where the linear and quadratic terms of $\alpha_s(\mu_R^2)$ are referred to as the Leading Order (LO) and Next-to-Leading Order (NLO) terms, respectively.

The last factor in Equation (3.7) is referred to as the FF [97] that encodes information on how

color-charged partons produced in hard scatterings are turned into colorless bound states X (hadrons). More specifically, the fraction z of the parton momentum is transferred to the hadron X, and the associated probability at energy scale μ_F is represented by $D_{k\to X}(z, \mu_F^2)$. Similar to the situation of the PDF determination, FFs constitutes in general nonperturbative components in QCD factorization, which can not be predicted from first principle by theoretical methods. Instead, FFs are extracted from experiments and the μ_F dependency of the FF is perturbatively calculable using the "DGLAP" equation.

3.3 Hadron Collisions

In addition to the cross-section calculations, collider physicists often need simulated events to compare with data. Several main stages are required to simulate the full picture of a hadron collision event down to the level of stable particles before the detector response kicks in. These main stages include: hard scattering, Parton Shower (PS), underlying event, hadronization, and unstable particle decay.

Generation of the hard scattering events is usually done by ME event generators, such as MadGraph5_aMC@NLO [98] and powheg [99]. Depending on what processes are targeted, these ME generators determine the relevant Feynman diagrams and use MC methods to generate initial- and final-state particles with properties such as four-momenta and spins. Each generated event is weighted by the corresponding transition rate, which is calculated numerically using the fixed-order perturbative theory. The NLO expansions are commonly used in these perturbative calculations, which typically means one extra parton is added to the ME.

Beyond the NLO, it will become increasingly challenging for numerical calculations to be implemented in ME generators. Therefore, the missing high-order terms in ME are often approximated using a method known as the PS. The PS uses splitting functions [100] to characterize the emissions of soft and collinear partons by the initial-state and final-state partons. Since the emitted partons can further emit partons themselves, this process will include partons with lower and lower energy until perturbative theory breaks down, and finally produces a shower of partons. The interaction scale in PS is considered to be perturbative.

In addition to the hard scattering process, multiple soft parton-parton interactions exist in every collision event. These soft parton interactions, referred to as underlying event, fill events with soft partons which can then interfere with hard scattering. These interactions typically carry a low momentum transfer and thus fall into the nonperturbative QCD regime. They are often described by data-driven phenomenological models in event generators [101].

The FF described in Section 3.2 does not give a detailed description of the mechanism by which partons produced in hard scatterings or heavy particle decays form the hadrons that are observed in the final state. For this reason, FFs are rarely used in MC event generators. A more physical description would be: i) high-energy partons will first create a cascade of partons through the PS

and ii) low-energy partons that emerge from the PS will then pick up color-matching partners to form color-neutral hadrons observed in the final state. The transition from low-energy partons to hadrons is referred to as hadronization, which is inherently an unperturbative process due to the low interaction scale near the end of the PS. Therefore, it can only be simulated using phenomenological models such as the so-called "Lund string" model [102].

Unstable hadrons produced in the hadronization process will decay sequentially, which is typically the final stage of event generation. These decays are often simulated by phenomenological models, such as the EvtGen package [103], which take input from Particle Data Group (PDG) [74].

Chapter 4

Beyond the Standard Model

Although the SM represents our best understanding of the fundamental particles and their interactions, it does contain some deficiencies. On the one hand, it remains silent on some important phenomena, such as gravity, dark matter, and dark energy. On the other hand, several anomalies have emerged from recent experiments, those in the flavor sector in particular. Two of the experimental results in the flavor sector that work against the SM and their phenomenological implications are discussed in Section 4.1. Section 4.2 introduces the leptoquark model that can be used to explain the unexpected results that occurred in the flavor sector.

4.1 BSM Phenomenology

As discussed in Section 2.3, the renormalizable SM Lagrangian exhibits a few continuous global symmetries, namely the $U(1)_e \bigotimes U(1)_\mu \bigotimes U(1)_\tau$ that gives rise to the conservation of lepton family numbers. Unlike gauge symmetries of the SM, which arise at the outset of the construction, these global $U(1)$ symmetries emerge accidentally due to the assumption (massless neutrino) that is solely driven by phenomenology. Despite the accidental nature of these symmetries, they have stood up to the tests of almost all particle physics experiments to date.

In fact, the first and so far the only hint of the broken global symmetries did not appear until the turn of the century through the oscillation of atmospheric neutrinos [11, 36]. Figure 4.1 shows the strong evidence of neutrino oscillations presented by the Super-Kamiokande Collaboration. This remarkable observation directed significant interest from both theorists and experimentalists to the flavor sector of the SM. On the one hand, it cements the calls for extensions of the SM by demonstrating the mixing of neutrino flavors. On the other hand, it also suggests that the $U(1)$ symmetries are indeed broken, and the CLFV is also expected to occur.

Although the exact mechanism behind neutrino mass remains unclear, it can be induced through two distinct ways that only require minimal departures from the original formulation of the SM. By adding right-handed neutrino fields, the Yukawa coupling [72] that describes the emergence of Dirac fermion masses can be naturally extended to neutrinos. The neutrino mass can also be realized by introducing an effective operator [104], sometimes referred to as the Weinberg operator. This operator gives rise to Majorana neutrino mass terms upon spontaneous symmetry

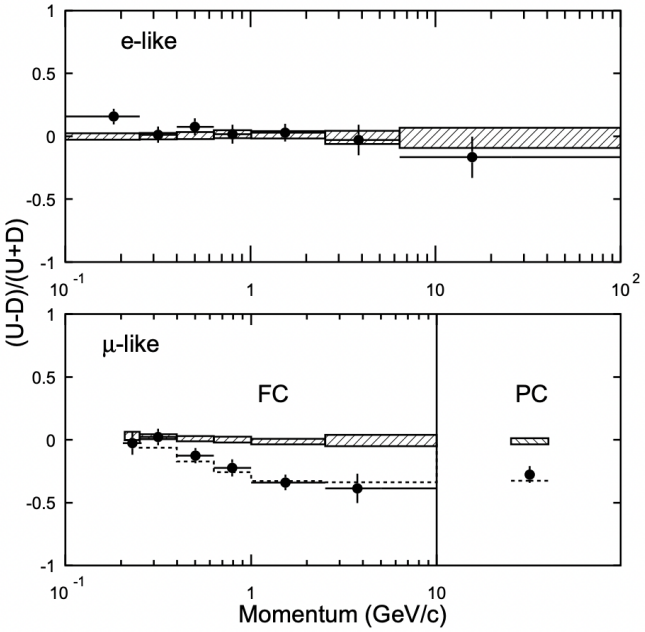

Figure 4.1: Evidence of neutrino oscillation presented by the Super-Kamiokande Collaboration in 1998 [11]. The asymmetry in the zenith angle is plotted as a function of momentum for e-like events (upper panel) and μ-like events. The data are represented with filled points. The expected distributions under the hypothesis of no neutrino oscillation are shown with filled bands while the dashed line is the expected distribution for the alternative hypothesis.

breaking. This operator is however nonrenormalizable, meaning its underlying theory is valid only up to a specific energy scale. Nevertheless, it can be viewed as an effective description of high-energy physics at a low-energy scale. This type of approach is known as the EFT, which is discussed further in Chapter 5.

In either case, the mass of neutrinos is accounted for and Equation (2.24) can be subsequently updated to include neutrino mass terms. The presence of massive neutrino fields also means that the PMNS matrix introduced in Section 2.3 will no longer be fully diagonal, for the same reason why the CKM matrix contains off-diagonal elements. The strength of the neutrino flavor mixing is therefore governed by the off-diagonal elements of the PMNS matrix – a nearly perfect analog to the CKM matrix.

The same PMNS matrix can also give rise to the CLFV process through loop diagrams involving charged current, as illustrated in Figure 4.2. However, these diagrams are highly suppressed and phenomenologically negligible due to the small neutrino mass relative to the EW scale. Therefore, any experimental observation of CLFV will be unambiguous evidence of new physics beyond the SM.

Recent tests of lepton flavor universality conducted by the LHCb [105] and various other

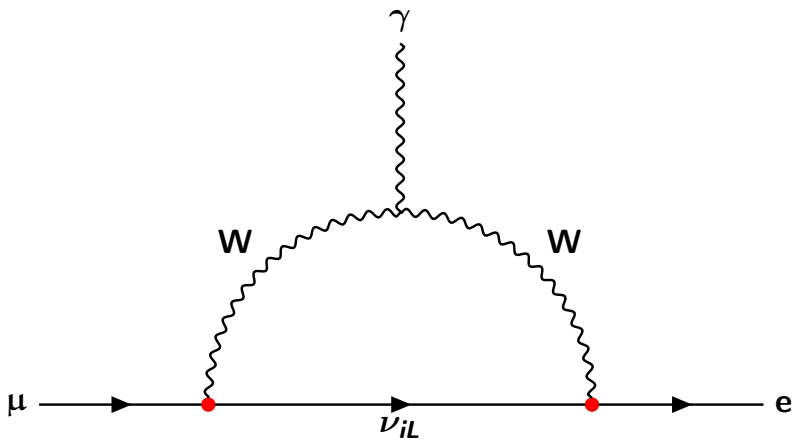

Figure 4.2: Feynman diagram that shows μ →e transition via W loop. The PMNS matrix elements enter this diagram through the starting and end points in the W loop, indicated with red dots. The index *i* runs over lepton generations.

experiments [12] in the b→c transitions established a mild tension (3σ) with respect to the SM predictions. These experiments measured the following ratio of branching fractions:

$$\mathcal{R}(D) = \frac{\Gamma(B \to D\tau^- \bar{\nu}_\tau)}{\Gamma(B \to D\mu^- \bar{\nu}_\mu)}, \tag{4.1}$$

which is sensitive to new physics where the flavor structure is different.

This anomaly is known as the "$\mathcal{R}(D)$" anomaly and its situation as of Summer 2023 is summarized in Figure 4.3. As discussed in Section 2.3, the coupling strength of the weak charged current does not distinguish between lepton flavors. However, results from these measurements seem to suggest the W→ $\tau\nu$ decay channel is favored over W→ $\mu\nu$ decay channel. Not only did these measurements provide a direct hint towards Lepton Flavor Universality Violation (LFUV), it also prompted renewed experimental interest in CLFV search since models that accommodate LFUV generally give rise to CLFV as well [106].

4.2 Leptoquark Model

Leptoquarks are hypothetical scalar or vector bosons that were first proposed nearly half a century ago [107]. They are simultaneously charged with color, isospin, and hypercharge quantum numbers, and thus can mediate lepton-quark couplings. When imposing the SM $SU(3)_C \bigotimes SU(2)_L \bigotimes U(1)_Y$ gauge symmetry, a large pool of possible leptoquark candidates can be reduced to six scalar leptoquarks and six vector leptoquarks [35], which is summarized in Table 4.1.

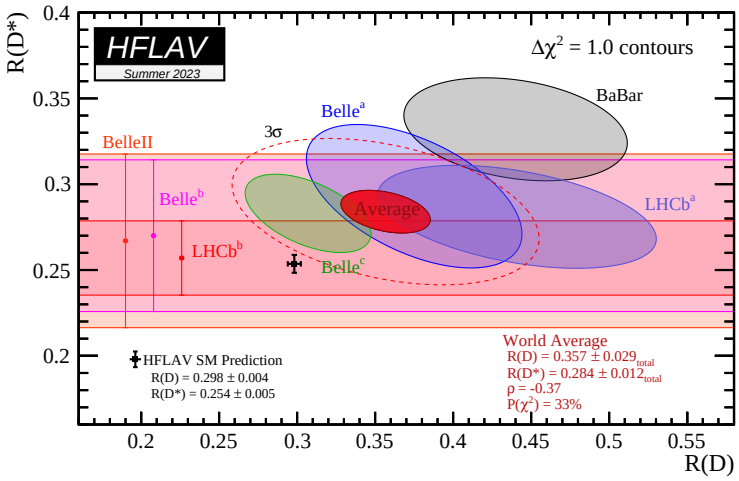

Figure 4.3: Recent results on $\mathcal{R}(D)$ and $\mathcal{R}(D^*)$ measurements compiled by the HFLAV Group [12]. Results are shown in a two-dimensional plane with the x-axis and y-axis representing $\mathcal{R}(D)$ and $\mathcal{R}(D^*)$, respectively. Contours with solid line boundaries represent results published by various experiments. The world average is shown in the middle. The 3σ contour is represented with a red dashed line. The SM prediction is represented with a data point with error bars.

A lot of phenomenological interests have gravitated towards the leptoquark models recently due to the emergence of $\mathcal{R}(D)$ anomaly. Taking the U_1 leptoquarks as an example. Assuming they only interact with left-handed fermions, the interaction term can be written as:

$$\lambda \beta_L^{ij} \bar{Q}_L^i \gamma^\mu L_L^j U_{1\mu}, \tag{4.2}$$

where λ is the coupling strength, and β_L^{ij} is a 3×3 matrix that encodes the flavor structure of U_1 interactions. This term can contribute at the tree level to the b→c transitions where the anomaly is reported. A side-by-side comparison of Feynman diagrams for the SM and leptoquark contributions to this process is shown in Figure 4.4.

An explanation of the $\mathcal{R}(D)$ anomaly is possible if U_1 leptoquarks interact strongly with the third generations while leaving out or interacting very weakly with the first and second generations. In other words, a β_L^{ij} matrix of the form

$$\begin{pmatrix} 0 & 0 & 0 \\ 0 & \mathcal{O}(0.01) & \mathcal{O}(0.1) \\ 0 & -\mathcal{O}(0.1) & 1 \end{pmatrix}, \tag{4.3}$$

Table 4.1: Possible leptoquark candidates that respect $SU(3)_C \bigotimes SU(2)_L \bigotimes U(1)_Y$ gauge symmetry, summarized in [35]. The spin-0 fields correspond to scalar leptoquark while spin-1 fields correspond to vector leptoquark.

$(SU(3), SU(2), U(1))$	Spin	Symbol	Type
$(\bar{\mathbf{3}}, \mathbf{1}, -2/3)$	0	$\bar{S}_1$	$\overline{RR}(\bar{S}_0^{\bar{R}})$
$(\bar{\mathbf{3}}, \mathbf{1}, 1/3)$	0	S_1	$LL(S_0^L)$, $RR(S_0^R)$, $\overline{RR}(S_0^{\bar{R}})$
$(\bar{\mathbf{3}}, \mathbf{1}, 4/3)$	0	$\tilde{S}_1$	$RR(\tilde{S}_0^R)$
$(\mathbf{3}, \mathbf{2}, 1/6)$	0	$\tilde{R}_2$	$RL(\tilde{S}_{1/2}^L)$, $\overline{LR}(\tilde{S}_{1/2}^{\bar{R}})$
$(\bar{\mathbf{3}}, \mathbf{2}, 7/6)$	0	R_2	$RL(S_{1/2}^L)$, $LR(S_{1/2}^R)$
$(\bar{\mathbf{3}}, \mathbf{1}, -2/3)$	0	S_3	$LL(S_1^L)$
$(\mathbf{3}, \mathbf{1}, -1/3)$	1	$\bar{U}_1$	$\overline{RR}(\bar{V}_0^{\bar{R}})$
$(\mathbf{3}, \mathbf{1}, 2/3)$	1	U_1	$LL(V_0^L)$, $RR(V_0^R)$, $\overline{RR}(V_0^{\bar{R}})$
$(\mathbf{3}, \mathbf{1}, 5/3)$	1	$\tilde{V}_1$	$RR(\tilde{V}_0^R)$
$(\bar{\mathbf{3}}, \mathbf{2}, -1/6)$	1	$\tilde{V}_2$	$RL(\tilde{V}_{1/2}^L)$, $\overline{LR}(\tilde{V}_{1/2}^{\bar{R}})$
$(\bar{\mathbf{3}}, \mathbf{2}, 5/6)$	1	V_2	$RL(V_{1/2}^L)$, $LR(V_{1/2}^R)$
$(\mathbf{3}, \mathbf{3}, 1/3)$	1	U_3	$LL(V_1^L)$

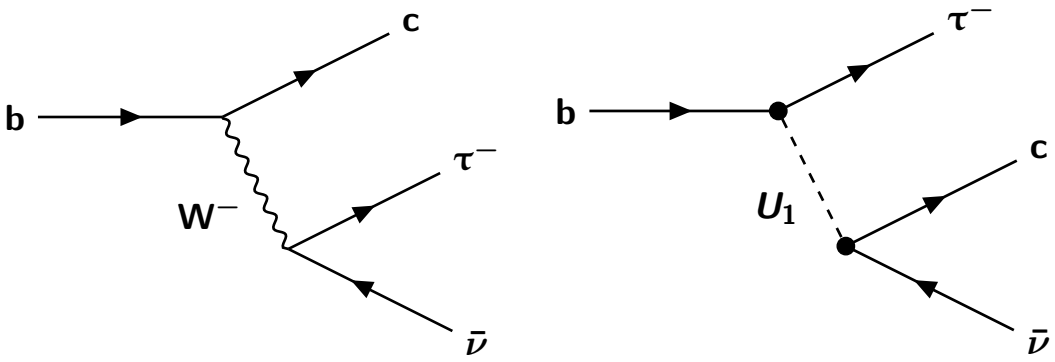

Figure 4.4: Representative Feynman diagram for tree-level $b \to c\tau\nu$ transition. The SM contribution is shown on the left. Possible contributions from the U_1 leptoquark, represented with a dashed line in the diagram, are shown on the right.

could be used to explain the $\mathcal{R}(D)$ anomaly, as pointed out by Ref. [108]. Direct searches for leptoquarks decaying into tau leptons (i.e. third generation) have been performed by both ATLAS [109, 110] and CMS [111, 112] Collaborations, and so far no conclusive evidence has been reported.

Secondly, the leptoquark model provides an interesting connection between the $\mathcal{R}(D)$ anomaly and flavor-changing phenomena at a higher energy scale. For example, the $\mathcal{R}(D)$ anomaly can also be explained by the S_1 leptoquark listed in Table 4.1. Because S_1 can interact with left-handed fields, the b quark and neutrino in the interaction vertex can be replaced with a top quark and a muon, as illustrated in Figure 4.5. This results in the flavor-violating $t \to \ell\ell' q$ decay, which is strongly suppressed in the SM by the mass hierarchy of both quarks and leptons. It was suggested in Ref. [113] that the $\mathcal{R}(D)$ anomaly, if true, can give rise to a sizable rate of CLFV events, which reaches $\mathcal{O}(10^{-6})$ at tree-level for $t \to \ell\ell' c$ process involving a top quark.

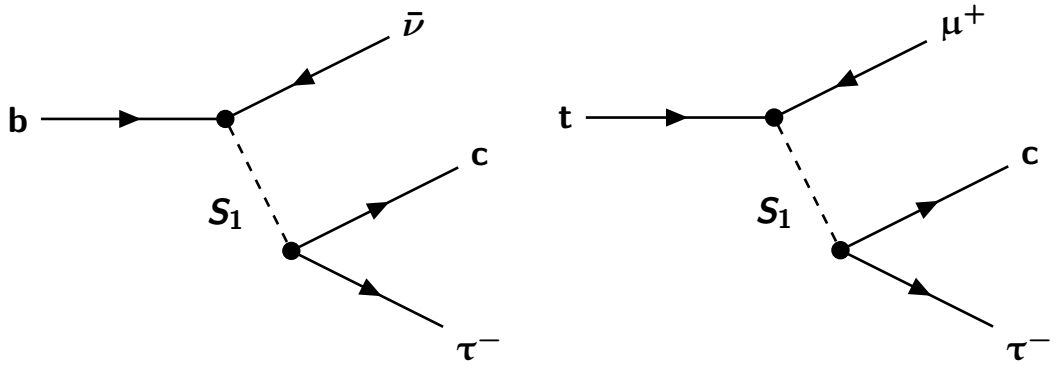

Figure 4.5: Feynman diagrams of processes mediated by S_1 leptoquark, represented with a dashed line in both diagrams. The left diagram shows a possible explanation for $\mathcal{R}(D)$ anomaly offered by the S_1. The same S_1 can give rise to CLFV in the top quark sector, which is shown on the right.

Finally, the CERN LHC can provide sensitivity to CLFV searches in two- or three-body decays of heavy particles, $X \to \ell\ell'(Y)$, and in heavy-particle production, $pp \to \ell\ell' X$. Here, X refers to a heavy SM particle such as a top quark or a Higgs, W, or Z boson, Y denotes an additional generic SM particle. For CLFV processes involving the heaviest of all fundamental particles, the top quark, competitive sensitivity is predicted at the LHC compared to previous bounds on such interactions [114]. Therefore, a search for CLFV in the top quark sector at the LHC could shed light on these flavor anomalies and further our understanding of the broken global symmetries.

Chapter 5

Effective Field Theory

The concept of effective interactions has been around for nearly a century since Fermi first introduced it in 1933 [115] to explain the β decay. The modern approach to effective interactions builds on the assumption that there is a separation between energy scales of different physics phenomena. When describing low-energy physics, the heavy mediators can be approximated to be point-like, and thus described by an effective coupling. This type of approach, collectively known as EFT, has been very successful in simplifying calculations and describing low-energy experiments with stunning precisions. Depending on the energy scale at which EFTs are operating, they can be classified into different versions. One version of the EFT that operates below the EW scale and integrates out all the heavy fields is called the Low-Energy Effective Field Theory (LEFT), which is described in Section 5.1. Another version of the EFT that operators above the EW scale is called the Standard Model Effective Field Theory (SMEFT). It retains all the SM fields and $SU(3)_C \otimes SU(2)_L \otimes U(1)_Y$ gauge symmetry. A description of the SMEFT is given in Section 5.2.

5.1 Low-Energy EFT

It is safe to say that Fermi did not have a complete description of the weak interactions in 1933. Instead, he constructed a phenological model to explain the β decay. In his theory, he modified the QED to include the following interaction vertex between four fermion fields:

$$-\frac{G_F}{\sqrt{2}}(\bar{\psi}_p \Gamma \psi_n)(\bar{\psi}_e \Gamma \psi_\nu) \tag{5.1}$$

where G_F is known as the Fermi constant, ψ are Dirac fields that represent up quark (proton), down quark (neutron), electron, and electron neutrino. Γ is a 4×4 matrix that encodes the Lorentz structure of the effective interaction.

From the point of view of the SM, the β decay is described by the charged-current interaction, whose amplitude in perturbative theory can be derived from the Lagrangian specified in Equation (2.30):

$$\frac{1}{8}(\bar{u}\Gamma d)\frac{g^2}{q^2 - m_W^2}(\bar{e}\Gamma\nu), \tag{5.2}$$

where q and m_W are the momentum and mass of the W propagator, respectively, and g is the strength of the $SU(2)_L$ gauge interaction as mentioned in Section 2.1.

Because $m_W \approx 80.4$ GeV, which is considered to be a lot higher than the energy scale associated with the β decay, the momentum of the W boson can be ignored and Equation (5.2) reduces to:

$$-\frac{g^2}{8m_W^2}(\bar{u}\Gamma d)(\bar{e}\Gamma\nu), \tag{5.3}$$

which is exactly the Fermi's theory with:

$$\frac{G_F}{\sqrt{2}} = \frac{g^2}{8m_W^2}. \tag{5.4}$$

As illustrated in Figure 5.1, Fermi's theory of weak interaction works very well at low energy. However, it ultimately breaks down when the momentum transfer is high enough.

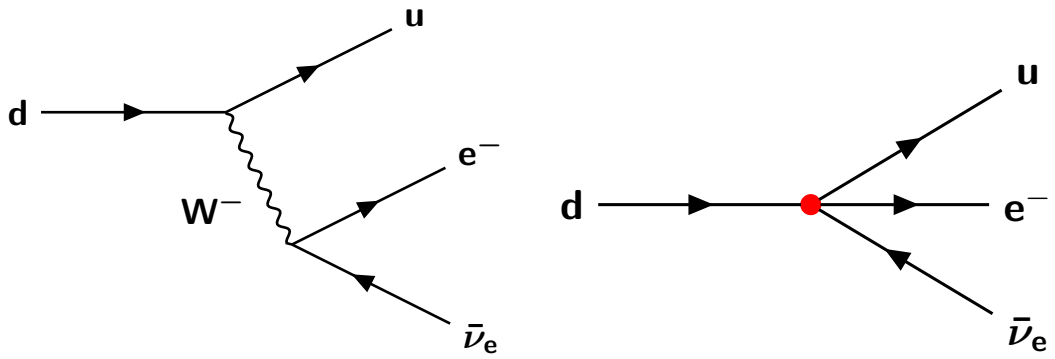

Figure 5.1: Representative Feynman diagrams for β decay. The SM description of this phenomenon with a massive weak mediator is illustrated on the left. At low energy, the heavy weak boson is approximated to be point-like in Fermi's theory of weak interactions, which is illustrated on the right. The effective coupling between four fermions indicated with a red dot, can be used to describe the same phenomenon.

The LEFT that we know today is not that different from Fermi's original theory of weak interactions. It operates below the EW scale, where the gauge symmetry of the SM reduces to $SU(3)_C \bigotimes U(1)_{EM}$. It makes no explicit assumptions about the structure of the theory at higher energy. Except for the intermediate vector bosons, the Higgs boson, and the top quark, all other fields are considered in the LEFT.

The LEFT is usually deployed in a "bottom-up" way to model high-energy physics, whose structure is not yet known. For example, assuming new physics at a very high energy scale is responsible for

the $\mathcal{R}(D)$ anomaly described in Section 4.1, the phenomenon observed at low-energy experiments can be therefore parameterized by the LEFT, as illustrated in Figure 5.2.

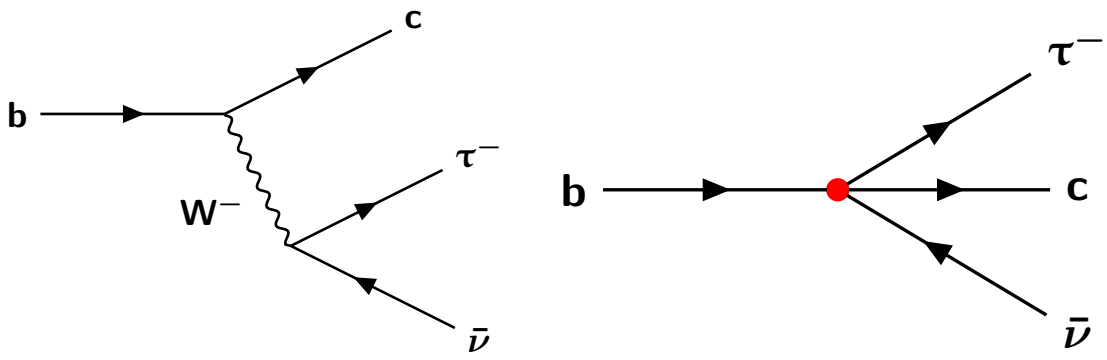

Figure 5.2: Representative Feynman diagram for b→c transtion in the SM (left). This process might also be enhanced by new physics with a much higher energy scale. The potential contributions from new physics can therefore be described by an effective coupling between four fermions, which is illustrated on the right.

5.2 Standard Model EFT

The SM can also be viewed as an EFT as it is commonly accepted that it is not valid up to an arbitrarily high energy scale. This view leads to a different version of EFT, known as the SMEFT. The SMEFT builds higher dimensional operators out of SM fields to systematically study SM deviations. These higher dimensional operators respect $SU(3)_C \bigotimes SU(2)_L \bigotimes U(1)_Y$ gauge symmetry and are added to SM Lagrangian:

$$\mathcal{L}_{\text{SMEFT}} = \mathcal{L}_{\text{SM}}^{(4)} + \frac{1}{\Lambda} C^{(5)} O^{(5)} + \frac{1}{\Lambda^2} \sum_a C_a^{(6)} O_a^{(6)} + ..., \tag{5.5}$$

where $\mathcal{L}_{\text{SM}}^{(4)}$ is the renormalizable Lagrangian of the SM. The $O^{(n)}$ denote dimension-n nonrenormalizable operators, and $C^{(n)}$ are the corresponding WCs. The high dimensional operators are suppressed by powers of a mass scale Λ where new physics is presumed to emerge.

The only SM gauge-invariant operator at dimension-five is the Weinberg operator [104], illustrated in Figure 5.3, of the following form

$$O^{(5)} = (\phi \cdot \bar{L})(L \cdot \phi), \tag{5.6}$$

where ϕ is the Higgs doublet mentioned in Section 2.2.

This operator gives rise to the Majorana mass terms for neutrinos upon EW symmetry breaking:

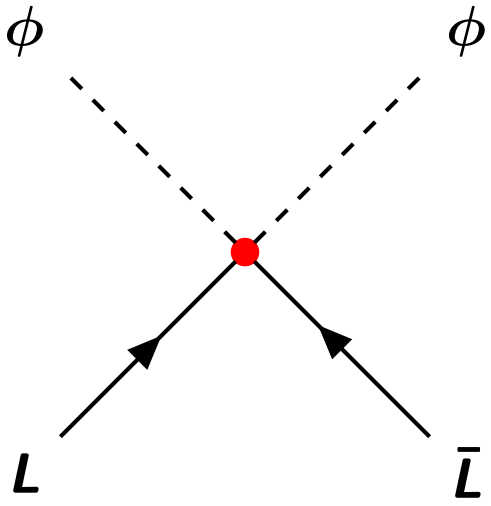

Figure 5.3: Illustration of the lepton-number violating Weinberg operator.

$$m_{\text{Majorana}} = C^{(5)} \frac{v^2}{\Lambda}, \tag{5.7}$$

where v is the vacuum expectation value mentioned in Section 2.2.

Many more dimension-six operators are invariant under the SM gauge transformations. They can be classified by the so-called Warsaw basis [116]. These operators are more relevant to this thesis as they can be formed by four fermionic fields that facilitate the flavor-violating $\ell\ell'$qt interactions. A summary of these four-fermion operators is given in Section 12.1.

Part II
Experimental Apparatus

Part II of this thesis gives a brief description of the experimental apparatus that provides the physical environment and data collection for analyses described in Part III and Part IV. Questions raised in Section 2.3 require the refinement of our knowledge of nature at its smallest scale. The LHC is best prepared to help us achieve this goal as it is the most powerful particle physics accelerator in the world, colliding protons at a center-of-mass energy of 13.6 TeV in 2023. The CMS detector is one of several detectors that is capable of recording data under the harsh physical environment created by the LHC. Part II is organized as follows. Chapter 6 discusses the LHC and its surrounding CERN accelerator complex. An overview of the CMS detector is given in Chapter 7. Details on event reconstruction in CMS are given in Chapter 8. I personally contributed to the CMS operations (taking responsibilities in roles such as the shifter leader, technical shifter, and Tracker DOC expert) and Phase-2 Upgrade, which are discussed in Chapter 9 and Chapter 10, respectively. Materials presented in Chapter 6-Chapter 8 are borrowed from various publications and public documents, to which I made no direct contributions. Except where noted, materials (i.e. figures and tables) presented in Chapter 10 are prepared by myself.

Chapter 6

The Large Hadron Collider

The LHC [39] is a circular particle physics accelerator located near Geneva, Switzerland. It collides protons at four interaction points, which correspond to the four major experiments hosted by the LHC: the A Large Ion Collider Experiment (ALICE) [117], ATLAS [118], CMS [29], and LHCb [119] experiments. Accelerating proton beams to TeV-level requires a chain of acceleration stages before proton beams are energetic enough for the final injection into the LHC ring. These stages of acceleration and the whole CERN accelerator complex are discussed in Section 6.1. The number of collision events delivered by the LHC is measured in units called "luminosity". The definition of luminosity is discussed in Section 6.2. The long-term schedule for the LHC is discussed in Section 6.3.

6.1 The CERN Accelerator Complex

Installed in a 27 km circular tunnel previously used for the Large Electron-Positron (LEP) collider [120], the LHC is the largest and most powerful particle accelerator that ever existed. The primary objective of the LHC is to deliver high-intensity and high-energy proton collisions, allowing physicists to study the laws of nature at the most fundamental scale. This objective is achieved through a complex system of accelerators, which rapidly accelerates protons to the target energy in a multistage process, maintains the proton energy, focuses, and collides them precisely at the designated locations. The full system is illustrated in Figure 6.1.

Until 2018, an older linear accelerator (LINAC 2) [121] was used to initially accelerate protons to 50 MeV. After 2018, negative hydrogen ions (H^-) are accelerated by the Linear Accelerator 4 (LINAC 4) [122] to 160 MeV using cylindrical conductors charged by radiofrequency cavities. Quadrupole magnets are placed along the accelerator to keep the beam focused. The hydrogen ions are then stripped of their two electrons during injection into the Proton Synchrotron Booster (BOOSTER) [123], which is a circular accelerator that boosts protons to 2 GeV. Protons are then injected into the Proton Synchrotron (PS) [124], which was CERN's first synchrotron. The PS utilizes alternating-gradient focusing, a principle developed by Brookhaven physicists [125, 126], and accelerates protons to 25 GeV before injecting them into the second largest machine in the accelerator complex called the Super Proton Synchrotron (SPS) [127]. The SPS is a 7 km circular accelerator that uses room-temperature dipole magnets to bend the protons. Protons

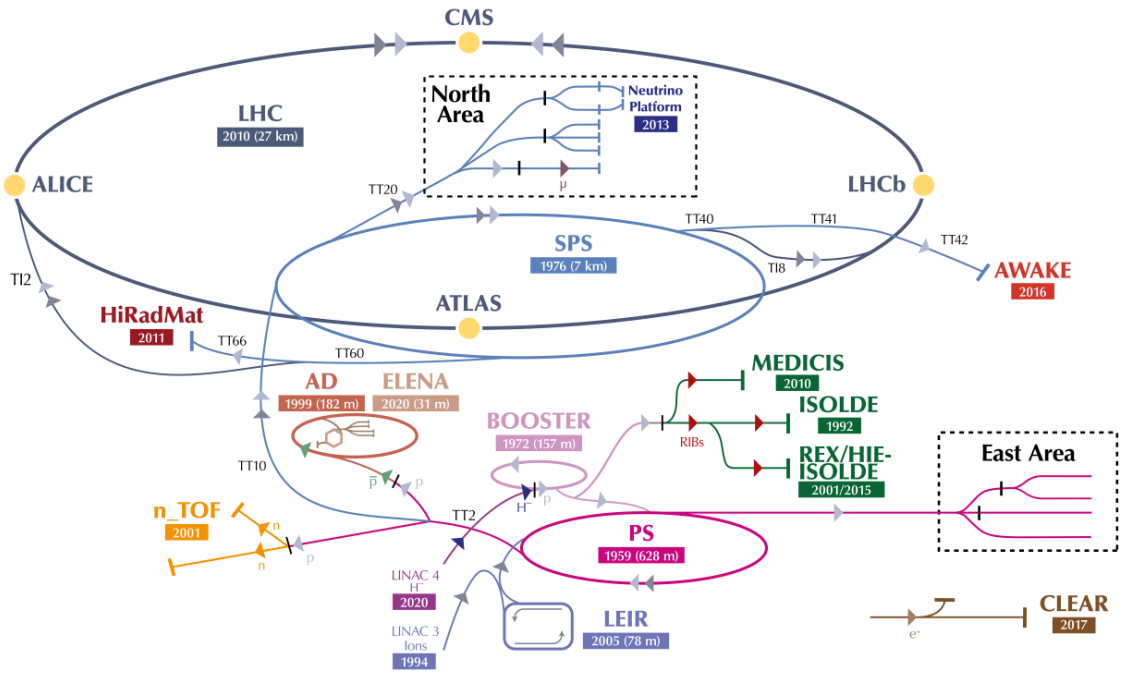

Figure 6.1: Layout of the CERN accelerator complex, adapted from [13].

are accelerated by the SPS to an energy of 450 GeV before entering the final accelerator ring – the LHC. The LHC uses super-conducting dipole magnets up to 8.4 T to bend protons and ultimately accelerate them to 6.8 TeV during Run-3. Quadrupole magnets are placed at four collision points to focus the proton beams, which eventually collide at the Interaction Point (IP) of each detector.

6.2 Luminosity

The total number of events of a given process is given by

$$N = \int \mathcal{L}\sigma dt, \tag{6.1}$$

where σ is the cross-section of the process and $\mathcal{L}$ is known as the instantaneous luminosity that can be written in a simplified form

$$\mathcal{L} = \frac{N^2 f}{A}, \tag{6.2}$$

where N is the total number of protons in each beam, f is the frequency of the beam crossing, and A is the cross-sectional area of the beam crossing.

The LHC is designed to deliver an instantaneous luminosity $\mathcal{L} = 10^{34}\text{cm}^{-2}\ \text{s}^{-1}$ which corresponds to an event rate of 1 billion collisions per second, assuming the inelastic cross-section $\sigma_{\text{in}}^{\text{pp}} = 100$ mb. The delivered integrated luminosity by year of data taking is shown in Figure 6.2 (left).

The peak instantaneous luminosity reached $2 \times 10^{34}\ \text{cm}^{-2}\text{s}^{-1}$ in 2018, which is a factor of two larger than the design value of the LHC. High instantaneous luminosity means more collision events are delivered by the LHC, but it also brings a side effect – multiple interactions per crossing, also known as PU. The average number of PU increased from 27 in 2016 to 52 in 2023, creating challenges for data-taking and event reconstruction. The PU profile for each year of data taking is shown in Figure 6.2 (right).

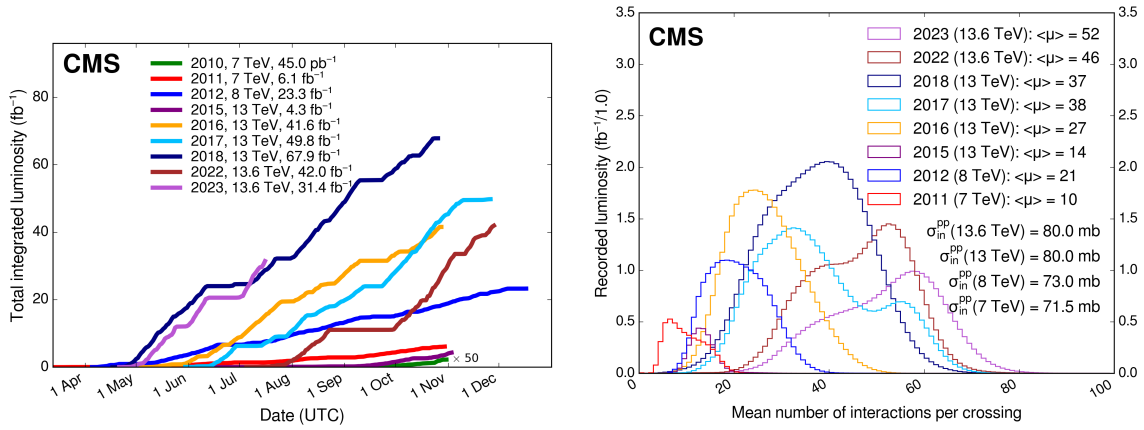

Figure 6.2: Delivered integrated luminosity versus time (left) and recorded luminosity versus mean number of interactions per crossing (left), adapted from [14].

6.3 LHC Long Term Schedule

The Long Shutdown (LS) 2 lasted for over three years until the LHC resumed data taking in mid-2022. The ongoing run of the LHC, known as Run-3, is expected to end in 2025. Between 2026 and 2028 is a period known as the LS 3, when major upgrades of the LHC and the hosted experiments will take place. A new era of the LHC, known as the HL-LHC [128] will arrive in 2029, after which the instantaneous luminosity will gradually increase by up to a factor 7.5 more than the designed value. The HL-LHC is expected to be operational for more than 10 years until the 2040s. A summary of the LHC future schedule is shown in Figure 6.3.

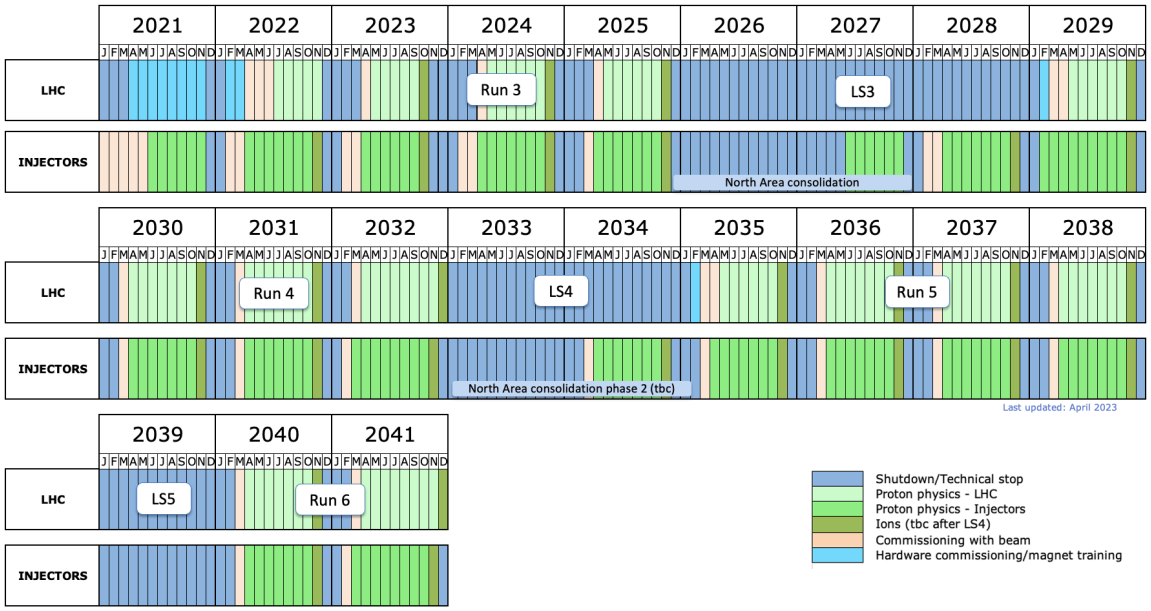

Figure 6.3: Future long term schedule of the LHC, adapted from [15] in November 2023.

Chapter 7

The Compact Muon Solenoid Detector

The CMS detector [29] is one of the two general-purpose detectors involved in the discovery of the Higgs boson in 2012 [4, 5]. It is located around 100 meters underground near the French town of Cessy. The full detector weighs over 14 thousand tonnes, and is roughly cylindrically symmetric with a length and diameter of 21 and 15 meters, respectively. It consists of several layers of subsystems, as illustrated in Figure 7.1.

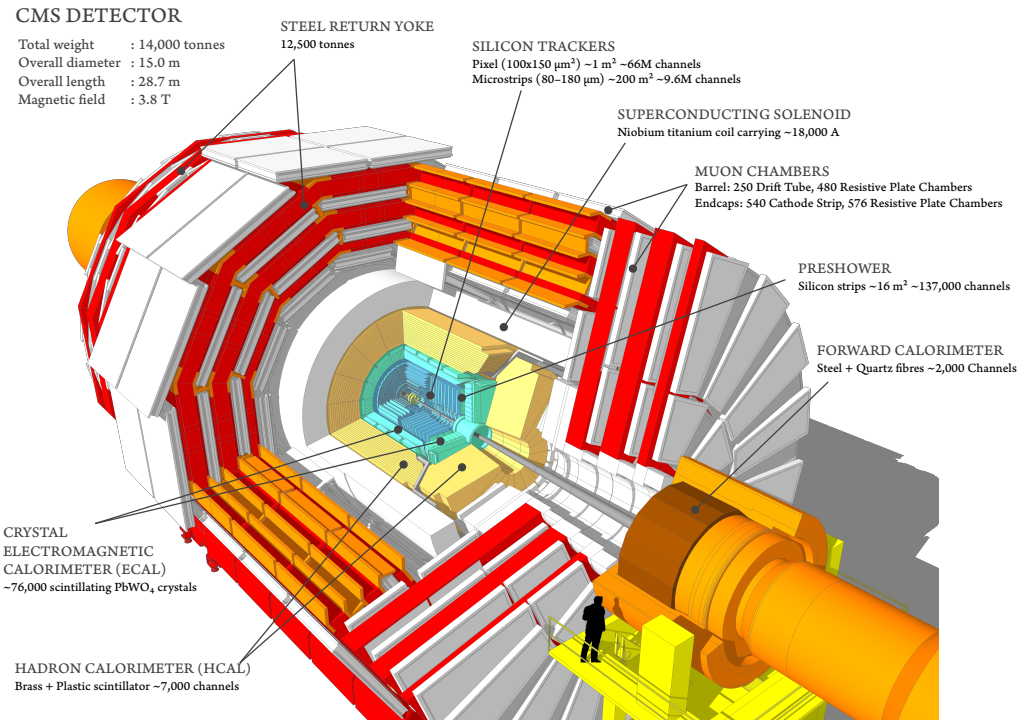

Figure 7.1: A sectional view of the CMS detector, adapted from [16].

Brief descriptions of these subsystems are given in Section 7.2-Section 7.7. The coordinate system adopted by CMS is introduced in Section 7.1.

7.1 Coordinate System Used in the CMS Detector

As illustrated in Figure 7.2, the coordinate system adopted by CMS uses the nominal IP as its origin, with the x-axis pointing radially inward towards the center of the LHC ring, the y-axis pointing vertically upward towards the sky, and the z-axis pointing along the beam line towards the west of the detector.

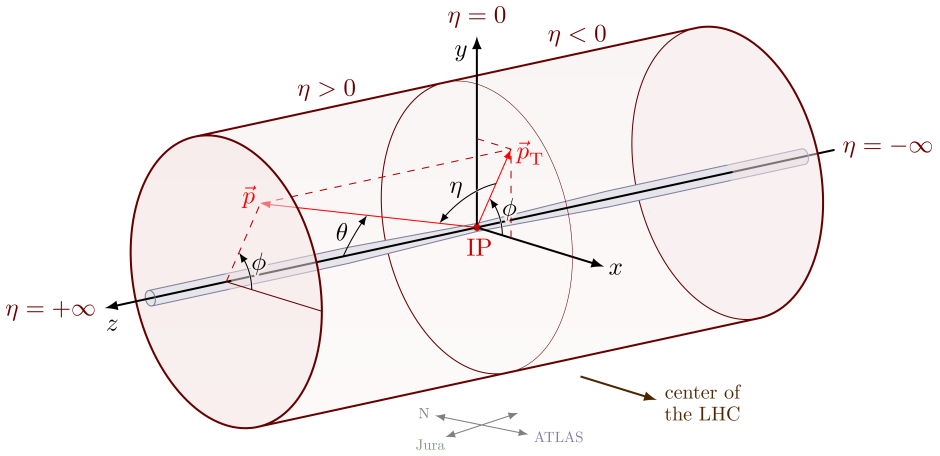

Figure 7.2: A sketch of the coordinate system adopted by CMS, adapted from [17].

The x- and y-axis form the transverse plane as they are both orthogonal to the beamline (z-axis). The distance from the IP in the transverse plane is defined as $r = \sqrt{x^2 + y^2}$. Variables defined entirely in the transverse plane, such as p_T, p_T^{miss}, and H_T, are often indicated by a subscripted T. The azimuthal angle ϕ is measured from the positive x-axis and the polar angle θ is measured from the positive z-axis. Another variable η, known as pseudorapidity, is defined as

$$\eta = -\ln(\frac{\theta}{2}) \tag{7.1}$$

or alternatively

$$\eta = \frac{1}{2}\ln(\frac{p + p_z}{p - p_z}). \tag{7.2}$$

It is preferred over θ mainly due to: i) particle production rate is roughly uniform in this variable, and ii) a difference in this variables, denoted by $\Delta\eta$, is invariant under Lorentz boosts. The conversion between η and θ is illustrated in Figure 7.3. The $\Delta\eta$ and the difference in azimuthal angles, denoted by $\Delta\phi$, are used to define the distance parameter ΔR

$$\Delta R = \sqrt{\Delta\eta^2 + \Delta\phi^2}. \tag{7.3}$$

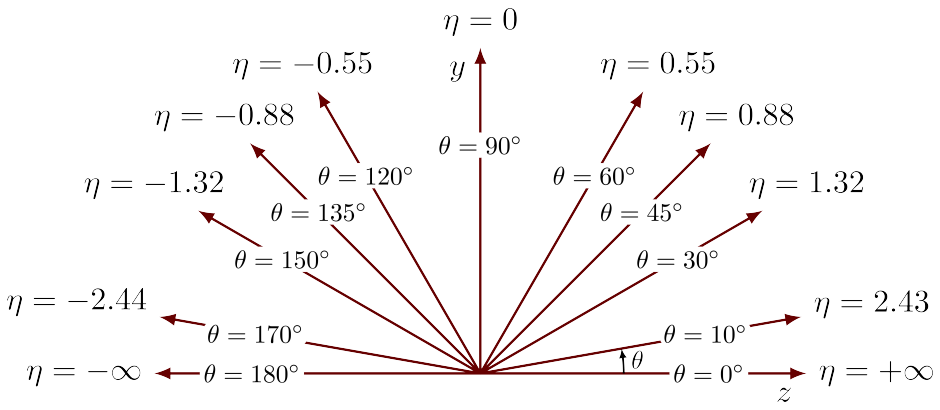

Figure 7.3: Examples of the conversion between the polar angle θ and the pseudorapidity η, adapted from [18].

7.2 The Tracking system

The tracking system [129] is the innermost subsystem of the CMS detector where the density of particles from the collisions is the highest. The full Tracking system is based on silicon technology to cope with the high radiation conditions and provide excellent spatial resolutions while maintaining a light material budget. The alterations of charged particle trajectories caused by detector materials are expected to be minimal. Hits from charged particles, such as electrons and muons, are measured by silicon sensors and used to reconstruct particle trajectories, known as "tracks". The curvature of tracks can be then used to determine the momentum of these final state particles. Tracks can also be used to reconstruct the Primary Vertex (PV), which corresponds to inelastic scatterings in collision events, and the Secondary Vertex (SV), which corresponds to the decay of heavy particles, such as tau leptons.

The Tracking system gives a coverage of up to $|\eta| < 2.5$, and is comprised of a pixel detector and a strip detector, which are also collectively known as the tracker detector. When charged particles go through tracker layers, they knock out electrons in detector materials. These electrons create electric pulses when they travel in electric fields, which are then amplified and detected in the readout electronics. A sketch of the CMS tracker created shortly before Run-1 of the LHC is shown in Figure 7.4.

The pixel tracker is comprised of roughly 66 million silicon sensors [130], and is divided into two subsystems: the Barrel Pixel (BPIX) and the Forward Pixel (FPIX). The BPIX is composed of three cylindrical layers with radii ranging from 44 mm to 102 mm. The FPIX is composed of two disks on each side of the forward region. To cope with the intensified LHC conditions in Run-2 and improve the overall tracking performance, an upgraded version of the pixel detector, referred to as the Phase-1 pixel detector, was installed during the year-end technical stop between 2016 and 2017 [20]. The Phase-1 pixel detector is comprised of roughly 124 million silicon sensors

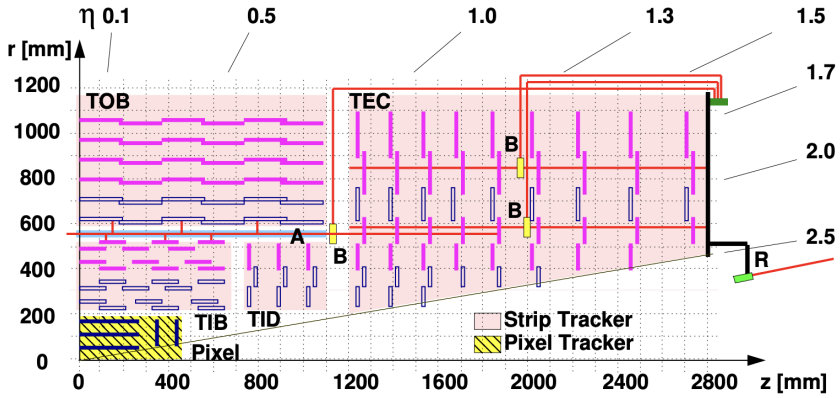

Figure 7.4: Layout of one quadrant of the CMS tracker in the $r - z$ plane, adapted from [19]. The strip tracker is shown in pink color while the original pixel detector with three barrel layers is shown in black color.

distributed over four BPIX layers and three FPIX disks on each side. Differences between the two pixel detectors are shown in Figure 7.5.

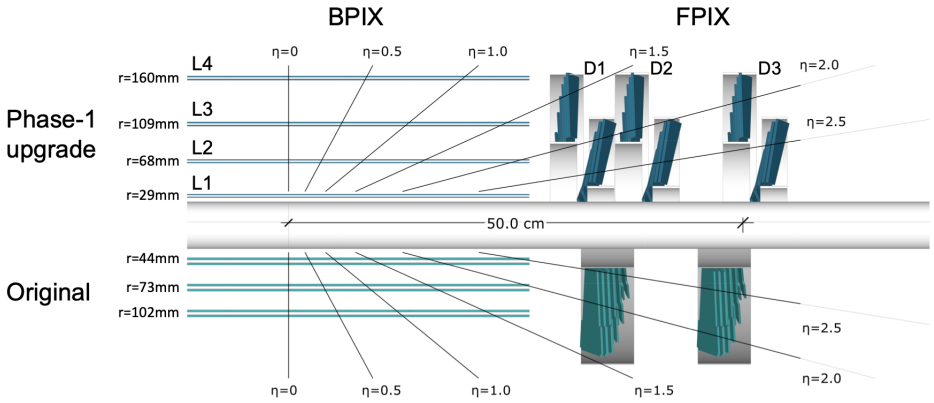

Figure 7.5: A comparison between the original pixel detector and the upgraded pixel detector in the $r - z$ plane, adapted from [20].

The strip tracker is much larger in size and is built around the pixel tracker. It is comprised of roughly 10 million silicon sensors and is divided into several subsystems: the tracker inner barrel (TIB), outer barrel (TOB), inner disks (TID), and endcaps (TEC). The TIB and TOB consist of four and six layers, respectively. The TID and TEC consist of three and nine disks, respectively.

7.3 The Electromagnetic Calorimeter

The ECAL [131] is a homogeneous calorimeter that encloses the tracker detector, and thus it is the second innermost subsystem of the CMS detector. It helps determine the energy and position of electrons and photons through their electromagnetic interactions with detector materials. The ECAL gives a coverage of up to $|\eta| < 3.0$ and is divided into three subsystems: the ECAL barrel calorimeter (EB), preshower calorimeter (ES), and endcap calorimeter (EE). A sketch of the ECAL layout is shown in Figure 7.6.

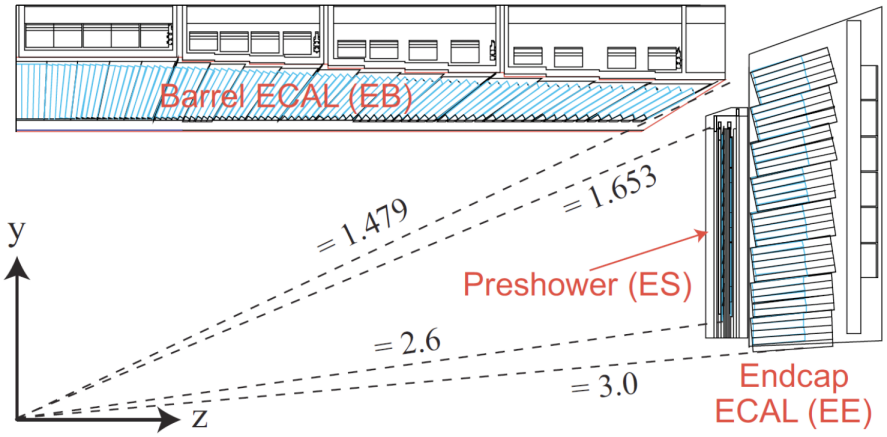

Figure 7.6: Layout of one quadrant of the ECAL in the $r - z$ plane, adapted from [21].

Unlike the tracker, the ECAL aims to stop electrons and photons entirely. It is composed of over 76 thousand lead tungstate ($PbWO_4$) crystals, which act as absorbers and scintillators simultaneously. When high-energy electrons and photons travel through these crystals, they create electromagnetic showers of low-energy electrons and photons. Over 98 % of the shower energy can be absorbed and converted to light through the scintillation process. The scintillation light is then amplified and detected by photodiodes. The energy of particles can be measured from the intensity of the scintillation light.

7.4 The Hadronic Calorimeter

The HCAL [132] is a sampling calorimeter placed outside of the ECAL. It measures the energy of hadrons through their strong interactions with detector materials. It also plays a crucial role in the measurement of the total energy in collision events, which allows for the determination of the MET. The HCAL gives a coverage of up to $|\eta| < 5.2$ and is divided into four subsystems: the HCAL barrel calorimeter (HB), endcap calorimeter (HE), outer barrel calorimeter (HO), and forward calorimeter (HF). A sketch of the HCAL layout is shown in Figure 7.7.

Similar to the ECAL, the HCAL aims to stop hadrons entirely as their momenta are only minimally affected by the tracker and ECAL. Unlike the ECAL, which is homogeneous in its detector

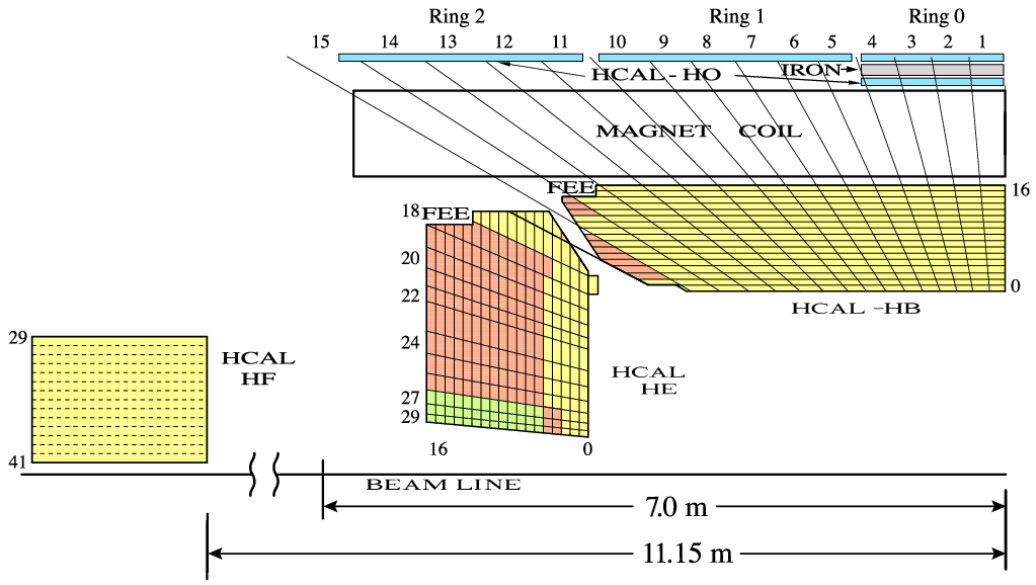

Figure 7.7: Layout of one quadrant of the HCAL in the $r - z$ plane, adapted from [22].

materials, the HCAL uses alternating layers of absorbers and scintillators made of different materials and hence it is classified as a sampling calorimeter. Brass absorber plates are placed between plastic scintillator plates in the HB and HE, which provides coverages of $|\eta| < 1.3$ and $1.3 < |\eta| < 3.0$, respectively. The HO is placed outside of the magnetic coil to provide additional materials in the barrel. It uses materials from the CMS magnet as absorbers. The HF is placed outside of the detector around the beam line. It provides coverage of forward jets and uses steel as an absorbing material.

7.5 The Superconducting Magnet

The superconducting magnet [133] is the central feature of the CMS detector. It has a diameter of roughly 6 meters and fully encloses the tracker, ECAL and the HCAL HB and HE. The magnet consists of two main parts: the steel return yoke and the superconducting solenoid. The yoke weighs more than 10 thousand tons and its main role is to improve the homogeneity of the magnetic field inside the tracker and return the magnetic flux to the solenoid. The superconducting solenoid is enclosed in the yoke and it produces a uniform magnetic field of $B = 3.8$ T inside the tracker volume. The paths of charged particles are curved by this magnetic field so that their momenta can be inferred from the curvatures of the trajectories according to the equation

$$p_T = |q|B\rho, \tag{7.4}$$

where q is the charge of the particle, B is the magnetic field in the z direction, and ρ is the radius of the curvature. A map of the magnetic field generated by the solenoid is shown in Figure 7.8. The solenoid operates at a current of over 18 thousand A and a temperature of 4.2 K (-268.95 °C). It is cooled by the liquid helium.

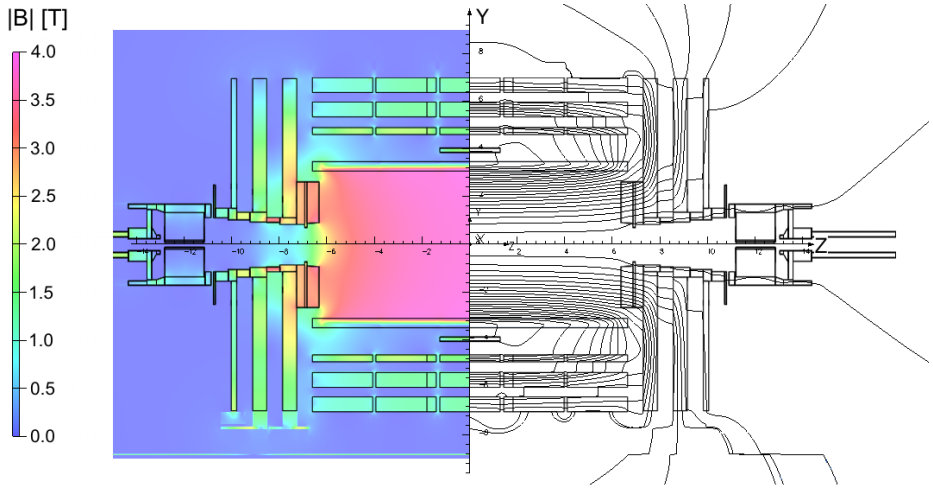

Figure 7.8: Predicted values of $|B|$ (left) and field lines (right) on a longitudinal section of the CMS detector, adapted from [23].

7.6 The Muon System

The Muon system [134] is located outside of the solenoid and embedded into the return yoke. It is the outermost and largest subsystem of the CMS detector, consisting of several subsystems that give an overall coverage of up to $|\eta| < 2.4$. All these subsystems all based on gas-ionization technology: the Drift Tube (DT) and Resistive Plate Chambers (RPC) together make up the barrel region of the Muon system, and the endcap Muon system consists of RPC and Cathode Strip Chambers (CSC). The Gas Electron Multiplier (GEM) [24] is the latest addition to the Muon system. It complements CSC in the forward region. A sketch of the Muon system layout is shown in Figure 7.9.

Muons produced in collision events retain most of their momenta when they penetrate the tracker and calorimeters, which allows for the precise determination of their trajectories by the Muon system. The barrel region ($|\eta| < 1.2$) is occupied by four stations of DTs, which consists of charged wires and is filled with gas. The DT is chosen for this region because the event rate is lower in this region and the magnetic field is weaker but more uniform relative to the forward region. When muons pass through the DT chambers, they knock out electrons from the gas atoms, which then move toward the positively charged wires due to their electric field. The charged wires are placed perpendicular to each other so that the x and y coordinates of the muon positions can be determined.

In region ($0.9 < |\eta| < 2.4$) where the event rate is higher, four stations of the CSC chambers

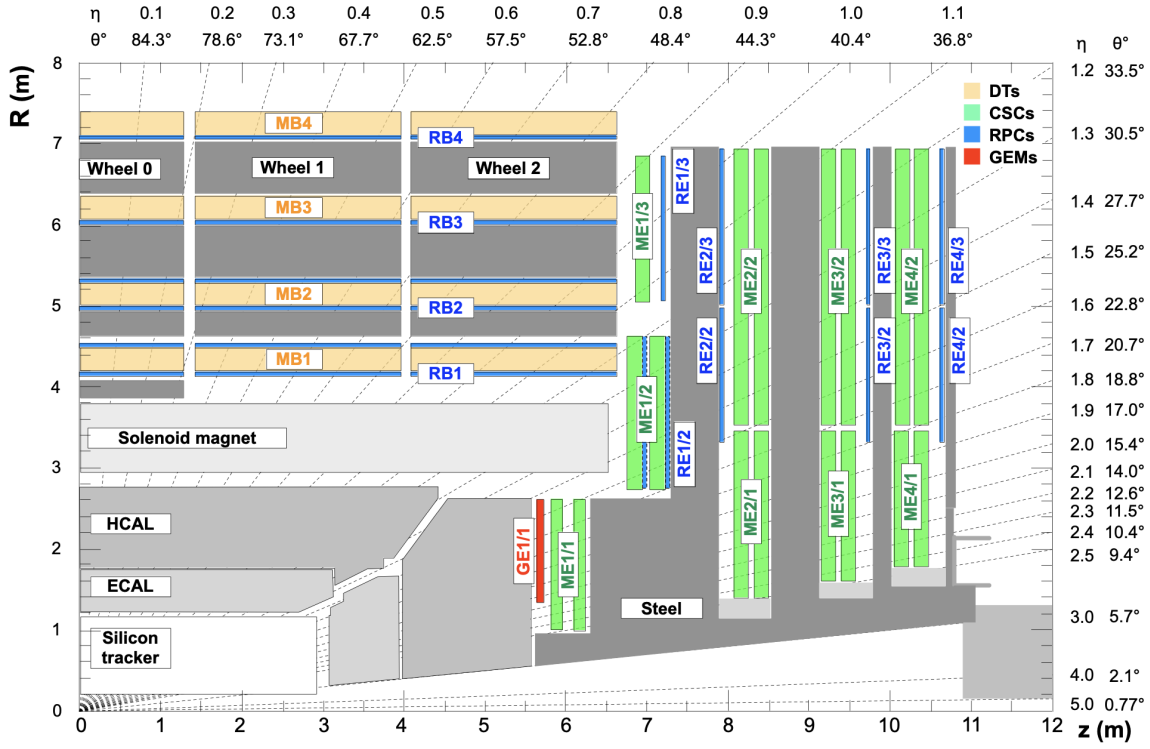

Figure 7.9: Layout of one quadrant of the Muon system in the $r - z$ plane, adapted from [24].

are positioned on each side. Similar to the detection mechanism in the DT, muons knock out electrons from gas atoms when they pass through the CSC chambers. Unlike the DT, which solely relies on positively charged wires, the CSC uses positively charged wires and negatively charged strips positioned perpendicular to each other. When electrons move to the wires, they create an avalanche of electrons. At the same time, a signal in the strips will be created by the ionized gas atoms. These two signals together allow for the determination of the x and y coordinates of the muon positions.

Complementary to the DT and CSC, the RPC chambers are positioned in both the barrel and endcap region ($|\eta| < 1.9$). They provide coarser position resolution but fast response and good time resolution, which is useful in the muon trigger. The GEM will extend the coverage of the Muon system to $|\eta| < 2.8$ and is expected to be fully operational before the start of Run-4.

7.7 The Trigger System

The LHC collides proton bunches every 25 ns, which corresponds to an event rate of 40 MHz. The size of the data generated at this collision rate is too large and it is beyond the hardware limit to record every event offline. Moreover, the vast majority of the events involve only soft QCD processes that are of little interest to particle physicists. The CMS trigger system [135] is

designed to reduce the data volume to a feasible level and select events that are interesting to the physics programs at the CMS. It consists of two layers: the L1 trigger and HLT.

The L1 trigger is the first layer of the trigger system and is based on custom-designed hardware. Before high-resolution collision events are recorded permanently, they are held in memory pipelines at the frontend electronics. The L1 trigger is tasked to analyze every event by only coarsely using the segmented data from the calorimeters and the Muon Systems, as illustrated in Figure 7.10. It makes an irreversible decision on which events to keep and which events to discard in less than 4 μs and reduces the event rate to about 100 kHz.

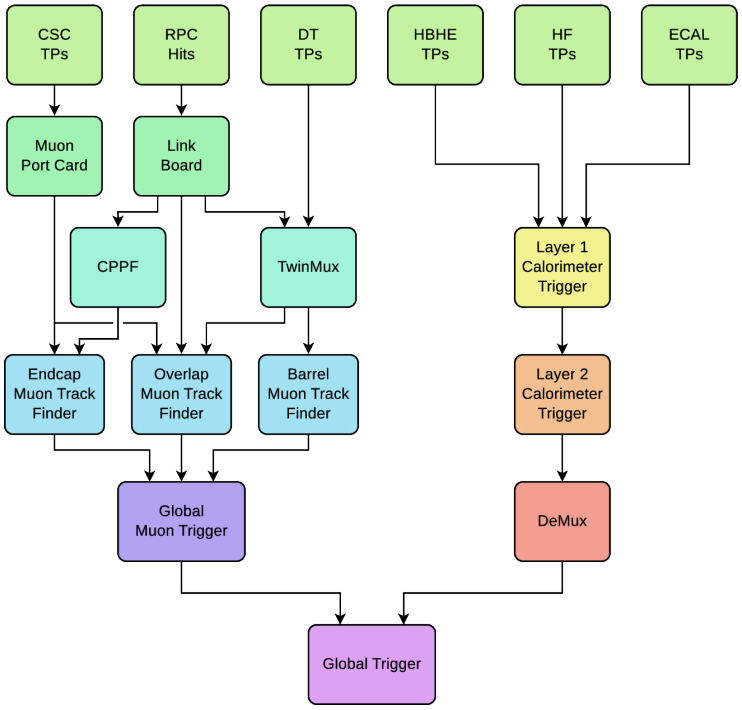

Figure 7.10: Diagram of the L1 trigger system during Run-2 of the LHC, adapted from [25].

Before the start of the Run-2, an upgraded version of the L1 trigger [136] was installed. This upgraded L1 trigger adds additional layers of correlators between the muon trigger and calorimeter trigger, which allows for more advanced computations such as muon isolation.

The HLT is the second layer of the trigger system and uses a software-based algorithm that runs on computer farms. Unlike the L1 trigger, the HLT has access to the full readout data, which allows for the deployment of more sophisticated algorithms to select events targeted by different physics groups. The event rate is further reduced by the HLT selection to about 400 Hz.

Chapter 8

Event Reconstruction in the CMS detector

Events selected by the CMS trigger system typically contain signatures of heavy particles, such as the top quark or the Higgs boson. However, the lifetime of these particles is extremely short and they travel a negligible distance before decaying into more stable particles, referred to as the final-state particles. Therefore, the reconstruction of an event produced in the proton-proton collisions requires the identification of all final state particles, which can be then used to infer the presence of heavy particles. Except for weakly interacting neutrinos, all final-state particles leave traces of their signatures in at least one subsystem of the CMS detector as illustrated in Figure 8.1.

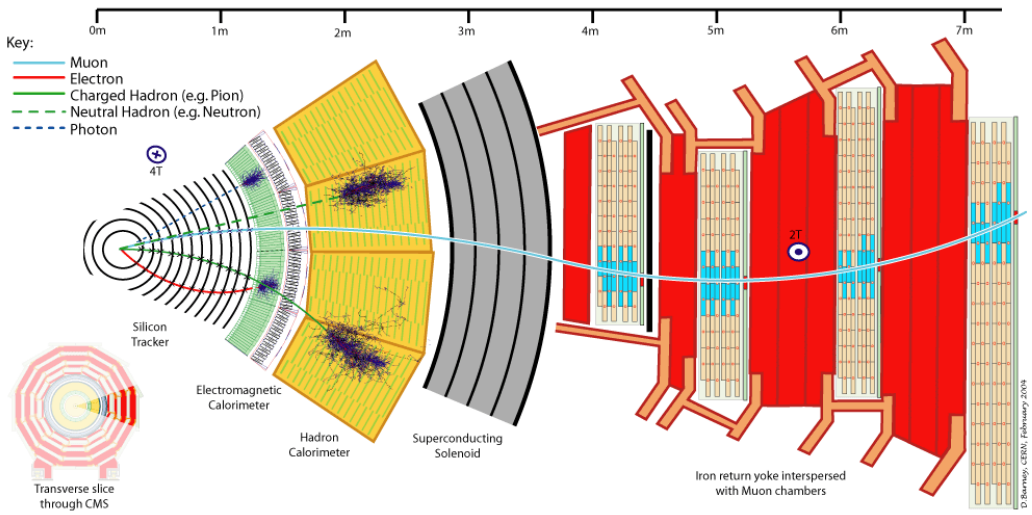

Figure 8.1: A cross-sectional view of a slice of the CMS detector in the transverse plane, adapted from [26]. Paths of different particles that interact with various subsystems of the CMS detector are highlighted.

The Particle Flow (PF) algorithm [137] is used by the CMS to combine measurements from all subsystems and provide a global event description. This algorithm consists of two main steps: i) reconstructing the PF elements (i.e. tracks and calorimeter clusters) using information from various subsystems and ii) linking these PF elements together to form the PF candidates. The calorimeter clusters refer to a group of adjacent energy deposits in the calorimeters. The PF candidates are labeled as electrons, photons, muons, charged hadrons, or neutral hadrons.

Descriptions of the track and vertex reconstruction are given in Section 8.1. The reconstruction of PF electrons and muons are discussed in Section 8.2 and Section 8.3, respectively. The PF candidates are also used to reconstruct hadronic jets, taus, and MET, which is discussed in Section 8.4, Section 8.5, and Section 8.6, respectively.

8.1 Track and Vertex

Tracks from the inner tracking system and the muon system serve as one of the basic elements of the PF algorithm. The standard track reconstruction algorithm at CMS is the so-called CTF [138], which is an extension of the KF algorithm [139] that combines the pattern recognition and parameter fitting. The procedure starts by forming a seed using only two or three hits. The initial estimate of the track parameters and their uncertainties are also made in the seeding stage. A KF-based pattern recognition is then used to build track candidates by propagating the trajectory of each seed to its nearby surfaces. If a hit is found in the expected window it is added to the candidate track while the track parameter is updated at the same time. As illustrated in Figure 8.2, the improved knowledge of the track parameter as a result of newly added hits allows for a tighter window for the next propagation.

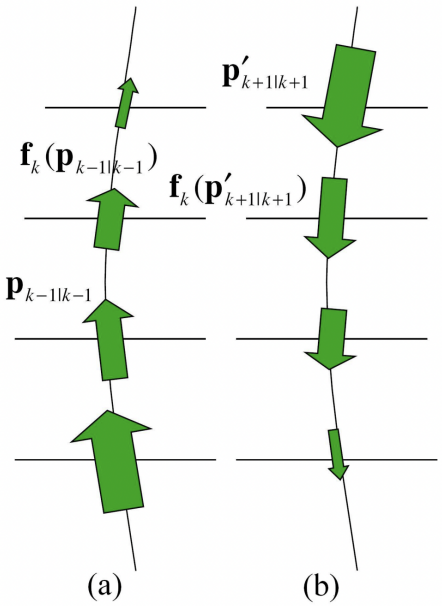

Figure 8.2: Illustration of the iterative tracking fitting in CTF, adapted from [27]. (a) shows the forward fitting while (b) shows the backward fitting. $\mathbf{p}_{k-1|k-1}$ is the KF state on surface $k-1$ calculated using the first $k-1$ hits. $\mathbf{f}_k(\mathbf{p}_{k-1|k-1})$ is the predicted KF state on surface k. The size of the green arrows symbolizes the accuracy of the KF state.

The update of the track parameter is done using a KF that performs an iterative fit to track parameters as new hits are added. Finally, a set of track quality selection criteria is applied to reduce the number of tracks that can not be associated with any particles, known as fake tracks.

Reconstructed tracks can also be linked together to form a vertex. Vertices that are associated with inelastic scatterings of a collision event are known as the PV. Due to the presence of PU, multiple PVs exist in any given collision event. Three main steps are involved in the reconstruction of the PVs. Firstly, a set of selection criteria is applied to reconstructed tracks to ensure they are promptly produced in the collisions. Secondly, reconstructed tracks are clustered into a vertex candidate based on their z-coordinates using the deterministic annealing algorithm [140]. Finally, candidate vertices with more than one associated track are fitted using adaptive vertex fitter [141]. For each event, the PV with the highest $\sum p_{\mathrm{T}}^2$ is often considered to be of the most importance to particle physicists as they carry the largest momentum transfer in an event. It is sometimes referred to as simply the PV of an event while other PVs are considered to originate from PU.

8.2 Electron

Charged particles may emit photons in a process called the *bremsstrahlung*. The intensity of this effect is inversely proportional to the squared mass of the charged particles. As the lightest charged particles, electrons produced in the hadron collisions are heavily affected by the bremsstrahlung effect, which comes in two different aspects. Firstly, the emission of a photon alters the electron trajectory, which undermines the performance of the standard tracking algorithm. A dedicated algorithm known as the Gaussian Sum Filter (GSF) [142] is therefore used to fit the electron parameters. Moreover, the bremsstrahlung photons emitted by electrons often cause a more widespread pattern of ECAL clusters along the ϕ direction. Therefore, multiple adjacent ECAL clusters are combined to form the so-called *superclusters*.

The electron reconstruction is fully integrated into the PF framework, which associates GSF tracks from the inner tracking system to the ECAL clusters. The final assignment of the electron energy is based on a weighted combination of the ECAL super cluster energy and tracker momentum [143]. In addition to the electron reconstruction, identification criteria are often applied and optimized for different analyses. For both analyses described in this thesis, the primary objective of the electron identification is to control the contamination of the *nonprompt* leptons. To this end, a BDT-based electron identification is deployed, which is discussed in Section 13.1.

8.3 Muon

In CMS, three types of muon tracks exist: standalone muons, tracker muons, and global muons [144]. The standalone muons refer to the muon tracks reconstructed purely from hits in the muon system. The tracker muons are built "inside-out" by propagating tracks from the tracker to the muon system and matching it with at least one hit from either the CSC or DT. The global muon is reconstructed "outside-in" by: i) matching the standalone muons with the inner tracks and ii) performing a combined fit using the KF to update the muon parameters.

Same as the electron, the muon reconstruction is fully integrated into the PF algorithm, which applies a set of selection criteria based on quality parameters in the muon reconstruction to the tracker muons and global muons. The so-called Medium muon ID [144] is used by analyses described in this thesis. This ID accepts both tracker muons and global muons and adjusts the selection criteria accordingly. The overall efficiency of this ID is estimated to be around 99.5% for muons from simulated W and Z events.

8.4 Jet

The CMS uses a sequential recombination algorithm, known as the anti-k_t algorithm [145], to cluster PF candidates into jets. The word "k_t" refers to the transverse momentum. This algorithm is designed to be Infrared and Collinear (IRC) safe, meaning the jet properties are invariant under the soft gluon emissions and collinear gluon splitting. The distance variable between two PF candidates i and j in this algorithm is defined by

$$d_{ij} = \min\left(\frac{1}{p_{\mathrm{T}_i}^2}, \frac{1}{p_{\mathrm{T}_j}^2}\right)\frac{\Delta R_{ij}}{R}, \tag{8.1}$$

where p_{T_i} and p_{T_j} corresponds to the transverse momentum of PF candidate i and j respectively. ΔR_{ij} is the angular distance between the two objects defined by

$$\Delta R_{ij} = \sqrt{\Delta y_{ij}^2 + \Delta\phi_{ij}^2}, \tag{8.2}$$

where $y = \frac{1}{2}\ln(\frac{E+p_z}{E-p_z})$, referred to as the rapidity, is not to be confused with the pseudorapidity η defined in Equation (7.2). R in Equation (8.2) denotes the size of the jet which is typically chosen to be smaller than 1. For example, jets described later in this thesis are reconstructed with $R = 0.4$. A second variable that measures the distance between particle k and the beam axis in momentum space is defined as

$$d_{kB} = \frac{1}{p_{\mathrm{T}_k}^2}. \tag{8.3}$$

The recombination procedure begins with calculating all combinations of d_{ij} and concatenating them with every d_{kB} to form the set $\{d_{ij}\} \cup \{d_{kB}\}$. The minimum of the entire set is then determined. If d_{ij} is the minimum, then PF candidates i and j are recombined into one candidate which replaces candidate i and j in the list. If d_{kB} is the minimum, then it is labeled as a jet and removed from the list. This process is iterated until no PF candidates are left. The name "anti-k_t" refers to the fact that the distance variable d_{ij} is defined with respect to k_t to the power of -2, which is different from the use of k_t^2 in k_t algorithm [146].

As indicated in Equation (8.1), the anti-k_t algorithm is dominated by hard particles. It typically

starts with the hardest particle in an event and clusters and walks its way down to softer particles. The final momentum assignment of a jet is determined by the vectorial sum of the momenta of all particles that are clustered into this jet. The softest particles in an event are typically among the last ones to be clustered and they do not affect hard jets. The infrared safety is therefore guaranteed. Moreover, two collinear particles will also be given high priority to be merged because of the small d_{ij} between them. This effectively ensures the collinear safety of the algorithm. Historically, sequential clustering algorithms are favored by theorists because of their IRC properties but not favored by experimentalists due to their computational complexity. The introduction of the FastJet program [147] improves significantly the the running speed of these sequential clustering algorithms, and they eventually become the standard jet clustering algorithm at the LHC.

The measured energy of a jet is calibrated by applying a multiplicative factor $\mathcal{C}$ to each of its four-momentum components:

$$p_\mu^{\text{corr}} = \mathcal{C} \cdot p_\mu^{\text{raw}}, \tag{8.4}$$

where $\mathcal{C}$ is factorized into several components [148],

$$\mathcal{C} = \mathcal{C}_{\text{offset}}(p_{\text{T}}^{\text{raw}}) \cdot \mathcal{C}_{\text{MC}}(p_{\text{T}}', \eta) \cdot \mathcal{C}_{\text{rel}}(\eta) \cdot \mathcal{C}_{\text{abs}}(p_{\text{T}}'') \tag{8.5}$$

where $\mathcal{C}_{\text{offset}}$ is the PU offset correction that removes the energy coming from the PU events. $\mathcal{C}_{\text{MC}}$ refers to the response correction. It accounts for the momentum difference between the reconstructed jets and particle-level jets. It is derived from simulation and applied to both data and MC. The $\mathcal{C}_{\text{rel}}$ and $\mathcal{C}_{\text{abs}}$ correspond to the relative and absolute residual corrections, respectively. They account for the small differences in jet energy scale between data and MC and are only applied to data.

8.5 Hadronic Tau

Hadronic tau leptons are reconstructed with the Hadron-Plus-Strips (HPS) algorithm [149] in CMS. This algorithm consists of several main steps: i) seeding, ii) "strip" reconstruction, iii) forming τ_h candidates, and iv) choosing the final τ_h object.

The HPS algorithm uses PF jets as "seeds" for the τ_h candidates. It is required that PF jets are reconstructed with the anti-k_t algorithm with a distance parameter $R = 0.4$. All PF candidates within $\Delta R < 0.5$ of the jets are considered in the following reconstruction steps.

Secondly, PF electrons and photons in the seeding area are clustered into one or more rectangular windows (0.05×0.2) in the $\eta - \phi$ plane known as "strips". Strips can be considered as proxies for the neutral hadron π^0, which appears in many decay modes of τ_h. Strips are narrow in η

direction but wider in ϕ direction to account for the bending of electrons by the magnetic field. τ_h candidates typically have 0, 1, or 2 strips.

Thirdly, charged hadrons with the highest energy (up to six) are combined with the strips to form τ_h candidates. It is required that the combinations of strips and charged hadrons are compatible with one of the seven reconstructed decay modes listed in Table 8.1.

Table 8.1: Reconstructed decay modes of τ_h expressed in combinations of reconstructed charged hadrons and strips and their targeted decay modes.

Reconstructed decay mode	DM	Targeted decay mode
1 hadron	0	$\tau_h^\pm \to h^\pm \nu_\tau$
1 hadron + 1 strip	1	$\tau_h^\pm \to h^\pm \pi^0 \nu_\tau$
1 hadron + 2 strips	2	$\tau_h^\pm \to h^\pm \pi^0 \pi^0 \nu_\tau$
2 hadrons + 0 strip	5	$\tau_h^\pm \to h^\pm h^\mp h^\pm \nu_\tau$
2 hadrons + 1 strip	6	$\tau_h^\pm \to h^\pm h^\mp h^\pm \pi^0 \nu_\tau$
3 hadrons + 0 strip	10	$\tau_h^\pm \to h^\pm h^\mp h^\pm \nu_\tau$
3 hadron + 1 strip	11	$\tau_h^\pm \to h^\pm h^\mp h^\pm \pi^0 \nu_\tau$

"DM" is a number assigned to each reconstructed decay mode, which is defined by

$$\mathrm{DM} = 5 \times (N_{\mathrm{prongs}} - 1) + N_{\mathrm{strips}}. \tag{8.6}$$

DM = 5 or 6 corresponds to the scenario where one of the hadrons in a 3-prong τ_h decay is not successfully reconstructed. The final assignment of a τ_h candidate momentum is determined by the vectorial sum of all charged hadrons and strip constituents of that candidate.

In final stage of the HPS algorithm, a set of selection criteria is applied to all reconstructed τ_h candidates that are seeded by the same jet. The candidate with the highest p_T and passes all the selection criteria is chosen as the final τ_h object.

8.6 Missing Transverse Momentum

It is assumed that the initial transverse momentum in hadron collisions is zero. It is therefore very useful to compute the vectorial sum of momenta of all reconstructed objects in events to infer the presence of weakly interacting particles that escape detections, such as neutrinos or hypothetical dark matter particles.

In CMS, PF candidates are used to reconstruct the MET vector [150]:

$$\overrightarrow{p}_{\mathrm{T}}^{\mathrm{miss}} = -\sum_{i} \overrightarrow{p}_{\mathrm{T}}^{i}. \tag{8.7}$$

The magnitude of the MET vector $p_{\mathrm{T}}^{\mathrm{miss}}$ is often considered to be analogous to p_{T} of the particle that escapes the detector.

Chapter 9

The Run-3 Operations of the CMS detector

The CMS detector resumed data-taking in July 2022, following the start of the Run-3 of the LHC. When compared to Run-2, the center of mass energy of the proton beams increases from 13 TeV to 13.6 TeV in Run 3. At the same time, the peak instantaneous luminosity is kept at the same or higher level as the 2018 data-taking year (2×10^{34} cm^{-2}s^{-1}), as illustrated in Figure 9.1.

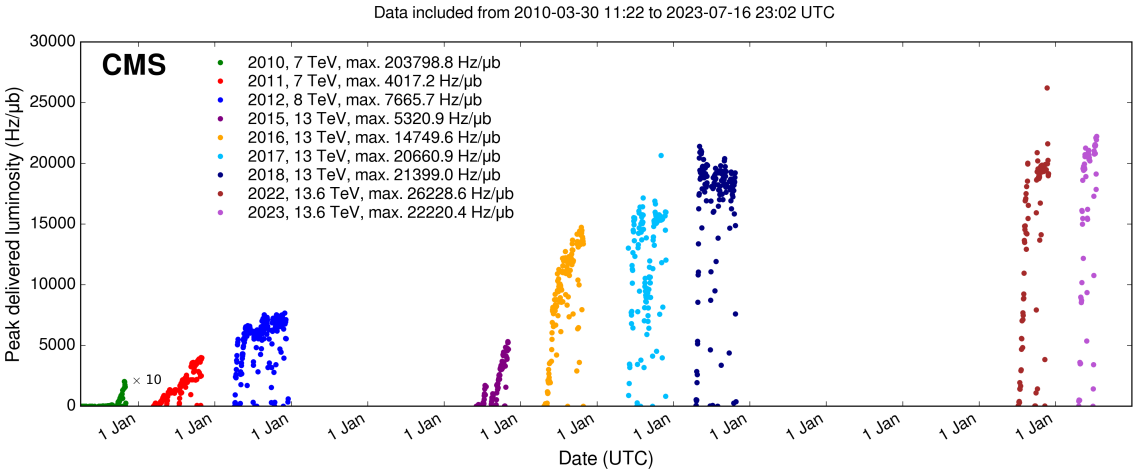

Figure 9.1: Peak luminosity versus day delivered to CMS during stable beams and for proton-proton collisions, adapted from [14].

Operations of the CMS detector are coordinated by the CMS Run Coordination, which is introduced in Section 9.1. The CMS control room is the commanding center of the CMS operations, which is staffed 24×7 during the active data-taking period. Personnel who monitor and operate the CMS detector from the control room are referred to as the "central shift crew", which is discussed further in Section 9.2. In the context of detector operations, the principal contacts of the subsystems of the CMS detector are known as the DOC experts, or simply the DOCs. Core duties of one of the DOCs, the tracker DOC, are described in Section 9.3.

9.1 The CMS Run Coordination

The CMS Run Coordination is nominally headed by two Run Coordinators and one deputy Run Coordinator whose mandate is to ensure the successful running of CMS. The Run Coordinators oversee all operations activities at the CMS and are nominally appointed for a two-year term. The Run Coordinators work closely with the Technical Coordination, the LHC team, and the subsystem operations teams to draft the long-term strategic goals for the central operations, as well as commissioning efforts in subsystems. These strategic goals are helped achieved by the RFMs who serve as the liaison between the Run Coordination and the central shift crew, as illustrated in Figure 9.2.

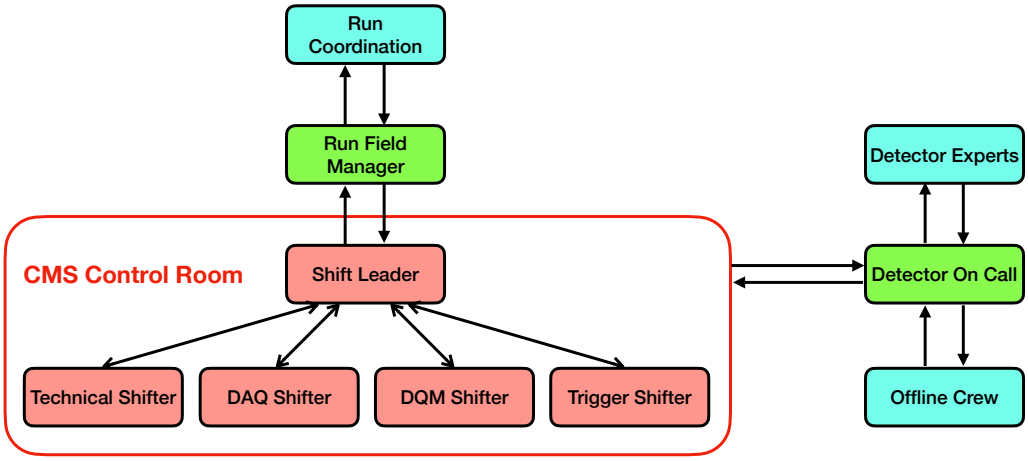

Figure 9.2: Main communication paths between various personnel within the CMS Run organization. The SL, technical, DAQ, DQM, and the trigger shifters are required to be present at the CMS control room 24×7. The RFMs and the DOCs are nominally present in the control room during working hours. The Run Coordinators, subsystem experts, and offline shifters are not required to be at the control room although they often do.

The RFM team is nominally appointed for a two-week term and typically consists of two members who have extended experiences in various roles of operations, particularly the SL. The RFMs, together with the Run Coordinators, organize the CMS daily run meetings in the morning every weekday to collect the feedback & requests from the subsystem DOCs and set the daily run plan. The RFMs also facilitates the SL in implementing these plans as the SL, like the rest of the central shift crew, nominally does not attend the daily run meeting.

9.2 Central Shift Crew

The CMS detector is considered to be "running" when all high-voltage channels are switched on and taking data. During this period, operations of various subsystems of the CMS detector are controlled by the central shift crew, which consists of five members: the SL, technical, DAQ, DQM, and trigger shifters, as illustrated in Figure 9.3.

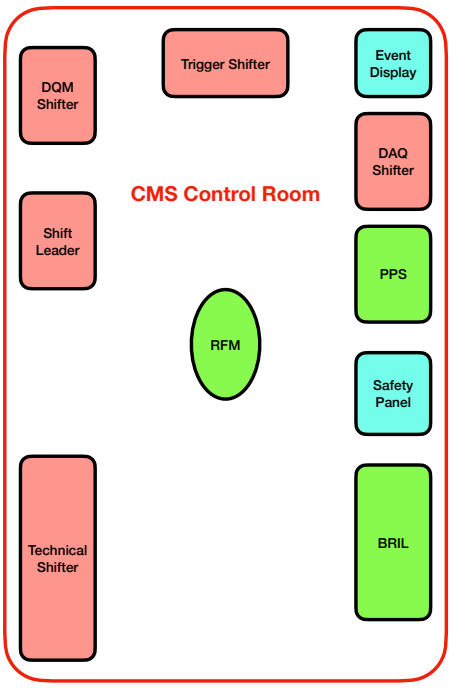

Figure 9.3: A sketch of the layout of the CMS control room. The area where the event display and the safety panel are located is nominally not designated for any personnel. The PPS [28] and BRIL [29] groups have designated working space in the control room although these groups do not maintain a 24×7 presence in the area.

In order to maximize the luminosity output and data-taking efficiency, the LHC normally takes no break at night once it starts producing high-intensity collisions. The CMS detector is therefore kept on 24×7 once the LHC is operational, and members of the CMS Collaboration take eight-hour shifts in relay from the control room. The running period when all subsystems are included in the data taking is considered to be a "global run". The data collected from global runs are then screened and certified by the CMS Physics Performance & Dataset (PPD) group for physics analyses.

The SL is nominally considered to be the leader of the central shift crew, whose primary duty is to ensure the successful execution of the daily run plan. The SL coordinates all activities in the CMS control room and communicates with the RFMs, CMS Run Coordination, as well as the CERN Control Centre (CCC) about the operations. The SL is also simultaneously the Shift Leader In Matters Of Safety (SLIMOS), who is in charge of the safety during the operation, together with the technical shifter.

The technical shifter is responsible for all things related to the Detector Control System (DCS) and Detector Safety System (DSS). The technical shifter is often the "first responder" when problems arise in the CMS detector or the surrounding infrastructures during the operation. The technical shifter coordinates the responses to these problems with the DOCs, CMS Technical

Coordination, as well as CERN technical team. The technical shifter is also co-responsible for safety during the operation as safety duties are nominally delegated from the SL to the technical shifter. These duties include: monitoring and responding to the DSS alerts, overseeing the underground access and the usage of all safety equipment in the control room, and performing safety tours in the surface as well as the underground area.

The core duty of the DAQ shifter is to ensure smooth and efficient data taking, where the efficiency is roughly measured as the ratio of the recorded luminosity and the delivered luminosity. When a subsystem DAQ runs into problems it can stop a global run and block the whole system entirely from running again, resulting in the so-called "downtime", which undermines the taking data taking efficiency. The DAQ shifter is in communication with the SL and DOCs about the readiness of all subsystems before initializing a global run, and is heavily involved in troubleshooting when subsystems are uncooperative in global runs.

The DQM shifter is responsible for the quality of the data taken by the CMS detector. The DQM shifter is nominally the first person to spot problems (related to data quality) in the running detector and is trained to do so by familiarizing him- or herself with the "normal" as well as the faulty patterns of the data collected in all subsystems. Traditionally DQM shifters attend shifts in person from the CMS control room just like the SL, technical, and DAQ shifters. In recent years, especially since the COVID-19 outbreak, more flexibility has been given to the DQM shifters, who can now choose to work from one of the CMS Remote Operations Centers or home.

The L1 and HLT rates during the data taking are monitored by the trigger shifter, who along with the SL determines the appropriate prescale column based on the real-time L1 rate. The trigger shifter makes sure all trigger subsystems are running correctly and he or she is in communication with the L1 and HLT DOCs when troubleshooting is needed. Similar to DQM shifters, trigger shifters have the option to work remotely provided that they have done in-person shifts more than a few times and are sufficiently familiar with the procedure.

9.3 Tracker Detector On-call Expert

Subsystems like the tracker do not maintain a 24×7 presence at the CMS control room. Instead, their shifters, known as DOCs, are appointed for one week and nominally only join the central shift crew in the control room during working hours. After the working hours, DOCs remain accessible by phone and they are ready to go to the control room at any time should the situation require.

The term "tracker DOC" usually refers to the strip tracker DOC while the pixel tracker has its own DOC known as the "pixel DOC". The tracker DOC is the main point of contact for the strip tracker during his or her mandate, which typically lasts for one week. On behalf of the strip tracker operations team, the tracker DOC reports the status of the strip tracker at the CMS daily run meeting. He or she also monitors the state of the strip tracker in all aspects (e.g. power,

DAQ) and coordinates the daily activities with tracker detector experts and the tracker offline shift crew whose primary duty is the certification of the data collected by the tracker.

A stable and safe operation of the strip tracker requires both well-trained tracker DOCs as well as a modern DCS. Built on top of the industrial product "WinCC", the CMS Tracker Control System (TCS) [151, 152] is designed to monitor the environmental conditions and safely operate the detector. As part of the TCS software, a FSM toolkit is introduced. It is a powerful tool that assists operators in their daily jobs. It groups the power, cooling, dry gas, and monitoring systems defined in the four TCS projects in one hierarchical tree. The global state of the detector is continuously evaluated and made visible from the root Tracker FSM node giving critical information to the detector operator, as illustrated in Figure 9.4.

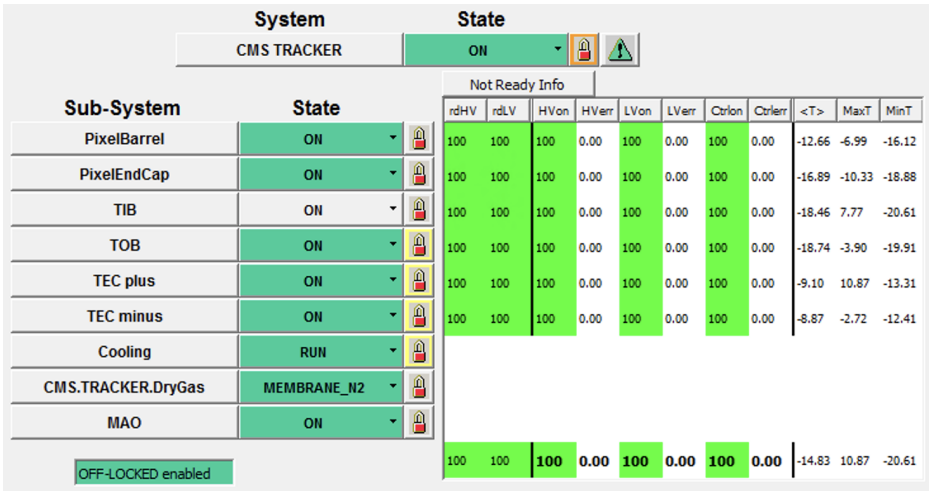

Figure 9.4: Main panel of the tracker FSM, screenshotted in October 2022 during the Run-3 data taking.

Chapter 10

The Phase-2 Upgrade of the CMS Detector

Planned to start in 2029, the HL-LHC [128] will reach a peak instantaneous luminosity of up to $7.5 \times 10^{34}\text{cm}^{-2}\text{s}^{-1}$, as illustrated in Figure 10.1. The increased luminosity will open up opportunities for ambitious physics programs including precision SM measurements and searches for physics BSM. To fully exploit the physics potential offered by the HL-LHC datasets and overcome the challenging operational conditions, such as intense radiation and up to 200 PU per event, the CMS detector will undergo substantial upgrades during the LS 3, known as the Phase-2 Upgrade [153].

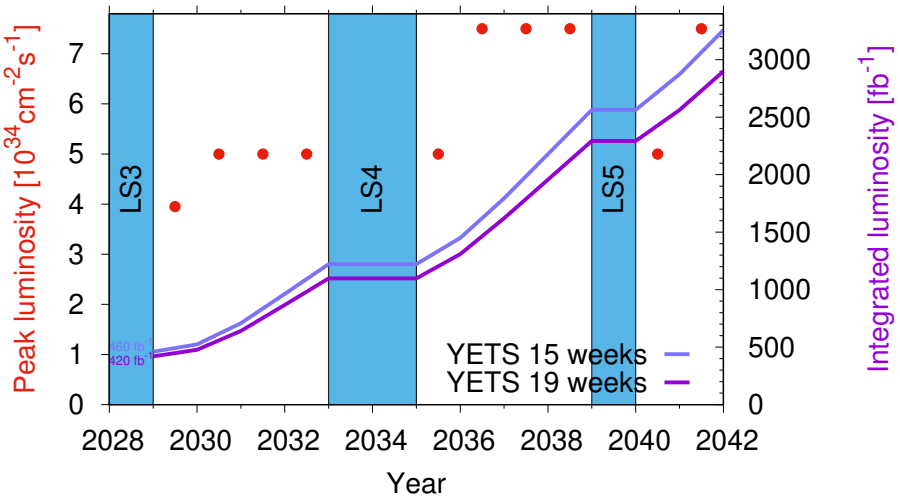

Figure 10.1: The peak and intergraded luminosity expected to be delivered by the HL-LHC, taken from [15] in November 2023. The left-hand *y*-axis shows the scale of the peak instantaneous luminosity, which is itself represented with red dots. The right-hand *y*-axis shows the scale of the intergraded luminosity. The two solid lines represent the intergraded luminosity under two YETS scenarios.

An overview of the Phase-2 Upgrade is given in Section 10.1. Among various systems upgrades, the upgrade of the Outer Tracker is more relevant to this thesis, which is described in Section 10.2. The Outer Tracker upgrade will enable tracking at the L1 trigger, which is discussed in Section 10.3. The tracking information can be combined with the calorimeter responses to build electron candidates at the L1 trigger, which is discussed in Section 10.4.

10.1 Overview of the Upgrade

A new silicon tracker [31] will replace the current tracker for the Phase-2. The Phase-2 tracker is divided into two subsystems: a pixel detector known as the Inner Tracker and the Outer Tracker composed of strip and macro-pixel sensors. Thanks to the extended coverage of the Inner Tracker, the Phase-2 Tracker will provide efficient tracking up to $|\eta| < 4$. The Phase-2 tracker is also much lighter with improved radiation hardness while enjoying a reduced material budget in the tracking volume. The granularity of the Phase-2 tracker will be increased by roughly a factor of 4, leading to a much better charged-particle p_T resolution. More importantly, the Phase-2 Outer Tracker is specially designed to be capable of delivering data to the L1 trigger, which is further discussed in Section 10.2.

The latency and event rate of the hardware-based L1 trigger will be increased (from 3.4 μs) to 12.5 μs and (from 100 kHz) 750 kHz, respectively, for the Phase-2 [154]. The increased latency leaves sufficient time for the track construction as well as correlating information from the tracker, calorimeters, and Muon system on L1 hardware. The addition of tracking information also enables the implementation of more sophisticated trigger algorithms at L1, such as those based on the PF [137] or Pileup Per Particle Identification (PUPPI) algorithms [155].

The frontend electronics of the ECAL Barrel Calorimeter will be replaced [156] to accommodate the latency and rate requirements of the Phase-2 L1 trigger, and to provide better timing resolution. The upgraded frontend electronics will enable the L1 trigger to exploit the information from single crystals as opposed to the trigger primitive of 5×5 crystals provided by the current system. The more granular trigger primitives will improve the precision of identifications and isolations of calorimeter objects and the matching between tracks and electromagnetic showers at L1.

The ECAL and HCAL Endcap Calorimeters will be replaced by a new endcap calorimeter known as the HGCAL [157]. The HGCAL is a sampling calorimeter consisting of both electromagnetic and hadronic sections, which are designed to withstand the extreme radiation level at the HL-LHC. It provides an excellent timing resolution and incorporates the concept of three-dimensional shower measurements from experiments at the International Linear Collider (ILC) [158]. Like both of its predecessors, the HGCAL is designed to contribute to the L1 trigger.

A brand new subsystem known as the MIP Timing Detector (MTD) [159] will be added to the CMS Phase-2 lineup. The MTD covers both barrel and endcap regions and it enables the measurements of the production timing of the MIPs. This addition enables the four-dimensional reconstruction of the interaction vertices, which represents a completely new capability added to the CMS detector. The timing information associated with the reconstructed vertices will provide a much-needed handle to cope with the high PU conditions at the HL-LHC.

As explained in Section 7.6, the CSC in the endcap region will be complemented by a new subsystem GEM, which is expected to be fully operational by LS 3. Similar to the ECAL Barrel,

the electronics of the Muon system will also be upgraded to meet the L1 trigger requirements [160].

Upgrades of the HLT and BRIL system are also planned and are documented in detail in Ref. [161] and [162], respectively.

10.2 The Outer Tracker Upgrade

The performance of the current CMS Tracker will be significantly degraded if it continues to take data beyond the designed radiation exposure (500 fb^{-1}) in the HL-LHC era. Therefore, it must be completely replaced by a new tracker by the end of Run-3, which is envisioned to be able to withstand radiation damage up to 3000 fb^{-1}.

The design of the Phase-2 Outer Tracker is largely driven by the task of providing tracking information to the L1 trigger. The feasibility of a track trigger at L1 is significantly challenged by the sheer data volume generated by the HL-LHC at a frequency of 40 MHz accompanied by up to 200 PU. A novel tracker module design, known as the "p_T module" [163] is used to reduce the data volume effectively while keeping interesting events for physics analyses. Under this design, the Outer Tracker will be composed of over three thousand p_T modules, and each consists of two closely spaced silicon sensors that are parallel to each other. Through correlating hits from the two parallel sensors, the p_T modules are capable of providing p_T discrimination, thus reducing the data volume at the front end. Correlated pairs of hits are referred to as "stubs", which serve as the trigger primitive to the L1 trigger. The stub mechanism is illustrated in Figure 10.2. With the current design, only hits over the threshold of 2 GeV will be read out, which corresponds to a data reduction rate of up to 100.

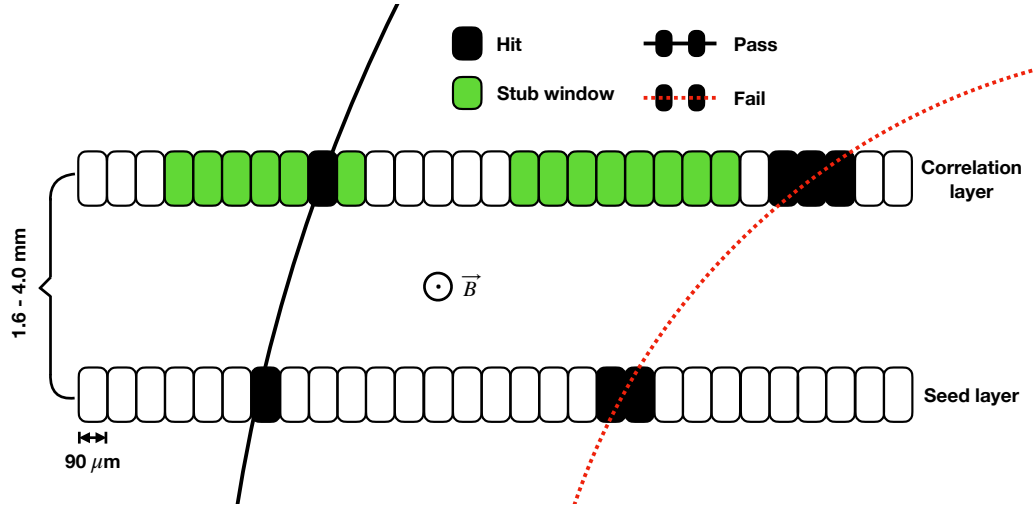

Figure 10.2: Illustration of the stub mechanism in a cross-sectional view of a p_T module (2S) in the magnetic field. Charged particles with a p_T higher than 2 GeV are represented with the black solid curve while the red dashed curve represents charge particles with lower p_T. The magnetic field will cause low p_T charged particles to bend with a smaller radius of curvature, and thus fail the pre-determined stub window corresponding to a p_T threshold of 2 GeV.

The Phase-2 Outer Tracker consists of six cylindrical barrel layers (L1-L6) and five disks (D1-D5) on each side of the endcap, as illustrated in 10.3. The layers and disks of the Outer Tracker are composed of two types of p_T modules, known as the "Pixel-Strip (PS)" modules and "Strip-Strip (2S)" modules. Sketches of the PS and 2S modules are shown in Figure 10.4. The PS modules occupy the first three barrel layers as well as regions of the disks that are closer to the beam line. The remaining regions of the disks as well as the last three barrel layers are occupied by the 2S modules. The Outer Tracker layout shown in figure 10.3 is known as the so-called "tilted geometry" where the PS modules in the barrel layers are positioned with various titled angles to increase the stub efficiency.

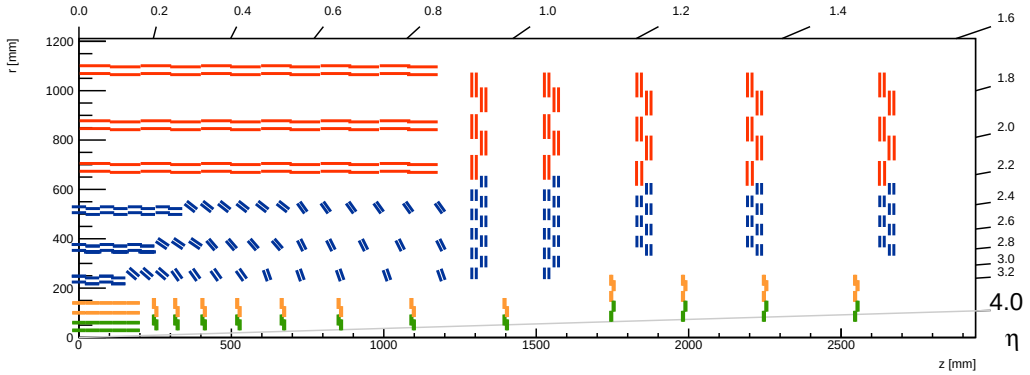

Figure 10.3: Layout of one quadrant of the Phase-2 CMS tracker in the $r - z$ plane, generated by the CMSSW [30]. The PS modules of the Outer Tracker are represented with blue lines while the 2S modules are represented with red lines. The radial region below 200 mm is occupied by the Inner Tracker, whose modules are represented with orange and green lines. The Inner Tracker does not contribute to the L1 trigger.

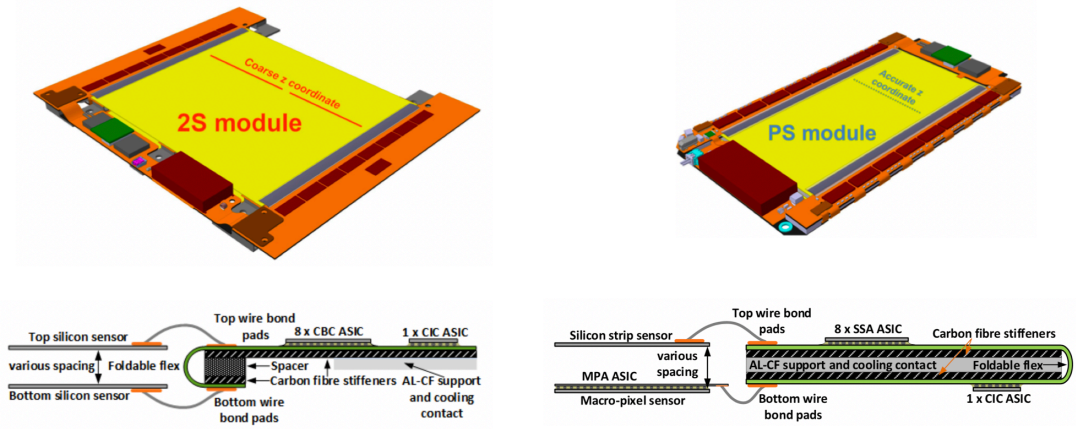

Figure 10.4: Illustrations of the 2S module (left) and PS module (right), adapted from [31]. Shown are views of the assembled modules (top) and sketches of the connection between frontend hybrids and silicon sensors (bottom).

The 2S module consists of two 90 cm^2 strip sensors separated by a few millimeters using a Carbon

Fibre Reinforced Aluminium (Al-CF) spacer. Each strip sensor consists of over two thousand strips arranged in two rows. Each strip is 5 cm long with a pitch of 90 μm. The two sensors are connected to hybrid circuits known as the frontend hybrid and service hybrid. The frontend hybrid consists of eight CMS Binary Chip (CBC) [164], which is responsible for readout. The service hybrid is mainly responsible for powering.

The PS module is about half the size of the 2S module in its active area. It has one strip sensor on the top and one macro-pixel sensor on the bottom, which provides very precise measurements of z-coordinates. Similar to the 2S module, the strip sensor of the PS module consists of roughly two thousand strips. Each strip is about 2.4 cm long with a pitch of 100 μm. The macro-pixel sensor contains 960 $\times$ 32 macro-pixels with a length and pitch of 1.5 cm and 100 μm, respectively. The two sensors are connected to hybrid circuits that are responsible for readout [165] and powering.

10.3 Level-1 Track Finder

The task for track finding algorithms at L1 can be broken down into two main parts: i) performing pattern recognition to identify and correlate all possible stubs that belong to the same charged particle trajectory and ii) obtaining the parameters of the trajectory by fitting the reconstructed tracks. A latency of roughly 4 μs is allocated to track finding algorithms, which becomes one of the critical constraints in algorithm development. Multiple approaches [31] have demonstrated the feasibility of delivering tracking information within the allowed latency and a so-called "hybrid" approach [154] is adopted by CMS as the way forward.

To meet the latency requirement and increase redundancy, the hybrid approach is parallelized both in space and in time. The Outer Tracker is partitioned into nine ϕ sectors and stubs in each sector are processed in parallel with a time-multiplexing factor of 18. The main stages of the hybrid approach are similar to the offline CTF algorithm described in Section 8.1, including seeding, pattern recognition, and parameter fitting, as illustrated in Figure 10.5. The main difference is that the parameter fitting is disentangled from the pattern recognition in the hybrid approach while these two stages are intergraded in the CTF algorithm.

The initial stage of the hybrid approach involves correlating two stubs from two different Outer Tracker layers or disks under the assumption that trajectories of the charged particles originate from the beam spot. The correlated pair of stubs is referred to as the "tracklet" which is later used as a seed for the pattern recognition. The tracklet also comes with coarse parameter estimates which will be updated in the fitting stage. Seven combinations of layers/disks are attempted in parallel for seeding: L1+L2, L3+L4, L5+L6, D1+D2, D3+D4, L1+D1, and L2+D1.

Based on its initial parameters, the tracklet is then extrapolated inward and outward to all possible layers or disks in parallel to look for stubs that belong to the same trajectory. A match is declared if a stub is found within a predetermined window around the projection in a layer or disk. At least two matches are needed in order to proceed to the following stage.

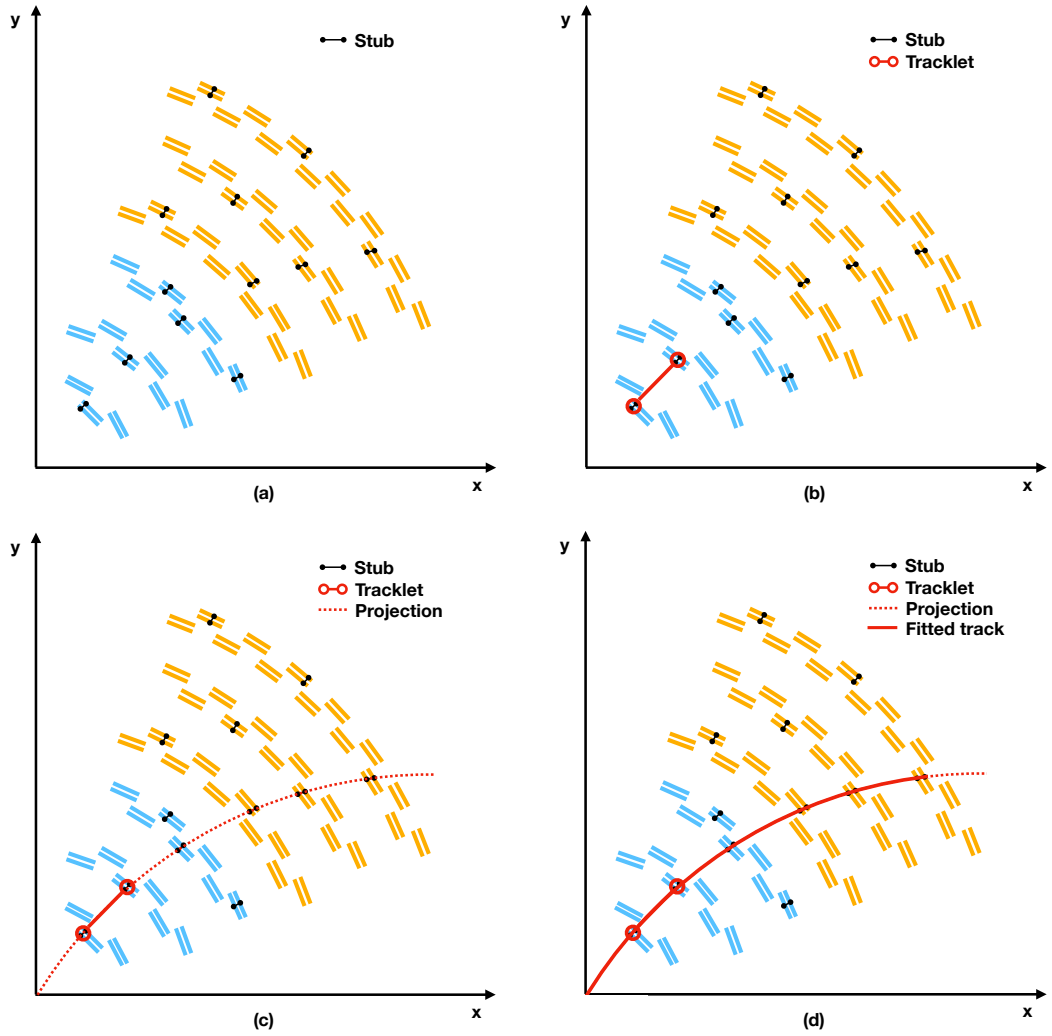

Figure 10.5: Illustration of different stages of the hybrid approach: (a) constructing stubs, (b) forming tracklet by correlating two stubs and the beam spot (origin), (c) projecting to other layers and finding matches, and (d) fitting track parameters using a KF.

Duplicates of the same track are produced as a result of the highly parallelized approach. Duplicated tracks are typically produced by two adjacent ϕ sectors when a charged particle is located near the sector boundary. Alternatively, they can be tracks that belong to the same sector but are seeded by different layer/disk combinations. To remove duplicates, tracks that share common stubs will be merged before the parameter fitting.

The fitting stage is done by a KF module that possesses the initial track parameters and adds stubs iteratively to update the track parameters. Each time a new stub is added, the consistency between the existing track parameters and the new stub will be checked which provides input to the parameter update. All potential combinations of stubs are attempted by the KF, and the final residual of each combination is calculated and compared. The stub combination with the

best residual is finally chosen as the KF output.

Tracks coming out of the fitting stage are considered to be the final product since all the track parameters are final. Similar to the offline track finder discussed in 8.1, fake tracks can still be reconstructed by the L1 track finder due to a variety of constraints and limitations of the algorithm. An additional module, referred to as the "track quality" is added to help distinguish, in a Multivariate Analysis (MVA) approach, between genuine tracks that can be associated with charged particles and fake tracks. A score between 0 and 1 is calculated for each track by combining multiple variables, such as the residuals produced by the KF, into a BDT. The score assigned to each track roughly translates to the probability of this track being genuine.

The hybrid track-finding algorithm has demonstrated a robust performance in software simulation, as shown in Figure 10.6. The baseline version of this algorithm requires stubs from at least four unique layers and constrains the origin of the trajectories to the beam spot. An "extended" version of the algorithm is also in development, in which the beam spot constraint is relaxed. The extended tracking is especially useful in scenarios where tracks originate with a small displacement in the transverse plane, such as displaced electrons as a result of bremsstrahlung in the Inner Tracker. It has been shown that sizable improvement in electron tracking efficiency can be achieved by the extended tracking algorithm, as shown in Figure 10.7.

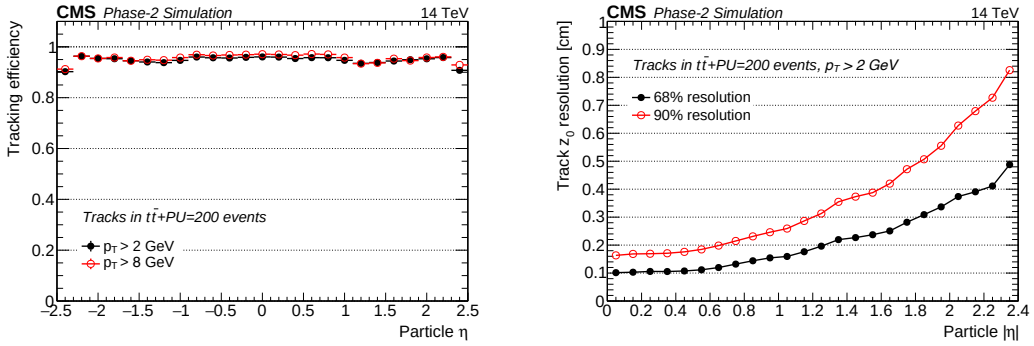

Figure 10.6: (Tracking efficiency vs particle η, measured in $t\bar{t}$ samples (left). Track z_0 resolution vs particle η (right).

10.4 Level-1 Electron Trigger Algorithm

With the increase of the instantaneous luminosity, triggering on electrons at L1 will face unprecedented challenges as the data volume generated in the calorimeters becomes too large for the legacy trigger algorithms. The addition of tracking information provides a much-needed handle for the electron trigger. It enables precise track-calorimeter shower matching to control the trigger rate. To take advantage of this new tool, a new electron trigger algorithm is developed and documented in Ref. [154].

The central feature of this algorithm is the fine-tuned matching between tracks produced by

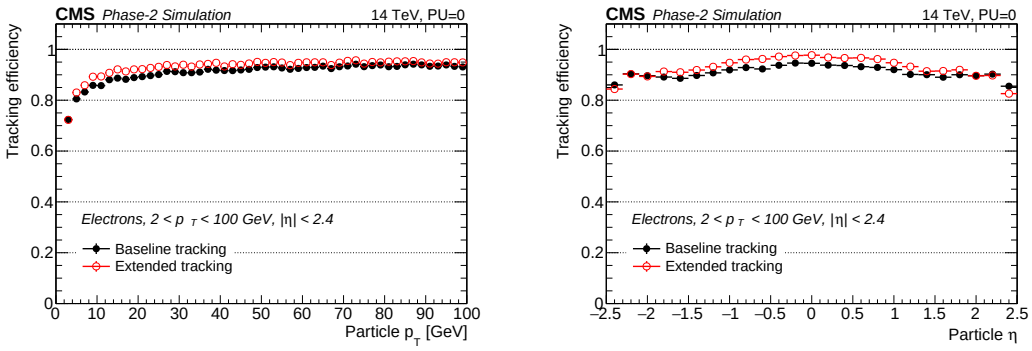

Figure 10.7: (Electron tracking efficiency vs particle p_T (left) and η (right), measured in simulated electron samples with 0 PU.

the L1 track finder and calorimeter clusters reconstructed in the ECAL Barrel or HGCAL. The baseline version of this algorithm extrapolates tracks to the calorimeter surface using the track p_T and matches them with calorimeter clusters. An elliptical cut in the $\eta - \phi$ plane is applied and illustrated in Figure 10.8. A wider window of $\Delta\phi$ is implemented to account for the bending of the electron trajectory in the ϕ direction, and the slightly less accurate ϕ resolution delivered by the L1 track finder.

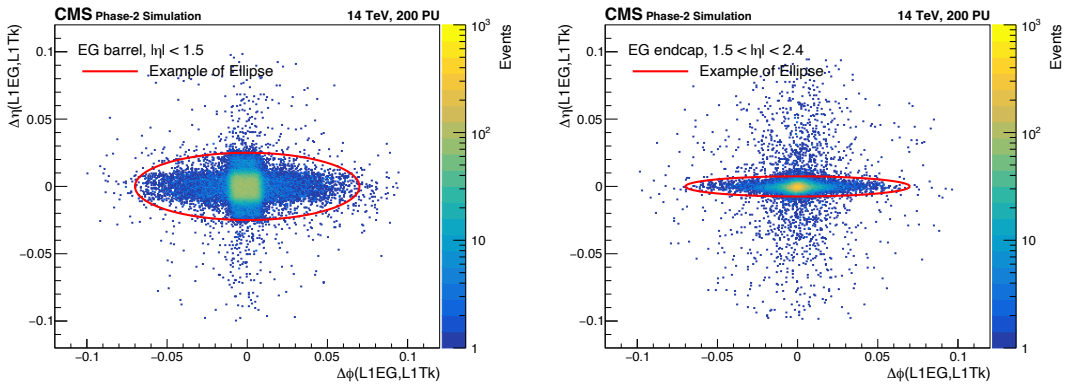

Figure 10.8: $\Delta\eta$ vs $\Delta\phi$ distances between calorimeter clusters and the closest L1 track in the ECAL Barrel (left) and HGCAL. Tracks are extrapolated using track p_T.

When compared to algorithms that only use calorimeter information, the baseline version of this new algorithm provides roughly a factor of three reduction in event rate while keeping the efficiency loss under control, as shown in Table 10.1-Table 10.2. The efficiency loss is largely driven by the inefficiencies in electron tracking, as illustrated in Figure 10.7.

An alternative version of this algorithm uses the energy estimate from the calorimeter instead of the Outer Tracker to extrapolate L1 tracks. The superior energy resolution delivered by the calorimeters further constrains the projected track η and ϕ coordinates to the targeted calorimeter

Table 10.1: Trigger rate of L1 trigger objects in the ECAL Barrel. Data in the first column shows the two reference trigger thresholds.

Rate	calorimeter only	track-matched
30 GeV	78.2 kHz	19.0 kHz
40 GeV	25.5 kHz	8.3 kHz

Table 10.2: Trigger efficiency for L1 trigger objects computed at two reference trigger thresholds in the ECAL Barrel.

Efficiency	calorimeter only	track-matched
30 GeV	97.5%	84.5%
40 GeV	98.7%	88.0%

clusters, as illustrated in 10.9. This enables the implementation of a much tighter ellipse in the $\eta - \phi$ plane.

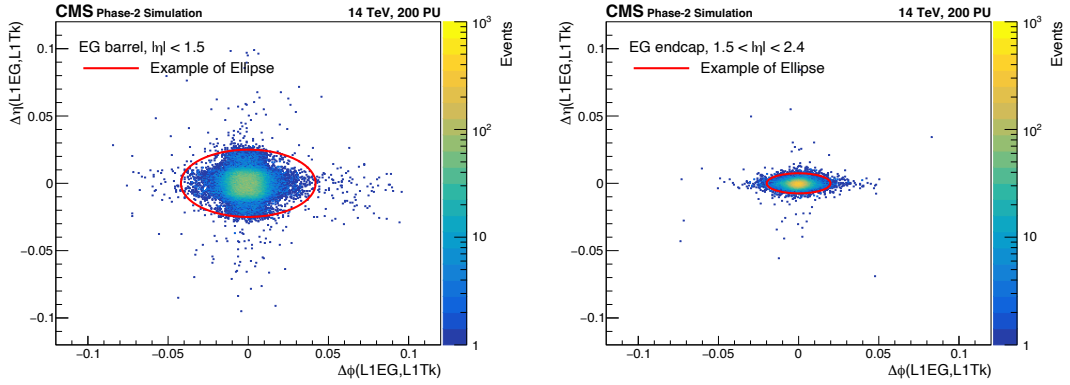

Figure 10.9: $\Delta\eta$ vs $\Delta\phi$ distances between calorimeter clusters and the closest L1 track in the ECAL Barrel (left) and HGCAL. Tracks are extrapolated using energy estimates from the calorimeter.

A comparison between two versions of the electron trigger algorithms is shown in Figure 10.10-10.11.

When compared to an older electron trigger algorithm for the Phase-2 [153], this newly designed algorithm (baseline) improves the electron reconstruction efficiency at L1 by 5% while reducing the background rate by a factor of 2. This improvement can be attributed to two main sources:

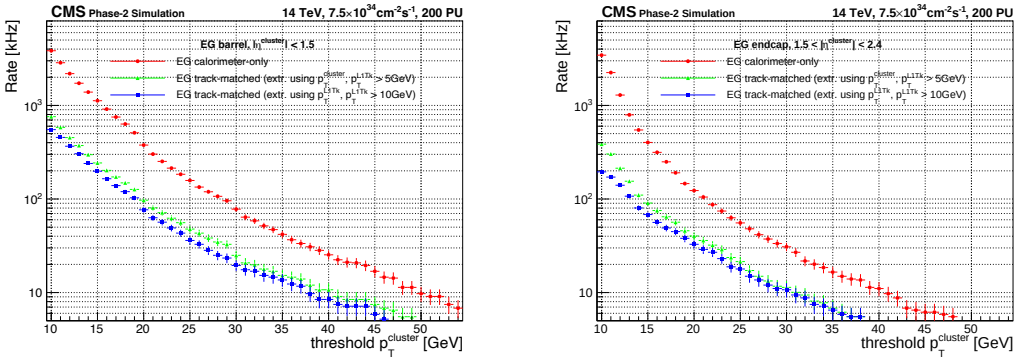

Figure 10.10: L1 event rate as a function of the electron trigger threshold in the ECAL Barrel (left) and HGCAL (right). The event rate computed for calorimeter-only objects is shown in red data points. Event rates computed for the objects reconstructed by the baseline and alternative electron trigger algorithms are represented with blue and green data points, respectively.

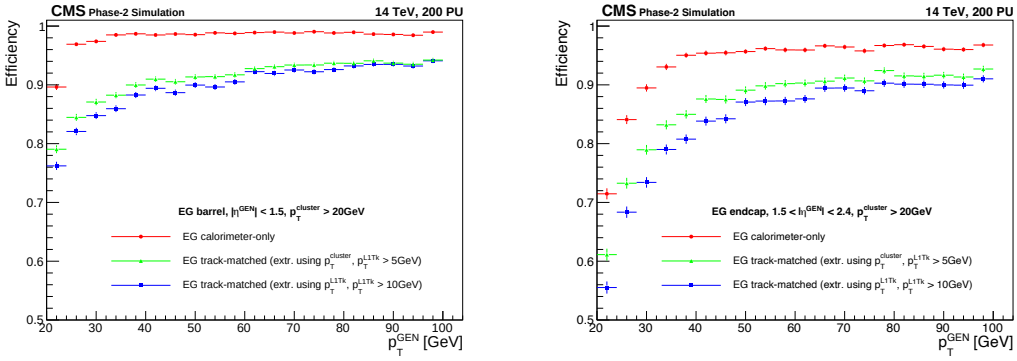

Figure 10.11: L1 electron trigger efficiency as a function of the particle p_{T} in the ECAL Barrel (left) and HGCAL (right). The efficiency computed for calorimeter-only objects is shown in red data points. Efficiencies computed for the objects reconstructed by the baseline and alternative electron trigger algorithms are represented with blue and green data points, respectively.

(i) the improved matching scheme between tracks and calorimeter objects, and (ii) the improved performance in L1 track finder.

Part III

Search for Flavor-Violating eμqt Interactions

Part III of this thesis documents a physics analysis that was performed in 2020-2023 using data collected by the CMS detector in 2016-2018. This analysis was submitted to the journal (PRD) and uploaded to the airXiv [166] in December 2023 and was largely done by myself with advice from Prof. Skinnari and technical support provided centrally by the CMS Collaboration. Part III is organized as follows. Chapter 11 gives a brief overview of this analysis as well as all past CLFV searches in the top quark sector performed at the ATLAS and CMS experiments. Chapter 12 describes the datasets, simulated samples, and triggers used by this analysis. Object- and event-level selection criteria are described in Chapter 13 and Chapter 14, respectively. Treatments of the *nonprompt* backgrounds and signal extraction using BDT are described in Chapter 15 and Chapter 16, respectively. Finally, the systematic uncertainties that affect this analysis and statistical interpretation of the results are described in Chapter 17 and Chapter 18, respectively. Except where noted, materials presented in Part III are prepared by myself.

Chapter 11

Overview of the Past and Present Analyses

CLFV searches involving top quarks is an active area of research at the LHC experiments. So far, no significant excess over the SM predictions has been reported, and the observations from the ATLAS and CMS experiments are interpreted using the framework of EFT. Brief reviews of two past ATLAS analyses and one past CMS analysis are given in Section 11.1 and Section 11.2, respectively. An overview of the present analysis is given in Section 11.3.

11.1 Preliminary ATLAS Analyses

The flavor-violating eμqt interactions were first studied by the ATLAS Collaboration [32] using data collected during 2015-2017 at 13 TeV, corresponding to an integrated luminosity of 79.8 fb^{-1}. In addition to three leptons, this analysis targets final states with two or more jets. Only the top quark decay signal mode is considered. Lorentz structures of dimension-6 operators are not probed separately. Discriminating variables, such as the p_T of the leptons, are combined into a BDT, which is used to interpret the observation. A representative Feynman diagram targeted by this analysis and the distributions of the BDT discriminator are shown in Figure 11.1.

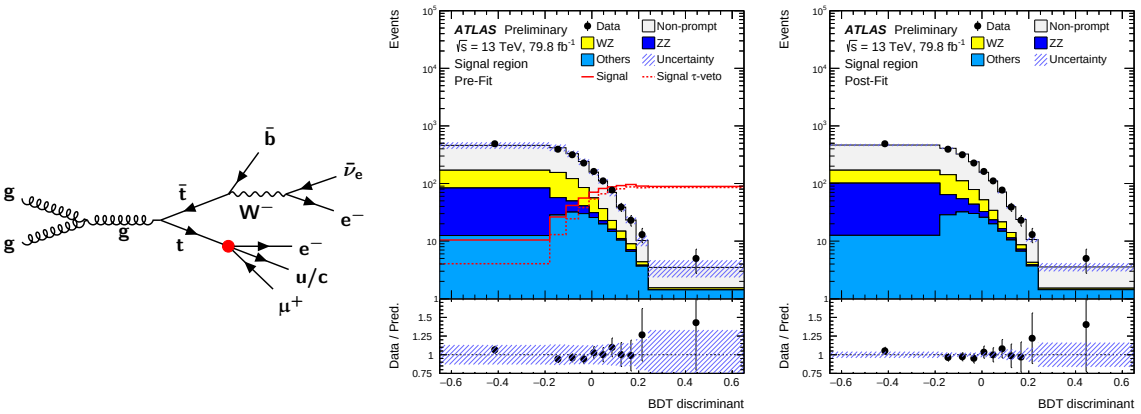

Figure 11.1: Representative Feynman diagram for the CLFV top quark decay processes that are targeted by [32] (left). The CLFV interaction vertex is shown as a solid red circle to indicate that it is not allowed in the SM. The middle (right) histogram shows the distribution of the pre-fit (post-fit) BDT discriminator targeting the CLFV top quark decay.

Data is found to be compatible with the SM predictions, and an upper limit on the branching fraction of $\mathcal{B}(t \to e\mu q) < 6.6 \times 10^{-6}$ is set at 95% CL [167]. This result improves a previous bound established in an indirect search [114] by three orders of magnitude. This analysis has yet to be published in a peer-reviewed journal.

The ATLAS Collaboration also studied the $\mu\tau qt$ interactions using 140 fb^{-1} data collected in 2015-2018 [33]. This analysis targets final states with two SS muons, one hadronic tau, and one or more jets. Both top quark production and decay signals are considered in this analysis. Operators with different Lorentz structures are considered separately. Representative Feynman diagrams are shown in Figure 11.2.

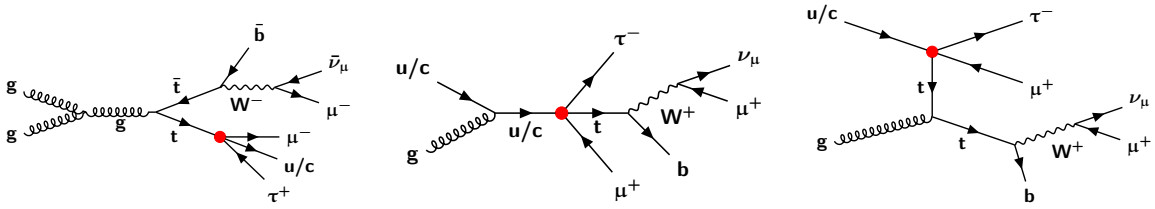

Figure 11.2: Representative Feynman diagrams for the signal processes that are targeted by [33]. Both top quark decay (left) and production (middle and right) CLFV processes are shown. The two muons in the final states are required to have the same electric charge.

Due to limited statistics, event yields of the SRs are directly used to interpret the observation, which is shown in Figure 11.3. An upper limit at 95% CL is placed on the branching fraction of $\mathcal{B}(t \to \mu\tau q) < 1.1 \times 10^{-6}$. The corresponding constraint on the WC improves the previous bound [168] by nearly a factor of 30. Like the previous ATLAS analysis, results represented in this analysis are still preliminary.

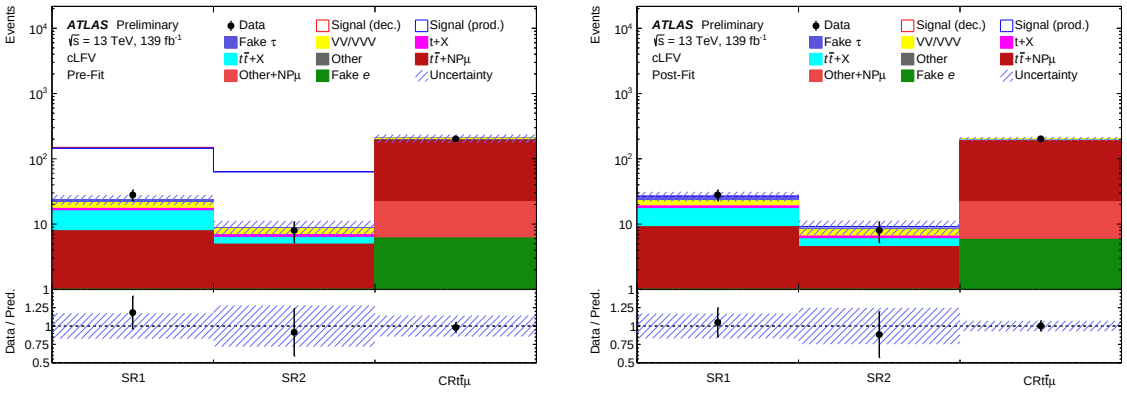

Figure 11.3: The left (right) histogram shows the pre-fit (post-fit) event yields of various regions studied by [33]. In these histograms, "SR1" denotes the signal region with two or more jets while "SR2" denotes the signal region with exactly one jet. "CRtt̄μ" denotes the control region of the tt̄μ background, where the μ is a *nonprompt* muon.

11.2 Past CMS Analysis

The CMS Collaboration followed up with a search for eμqt interactions using data collected in 2016-2018 [34] (published). Unlike the previous ATLAS analysis [32], this CMS analysis targets final states with two leptons and a hadronically decaying top quark. Both top quark production and decay signals are considered in this analysis. Operators with different Lorentz structures are considered separately. Representative Feynman diagrams are shown in Figure 11.4.

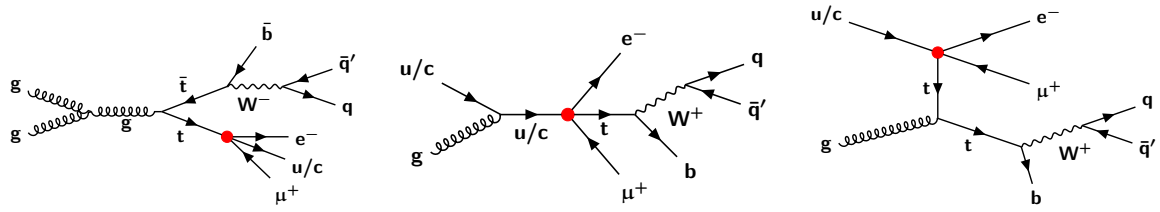

Figure 11.4: Representative Feynman diagrams for the signal processes that are targeted by [34]. Both top quark decay (left) and production (middle and right) CLFV processes are shown. The top quark that does not participate in the CLFV interaction is required to produce fully hadronic final states.

A BDT using multiple discriminating variables is trained to further enhance the sensitivity. Distributions of the BDT discriminator are shown in Figure 11.5. An upper limit at 95% CL is placed on the branching fraction of $\mathcal{B}(t \to \mu\tau q) < 7 \times 10^{-8}$, which improves the previous bound established by the ATLAS Collaboration [32] by two orders of magnitude.

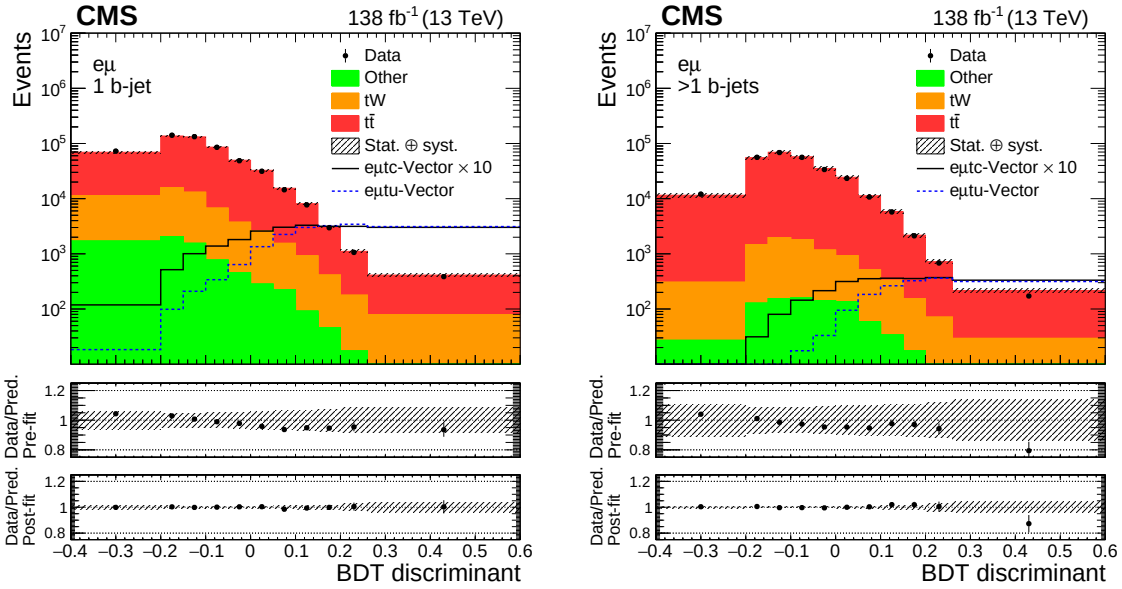

Figure 11.5: The left (right) histogram, taken from [34], shows the distribution of the BDT discriminator in regions with exactly (more than) one b-tagged jet. The middle (bottom) panel shows the ratio of data events and the pre-fit (post-fit) predictions.

11.3 Overview of the Present CMS Analysis

The analysis presented in this thesis searches for flavor-violating eμqt interactions using data collected by the CMS detector in 2016-2018, corresponding to an integrated luminosity of 138 fb^{-1}. The targeted final states of this analysis contain exactly three charged leptons, similar to the past ATLAS analysis [32]. In addition to the top quark decay signals, this analysis also considers the top quark production signals, which were first introduced by CMS in [34]. Separate SRs are defined to target these two different signals. Operators with different Lorentz structures and quark flavors are considered separately. Representative Feynman diagrams are shown in Figure 11.6.

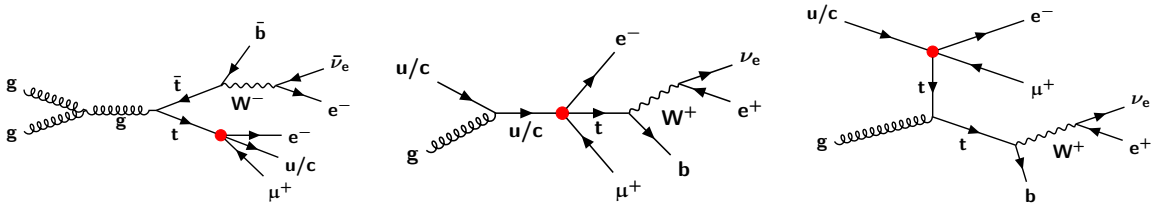

Figure 11.6: Representative Feynman diagrams for the signal processes that are targeted by this analysis. Both top quark decay (left) and production (middle and right) CLFV processes are shown. The top quark that does not participate in the CLFV interaction is required to produce leptonic final states.

For each SR, one binary BDT is trained to enhance the sensitivity of the corresponding signal mode. The *nonprompt* background is estimated using a data-driven method. An upper limit at 95% CL is placed on the branching fraction of $\mathcal{B}(t \to e\mu q) < 1.2 \times 10^{-8}$, which further improves the constraint from the previous CMS analysis [34] by nearly a factor of 6.

Chapter 12

Datasets, Simulated Samples and Triggers

This analysis is based on data collected by the CMS experiment in 2016-2018 from pp collisions at a center-of-mass energy of 13 TeV corresponding to an integrated luminosity of 138 fb^{-1}. Approximately 30 simultaneous pp collisions were occurring per 25 ns. Based on online selection criteria, fully reconstructed collision data that contain high-level physics objects are divided into "Primary Datasets (PDs)". The PDs that make use of lepton information for selection include "DoubleEG", "DoubleMu", "MuonEG", "SingleElectron", and "SingleMuon" for the 2016 and 2017 data-taking era. In 2018, "SingleElectron" and "DoubleEG" were replaced by "EGamma". The names of these PDs reflect the selection criteria. In addition to these PDs, MC samples are also generated to model both signal and background processes, which are described in Section 12.1 and Section 12.2, respectively. To account for the different data-taking conditions across the years, all MC samples are generated separately for each year. HLT triggers are used to select events offline, which is described in Section 12.3.

12.1 Signal Samples

In this analysis, New Physics is described by Dimension-6 EFT operators,

$$\mathcal{L} = \mathcal{L}_{SM}^{(4)} + \frac{1}{\Lambda^2}\sum_a C_a^{(6)} O_a^{(6)} + O\left(\frac{1}{\Lambda^4}\right). \tag{12.1}$$

From the many of the Dimension-6 operators in the Warsaw basis [116, 169], a total of 6 operators are considered, which are summarized in Table 12.1. To reduce the number of free parameters, the permutations of fermion flavors are combined. Taking the $e\mu ut$ vertex as an example, the WCs are parameterized in the following way:

$$C_{lq} = C_{lq}^{(1)1213} + C_{lq}^{(1)2113} + C_{lq}^{(1)1231} + C_{lq}^{(1)2131}, \tag{12.2}$$
$$C_{lu} = C_{lu}^{1213} + C_{lu}^{2113} + C_{lu}^{1231} + C_{lu}^{2131}, \tag{12.3}$$
$$C_{eq} = C_{eq}^{1213} + C_{eq}^{2113} + C_{eq}^{1231} + C_{eq}^{2131}, \tag{12.4}$$
$$C_{eu} = C_{eu}^{1213} + C_{eu}^{2113} + C_{eu}^{1231} + C_{eu}^{2131}, \tag{12.5}$$

Table 12.1: Summary of relevant dimension-6 operators considered in this analysis. Here, ε is the two dimensional Levi-Civita symbol, γ^μ the Dirac gamma matrices, and $\sigma^{\mu\nu} = \frac{i}{2}[\gamma^\mu, \gamma^\nu]$. The l and q denote left-handed doublets for leptons and quarks, respectively, whereas u and e denote right-handed singlets for quarks and leptons, respectively. The indices i and j are lepton flavor indices that run from 1 to 2 with $i \neq j$; m and n are quark flavor indices with the condition that one of them is 3 and the other one is 1 or 2. The four vector-like operators are merged in this analysis because the final-state particles produced by these operators have very similar kinematics.

Lorentz Structure	Operator		
vector	$O_{lq}^{(1)ijmn}$	$=$	$(\bar{l}_i\gamma^\mu l_j)(\bar{q}_m\gamma_\mu q_n)$
	O_{lu}^{ijmn}	$=$	$(\bar{l}_i\gamma^\mu l_j)(\bar{u}_m\gamma_\mu u_n)$
	O_{eq}^{ijmn}	$=$	$(\bar{e}_i\gamma^\mu e_j)(\bar{q}_m\gamma_\mu q_n)$
	O_{eu}^{ijmn}	$=$	$(\bar{e}_i\gamma^\mu e_j)(\bar{u}_m\gamma_\mu u_n)$
scalar	$O_{lequ}^{(1)ijmn}$	$=$	$(\bar{l}_i e_j)\ \varepsilon\ (\bar{q}_m u_n)$
tensor	$O_{lequ}^{(3)ijmn}$	$=$	$(\bar{l}_i\sigma^{\mu\nu} e_j)\ \varepsilon\ (\bar{q}_m\sigma_{\mu\nu} u_n)$

$$C_{lequ}^{(1)} = C_{lequ}^{(1)1213} + C_{lequ}^{(1)2113} + C_{lequ}^{(1)1231} + C_{lequ}^{(1)2131}, \tag{12.6}$$
$$C_{lequ}^{(3)} = C_{lequ}^{(3)1213} + C_{lequ}^{(3)2113} + C_{lequ}^{(3)1231} + C_{lequ}^{(3)2131}. \tag{12.7}$$

Additionally, all vector-like operators are combined,

$$O_{e\mu ut}^{vector} = O_{lq} + O_{lu} + O_{eq} + O_{eu}, \tag{12.8}$$
$$O_{e\mu ut}^{scalar} = O_{lequ}^{(1)} + h.c, \tag{12.9}$$
$$O_{e\mu ut}^{tensor} = O_{lequ}^{(3)} + h.c, \tag{12.10}$$

which results in 6 independent WCs: $C_{e\mu ut}^{vector}$, $C_{e\mu ut}^{scalar}$, $C_{e\mu ut}^{tensor}$, $C_{e\mu ct}^{vector}$, $C_{e\mu ct}^{scalar}$, $C_{e\mu ct}^{tensor}$, where the subscript describes the CLFV interaction vertex and the superscript indicates the Lorentz structure of the operators. The signal samples are produced for each of these six couplings, separately for production and decay signal modes.

To generate signal MC samples, the effective Lagrangian described above is implemented using the SmeftFR v2 [170] model, and saved in the "UFO" format [171]. Additionally, all the WCs are set to 1 with $\Lambda = 1$ TeV in the UFO, which then interfaces with the FeynRules [172] package

to calculate Feynman diagrams. The output of the FeynRules is used in ME event generator MadGraph5_aMC@NLO v2.4.2 [98] to generate events at LO.

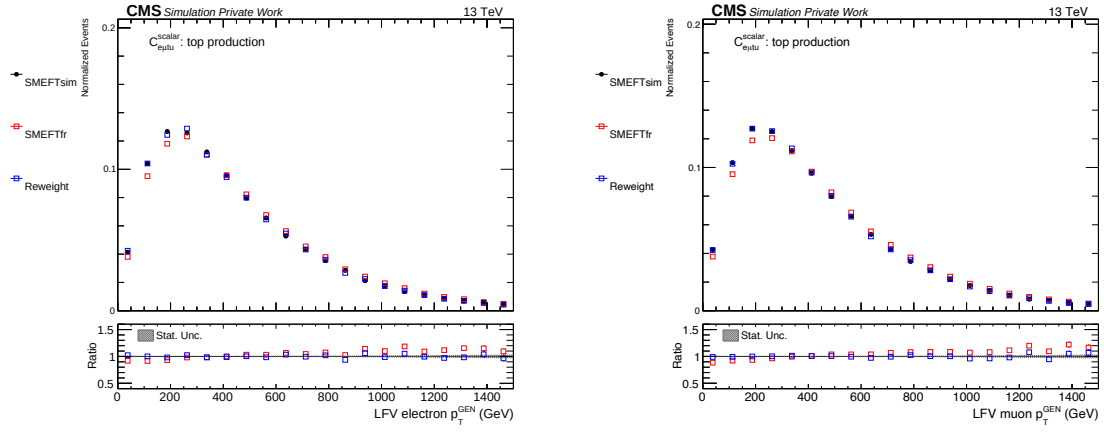

Figure 12.1: Comparison of kinematic distributions at ME-level produced by different models: LFV electron p_T (left), LFV muon p_T (right). The "SmeftFR" samples (shown in red curve) and "SMEFTsim" samples (shown in black curve) are statistically independent of each other. The "Reweight" (shown in blue curve) is produced by applying weights calculated by Equation (12.11) to "SmeftFR" samples.

In general, the calculations done by the ME event generators are model-agnostic assuming the same EFT configurations. In other words, models like SmeftFR or SMEFTsim [173] are expected to give the same or very similar results in terms of cross sections and four-momenta of final-state particles. Nevertheless, visible differences in kinematics have been observed and are shown in Figure 12.1. Furthermore, the cross sections predicted by SmeftFR v2 also yield more than 20% difference relative to SMEFTsim due to a bug that was later fixed in SmeftFR v3. In light of these differences, the CMS and ATLAS Collaborations agreed to adopt the SMEFTsim model as the common standard. This decision was made after Ref. [34] has already been published, and Ref. [34] uses cross sections calculated by SmeftFR v2. To quantify the impact of the choice of models on kinematics, the following ratio is calculated for each event i,

$$R^i_{\text{reweight}} = \frac{\omega^i_{\text{SMEFTsim}}}{\omega^i_{\text{SmeftFR}}}, \tag{12.11}$$

where ω^i_X is the per-event ME weight calculated by MadGraph5_aMC@NLO using model X. Since SMEFTsim was not used by CMS at the time when the signal samples were generated, R_{reweight} are used to "reweight" the original samples generated using SmeftFR.

Due to the significant differences in kinematic distributions between top decay and production signals, MC samples are generated separately for these processes. The cross sections for top production signals are taken directly from MadGraph5_aMC@NLO with SMEFTsim UFO as input. The event generation for top decay signals at the ME-level takes two steps: (i) production

of the SM $t\bar{t}$, and (ii) CLFV decay of one of the top quarks. Therefore, the $t\bar{t}$ cross-section at NNLO precision [174] is used to normalize the top decay signals,

$$\sigma_{\text{CLFV}}^{\text{Top Decay}} = 2 \times \sigma_{t\bar{t}}^{\text{NNLO}} \times \mathcal{B}(t \to e\mu q), \tag{12.12}$$

where q={u,c}, and $\mathcal{B}(t \to e\mu q)$ [175] can be expressed as,

$$\mathcal{B}(t \to e\mu q) = \begin{cases} \frac{|C_{e\mu qt}^{\text{vector}}|^2}{\Lambda^4} \frac{m_t^5}{384\pi^3\Gamma_t^{\text{SM}}}, \\ \frac{|C_{e\mu qt}^{\text{scalar}}|^2}{\Lambda^4} \frac{m_t^5}{3072\pi^3\Gamma_t^{\text{SM}}}, \\ \frac{|C_{e\mu qt}^{\text{tensor}}|^2}{\Lambda^4} \frac{m_t^5}{64\pi^3\Gamma_t^{\text{SM}}}, \end{cases} \tag{12.13}$$

where m_t and Γ_t^{SM} are taken to be 172.5 GeV and 1.33 GeV in this analysis, respectively. The choice of u or c quark in final states does not affect the cross sections of the top decay signals. The cross sections for all signal MC samples are summarized in Table 12.2. These cross-sections are used as a baseline to define the signal strength μ, which is used to quantify the relative strength of the signals when their normalization changes,

$$\mu(C/\Lambda^2) = \frac{\sigma_{\text{CLFV}}(C/\Lambda^2)}{\sigma_{\text{CLFV}}(1\text{TeV}^{-2})} \propto (C/\Lambda^2)^2. \tag{12.14}$$

Table 12.2: Theoretical cross sections for top production and decay for each CLFV coupling, calculated at $C/\Lambda^2 = 1$ TeV^{-2}, $m_t = 172.5$ GeV, and $\Gamma_t^{\text{SM}} = 1.33$ GeV by MadGraph5_aMC@NLO with SMEFTsim. The first uncertainty represents the effect of QCD renormalization and factorization scales. The second uncertainty is the PDF uncertainty.

Lorentz Structure	Samples	XS (fb)
vector	top production via u quark	$460^{+81}_{-64} \pm 6$
	top production via c quark	$33^{+5}_{-4} \pm 6$
	top decay via u/c quark	$32.0^{+0.8}_{-1.1} \pm 1.3$
scalar	top production via u quark	$97^{+18}_{-14} \pm 1$
	top production via c quark	$6.3^{+0.9}_{-0.8} \pm 1.4$
	top decay via u/c quark	$4.0^{+0.1}_{-0.1} \pm 0.2$
tensor	top production via u quark	$2140^{+370}_{-290} \pm 30$
	top production via c quark	$164^{+22}_{-18} \pm 27$
	top decay via u/c quark	$187^{+5}_{-6} \pm 8$

Steps other than the ME calculation concerning signal MC generation follow the CMS standard, which is described in the following section.

12.2 Background Samples

The background processes are divided into two categories: (i) processes with three or more *prompt* leptons in the final states are classified as "*prompt* background", and (ii) other processes are classified as "*nonprompt* background". The *nonprompt* backgrounds in this analysis are modeled with a data-driven technique, which is discussed in Chapter 15. The MC samples listed in the "*nonprompt*" category in Table 12.3 are therefore only used for validations.

Besides tZq, tHq, tHW, and tWZ processes, the NLO PDF set from NNPDF3.0 [93] is used in 2016 to generate background MC samples. The NNLO PDF set from NNPDF3.1 [10] is used for tZq while the LO PDF set from NNPDF3.0 is used for tHq, tHW, and tWZ in 2016. In 2017 and 2018, the NNLO PDF set from NNPDF3.1 was used to generate all the samples.

The default choice of ME event generator is MADGRAPH5_aMC@NLO v2.4.2 (v2.2.2 for 2016), which is used to generate all but ZZ, $t\bar{t}H$, and $t\bar{t}$ samples. These three samples are generated with POWHEG v2 [99] instead. Samples with small contributions (tHq, tWZ, tHW, and low mass DY) are generated at LO while other samples are generated at NLO. Whenever possible and relevant, theoretical cross sections from high-order QCD calculations are used. The references of these calculations are included in Table 12.3.

The PYTHIA v8.2 [101] is used to model parton shower and hadronization. The CUETP8M1 [176] was used in 2016 for underlying event tuning while the CP5 [177] was used in 2017 and 2018. The configurations of the MC samples are summarized in Table 12.3.

All simulated events include a detailed simulation of the CMS detector response based on GEANT4 [182], and are processed using the same CMS event reconstruction software as used for the data.

12.3 Triggers

The target final states of this analysis contain three prompt leptons, which make lepton triggers the most optimal choice to select events. To achieve maximum acceptance, a combination of single-lepton, di-lepton, and tri-lepton triggers are used. These triggers are summarized in Appendix A. Events in simulated samples are required to fire at least one of the triggers listed in Table A.1-A.3. Since multiple PDs are used to record data events and the orthogonality of these PDs is not guaranteed by the online selection criteria, the following trigger logic is implemented to remove the overlap between different PDs:

- Events in SingleMuon datasets are required to fire at least one of the triggers listed under "SingleMuon".

Table 12.3: Summary of the configurations of the MC samples. DYM50 (DYM10to50) denotes a DY sample with a dilepton invariant mass greater than 50 GeV (between 10 and 50 GeV). V includes W and Z bosons. The cross-sections for samples without a citation are taken directly from their event generators.

Category	Process	Event Generator	Perturbative QCD	Tune	XS precision
prompt background	WZ	MadGraph	NLO	CUETP8M1(CP5)	NLO [178]
	ZZ	powheg	NLO	CUETP8M1(CP5)	NLO [178]
	VVV	MadGraph	NLO	CUETP8M1(CP5)	NLO
	$t\bar{t}W$, $t\bar{t}Z$	MadGraph	NLO	CUETP8M1(CP5)	NLO [179, 180]
	$t\bar{t}H$	powheg	NLO	CUETP8M1(CP5)	NLO [180]
	tZq	MadGraph	NLO	CP5	NLO
	tHq, tHW, tWZ	MadGraph	LO	CUETP8M1(CP5)	LO
nonprompt background	$t\bar{t}$	powheg	NLO	CUETP8M1(CP5)	NNLO [174]
	DYM50	MadGraph	NLO	CUETP8M1(CP5)	NNLO [181]
	DYM10to50	MadGraph	LO	CUETP8M1(CP5)	NLO [181]

- Events in DoubleMuon datasets are required to fire at least one of the triggers listed under "DoubleMu". Events are removed if they also fire at least one of the triggers listed under "SingleMuon".
- Events in "MuonEG" datasets are required to fire at least one of the triggers listed under "MuonEG". Events are removed if they also fire at least one of the triggers listed under "SingleMuon" or "DoubleMu".
- Events in Single Electron datasets are required to fire at least one of the triggers listed under "SingleElectron". Events are removed if they also fire at least one of the triggers listed under "SingleMuon", "DoubleMu", or "MuonEG".
- Events in DoubleEG datasets are required to fire at least one of the triggers listed under "DoubleEG". Events are removed if they also fire at least one of the triggers listed under "SingleMuon", "DoubleMu", "MuonEG", or "SingleElectron".
- Events in EGamma datasets are required to fire at least one of the triggers listed under "EGamma". Events are removed if they also fire at least one of the triggers listed under "SingleMuon", "DoubleMu", or "MuonEG".

Chapter 13

Object Selection

Reconstructed objects described in Chapter 8, referred to as "candidates", are further selected with more stringent requirements to suppress the contributions from background processes while maintaining a high signal acceptance. In particular, prompt electron and muon candidates are identified through a custom-trained BDT classifier, which is discussed in Section 13.1. Two jet identification algorithms are deployed to select jet candidates originating from hard collisions, which is discussed in Section 13.2. Furthermore, jet candidates that originate from b quarks are identified with a Neural Network (NN) based algorithm, which is discussed in Section 13.3.

13.1 Lepton Selection

The target final states of this analysis feature exactly three leptons that originate either from decays of EW bosons or from the CLFV interaction, which in this analysis is a contact interaction that involves four fermions. These leptons, referred to as *prompt* leptons, typically appear to be isolated and not far away from the PV. In contrast, *nonprompt* leptons are leptons that originate from decays of hadrons, photon conversions, or misidentified leptons. They often travel a noticeable distance away from the PV and appear to be less isolated due to nearby activities. Due to the high multiplicity of leptons in our selection, backgrounds with at least one *nonprompt* lepton outnumber any other SM processes that produce three or more *prompt* leptons. It is therefore crucial to exploit the differences between *nonprompt* and *prompt* leptons and bring the *nonprompt* background under control.

13.1.1 TOP LeptonMVA

The TOP LeptonMVA is an offline lepton identification algorithm that was originally developed for tZq analyses [183, 184]. It is based on a Gradient BDT implemented using the TMVA package [185]. A total of 13 features are used as input to the BDT. They can be categorized into four groups: (i) positions and momenta of the lepton candidates, (ii) isolation variables, (iii) variables associated with the closest jet, and (iv) a quality variable that is specific to the electron or muon candidate. The version of TOP LeptonMVA used by this analysis is the same as [184], where a detailed description of all input features can be found.

Prompt leptons from $t\bar{t}W$, $t\bar{t}Z$, and tZq samples are used as signals in the BDT training while *nonprompt* leptons from $t\bar{t}$ samples are used as backgrounds. The trained BDT outputs a single score for each lepton candidate ranging from -1 to 1 with -1 (1) being the most background-(signal-) like. The tight working point with a threshold of (>) 0.9 is chosen as the selection criteria for both electron candidates and muon candidates, which corresponds to a signal(background) efficiency of 90%(1%). The strategy is to trade a small percentage (<10%) of signal efficiency for several factors of background rejection.

13.1.2 Full Selection

In addition to the TOP LEPTONMVA requirement, a set of common selection criteria is applied to both electron and muon candidates. The minimum p_T requirement is 38 GeV, 20 GeV, and 20 GeV for the leading, sub-leading, and trailing lepton in p_T, respectively. This requirement is driven by the p_T thresholds of the HLT triggers to avoid inefficiency at turn-on. Electron and muon candidates are required to be in the pseudorapidity range $|\eta| < 2.4$, which corresponds to the acceptance of CMS tracker and muon system in 2016-2018. The transverse (longitudinal) impact parameters with respect to the PV, denoted as d_{xy} (d_z), is required to be in the range $|d_{xy}| < 0.05$ cm ($|d_z| < 0.05$ cm). The significance of the 3-dimensional impact parameter, denoted as SIP_3, is defined as the 3-dimensional impact parameter divided by its uncertainty. It is required that $SIP_3 < 8$. The three cuts on impact parameters are added due to the difference in distributions of these parameters between *prompt* and *nonprompt* leptons. Also, they are part of the pre-selection requirement in the BDT training.

Furthermore, all lepton candidates are required to be isolated. This is achieved by first defining a cone with a distance parameter of ΔR, defined in Equation (7.3) around each lepton candidate. Only PF candidates within $\Delta R < R_{max}$ can contribute to the isolation variable, where R_{max} is referred to as the size of the cone. Secondly, an isolation variable is defined as,

$$I^{rel}_{mini} = \frac{1}{p^{\ell}_T}\{\sum_{charged} p_T + \max(0, \sum_{neutral} p_T - \rho\mathcal{A}[\frac{\Delta R}{0.3}]^2)\}, \tag{13.1}$$

where p^{ℓ}_T is the p_T of the lepton candidate, the first term inside the curly braces is the scalar sum of all charged particles associated with the PV while the second term evaluates the contribution from neutral particles. This is done by first scalar-summing over p_T of all neutral particles associated with the PV. A correction term, known as effective area correction [186], is then subtracted. This term is used to mitigate the impact of PU interactions. The size of the cone scales with p^{ℓ}_T as,

$$R_{max} = \max(0.05, \min(0.2, \frac{10\text{GeV}}{p^{\ell}_T})). \tag{13.2}$$

This type of isolation variable is known as "mini isolation", which maximizes the signal efficiency

at p_T^{ℓ} by reducing the cone size. It is required that lepton candidates to have $I_{\text{mini}}^{\text{rel}} < 0.12$.

For electrons specifically, candidates are required to have a GSF track with one or fewer missing inner hits. Electron candidates reconstructed in the transition region between the ECAL barrel and endcap (i.e. $1.44 < |\eta_{\text{SC}}| < 1.57$) are removed from consideration. For muons specifically, candidates are required to be PF muons and pass the Medium muon ID discussed in Section 8.3.

Lepton candidates that pass all requirements stated above are referred to as "*tight*" leptons. Leptons selected with a separate set of criteria, known as "*loose*", is used in estimating the *nonprompt* background, which is discussed in Chapter 15. Unless explicitly stated, all lepton objects presented in this search are *tight* leptons.

The energy scale and resolution are calibrated for all electron candidates, as discussed in Section 8.2. The energy scale and resolution are also calibrated for muon candidates with $p_T < 200$ GeV, as discussed in Section 8.3. Per-object scale factors are applied to *tight* leptons in simulated events to correct for the differences in reconstruction, isolation, and identification between data and MC. These scale factors are obtained using dilepton events in the Z resonance window.

13.2 Jet Selection

Jet candidates are reconstructed from PF candidates using the anti-k_T algorithm [145] described in Section 13.2 with a cone size $R = 0.4$. These jets are often referred to as the "AK4" jets. To mitigate the effect of pileup interactions, a procedure known as the charged hadron subtraction (CHS) [187] is carried out to remove charged hadrons that are not associated with the PV before the jet clustering. Jet candidates are required to have a minimum p_T of 30 GeV and in the pseudorapidity range $|\eta| < 2.4$, where b-tagging is still effective. It is further required that all jet candidates be isolated from *tight* leptons. A cone of the size 0.4 around each jet candidate is defined and candidates will be removed if any *tight* leptons are found within such a cone. This procedure is implemented to remove the overlap between leptons and jets.

The two primary sources of background are (i) detector noise, and (ii) jets from PU interactions. To suppress detector noise, a set of cut-based selections, referred to as the PF Jet ID [188], is applied to jet candidates. This algorithm utilizes information from PF candidates, including: (i) fraction of charged (neutral) hadrons energy, (ii) fraction of charged (neutral) EM energy, (iii) fraction of muon energy, and (iv) object multiplicity. The "tightLepVeto" working point is chosen to select jet candidates, which corresponds to 98-99% signal efficiency.

The second algorithm, referred to as the PU ID [189, 190], is designed to reject jet candidates that originate from PU interactions. This algorithm is based on a BDT that utilizes: (i) the trajectories of tracks associated with the jets, (ii) the topology of the jet shape, and (iii) object multiplicity. The *loose* working point is chosen to select jet candidates with $p_T < 50$ GeV, which corresponds to 99% signal efficiency. Applying this algorithm to jet candidates with $p_T > 50$ GeV is both ineffective and unnecessary as PU jets mostly reside in the low p_T spectrum. The

overall effect of this algorithm on this analysis is small as PU jets constitute only a small fraction of all jet candidates in the phase space of this analysis.

As discussed in Section 8.4, the energy scale for all jet candidates (data and MC) are calibrated. One extra correction, referred to as the JER, is applied to simulated jets to recreate the jet energy resolution as measured in data.

13.3 Identification of b jets

The DeepJet algorithm [191] is used to identify jets that originate from a b quark. The core strategy of this algorithm is to minimize information loss. This is achieved by removing entirely the selection of jet constituents, which limits the number of jet constituents considered. Additionally, an effort is made to use as many low-level features as possible, which further deepens the feature space. Approximately a total of 650 input features are used, which can be categorized into four groups: (i) global variables, (ii) charged PF candidate features, (iii) neutral PF candidate features, and (iv) SV features associated with the jet. When compared to the existing DeepCSV algorithm [192], the DeepJet algorithm delivers up to 20% improvement in signal efficiency while maintaining the same background rejection rate.

The DeepJet algorithm outputs a score ranging between 0 and 1, with 0 (1) being the most background- (signal-) like. The "Medium" working point is chosen to tag b jet candidates, which corresponds to 70%-80% signal efficiency [193]. The shape of the DeepJet output distribution is corrected for the differences between data and MC in signal and background efficiencies. The per-event correction weight ω is defined as,

$$\omega = \prod_{i}^{N_{\text{jets}}} \text{SF}(p_{T_i}, \eta_i, F_i, D_i), \tag{13.3}$$

where SF is the ratio of efficiency in data to efficiency to MC parameterized as a function of p_{T}, η, (MC truth) flavor F, as well as DeepJet output D of each jet in the event. ω is applied to all MC events.

Additional corrections are applied to remove the normalization effect of ω before jet selection. These scale factors are measured using MC in e$\mu\ell$ channel described in Chapter 14. The effect of these scale factors is shown in Figure 13.1.

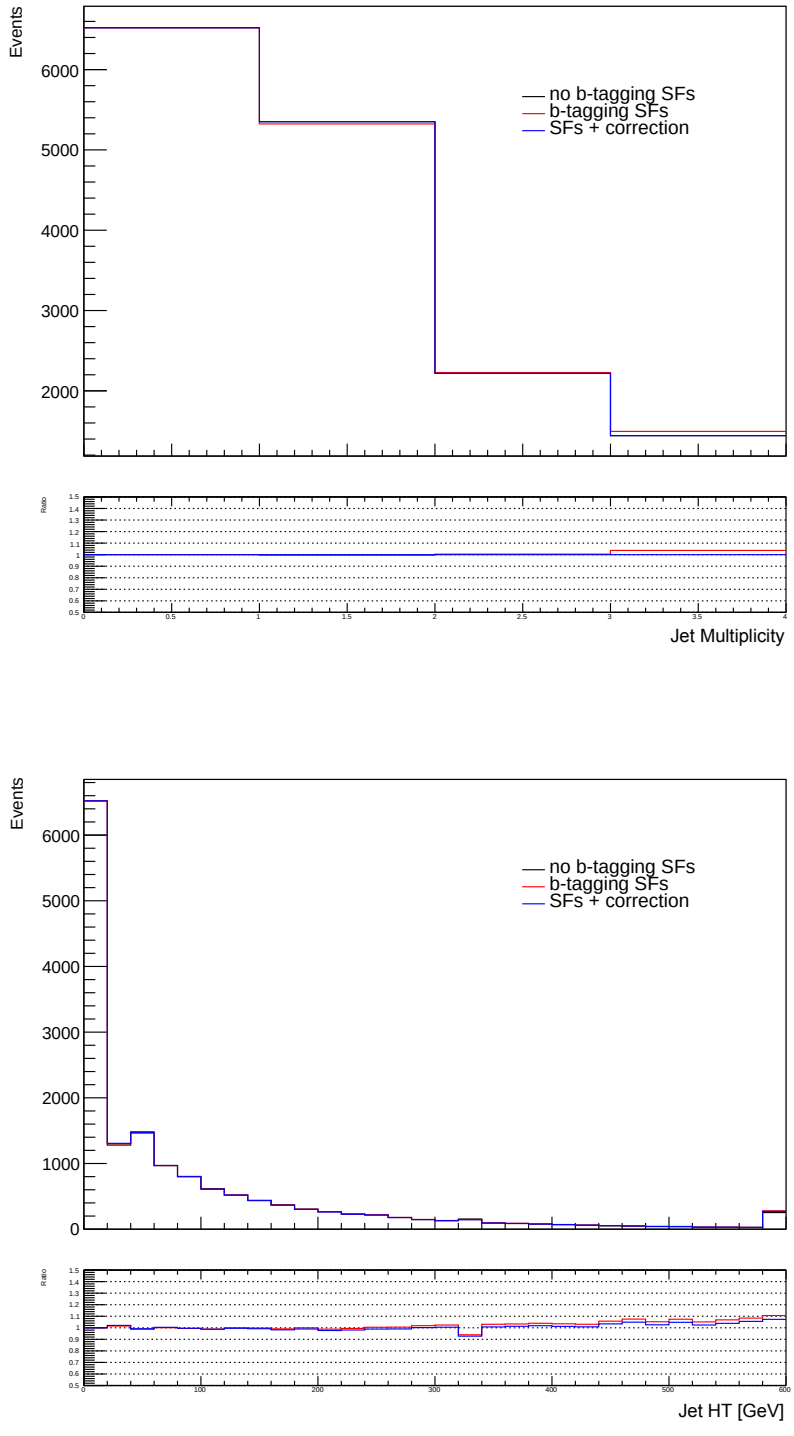

Figure 13.1: Simulated events in eμℓ channel without additional requirements on jets. The top histogram shows the distribution of jet multiplicity while the bottom histogram shows the distribution of H_T, which denotes the scalar sum of the p_T of all jets. Distributions without any jet-related scale factors are shown in black lines. Distributions with only b-tagging scale factors are shown in red lines. Distributions with b-tagging scale factors and corrections to remove normalization effects are shown in blue lines.

Chapter 14

Event Selection

Events are required to contain exactly three *tight* leptons described in Section 13.1. Furthermore, events are selected with HLT triggers discussed in Section 12.3. Events with different lepton flavor composites are further categorized into three exclusive channels: eee, μμμ, eμℓ. In all three channels, the sum of the electric charges of the selected leptons is required to be 1 or -1. The leading leptons in all selected events are required to be matched with trigger objects within $\Delta R < 0.2$. Within each channel, different regions are defined to further understand signal and background.

eμℓ is the channel where close to 100% of the simulated signal events reside. This channel is divided into signal-enriched SRs and signal-depleted VRs, which are discussed in Section 14.1 and Section 14.2, respectively. Due to the lack of different flavors, the eee and μμμ channels are signal-depleted by definition. Therefore, events found in these two channels are only used to study background processes, which are discussed in Section 14.2. The kinematic reconstruction of heavy particles, such as the top quark, is described in Section 14.3.

14.1 Signal Region

The core feature of the signal events is the presence of the "LFV eμ" pair, which consists of a pair of Opposite-Sign and Different-Flavor (OSDF) leptons. It is guaranteed that there is at least one OSDF pair in all events residing in the eμℓ channel due to the requirement on electric charges. The OSDF pair is immediately labeled as the LFV eμ pair if it is only possible to reconstruct one OSDF pair. In events where a pair of Same-Sign and Same-Flavor (SSSF) leptons are present, a kinematic reconstruction is used to determine which one of two leptons form the LFV eμ pair with the third lepton, which is detailed in Section 14.3. Leptons that form the LFV eμ pair are referred to as the LFV electron or muon as it is assumed that they originate from the CLFV interaction. Based on the event topology of the signal process, further selection criteria are applied to define the SR. These selection criteria help achieve an optimal signal-to-background ratio by removing the majority of the background events present in the eμℓ channel.

At the tree level, signal events are expected to contain one or two jets, which motivates a requirement of at least one jet in SR. Furthermore, it is required that there is no more than one

b-tagged jet to suppress the contribution from $t\bar{t}$ events. Another prominent background is DY production that features an OSSF pair. To suppress DY processes in SR, events that contain an OSSF lepton pair with an invariant mass between 50 GeV and 106 GeV are removed. The lower bound of this veto is lower than the typical value (e.g. 75 GeV) because the mass range between 50 GeV and 75 GeV has very few signal events and is dominated by *nonprompt* background from photon conversion. Additionally, a modest threshold of 20 GeV is applied to $p_{\mathrm{T}}^{\mathrm{miss}}$ due to the presence of neutrinos in the signal events.

Distributions of the LFV eμ mass and the mass of the OSSF lepton pair are shown in Figure 14.1. All backgrounds in Figure 14.1 are estimated using MC simulation even though the strategy is to use a data-driven method to estimate the *nonprompt* background. This serves as a preliminary check to understand the components of different backgrounds in SR. Distributions of more variables in SR are included in Appendix B.

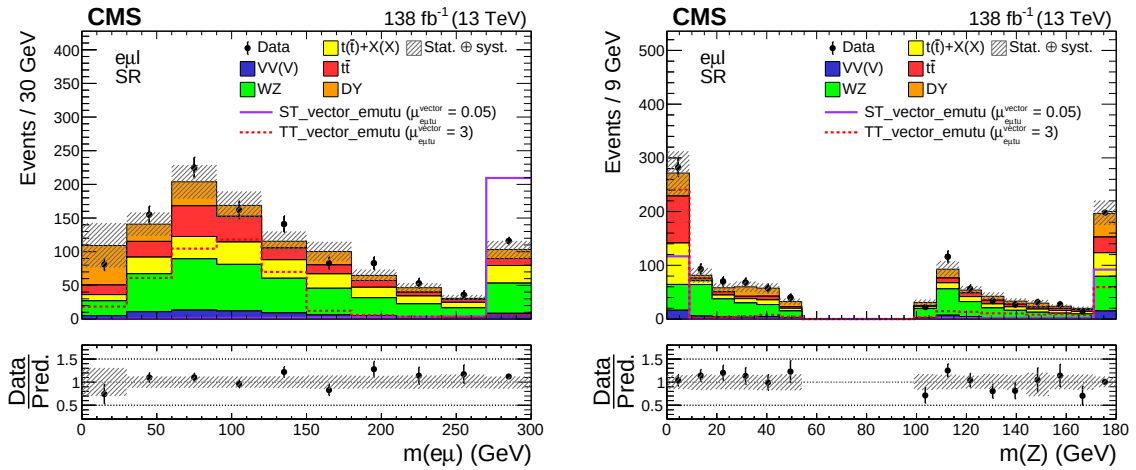

Figure 14.1: Distributions of the LFV eμ mass (left) and the mass of the OSSF lepton pair (right) in SR. The data are shown as filled points and the SM background predictions as histograms. The VV(V) background includes ZZ and triboson production, while the $t\bar{t}$ + X(X) component includes $t\bar{t}W$, $t\bar{t}Z$, $t\bar{t}H$, tZq, and smaller backgrounds containing one or two top quarks plus a boson or quark. All backgrounds are estimated using MC simulation. The hatched bands indicate statistical and systematic uncertainties for the SM background predictions. The normalization of the signal processes is chosen arbitrarily for improved visualization. The last bin of both histograms includes the overflow events.

Using the LFV eμ mass, the SR is further divided into two subsets to create top production and decay enriched regions:

- SR1, m(eμ) $<$ 150 GeV: top quark decay enriched.
- SR2, m(eμ) $>$ 150 GeV: top quark production enriched.

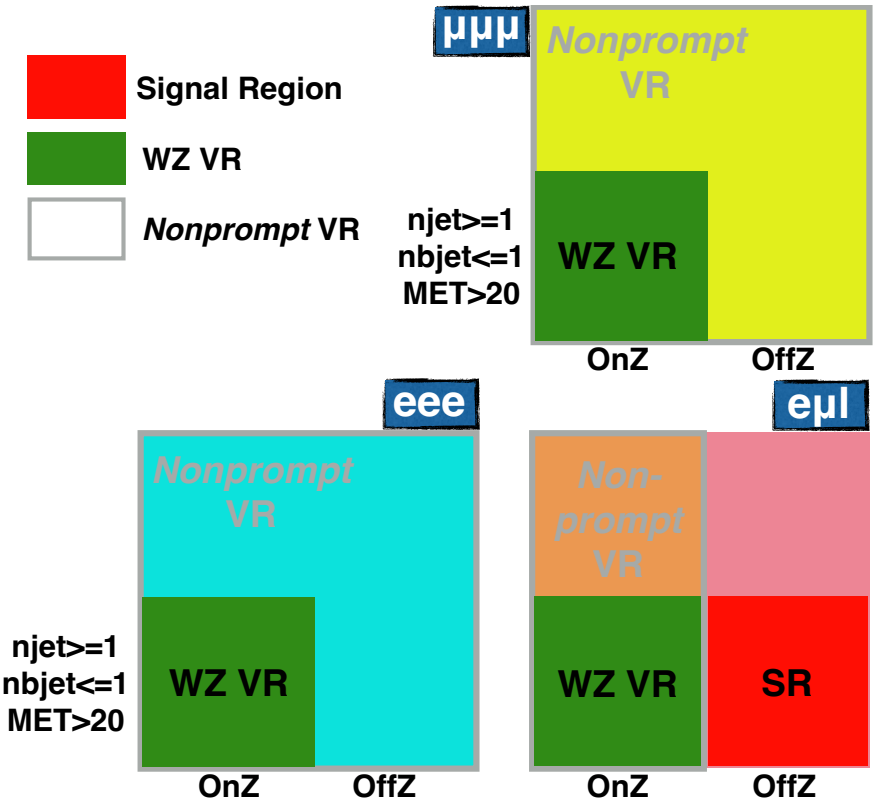

Figure 14.2: Illustration of selection criteria used to define different regions. "OnZ" means the presence of at least one OSSF pair with an invariant mass between 50 GeV and 106 GeV. Events are labeled as "OffZ" when they fail "OnZ" criteria.

14.2 Validation Region

There are two types of signal-depleted VR defined across three channels: *nonprompt* VR and WZ VR. The purpose of these two types of VR is only limited to the validation of the background modeling as neither of them enters the final fit. It is expected that the *nonprompt* VR has a significant fraction of *nonprompt* background while WZ production is responsible for most of the backgrounds in the WZ VR. Distributions of leading lepton p_{T} and leading lepton η in the WZ control region can be found in Figure 14.3. The *nonprompt* VRs are further discussed in Chapter 15.

Selection criteria used to define different regions are illustrated in Figure 14.2 and are summarized in Table 14.1.

14.3 Kinematic Reconstruction

As mentioned, the LFV eμ pair is assumed to be the product of the CLFV interaction, while the third lepton, referred to as the standalone lepton, is assumed to originate from the leptonically

Table 14.1: Summary of the selection criteria used to define different event regions. "OnZ" means the presence of at least one OSSF pair with an invariant mass between 50 GeV and 106 GeV. Events are labeled as "OffZ" when they fail "OnZ" criteria.

Channel	Region	OnZ	OffZ	MET > 20 GeV	njet>=1	nbjet<=1
eee	VR	-	-	-	-	-
	WZ VR	✓	-	✓	✓	✓
eμℓ	SR	-	✓	✓	✓	✓
	Nonprompt VR	✓	-	-	-	-
	WZ VR	✓	-	✓	✓	✓
μμμ	Nonprompt VR	-	-	-	-	-
	WZ VR	-	✓	✓	✓	✓

decaying top quark. To distinguish this top quark (t→ $\ell\nu$b) from the top quark that decays via the CLFV interaction (t→ eμq), the former is referred to as the SM top quark while the latter is referred to as the LFV top quark.

The jet with the highest b-tagging score, regardless of whether or not it crosses the medium working point threshold, is assumed to originate from a bottom quark decay. Therefore, it is combined with p_T^{miss} to build the SM top quark. The x and y components of p_T^{miss} are taken as measurements of neutrino p_x and p_y. The z component of neutrino momentum is calculated by imposing the constraint that the invariant mass of the combined object (standalone lepton + neutrino) must be equal to W boson mass. If there is no real solution, the real part of the complex solution is taken. If there is more than one real solution, the solution that is the closest to the p_z of the standalone lepton is taken. In events where there is more than one candidate of standalone lepton (i.e. the presence of the SSSF pair), the lepton that gives a top mass that is the closest to the SM top quark mass (m_t = 172.5 GeV) is taken as the standalone lepton.

Once the standalone lepton has been determined, the remaining two leptons are labeled as the LFV eμ pair and are combined with each selected jet to reconstruct the LFV top quark candidates. The jet with the highest b-tagging score is excluded from this reconstruction since it is assumed to be from the decay of the SM top quark. Out of all the LFV top quark candidates, the candidate that gives a top mass that is the closest to the SM top quark mass is taken. The LFV top quark mass is set to 0 in events where there are less than two jets.

A Z boson candidate is reconstructed using the OSSF pair, which is not guaranteed to be present in the eμℓ channel. The mass of the OSSF lepton pair is set to 0 in events where the OSSF is absent. The Z boson candidate is the only heavy particle reconstructed in the eee and μμμ

channels. Since there are always two ways to form the OSSF pair, the OSSF pair with an invariant mass that is closer to the Z boson mass ($m_Z = 91.2$ GeV) is taken.

Jets with high b-tagging scores are combined with leptons to form so-called "$m_{b\ell}$" systems. The first $m_{b\ell}$ system takes the jet with the highest b-tagging score and combines it with each *tight* lepton in events. Out of the three $m_{b\ell}$ system candidates, the one with the lowest $m_{b\ell}$ is taken, and the two constituents are excluded from the consideration of the second $m_{b\ell}$ system. If additional jets exist, the second $m_{b\ell}$ system takes the jet with the highest b-tagging score and combines it with two of the remaining leptons separately. Out of the two candidates, the one with the lowest $m_{b\ell}$ is taken. $m_{b\ell}$ is set to 0 if no additional jet exists after the formation of the first $m_{b\ell}$ system.

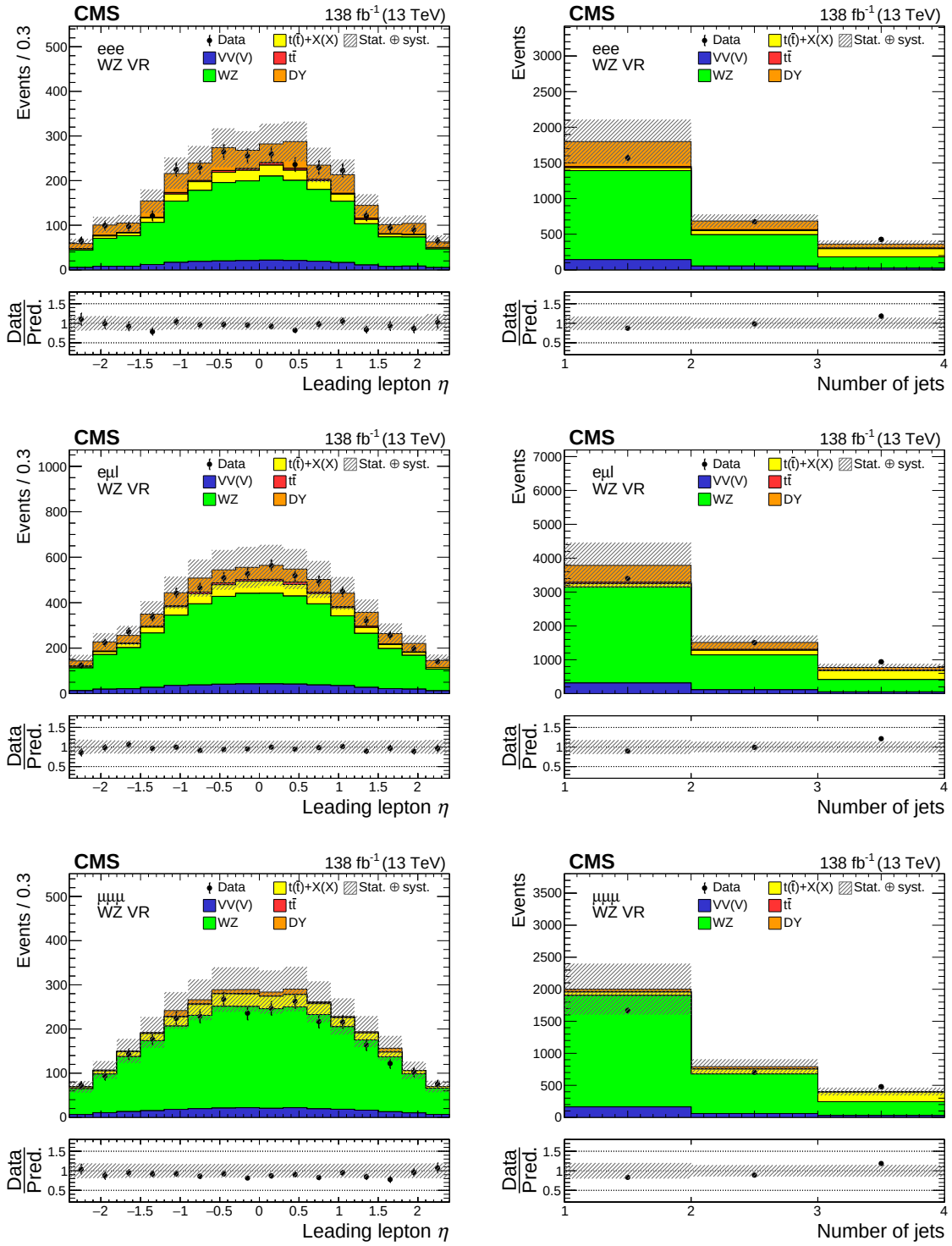

Figure 14.3: Distributions of the leading lepton η (left column) and the jet multiplicity (right column) in the WZ VRs. Events in the eee, e$\mu\ell$, and $\mu\mu\mu$ WZ VRs are shown in the upper, middle, and lower rows, respectively. The data are shown as filled points and the background predictions as histograms. All backgrounds are estimated with MC simulation. The hatched bands indicate statistical and systematic uncertainties for the background predictions. The last bin of the right column histograms includes the overflow events.

Chapter 15

Nonprompt Background Estimation

In this analysis, the term *prompt* leptons refers to leptons that originate from the CLFV vertex, the DY process, or an EW boson decay, including leptons from τ decays if the τ lepton originates from the latter two processes. *Nonprompt* leptons refer to leptons that originate from hadron decays and photon conversions, as well as particles misidentified as leptons. *Nonprompt* leptons are suppressed through isolation requirements and a MVA-based identification specifically trained to reject them.

Nonprompt backgrounds are defined to be backgrounds with at least one *nonprompt* lepton passing the *tight* selection criteria, in this case generally dominated by DY and $t\bar{t}$ production. An accurate estimation of *nonprompt* backgrounds is difficult to achieve through MC modeling. Therefore, a data-driven technique called the "*matrix method*" [194] is used to estimate the *nonprompt* backgrounds.

A brief description of the *matrix method* in its simplest form is given in Section 15.1 followed by its generalization and implementation in Section 15.2. This method is validated using three VRs and is described in Section 14.2. Lastly, the *nonprompt* estimation in the SR is presented in Section 15.4.

15.1 The Matrix Method

The *matrix method* is a data-driven technique used to estimate the fraction of *nonprompt* leptons that pass a given lepton selection, referred to as "*tight*". The *tight* selection usually incorporates tight lepton identification and isolation requirements and corresponds to the full lepton selection used in an analysis. The *loose* selection is obtained by loosening the *tight* selection. The *loose* selection is used as a baseline such that any *loose* leptons fall into one of the two exclusive categories: *tight* or *not tight*. The *matrix method* deals with *prompt* and *nonprompt* leptons separately. As a result, *prompt* and *nonprompt* efficiencies are introduced, as illustrated in Figure 15.1.

In a simplified scenario with only one lepton in the final state, the *prompt* efficiency r measures the probability of *prompt* leptons passing *tight* selection. It is treated as an observable that can be obtained through measurement,

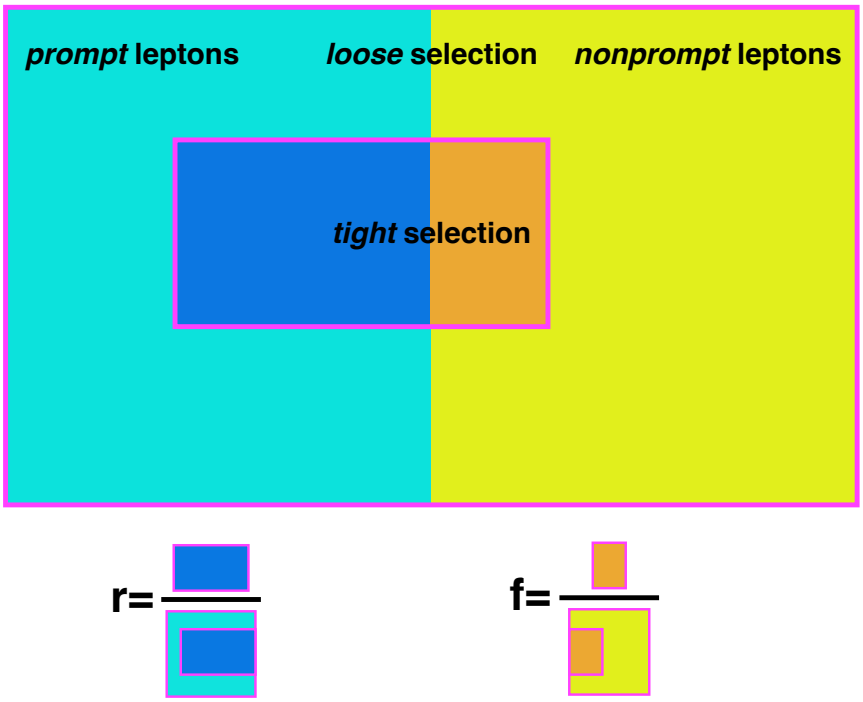

Figure 15.1: Illustration of the *prompt* efficiency r and the *nonprompt* efficiency f. The *tight* selection is typically a subset of the *loose* selection, which guarantees both r and f to be greater than 0 and smaller 1.

$$r = \frac{n_P^T}{n_P^T + n_P^{\overline{T}}}, \tag{15.1}$$

in which $n_P^T / n_P^{\overline{T}}$ denotes the number of events with a *prompt* lepton that is *tight*/*not tight*.

Similarly, *nonprompt* efficiency f can be expressed as,

$$f = \frac{n_N^T}{n_N^T + n_N^{\overline{T}}}, \tag{15.2}$$

in which $n_N^T / n_N^{\overline{T}}$ denotes the number of events with a *nonprompt* lepton that is *tight*/*not tight*.

The measurement of r/f is often performed in dedicated control regions, where high purity of *prompt*/*nonprompt* leptons is expected. These regions are referred to as the MR. It is assumed that r/f is a universal property of *prompt*/*nonprompt* leptons that is independent of physics processes. Therefore, r/f extracted from MR can be used to estimate the contamination of *nonprompt* leptons in a different region (e.g. SR) even though these two regions are orthogonal to each other.

In this simplified scenario, the total number of events in the region of interest (e.g. SR/VR) with a *tight*/*not tight* lepton can be expressed in a system of equations,

$$\begin{aligned} N^T &= N_P^T + N_N^T \\ N^{\overline{T}} &= N_P^{\overline{T}} + N_N^{\overline{T}}, \end{aligned} \tag{15.3}$$

in which the capital letter "N" is used to indicate that these numbers are referring to events in a region that is different from MR. $N_P^{\overline{T}}/N_N^{\overline{T}}$ can be expressed in terms of r/f and N_P^T/N_N^T according to Equation 15.1/15.2 and the assumption that r/f remains the same across different regions,

$$\begin{aligned} N^T &= r\frac{N_P^T}{r} + f\frac{N_N^T}{f} \\ N^{\overline{T}} &= (1-r)\frac{N_P^T}{r} + (1-f)\frac{N_N^T}{f}. \end{aligned} \tag{15.4}$$

Equation (15.4) can also be expressed in the form of a matrix,

$$\begin{pmatrix} N^T \\ N^{\overline{T}} \end{pmatrix} = \begin{pmatrix} r & f \\ 1-r & 1-f \end{pmatrix} \begin{pmatrix} N_P^T/r \\ N_N^T/f \end{pmatrix}. \tag{15.5}$$

Regions that correspond to the two numbers that appear in the right-hand side vector of Equation (15.5) are referred to as the "Application Regions (ARs)", which can be constructed using experimental data. The estimation of *nonprompt* background, denoted by N_N^T, can be obtained by a simple matrix inversion.

15.2 Generialization and Implementation of the Matrix Method

The description in the previous section deals with a scenario where only one lepton is studied. This analysis uses a generalized version of the *matrix method*, where all three *tight* leptons are considered to be possibly *nonprompt*. Equation (15.5) is generalized as,

$$
\begin{pmatrix} N^{TTT} \\ N^{TT\bar{T}} \\ N^{T\bar{T}T} \\ N^{T\bar{T}\bar{T}} \\ N^{\bar{T}TT} \\ N^{\bar{T}T\bar{T}} \\ N^{\bar{T}\bar{T}T} \\ N^{\bar{T}\bar{T}\bar{T}} \end{pmatrix}
=
\begin{pmatrix}
r_1r_2r_3 & r_1r_2f_3 & r_1f_2r_3 & r_1f_2f_3 & f_1r_2r_3 & f_1r_2f_3 & f_1f_2r_3 & f_1f_2f_3 \\
r_1r_2(1-r_3) & r_1r_2(1-f_3) & r_1f_2(1-r_3) & r_1f_2(1-f_3) & f_1r_2(1-r_3) & f_1r_2(1-f_3) & f_1f_2(1-r_3) & f_1f_2(1-f_3) \\
r_1(1-r_2)r_3 & r_1(1-r_2)f_3 & r_1(1-f_2)r_3 & r_1(1-f_2)f_3 & f_1(1-r_2)r_3 & f_1(1-r_2)f_3 & f_1(1-f_2)r_3 & f_1(1-f_2)f_3 \\
r_1(1-r_2)(1-r_3) & r_1(1-r_2)(1-f_3) & r_1(1-f_2)(1-r_3) & r_1(1-f_2)(1-f_3) & f_1(1-r_2)(1-r_3) & f_1(1-r_2)(1-f_3) & f_1(1-f_2)(1-r_3) & f_1(1-f_2)(1-f_3) \\
(1-r_1)r_2r_3 & (1-r_1)r_2f_3 & (1-r_1)f_2r_3 & (1-r_1)f_2f_3 & (1-f_1)r_2r_3 & (1-f_1)r_2f_3 & (1-f_1)f_2r_3 & (1-f_1)f_2f_3 \\
(1-r_1)r_2(1-r_3) & (1-r_1)r_2(1-f_3) & (1-r_1)f_2(1-r_3) & (1-r_1)f_2(1-f_30 & (1-f_1)r_2(1-r_3) & (1-f_1)r_2(1-f_3) & (1-f_1)f_2(1-r_3) & (1-f_1)f_2(1-f_3) \\
(1-r_1)(1-r_2)r_3 & (1-r_1)(1-r_2)f_3 & (1-r_1)(1-f_2)r_3 & (1-r_1)(1-f_2)f_3 & (1-f_1)(1-r_2)r_3 & (1-f_1)(1-r_2)f_3 & (1-f_1)(1-f_2)r_3 & (1-f_1)(1-f_2)f_3 \\
(1-r_1)(1-r_2)(1-r_3) & (1-r_1)(1-r_2)(1-f_3) & (1-r_1)(1-f_2)(1-r_3) & (1-r_1)(1-f_2)(1-f_3) & (1-f_1)(1-r_2)(1-r_3) & (1-f_1)(1-r_2)(1-f_3) & (1-f_1)(1-f_2)(1-r_3) & (1-f_1)(1-f_2)(1-f_3)
\end{pmatrix}
\begin{pmatrix} N_{PPP}^{TTT}/r_1r_2r_3 \\ N_{PPN}^{TTT}/r_1r_2f_3 \\ N_{PNP}^{TTT}/r_1f_2r_3 \\ N_{PNN}^{TTT}/r_1f_2f_3 \\ N_{NPP}^{TTT}/f_1r_2r_3 \\ N_{NPN}^{TTT}/f_1r_2f_3 \\ N_{NNP}^{TTT}/f_1f_2r_3 \\ N_{NNN}^{TTT}/f_1f_2f_3 \end{pmatrix}
\tag{15.6}
$$

Except for the first number, all other numbers that appear in the right-hand side vector correspond to events with at least one *nonprompt* lepton that passes *tight* selection criteria. Therefore, the overall *nonprompt* background is expresses as,

$$N^{TTT}_{Nonprompt} = N^{TTT}_{PPN} + N^{TTT}_{PNP} + N^{TTT}_{PNN} + N^{TTT}_{NPP} + N^{TTT}_{NPN} + N^{TTT}_{NNP} + N^{TTT}_{NNN}, \quad (15.7)$$

which can be obtained by first constructing 8 ARs to form the lefthand side vector. Secondly, the 8×8 matrix is constructed and inverted. Lastly, the righthand side vector can be obtained by multiplying the lefthand side vector by the inverted matrix.

Only two PDs "SingleElectron" and "SingleMuon" are used in the construction of MR in 2016 and 2017 while "SingleElectron" is replaced with "EGamma" in 2018. In addition to PDs, the measurements of r/f also utilize the $t\bar{t}$ sample and all MC samples listed under the "*prompt* background" category in Table 12.3. Depending on the flavor of the leading lepton in MC, events are selected with either a single-electron or a single-muon trigger, which is summarized in Table 15.1. Data events are selected with the same HLT triggers as well but events in "SingleMuon" ("SingleElectron" or "EGamma") PD are only accepted if the leading lepton is a muon (electron).

Table 15.1: Summary of the HLT triggers used in the measurement of r and f. These are unprescaled single-lepton triggers with the lowest p_T threshold. The threshold of the electron trigger is higher in the 2017 and 2017 datasets due to increased instantaneous luminosity in those two years.

Channel	Path	Dataset	2016	2017	2018
Electron	HLT_Ele27_WPTight_Gsf	Data & MC	✓	-	-
	HLT_Ele35_WPTight_Gsf	Data & MC	-	✓	✓
Muon	HLT_IsoMu27	Data & MC	✓	✓	✓

Both r and f are parameterized in bins of lepton p_T, $|\eta|$, and jet multiplicity. The bin range is optimized to retain sufficient statistics for each bin:

- Electron p_T bin range: {20.0, 24.6, 28.8, 33.0, 37.2, 41.4, 46.1, 52.1, 59.3, 68.3, 82.7, 110.6} GeV,
- Muon p_T bin range: {20.0, 23.8, 27.7, 31.3, 35.0, 38.9, 42.8, 45.6, 50.7, 59.5, 72.9, 94.3} GeV,
- $|\eta|$ bin range: {0, 0.8, 1.6, 2.4},
- Jet multiplicity: {0 jets, $\geq$ 1 jet}.

The jet multiplicity bin is a proxy for variation in the composition of physics processes. In addition

to requiring at least one jet, the MR corresponding to the second jet multiplicity bin requires no more than one b-tagged jet as this is also required in the SR.

The *nonprompt* efficiency is measured in SS dilepton regions, in which the leading lepton in p_T, used as a *tag*, is required to be matched with trigger objects within $\Delta R < 0.2$. The sub-leading lepton is required to pass the *loose* selection and is taken as the *probe*. Events that have two SS electrons with an invariant mass between 76 and 106 GeV are removed from MR to suppress the backgrounds that originate from charge misidentification. No such requirement has been introduced to the muon MR due to its negligible rate of charge misidentification.

The contribution from *prompt* backgrounds, estimated from MC simulation, is subtracted from the data. A representative composition of backgrounds in MR is shown in Figure 15.2.

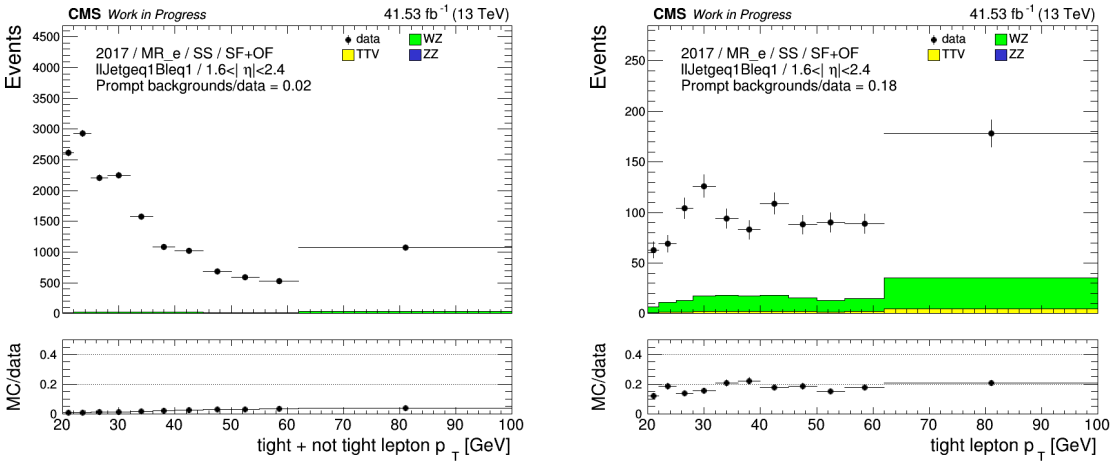

Figure 15.2: Distribution of lepton p_T in a representative electron *nonprompt* efficiency MR. In this particular example, both ee and μe flavor composites are considered. At least one jet and at most one b-tagged jet are required (the second jet multiplicity bin). *Probe* electron is required to have $1.6 < |\eta| < 2.4$ (the third η bin). Contamination from *prompt* backgrounds are estimated with MC simulation, and are shown as histograms. The data are shown as filled points. From left to right: *loose* (i.e. *tight + not tight*) electron p_T, *tight* electron p_T.

The *nonprompt* efficiency f is calculated as:

$$f = \frac{n_{data}^{tag+tight} - n_{MC(prompt)}^{tag+tight}}{n_{data}^{tag+loose} - n_{MC(prompt)}^{tag+loose}}, \tag{15.8}$$

where the numerator is selected with one *tag* and one *tight* lepton while the denominator is selected with one *tag* and one *loose* lepton. The selection criteria for *tag*, *loose*, and *tight* lepton is summarised in Table 15.3.

The measured *nonprompt* efficiency f exhibits a dependency on flavor composition, as is shown in Figure 15.3. This dependency is treated as a source of systematic uncertainty of the *nonprompt*

Table 15.2: Summary of the lepton selections needed for the measurement of r and f. Please note: (i) the minimum p_T cut for *tag* electron in the 2016 dataset is reduced to 30 GeV to adjust for the trigger threshold, and (ii) the *tight* selection here is the same as the *tight* lepton selection described in Section 13.1.

Lepton	Selection	*loose*	*tag*	*tight*[ii]
Electron	p_T	$>$ 20 GeV	$>$ 38 GeV[i]	$>$ 20 GeV
	I^{rel}_{mini}	$<$0.4	$<$0.1	$<$0.12
	TOP LeptonMVA	$>$-0.9	$>$0.95	$>$0.9
	Match with trigger objects	-	✓	-
Muon	p_T	$>$ 20 GeV	$>$ 30 GeV	$>$ 20 GeV
	I^{rel}_{mini}	$<$0.4	$<$0.1	$<$0.12
	Cut-based ID	-	Medium WP	Medium WP
	TOP LeptonMVA	$>$0.5	$>$0.9	$>$0.9
	Match with trigger objects	-	✓	-

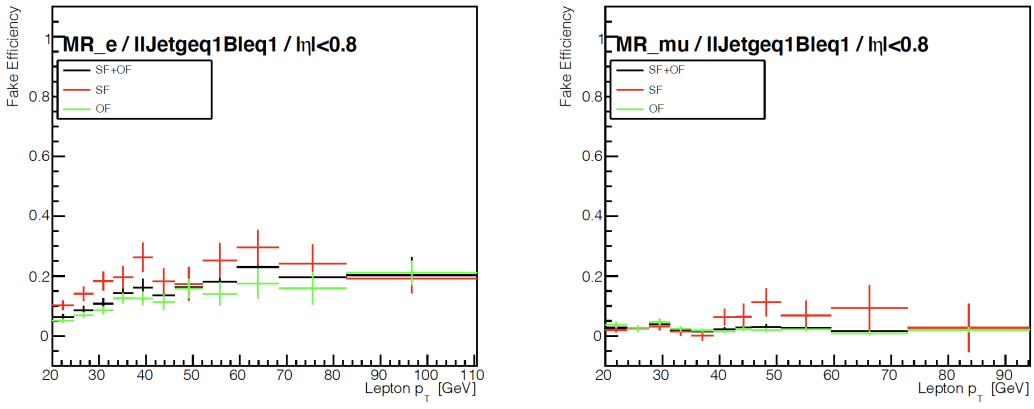

Figure 15.3: Representative *nonprompt* electron efficiency measured in data events. From left to right: electron f, muon f. Events with a same-flavor lepton pair are shown in red points while events selected with a different-flavor lepton pair are shown in green points. Events with a same-flavor or different-flavor lepton pair are shown in black points. These plots correspond to the first $|\eta|$ bin ($|\eta|$ <0.8) and the second jet multiplicity bin. Error bars displayed in these plots include statistical uncertainty only.

estimation and is further discussed in Section 17.2.

The *prompt* efficiency r is measured in simulated $t\bar{t}$ events in OS dilepton regions. The same lepton selection listed in Table 15.2 is used to perform the *Tag-and-Probe*. The leading lepton in p_T is used as a *tag* while the oppositely charged sub-leading lepton is taken as a *probe*. The variation of r between different flavor compositions is negligible, as is shown in Figure 15.4. Therefore, only eμ events are used to measure the *prompt* efficiency in order to minimize the contamination of *nonprompt* leptons.

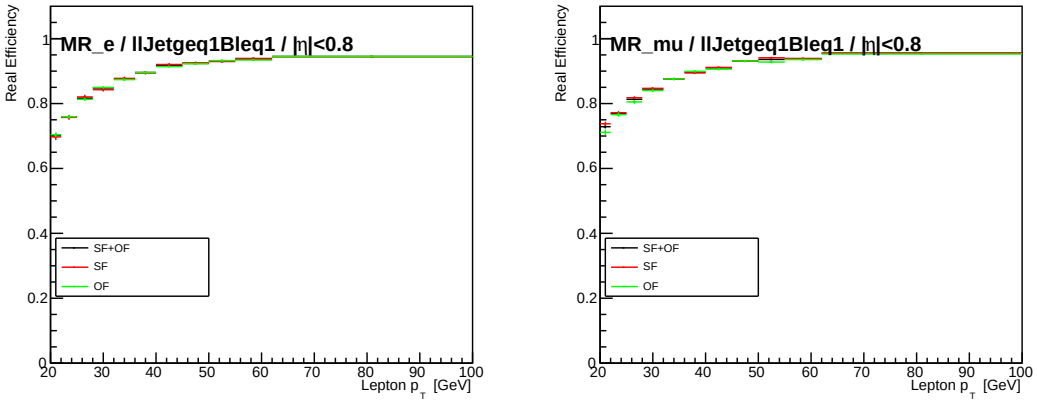

Figure 15.4: Representative *prompt* efficiency measured in simulated $t\bar{t}$ events. From left to right: electron r, muon r. Events with a same-flavor lepton pair are shown in red points while events selected with a different-flavor lepton pair are shown in green points. Events with a same-flavor or different-flavor lepton pair are shown in black points. These plots correspond to the first $|\eta|$ bin ($|\eta|$ <0.8) and the second jet multiplicity bin. Error bars displayed in these plots include statistical uncertainty only.

The selection criteria for various MRs is summarised in Table 15.3.

Table 15.3: Summary of the selection criteria applied to the measurement regions of r and f. "OffZ" means events containing two SS electrons with an invariant mass between 76 and 106 GeV are removed. C_i denotes the electric charge of the selected lepton.

Observable	jet bin	# of selected leptons	lepton flavor composite	$\lvert\sum_i C_i\rvert$	OffZ	njet	nbjet
f	0 jet	2	any	2	same-sign ee	$= 0$	$= 0$
	1 or more jet	2	any	2	same-sign ee	≥ 1	≤ 1
r	0 jet	2	eμ only	0	-	$= 0$	$= 0$
	1 or more jet	2	eμ only	0	-	≥ 1	≤ 1

15.3 Validation of the Matrix Method

The performance of the *matrix method* is validated using three regions that are tangential to the SR, referred to as VRs. In these VRs, *prompt* backgrounds are estimated using MC simulation while *nonprompt* background is estimated with the *matrix method*. A summary of the selections applied to these VRs is given in Chapter 14.

Distribution of the leading lepton η and jet multiplicity are shown in Figure 15.5. Good agreement between data and background estimate has been observed in all three VRs.

15.4 Nonprompt Estimate in SR

The *matrix method* is used to estimate *nonprompt* background in the SR. Distributions of the LFV eμ mass and the Z boson mass are shown in Figure 15.6. When compared to the background estimate from pure MC simulation (Figure 14.1), the updated background template is smoother with lower statistical uncertainties.

The number of expected events from various kinds of backgrounds is shown in Table 15.4.

Table 15.4: Expected background contributions and the number of events observed in data collected during 2016–2018. The statistical and systematic uncertainties are added in quadrature. The category "other backgrounds" includes smaller background contributions containing one or two top quarks plus a boson or quark. The CLFV signal, generated with $C_{e\mu ut}^{vector}/\Lambda^2 = 1\text{TeV}^{-2}$, is also listed for reference. The signal yields include contributions from both top production and decay modes.

Process	m(eμ) < 150 GeV	m(eμ) > 150 GeV
Nonprompt	351 ± 92	146 ± 38
WZ	275 ± 64	145 ± 35
ZZ	33.2 ± 6.5	13.1 ± 2.6
VVV	17.0 ± 8.5	12.0 ± 6.0
$t\bar{t}W$	47.6 ± 10.0	40.0 ± 9.1
$t\bar{t}Z$	39.1 ± 7.9	25.8 ± 5.4
$t\bar{t}H$	28.2 ± 4.5	10.0 ± 1.6
tZq	5.5 ± 1.1	2.5 ± 0.5
Other	7.3 ± 3.7	4.5 ± 2.3
Total expected	805 ± 123	398 ± 57
Data	783	378
CLFV	207 ± 15	4440 ± 215

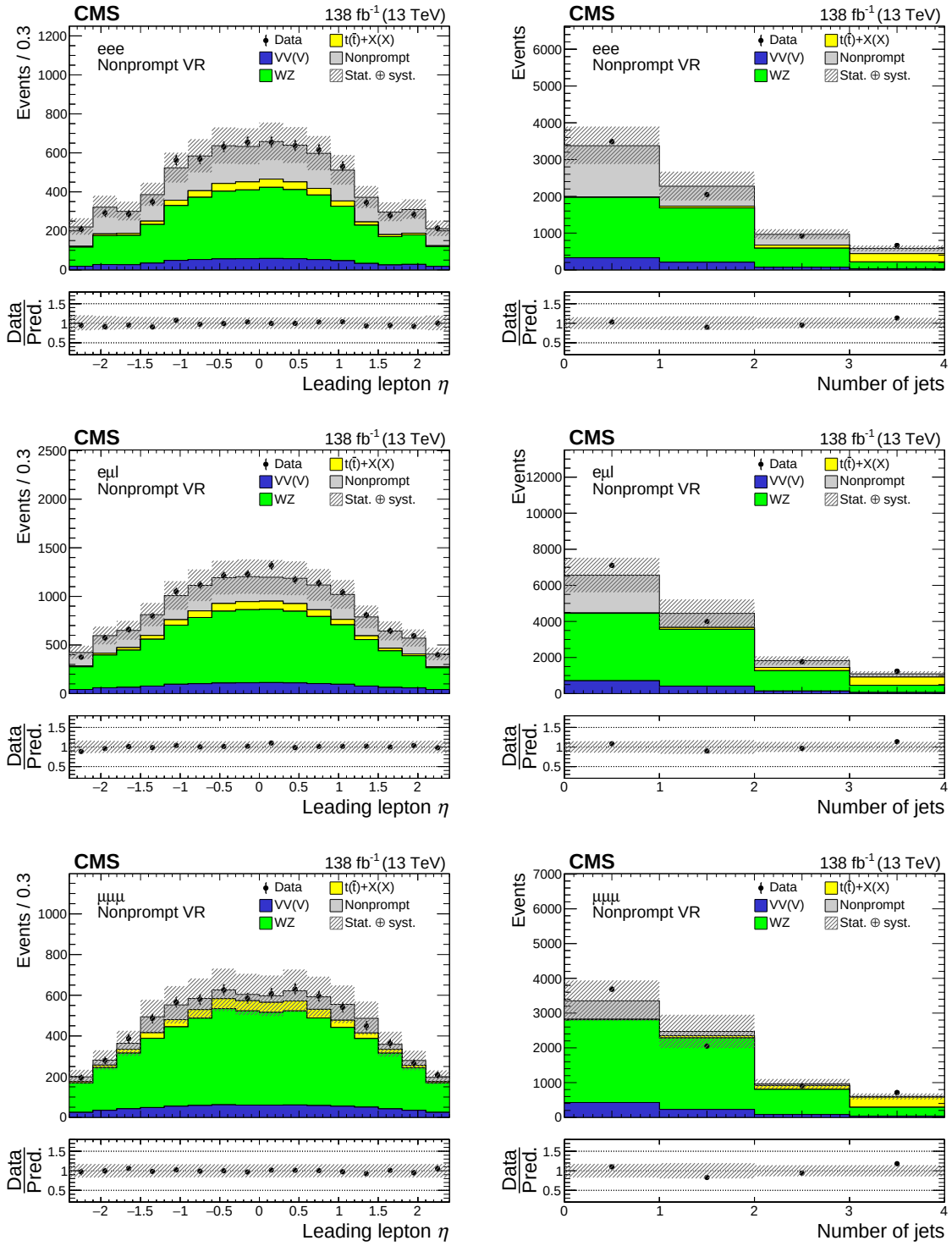

Figure 15.5: Distributions of the leading lepton η (left column) and the jet multiplicity (right column) in the *nonprompt* VRs. Events in the eee, e$\mu\ell$, and $\mu\mu\mu$ *nonprompt* VRs are shown in the upper, middle, and lower rows, respectively. The data are shown as filled points and the SM background predictions as histograms. The *nonprompt* background is estimated using control samples in data, while other backgrounds are estimated using MC simulation. The hatched bands indicate statistical and systematic uncertainties for the SM background predictions. The last bin of the right histogram includes the overflow events.

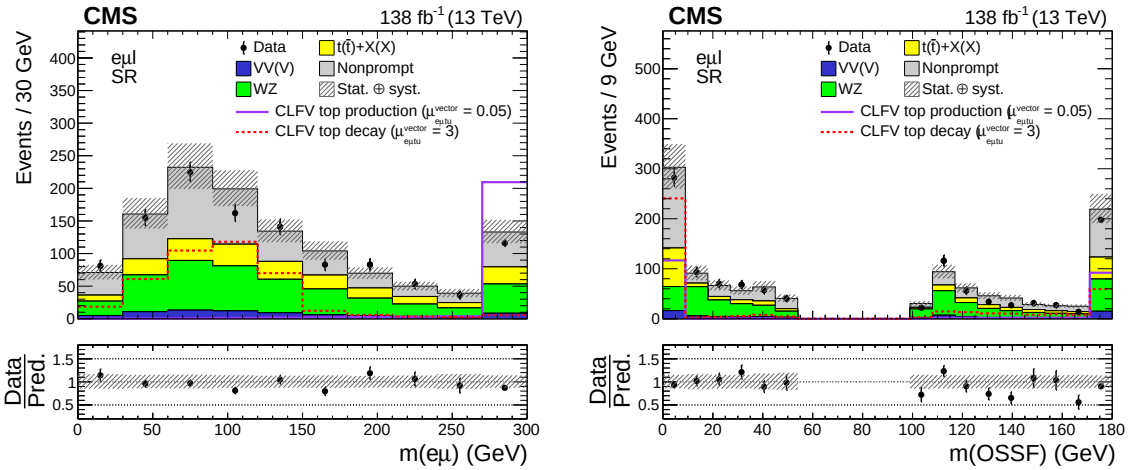

Figure 15.6: Distributions of the LFV eμ mass (left) and the mass of the OSSF lepton pair (right) in SR. The data are shown as filled points and the SM background predictions as histograms. The *nonprompt* background is estimated using control samples in data, while other backgrounds are estimated using MC simulation. The hatched bands indicate statistical and systematic uncertainties for the SM background predictions. The normalization of the signal processes is chosen arbitrarily for improved visualization. The last bin of both histograms includes the overflow events.

Chapter 16

Signal Extraction with Boosted Decision Trees

A MVA is performed in the SR to further separate the LFV signals from the backgrounds, and enhance the sensitivity of this analysis. More specifically, a dozen of discriminating variables, referred to as "features", are selected and combined by a gradient-BDT, which is implemented using the XGBoost package [195]. There are several reasons why a BDT is chosen: (i) the goal of the MVA is to achieve maximum separation between signals and backgrounds using a small number of already well-separated kinematic variables, instead of exploring some complicated structures hidden in event topology, (ii) under such a goal, the potential performance gain from a more sophisticated algorithm like a NN is limited, (iii) a BDT-based algorithm is straightforward to implement and consumes only a moderate amount of computational resources, and (iv) the interpretability of a BDT-based algorithm is excellent.

The top quark production and decay signals are no longer distinguished by the BDT. They are combined into a single signal class, just like all backgrounds are combined into a single background class. The training of the BDT depends entirely on MC samples that are statistically orthogonal to the samples used in the actual background estimation. More details on the configurations of the BDT are described in Section 16.1. The input features are described in Section 16.2. The output of the BDT is presented in Section 16.3.

16.1 BDT Configuration

The LFV eμ mass of the top quark decay signal is bounded by the SM top quark mass, as is shown in Figure 14.1. On the contrary, the LFV eμ mass of the top quark production signal has no such restriction and often reaches the TeV level. Therefore, a 150 GeV threshold is used to divide the SR into two SRs enriched in different signal modes. The MVA strategy is to combine two signal modes within each SR and train binary BDTs separately for each SR. In other words, only two signal datasets and two background datasets are needed.

Other aspects of the signal MC samples, such as the Lorentz structure and the flavor of the up-type quark involved in LFV interaction, are shown to have a relatively small impact on the kinematics of final state particles, as is shown in Figure 16.1. Therefore, they are not distinguished by the BDT. The selection criteria used to define SR, described in Section 14.1, are used to

preselect events before the construction of both signal and background datasets.

The construction of the signal datasets takes a few steps. Firstly, the cross-sections of all top quark production signal samples, regardless of the Lorentz structure or the quark flavor, are set to the cross-section of the vector-like top quark production signal with an eμut vertex, which is shown in Table 12.2. This is done to remove potential bias towards the signals with higher cross sections. Similarly, the cross-sections of all top quark decay signal samples are set to the cross-section of the vector-like top quark decay signal. For each sample, a normalization weight is calculated and is used to replace the original normalization component of the MC weights. These updated MC weights are eventually passed on to the BDT to weight each signal event. Secondly, all top quark production and decay signal samples are combined into a single dataset, which is then subdivided into two datasets using a 150 GeV threshold on LFV eμ. The last step is to adjust the overall normalization (i.e. sum of the MC weights) of each of the two signal datasets to match the overall normalization of the corresponding background dataset.

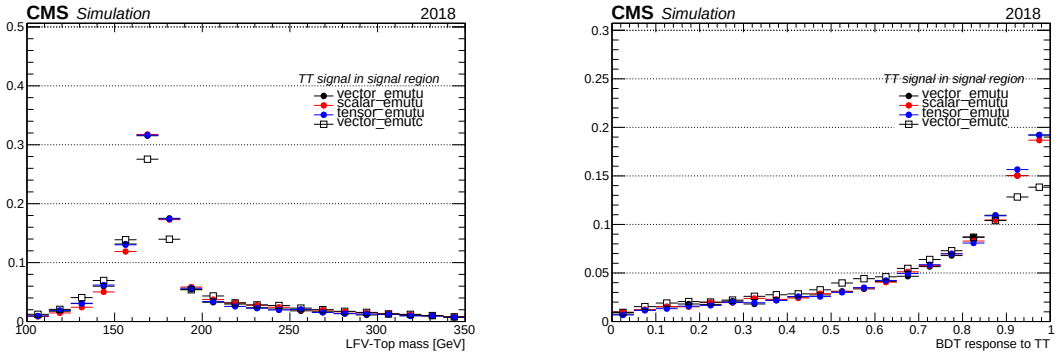

Figure 16.1: Normalized distributions of the simulated top quark decay signals in SR1 using the 2018 dataset. From left to right: LFV top mass, BDT output. In the legend of these histograms, "vector", "scalar", and "tensor" denote the Lorentz structures of EFT operators, and "emutu(c)" denote the eμu(c)t interaction vertex.

The *prompt* background dataset is constructed by combining all MC samples listed under the "prompt" category listed in Table 12.3. Cross sections referenced Table 12.3 are directly used to normalize the *prompt* backgrounds. The construction of the *nonprompt* background dataset is different since the *nonprompt* backgrounds are modeled with the *matrix method*, which is itself constructed from 8 ARs. Therefore, 8 ARs are constructed to collect simulated $t\bar{t}$ and DY events. These events are used to form the *nonprompt* dataset. Each event in the *nonprompt* dataset is then "weighted" using the output of the *matrix method*. Finally, the *nonprompt* dataset is combined with the *prompt* dataset and then divided into two datasets using a 150 GeV threshold on LFV eμ mass.

A technique known as the "k-fold cross validation" is used to minimize the loss of statistics when partitioning datasets into training, validation, and test sets. For each targeted SR, the corresponding signal/background set is divided evenly into five subsets. Three out of the five

subsets are used in the training while a fourth subset is used as a validation set. The fifth set is used to test the performance of the trained BDT. A second BDT is trained using a different combination of subsets to form training, validation, and test sets. This process is repeated five times until a unique test set no longer exists, which is illustrated in Figure 16.2. This technique ensures that the test set is always statistically independent of the process of parameters tuning, which serves as the basis for the bias-free evaluation after training: when evaluating each event using the trained model, it is always possible to pick one of the five BDTs where this particular event was not included in the training or validation.

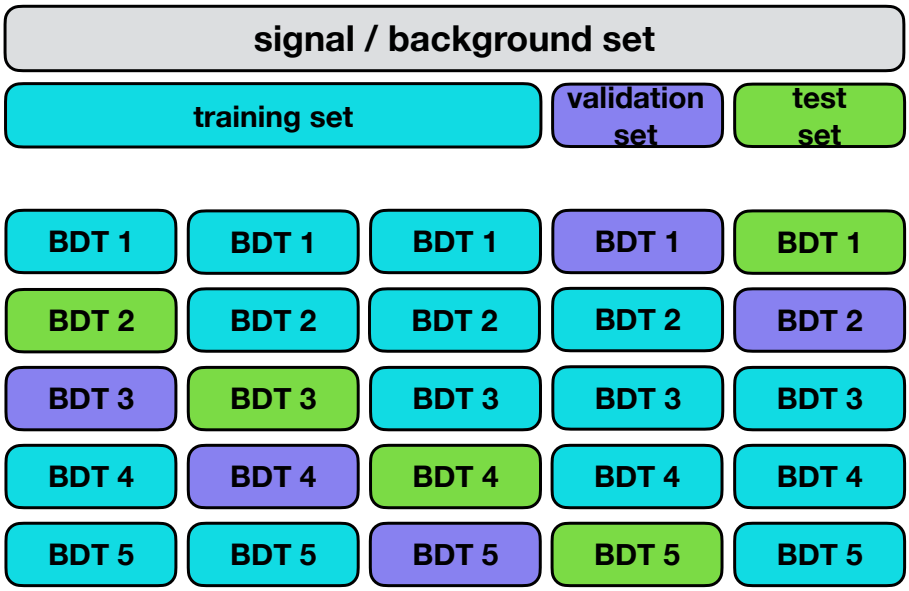

Figure 16.2: Illustration of a 5-fold cross-validation. In this setup, five BDTs are trained/tested using the same dataset arranged in different configurations. Each of the bottom five rows represents the configuration of a BDT.

The same set of hyperparameters is used for all BDTs, which are optimized using a randomized grid search algorithm. The number of estimators is set to 1000 with a max depth of 5. The standard loss function implemented in [195] is used as the evaluation metric. The performance of the BDT is visualized using a metric known as the "ROC curve", which is shown in Figure 16.3. In general, the BDTs trained in SR2 (i.e. $m(e\mu) > 150$ GeV) are much more performant due to the high p_T objects in the final states.

16.2 BDT Features

The discriminating variables used as input in training are referred to as "features" in this analysis. A total of 14 features are used for BDT trained in both SR1 and SR2. The names and descriptions of these 14 features are summarized in Table 16.1. Many of these features are derived from reconstructed heavy objects which are described in Section 14.3.

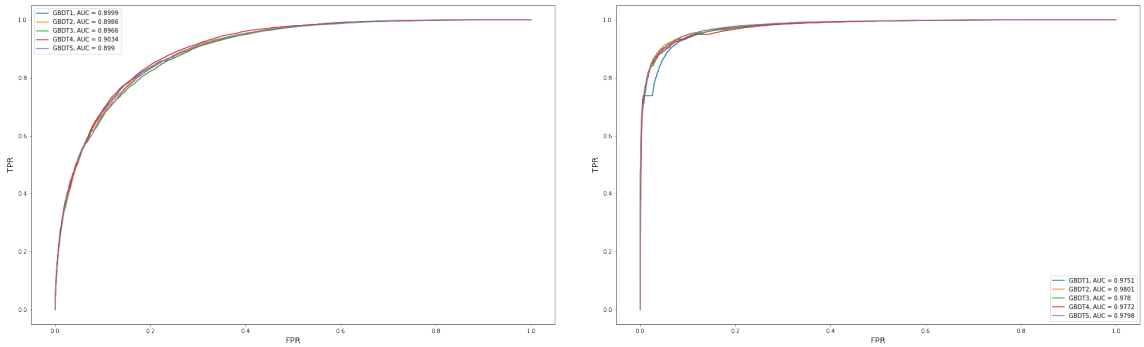

Figure 16.3: ROC curves extracted using the test sets specified in the 5-fold cross-validation. The left (right) figure shows the ROC curves of the BDTs trained in SR1 (SR2). The area under the ROC curves are shown in the legends.

Four additional features are added to the BDT trained in SR1. Among these four features, the "MVA_JeDr" and "MVA_JmuDr" variables are defined by: i) using the jet that forms the LFV top quark candidate, and ii) calculating the opening angle between this jet and the LFV leptons. It is expected that this angle is smaller in the LFV decay mode than LFV production mode. Two additional features are added to the BDT trained in SR2. A description of how the standalone lepton is determined can be found in Section 14.3.

Distributions of selected features are shown in Figure 16.4-16.8. Distributions of the full list of features can be found in Appendix B. The relative importance of these features is extracted using the "gain" method and is shown in Figure 16.9. The correlations between different features are shown in Figure 16.10-16.11.

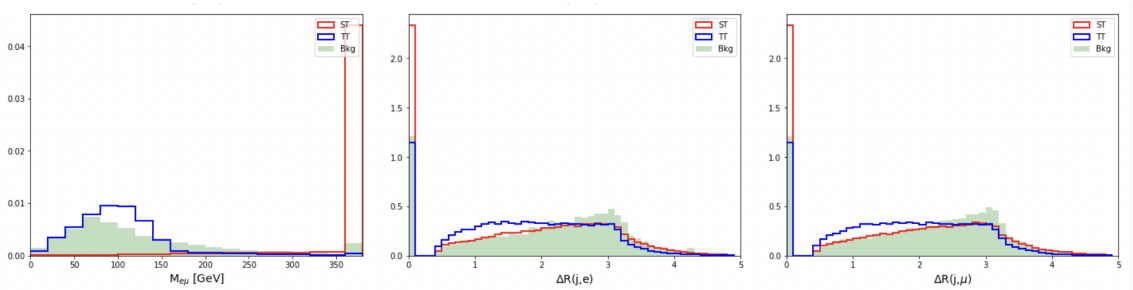

Figure 16.4: Normalized distribution of various features in SR. From left to right: MVA_$M_{e\mu}$, MVA_JeDr, MVA_JmuDr. "ST" ("TT") denotes top quark production (decay) signal while "Bkg" denotes backgrounds.

16.3 BDT Output

The output of the BDTs in SRs are shown in Figure 16.12. The *nonprompt* background is estimated with the matrix method. Other backgrounds are estimated with MC simulation.

Table 16.1: Common features shared by BDTs trained in SR1 and SR2

Name	Description
MVA_Memu	invariant mass of the LFV-eμ pair
MVA_LFVePt	p_T of the LFV electron
MVA_LFVmuPt	p_T of the LFV muon
MVA_LFVTopmass	invariant mass of the LFV top quark candidate
MVA_Zmass	invariant mass of the Opposite-Sign and Same-Flavor lepton pair
MVA_Jet2Btag	b-tagging score of the jet with the second highest b-tagging score
MVA_Mbl2	invariant mass of the second $m_{b\ell}$ system
MVA_njet	number of jets
MVA_nbjet	number of b-tagged jets
MVA_tM	transverse mass of the W boson candidate (from the SM top quark)
MVA_llDr	ΔR between LFV electron and LFV muon
MVA_SSee_Zmass	invariant mass of a Same-Sign di-electron pair
MVA_Topmass	invariant mass of the SM top quark candidate
MVA_Met	missing transverse momentum (MET)

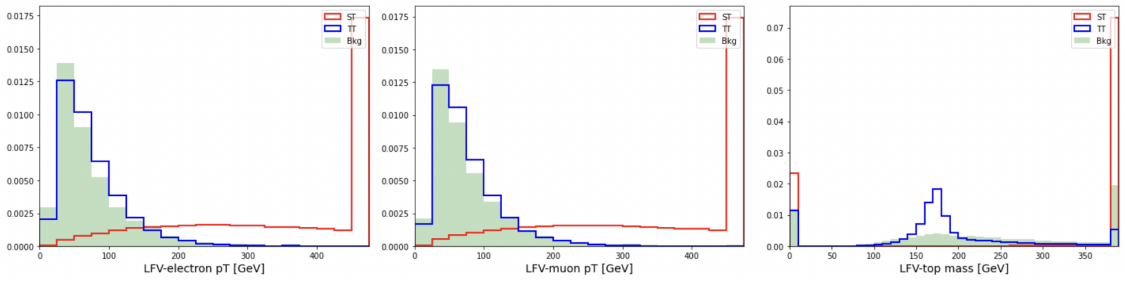

Figure 16.5: Normalized distribution of additional features in SR. From to left to right: MVA_LFVePt, MVA_LFVmuPt, MVA_LFVTopmass. "ST" ("TT") denotes top quark production (decay) signal while "Bkg" denotes backgrounds.

Table 16.2: Features only used by BDT trained in SR1

Name	Description
MVA_Ht	scalar sum of the p_T of all jets and leptons
MVA_Mbl1	invariant mass of the second $m_{b\ell}$ system
MVA_JeDr	ΔR between LFV electron and a light jet (non b jet)
MVA_JmuDr	ΔR between LFV muon and a light jet (non b jet)

Table 16.3: Features only used by BDT trained in SR2

Name	Description
MVA_BaPt	p_T of the standalone lepton
MVA_JetHt	scalar sum of the p_T of all jets

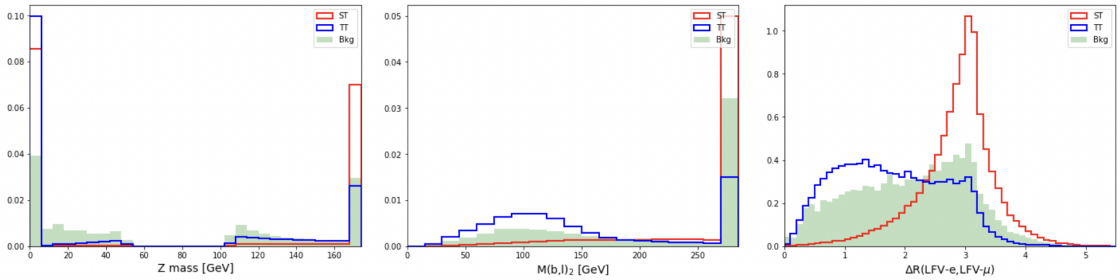

Figure 16.6: Normalized distribution of additional features in SR. From left to right: MVA_Zmass, MVA_Mbl2, MVA_llDr. "ST" ("TT") denotes top quark production (decay) signal while "Bkg" denotes backgrounds.

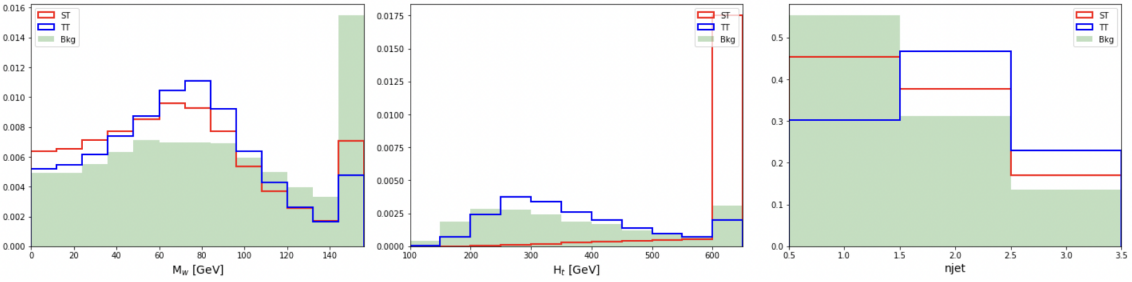

Figure 16.7: Normalized distribution of additional features in SR. From left to right: MVA_tM, MVA_Ht, MVA_njet. "ST" ("TT") denotes top quark production (decay) signal while "Bkg" denotes backgrounds.

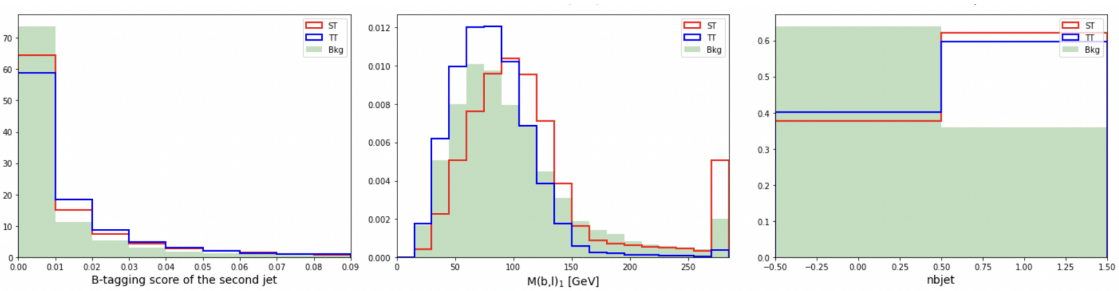

Figure 16.8: Normalized distribution of additional features in SR. From left to right: MVA_Jet2Btag, MVA_Mbl1, MVA_nbjet. "ST" ("TT") denotes top quark production (decay) signal while "Bkg" denotes backgrounds.

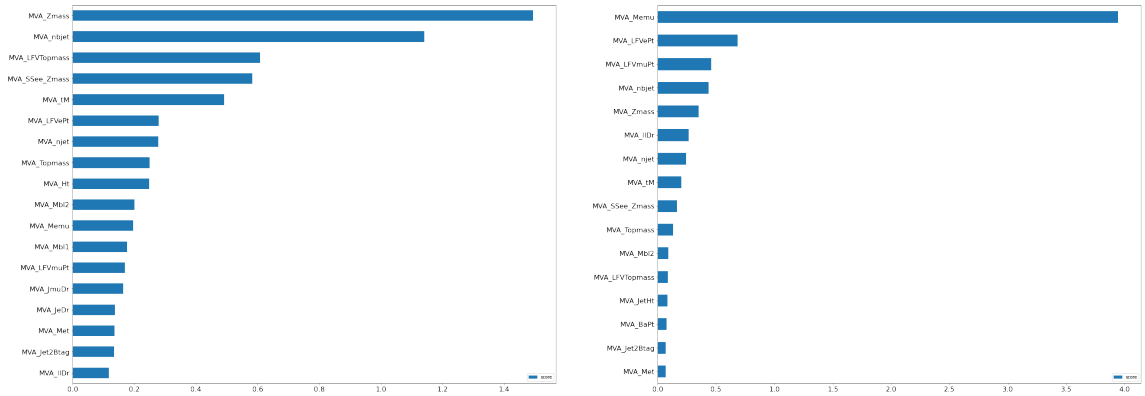

Figure 16.9: List of features ranked by their relative importance. From left to right: BDT trained in SR1, BDT trained in SR2.

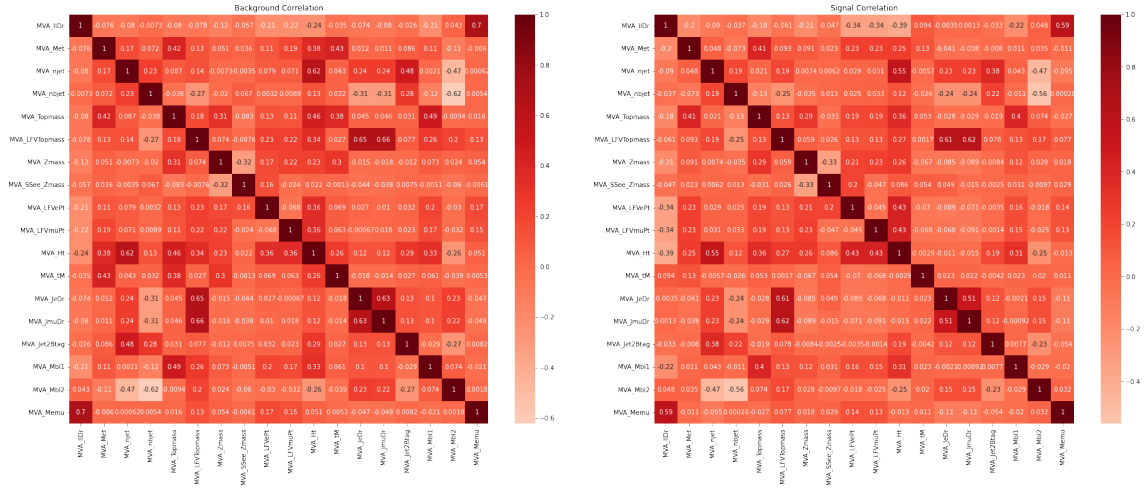

Figure 16.10: Correlation matrices of the features of the BDT trained in SR1. From left to right: background correlation, signal correlation.

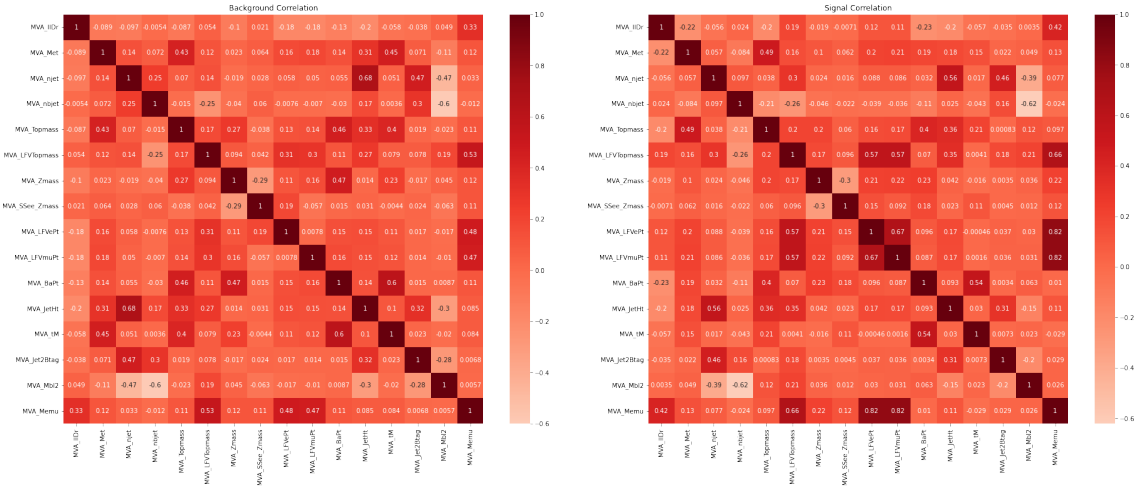

Figure 16.11: Correlation matrices of the features of the BDT trained in SR1. From left to right: background correlation, signal correlation.

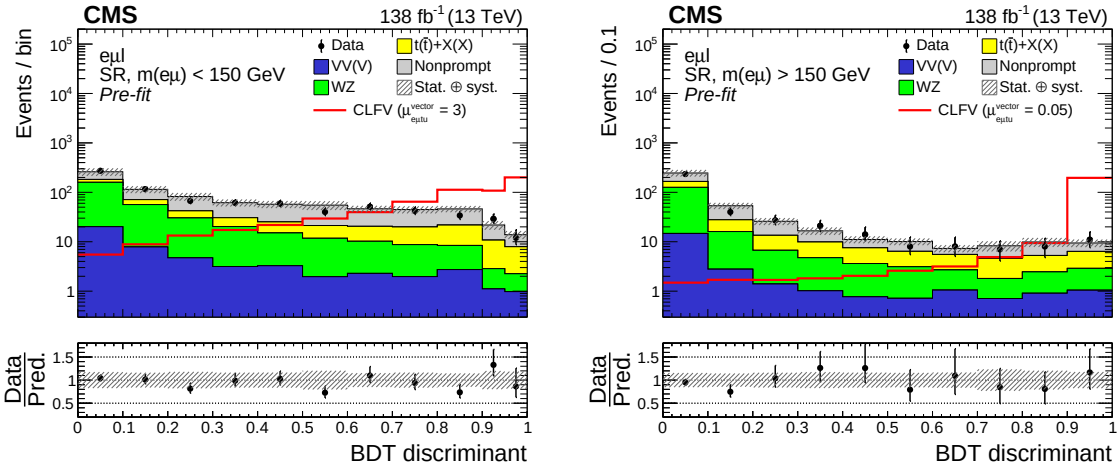

Figure 16.12: Distributions of the BDT discriminator targeting the CLFV top quark decay (left) and production (right) signal. Contributions from the two signal modes (production and decay) are combined within each SR and are shown as the solid red line. The pre-fit signal strength ($\mu^{\text{vector}}_{\text{e}\mu\text{u}t} = 1$), corresponding to $C^{\text{vector}}_{\text{e}\mu\text{u}t}/\Lambda^2 = 1$ TeV^{-2}, is used to normalise the signal cross sections. The hatched bands indicate statistical and systematic uncertainties for the background predictions.

Chapter 17

Systematic Uncertainties

Different sources of systematic uncertainty contribute to the estimation of background events and modeling of the signal. The chapter is organized as follows. Theoretical uncertainties concerning signals and major backgrounds are discussed in Section 17.1. Uncertainties concerning the *nonprompt* background are discussed in Section 17.2. Uncertainties concerning the modeling of the diboson processes are described in Section 17.3. Finally, other systematic uncertainties are discussed in Section 17.4.

17.1 Theoretical Uncertainties

Variations on theoretical cross sections for *prompt* backgrounds are introduced to cover the uncertainties in perturbative QCD calculations. A 6% normalization uncertainty is assigned to WZ and ZZ processes [178]. A 15% normalization uncertainty is assigned to $t\bar{t}W$, $t\bar{t}Z$, and $t\bar{t}H$ processes [179, 180]. A 20% normalization uncertainty is assigned to the tZq process, which is a conservative estimate taken from the MC generator. A conservative 50 % normalization uncertainty is assigned to other smaller *prompt* backgrounds. All normalization uncertainties are considered uncorrelated between different processes but correlated across the years.

Uncertainties associated with the PDF are evaluated by using 100 replicas of the NNPDF sets [93, 10]. The procedure described in [196] is followed. Firstly, the sum of the generator weights of each replica is normalized to the nominal sum of the generator weights. This is done before any event selection to ensure no additional normalization effect is introduced. After the previous step, the bin-by-bin variations of the BDT templates are obtained by calculating the bin-by-bin difference of the BDT templates when switching from nominal PDF to each PDF replica. Finally, PDF uncertainty for each bin is assigned by taking the root mean square value of the 100 variations of the corresponding bin. This uncertainty is treated as uncorrelated between different processes but correlated across the years. This uncertainty is considered for all the signals and major prompt backgrounds (i.e. WZ, $t\bar{t}W$, $t\bar{t}Z$, and $t\bar{t}H$).

QCD scale uncertainties are evaluated by varying the renormalization scale μ_R and factorization scales μ_F in the ME. A total of six variations are considered: varying μ_R by a factor of 2 and 0.5, varying μ_F by a factor of 2 and 0.5, and varying μ_R and μ_F simultaneously by a factor of 2 and 0.5.

Similar to PDF uncertainty, the normalization effects of each variation are removed. An envelope that covers all six variations is used to represent the scale uncertainty. This uncertainty is treated as uncorrelated between different processes but correlated across the years. This uncertainty is considered for all the signals and major prompt backgrounds (i.e. WZ, $t\bar{t}W$, $t\bar{t}Z$, and $t\bar{t}H$).

Uncertainties associated with the PS are evaluated by varying the renormalization scale μ_R in the initial and final state radiations, which effectively changes the strong coupling constant in the PS. Similarly, μ_R is varied by a factor of 2 and 0.5 and the normalization effects of each variation are removed. This uncertainty is treated as uncorrelated between different processes but correlated across the years. This uncertainty is only considered for signal events.

17.2 Nonprompt Uncertainties

There are several sources of uncertainties associated with the determination of the *nonprompt* efficiency f. One of these uncertainties comes from the estimate of *prompt* contamination in MR. As is discussed in Chapter 15, *prompt* backgrounds (estimated with MC) are subtracted from total event yields measured in data. A flat 20 % uncertainty (α in Equation 17.1) is assigned to the event yields of the *prompt* background and the resulting variation of f is taken as the uncertainty.

$$f = \frac{n_{data}^{tag+tight} - (1+\alpha) n_{MC(prompt)}^{tag+tight}}{n_{data}^{tag+loose} - (1+\alpha) n_{MC(prompt)}^{tag+loose}}. \tag{17.1}$$

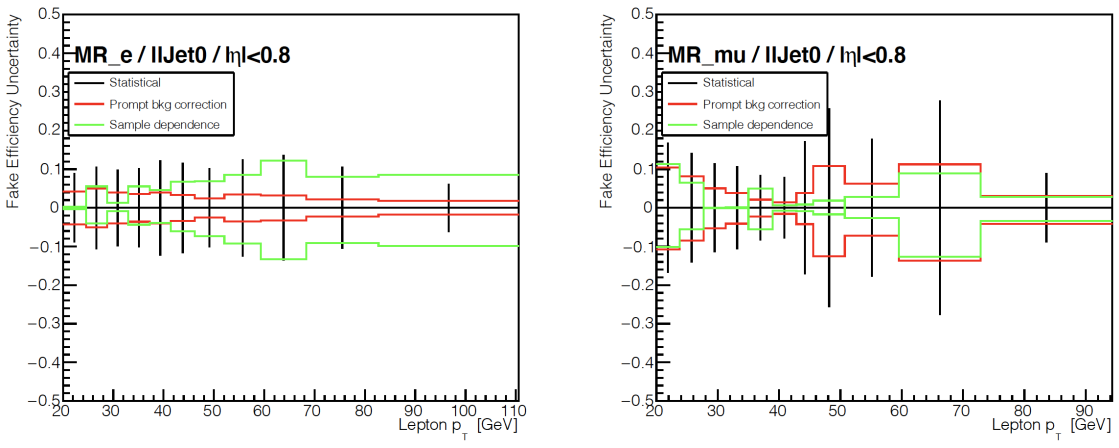

Figure 17.1: Comparison of different components of the uncertainties associated to the *nonprompt* efficiency measured in the 2017 dataset (njet = 0 bin, $|\eta| < 0.8$ bin). From left to right: electron f uncertainty, muon f uncertainty.

Another source of uncertainty associated with the determination of the *nonprompt* efficiency f is concerned with the observation that f exhibits a flavor dependency, as is shown in Figure 15.3. This can happen when different physics processes enter MRs with different lepton flavor compositions,

which lead to differences in *nonprompt* lepton behaviors. This type of uncertainty, referred to as "sample dependence", is estimated by introducing a variation factor β between the proportions of same-flavor and different-flavor pairs in MR. For example, electron f can be calculated as (prompt background correction is ignored from the equation),

$$f_e = \frac{(1+\beta)n_{e+e}^{tag+tight} + (1-\beta)n_{e+\mu}^{tag+tight}}{(1+\beta)n_{e+e}^{tag+loose} + (1-\beta)n_{e+\mu}^{tag+loose}}. \tag{17.2}$$

A 20% variation (β) is assigned and the resulting variation of f is taken as the uncertainty.

Statistical uncertainty is also considered when determining f. A comparison of different sources of uncertainties is shown in Figure 17.1 and Figure 17.2. All sources of uncertainties are added in quadrature to form the final uncertainty on f.

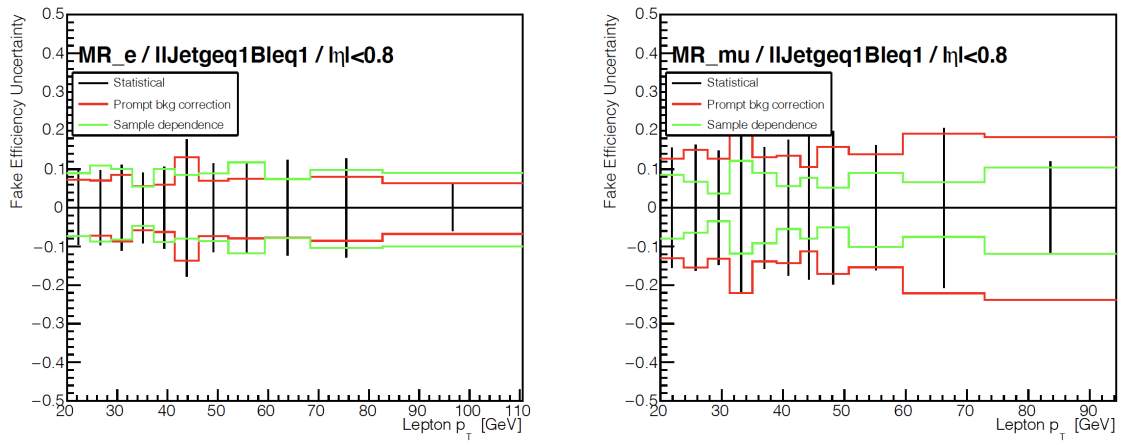

Figure 17.2: Comparison of different components of the uncertainties associated to the *nonprompt* efficiency measured in the 2017 dataset (njet $>$ 0 bin, $|\eta|$ $<$ 0.8 bin). From left to right: electron f uncertainty, muon f uncertainty.

Since the *prompt* efficiency r is measured in simulated $t\bar{t}$ events, MC uncertainties described in Section 17.4 are propagated to r as the uncertainties. Additionally, statistical uncertainty is added in quadrature to the MC uncertainties to form the final uncertainty on r.

The uncertainties associated with the *prompt* efficiency are relatively small when compared to the *nonprompt* efficiency uncertainties. A comparison of different sources of *prompt* efficiency uncertainties is shown in Figure 17.3.

Uncertainties associated with r and f are determined separately for electrons and muons. Therefore, there are four independent uncertainties: r_e, r_μ, f_e and f_μ.

A fifth uncertainty is considered that accounts for the potential bias caused by the way the generalized *matrix method* is implemented. Four out of the eight ARs that appear on the lefthand side of the Equation 15.6 (i.e. $N^{\overline{T}TT}$, $N^{T\overline{T}T}$, $N^{\overline{TT}T}$, $N^{T\overline{TT}}$) are selected by requiring the

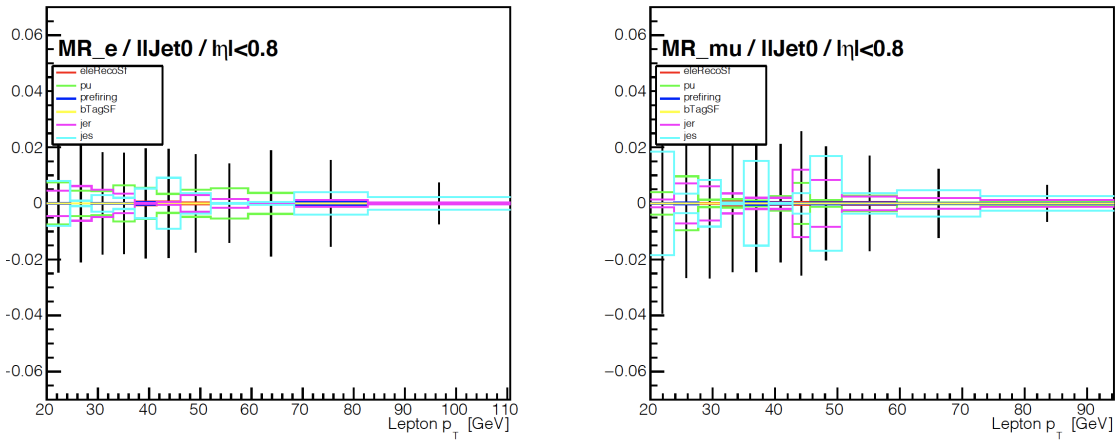

Figure 17.3: Comparison of different components of the uncertainties associated to the *prompt* efficiency measured in the 2017 dataset (njet = 0 bin, $|\eta| < 0.8$ bin). From left to right: electron *r* uncertainty, muon *r* uncertainty.

leading lepton in p_T to fail the *tight* criteria described in Table 15.2. Effectively this means that the isolation requirement is reversed for the leading lepton that enter these four ARs. Selecting the leading lepton by a loose requirement is not ideal since the leading lepton is required to match with isolated trigger objects. To account for this bias, a 50 % uncertainty is assigned to f_1 (*nonprompt* efficiency associated with the leading lepton) for events that enter these four ARs. The variation of the *nonprompt* estimate due to trigger matching is largely covered by this uncertainty, as is shown in Figure 17.4.

The five components of the uncertainties discussed in this section are propagated through the matrix inversion. The resulting variations of the *nonprompt* estimates are taken as the uncertainties, which contain both normalization and differential effects to the BDT templates. These uncertainties are treated uncorrelated between different components but correlated across the years. In addition to these five uncertainties, an overall normalization uncertainty of 10% is assigned to cover any other potential variations of the *nonprompt* backgrounds.

17.3 Diboson Uncertainties

Mismodeling of the jet multiplicity is observed in the WZ control region, as is shown in Figure 14.3. This is largely due to the fact that the WZ process is modeled at LO with one extra parton in the ME. Any other extra jets are modeled by the PS, which tends to be less accurate [183, 197]. To take this into account, a dedicated jet-dependent uncertainty is assigned to each event. This uncertainty is determined using a diboson VR that has the same OnZ requirement as the WZ VR, no jet multiplicity requirement, a $p_T^{miss} > 85$ GeV requirement, and a requirement of no b-tagged jets with $p_T > 20$ GeV. Unlike for the WZ VR, events with different lepton flavor compositions

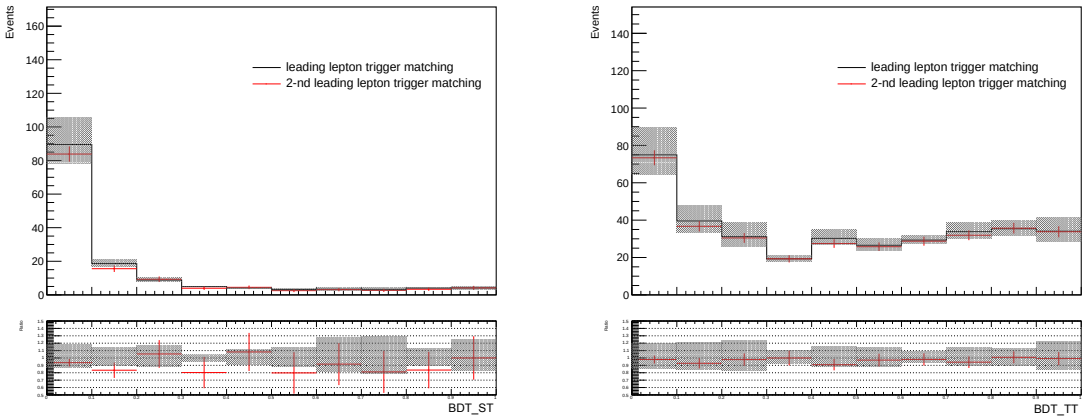

Figure 17.4: The impact of matching leptons to trigger objects on *nonprompt* estimate. From left to right: *nonprompt* estimate in top production enriched SR, *nonprompt* estimate in top decay enriched SR. The nominal configuration of the *matrix method* is to match the leading lepton with trigger objects. Matching the sub-leading with the trigger objects is taken as an alternative to evaluating the robustness of the *nonprompt* estimate. The uncertainty band only covers the variation of the *nonprompt* estimate as a result of varying leading lepton f by 50 %. Uncertainty bars only include statistical uncertainties.

are combined.

The jet multiplicity distributions in diboson VR are shown in Figure 17.5. For each year, a scale factor parameterized in bins of jet multiplicity is derived,

$$\epsilon = \frac{N_{data} - N_{VVV} - N_{t\bar{t}+X(X)} - N_{t\bar{t}} - N_{others}}{N_{VV}}. \tag{17.3}$$

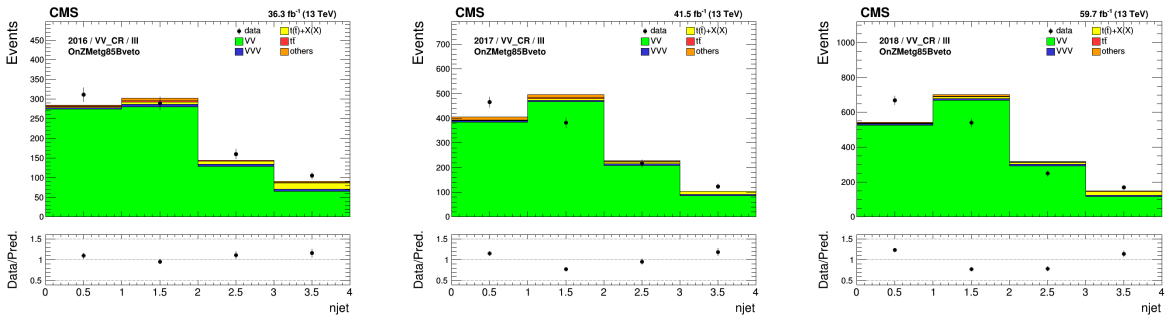

Figure 17.5: Distributions of the jet multiplicity in the diboson VRs in the 2016 (left), 2017 (middle) and 2018 (left) datasets. Events are required to contain exactly three *tight* leptons with any composition of flavors. "VV" denotes the WZ and ZZ processes.

The scale factor ϵ is used to estimate the uncertainty, denoted by Δ,

$$\Delta = |1 - \epsilon| \tag{17.4}$$

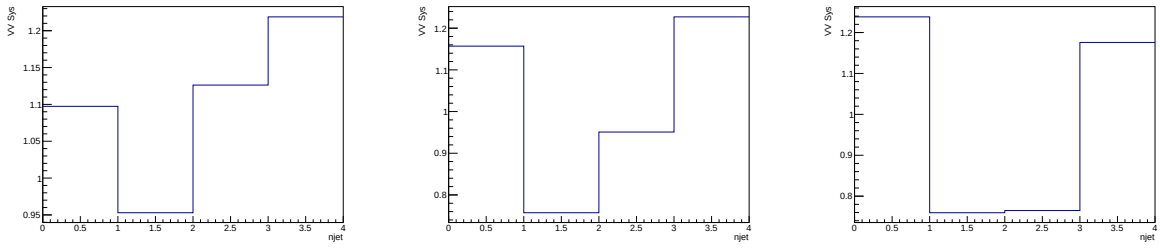

Figure 17.6: Scale factors derived from the diboson VRs in 2016 (left), 2017 (middle), and 2018 (right) datasets. These scale factors are used to assign uncertainties instead of correcting simulated events.

This uncertainty modifies the predictions of WZ and ZZ processes by up to 20%, as is shown in Figure 17.6.

17.4 Other Experimental Uncertainties

Uncertainties of 1.2, 2.3, and 2.5% are assigned to the integrated luminosity for 2016, 2017, and 2018, respectively [198, 199, 200]. These uncertainties affect the normalization of the BDT templates of all signals as well as *prompt* backgrounds. The correlation between these uncertainties is taken into account when combining the 2016-2018 datasets.

PU distributions of all signals and *prompt* backgrounds are reweighted using per-event scale factors to recreate the PU profile measured in data. The uncertainties associated with these scale factors are evaluated by varying the inelastic pp cross-section by $\pm 4.6\%$ [201]. These uncertainties are considered correlated across the years.

Calibrations of the reconstruction of electrons and muons are done centrally at CMS by using a "tag-and-probe" approach [202] in DY enriched dilepton events. Per-object scale factors are used to correct for the discrepancy between reconstruction efficiencies measured in data and MC. Limited sample size as well as the choice of fit models contribute to the uncertainties associated with these scale factors. These uncertainties are considered correlated across the years.

The TOP LeptonMVA covers both identification and isolation of *prompt* leptons. Similar to lepton reconstruction, the calibration of TOP LeptonMVA is done using a tag-and-probe approach in DY enriched dilepton events. Per-object scale factors are used to correct for the discrepancy between reconstruction efficiencies measured in data and MC. Uncertainties of these scale factors are divided into two separate uncertainties: the statistical components of these uncertainties are treated as uncorrelated across the years while the other components are merged and treated as fully correlated across the years. For high p_T electrons and muons ($p_T >$

200 GeV), an additional uncertainty, denoted by "eleIDHighPt/muIDHighPt", is assigned and it increases linearly from 0 to 10% (200 GeV-1000 GeV) and is capped at 10% after 1000 GeV. These additional uncertainties are introduced because the efficiency calibration is largely done in low p_T phase space. This additional uncertainty is considered correlated across the years.

Calibrations of energy scale and resolution of electrons are done centrally at CMS [203] and no uncertainties are considered as they are largely negligible. Calibrations of muon energy scale and resolution are done using the "Rochester algorithm" [204] for muons with $p_T < 200$ GeV. "MuonScale" is used to denote the uncertainties associated with this correction, which comes primarily from a limited sample size. For muons with $p_T > 200$ GeV, no corrections are applied as there are not enough events for a robust correction from the "Rochester algorithm". An additional uncertainty, also denoted by "MuonScale" is assigned to the momentum of these high p_T muons using the "Generalized Endpoint method" [144]. The "MuonScale" uncertainty is considered correlated across the years.

No calibration is done for trigger efficiency as they are generally close to 1 in both data and MC. A flat 2% uncertainty is assigned to all signals and *prompt* backgrounds to cover statistical fluctuations. This uncertainty is treated as uncorrelated across the years.

Calibrations of the DeepJet scores are described in Section 13.2. Uncertainties associated with the calibrations are divided into 8 different sources to properly account for the correlations, which are summarized in Table 17.1. For b and udsg jets, lf, hf, hfstats1/2, and lfstats1/2 uncertainties are applied. For c jets, cferr1/2 uncertainties are applied.

Table 17.1: Summary of the sources of uncertainties associated with the b-tagging calibration, excluding those originating from JES and JER. A hyphen (−) denotes that a source is not correlated across the years.

Source	Correlated	Description
lf	✓	udsg+c jets in heavy flavor region
hf	✓	b+c jets in light flavor region
hfstats1	-	Linear fluctuations of c jets
hfstats2	-	Quadratic fluctuations of c jets
lfstats1	-	Linear fluctuations of udsg jets
lfstats2	-	Quadratic fluctuations of udsg jets
cferr1	✓	Linear fluctuations of c jets
cferr2	✓	Quadratic fluctuations of c jets

Calibrations of JES and JER are done centrally at CMS [205]. Uncertainties associated with the JES calibrations are divided into 27 sources to properly account for correlations, which are summarized in Table 17.2. Uncertainties associated with the calibrations of JER are combined

into a separate uncertainty, which is considered uncorrelated across the years. Variations of JES and JER due to these uncertainties are propagated to the p_T^{miss} and calibrations of the DeepJet scores: scale factors used to correct DeepJet scores and the p_T^{miss} vector are recomputed for each of the jet energy variations and treated as uncertainties that are fully correlated to the respective jet energy variation.

Table 17.2: Summary of the sources of uncertainty associated with JES. A hyphen (−) denotes that a source is not correlated across the years.

Source	Correlated	Source	Correlated
AbsoluteStat	-	RelativePtHF	✓
AbsoluteScale	✓	RelativeBal	✓
AbsoluteMPFBias	✓	RelativeSample	-
Fragmentation	✓	RelativeFSR	-
SinglePionECAL	✓	RelativeStatFSR	✓
SinglePionHCAL	✓	RelativeStatEC	-
FlavorQCD	✓	RelativeStatHF	-
TimePtEta	-	PileUpDataMC	✓
RelativeJEREC1	-	PileUpPtRef	✓
RelativeJEREC2	-	PileUpPtBB	✓
RelativeJERHF	✓	PileUpPtEC1	✓
RelativePtBB	✓	PileUpPtEC2	✓
RelativePtEC1	-	PileUpPtHF	✓
RelativePtEC2	-		

One additional uncertainty is assigned to the unclustered p_T^{miss} is considered [150] and is treated as uncorrelated across the years.

In the 2016 and 2017 runs, L1 ECAL triggers fired early [25] causing many uninteresting events to be recorded while the later interesting events were rejected. Since this effect is not present in the MC simulation, a correction is applied to all signals and *prompt* backgrounds. This correction is varied by 20% and the resulting change in per-event weight is taken as the uncertainty. This uncertainty is treated as correlated across the years.

In the 2018 runs, two HCAL modules had power supplies that died in the middle of the data taking. This affected the measurement of jet energy and p_T^{miss}. No correction is applied as this effect is not well-understood and likely not significant relative to other corrections. Nevertheless, an uncertainty, denoted by "HEM", is assigned to cover the variations of jet energy and p_T^{miss} caused

by those two dead modules.

A comparison of different sources of systematic uncertainties of the background estimates in the SRs is shown in Figure 17.7.

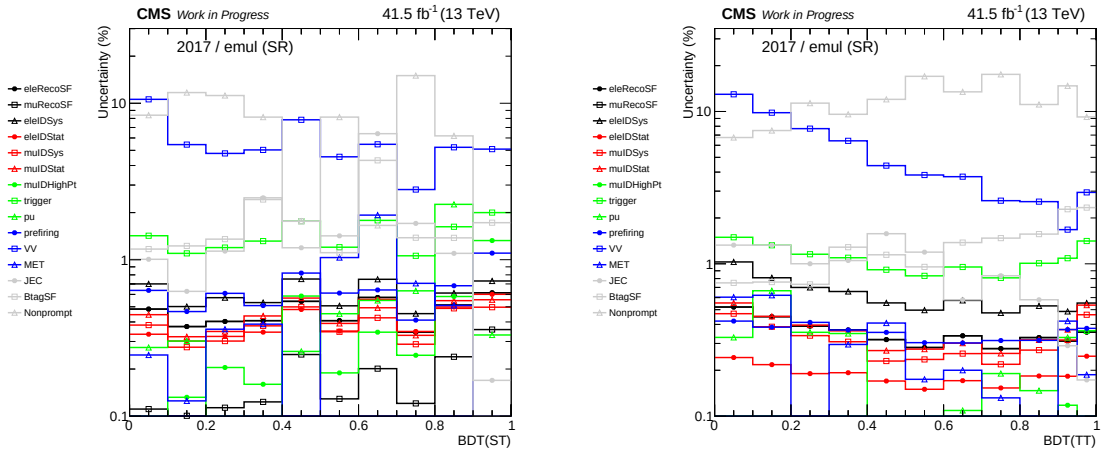

Figure 17.7: Distributions of relative uncertainties on total expected backgrounds as a function of BDT output in top production enriched SR (left), top decay enriched SR (right). The 2017 dataset is used to produce these histograms. Luminosity and cross-section uncertainties are not included in these plots. JES, JER, and HEM are combined into "JEC". Sources of b-tagging uncertainties listed in Table 17.1 are combined into "BtagSF".

A comparison of different sources of systematic uncertainties of the signal estimates in the SRs is shown in Figure 17.8.

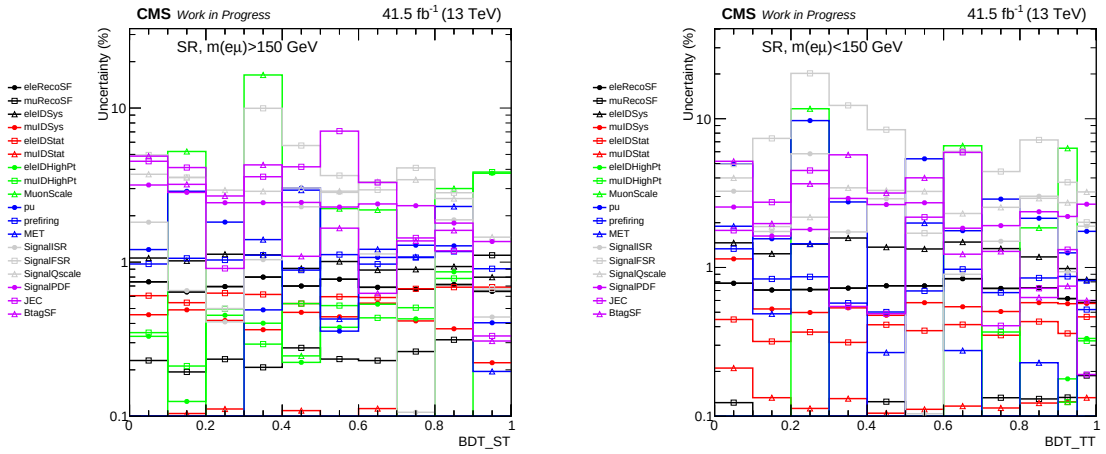

Figure 17.8: Distributions of relative uncertainties on signal ($C_{e\mu ut}^{vector}$ is used as an example) as a function of BDT output in top production enriched SR (left), top decay enriched SR (right). The 2017 dataset is used to produce these histograms. Luminosity and cross-section uncertainties are not included in these plots. JES, JER, and HEM are combined into "JEC". Sources of b-tagging uncertainties listed in Table 17.1 are combined into "BtagSF".

A summary of systematic uncertainties and their average impact on predicted yields in the SRs can be found in Table 17.3. These uncertainties are extracted from pre-fit BDT templates shown in Figure 16.12.

Table 17.3: Summary of systematic uncertainties and the average change in signal and overall background yields in the SRs. Uncertainties that only contain normalization effects, such as luminosity uncertainties and uncertainties on theoretical cross sections, are not included in this table.

Systematic uncertainty	m(eμ) < 150 GeV		m(eμ) > 150 GeV	
	Background	Signal	Background	Signal
Lepton reconstruction	< 0.1%	0.6%	< 0.1%	1.7%
Lepton identification and isolation	1.0%	1.4%	1.0%	1.3%
High p_T lepton	< 0.1%	0.2%	< 0.1%	3.4%
Muon momentum scale and resolution	< 0.1%	0.3%	< 0.1%	0.1%
PDF	< 0.1%	2.3%	< 0.1%	1.3%
QCD scale	4.0%	2.8%	5%	1.4%
ISR/FSR	-	7.6%	-	1.0%
Pileup	< 0.1%	0.4%	< 0.1%	0.3%
L1 prefiring	< 0.1%	0.4%	< 0.1%	0.4%
Jet energy scale and resolution	< 0.1%	1.0%	1.0%	0.4%
b tagging	< 0.1%	0.9%	1.0%	0.5%
Nonprompt	11.0%	-	9.0%	-
Jet modeling	6.0%	-	7.0%	-

Chapter 18

Statistical Analysis

In the absence of significant excess over the SM prediction, the observed distributions of the BDT discriminator are used to test various hypotheses, where the coexistence of the CLFV signals and backgrounds are assumed. A statistical method called "profile likelihood" is used to move the focus on the cross sections of the CLFV signals while also keeping track of the systematic uncertainties. The profile likelihood fit performed on the distributions of the BDT discriminator is discussed in Section 18.1. Upper limits on various WCs and branching fractions established by this analysis are presented in Section 18.2.

18.1 Profile Likelihood Fit

A binned likelihood function $\mathcal{L}(\mu, \theta)$ is constructed to perform the statistical analysis using the binned BDT discriminant distributions. The choice of intervals for the bins in the likelihood function is the same as in Figure 16.12. Six WCs ($C_{e\mu ut}^{tensor}$, $C_{e\mu ut}^{vector}$, $C_{e\mu ut}^{scalar}$, $C_{e\mu ct}^{tensor}$, $C_{e\mu ct}^{vector}$, and $C_{e\mu ct}^{scalar}$) are considered separately in the statistical analysis, where only one of them is activated while the others are set to zero. The top quark production and decay signal modes that correspond to the same WC are combined. The signal strength μ, defined previously in Equation (12.14), governs the cross section of the two signal modes simultaneously.

All systematic uncertainties are incorporated into the likelihood function as nuisance parameters, denoted by θ. The uncertainties that affect the shape of the BDT discriminant distributions utilize Gaussian distributions while other uncertainties that only affect the normalizations utilize log-normal distributions. The "Barlow-Beeston lite" method [206] is used to incorporate the statistical uncertainties in the signal and background predictions.

A profile likelihood fit is performed simultaneously in six regions (three data-taking years and two SRs) by maximizing the likelihood function $\mathcal{L}(\mu, \hat{\theta}_\mu)$, where $\hat{\theta}_\mu$ are the values of the nuisance parameters that maximize the likelihood for a specific signal strength. The post-fit distributions of the BDT discriminants are shown in Figure 18.1. The largest post-fit uncertainties are the statistical uncertainties from the limited number of simulated events.

The impacts of the nuisance parameters on the profile likelihood fit are quantified and a representative ranking of the impacts is shown in Figure 18.2. In general, the most prominent

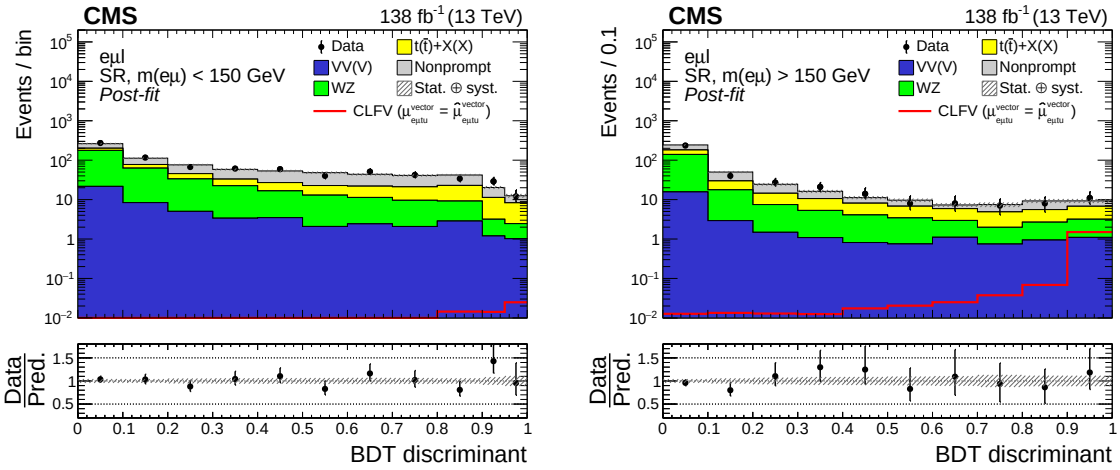

Figure 18.1: Distributions of the post-fit BDT discriminator targeting the CLFV top quark decay (left) and production (right) signal. Contributions from the two signal modes (production and decay) are combined within each SR and are shown as the solid red line. The post-fit signal strength ($\mu^{vector}_{eμut} = \hat{\mu}^{vector}_{eμut}$) is used to normalise the signal cross sections. The hatched bands indicate post-fit uncertainties (statistical and systematic) for the SM background predictions.

uncertainties affecting the likelihood fit are the statistical uncertainties that arise from limited sample size. A full collection of nuisance parameter impacts can be found in Appendix C.

18.2 Upper Limits

The results are interpreted as 95% CL upper limits on the signal strength μ, which is equivalent to $(C/\Lambda^2)^2$, as shown in Equation (12.14). The limit setting procedure uses a modified frequentist CL_s method [207, 167] as the criterion, which is based on a profile likelihood ratio test statistic. An asymptotic approximation [208] is used to determine the distributions of the test statistic. By convention, positive WCs are assumed, and the one-dimensional upper limits on a given WC, C_a/Λ^2, are obtained by taking the square root of the upper limits on the corresponding signal strength μ_a. The branching fractions, $\mathcal{B}(t \to eμq)$ with q = u or c, are obtained using Equation (12.13) taken from Ref. [175].

The resulting one-dimensional limits are summarized in Table 18.1. Tabulated results are provided in the HEPData record for this analysis [209]. The upper limits on WCs associated to operators with a tensor-like Lorentz structure are more stringent because the predicted cross sections for tensor-like operators are higher when all WCs are set to the same value (i.e. $C_a/\Lambda^2 = 1\text{TeV}^{-2}$), as shown in Table 12.2. Signal processes initiated by an up quark receive large contributions from valence quarks coming from protons, which lead to larger cross sections, and consequently limits on WCs involving an up quark are more stringent that those with a charm quark. In addition to the cross sections, the sensitivity for the branching fractions $\mathcal{B}(t \to eμq)$ are also

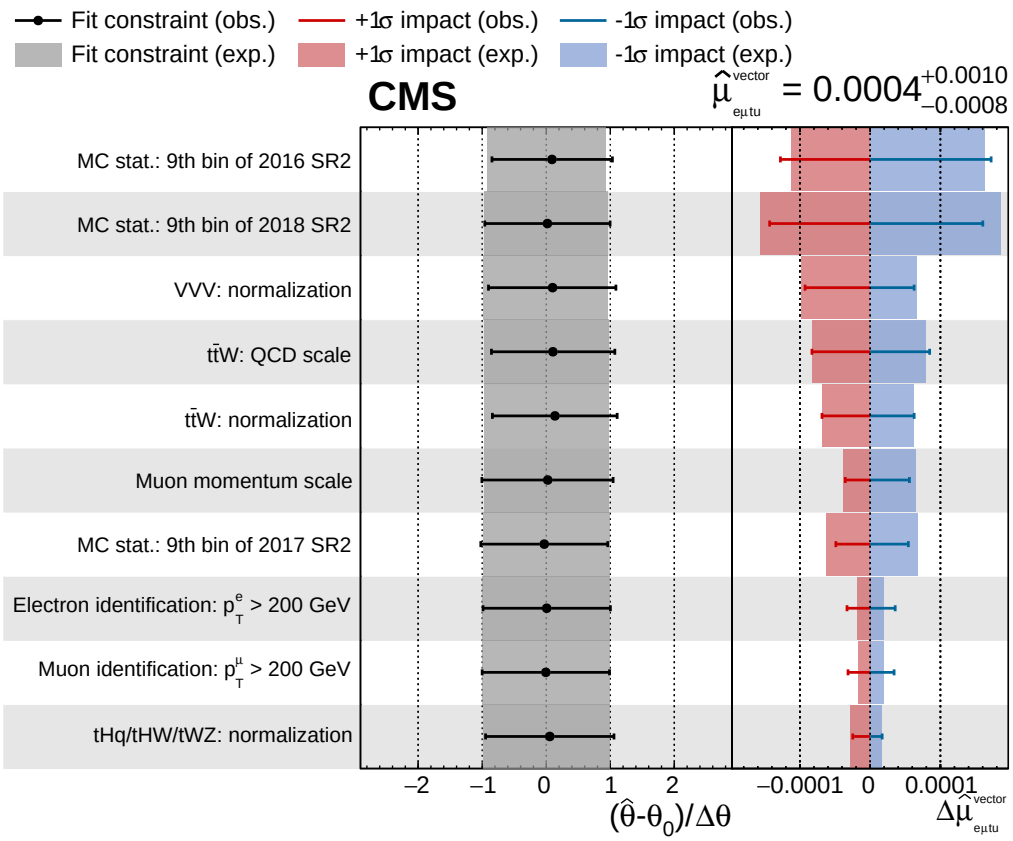

Figure 18.2: The nominal value of the observed signal strength $\hat{\mu}$ and its uncertainty is shown in the top right corner. Ranking of the nuisance parameters according to their observed impacts on $\hat{\mu}$ (represented with error bars) is shown in the right panel. Only the 10 nuisance parameters with the largest observed impacts are shown. The expected impacts (represented with red and blue rectangles) are derived using Asimov fits, where data is replaced by a background-only template (i.e. the nominal value of the expected $\hat{\mu}$ is 0). The impact of each nuisance parameter, $\Delta\hat{\mu}$, is calculated as the difference between the nominal $\hat{\mu}$ and the value of $\hat{\mu}$ when the corresponding nuisance parameter is fixed to $\hat{\theta} \pm \sigma$, where $\hat{\theta}$ (σ) is its post-fit value (uncertainty). The left panel shows the pulls (represented with black dots) and uncertainties (represented with error bars and grey rectangles) of the nuisance parameters in units of the pre-fit uncertainties. The pulls are calculated as the difference between the nominal and the post-fit values of the nuisance parameters. The "SR2" quoted in the label corresponds to the top quark production enriched signal region.

correlated to several constants specified in Equation (12.13). Relative to the vector- and scalar-like interactions, the tensor-like CLFV interactions have the least stringent limits on the corresponding branching fractions due to the small combinatorial factor that appears in the denominator of Equation (12.13).

The one-dimensional limits on eμut and eμct couplings are interpolated to obtain the two-dimensional limits, which are shown in Figure 18.3. These limits constitute the most stringent

ones to date on these processes.

Table 18.1: Upper limits at 95% CL on WCs and the branching fractions. The expected and observed upper limits are shown in regular and bold fonts, respectively. The intervals that contain 68% of the distribution of the expected upper limits are shown in parentheses.

CLFV coupling	Lorentz structure	$C_{e\mu qt}/\Lambda^2$ (TeV^{-2}) Exp. (68% range)	Obs.	$\mathcal{B}(t \to e\mu q) \times 10^{-6}$ Exp. (68% range)	Obs.
eμut	Tensor	0.022 (0.018–0.026)	**0.024**	0.027 (0.018–0.040)	**0.032**
	Vector	0.044 (0.036–0.054)	**0.048**	0.019 (0.013–0.028)	**0.022**
	Scalar	0.093 (0.077–0.114)	**0.101**	0.010 (0.007–0.016)	**0.012**
eμct	Tensor	0.084 (0.069–0.102)	**0.094**	0.396 (0.272–0.585)	**0.498**
	Vector	0.175 (0.145–0.214)	**0.196**	0.296 (0.203–0.440)	**0.369**
	Scalar	0.385 (0.318–0.471)	**0.424**	0.178 (0.122–0.266)	**0.216**

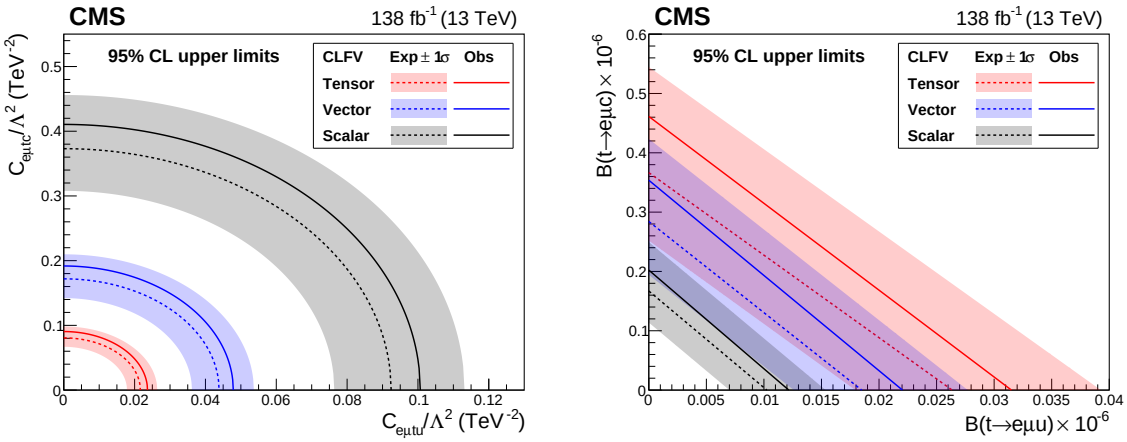

Figure 18.3: Two-dimensional 95% CL upper limits on the WCs (left) and the branching fractions (right). The observed (expected) upper limits for tensor-, vector-, and scalar-like CLFV interactions are shown in red, blue, and black solid (dotted) lines, respectively. The shaded bands contain 68% of the distribution of the expected upper limits.

Part IV
Outlook for CLFV Searches Using Top Quarks

Part IV of this thesis describes an ongoing physics analysis that is an extension of the analysis documented in Part III. Under the supervision of Prof. Skinnari, Emily Minyun Tsai and I started working on this analysis in January 2023. Materials presented in Part IV have not yet been fully approved by the CMS Collaboration and shall not be considered to be finalized. Part IV is organized as follows. Chapter 19 gives a description of the signal processes targeted by this analysis and how they are generated. Object- and event-level selection criteria used by this analysis are described in Chapter 20 and Chapter 21, respectively. Chapter 22 presents results of a preliminary sensitivity study. Except where noted, materials presented in Part IV are prepared by Emily and myself.

Chapter 19

Inclusive CLFV Signals

As discussed in Chapter 11, the CLFV processes involving top quarks have been studied by the ATLAS and CMS Collaborations in many orthogonal channels. Among all possible charged-lepton flavor mixing modes (i.e. $e\mu$, $e\tau$, and $\mu\tau$), the $e\mu$ mode receives the most extensive scrutiny [32, 34, 166], yielding a very tight constraint at $\mathcal{O}(10^{-8})$ on $\mathcal{B}(t \to e\mu q)$. On the other hand, there exists only one preliminary study on the $\mu\tau$ mode carried out by the ATLAS Collaboration [33], and the $e\tau$ mode remains completely unexplored at the LHC experiments. Therefore, the objective of this analysis is to probe as many unexplored channels as possible and search for all three charged-lepton flavor mixing modes simultaneously using data collected by the CMS detector in 2016-2018. Section 19.1 gives a brief description of the targeted final states while signal event generation is described in Section 19.2.

19.1 Targeted Final States

One of the central features of this analysis is the inclusion of a hadronic tau lepton, which remains relatively unexplored in the top quark sector. The target final states of this analysis contain exactly two light leptons (electron or muon) and one hadronic tau. The two light leptons can come with any flavor and charge compositions, as long as the sum of the electric charges of all three leptons is 1 or -1. Effectively, this guarantees all three lepton flavor mixing modes are covered by this analysis. In addition to leptons, the target final states at LO also feature one or two jets with exactly one jet originating from a b quark and some imbalances in p_T caused by neutrinos. Representative Feynman diagrams are shown in Figure 19.1.

Even though the $e\mu$ flavor mixing mode is covered by this analysis, the corresponding processes can only enter the event selection through the OS-$e\mu$ channel with a hadronic tau produced by the SM top quark. Depending on the charge assignment, the same event topology may also contribute to the $e\tau$ or $\mu\tau$ modes, as the hadronic tau may also come from the flavor-violating vertex. Furthermore, the $e\tau$ and $\mu\tau$ signals can enter the event selection through SS dilepton channels, where the background yields are much lower. Therefore, it is expected that this analysis is more competitive in its sensitivity on $e\tau$ and $\mu\tau$ modes.

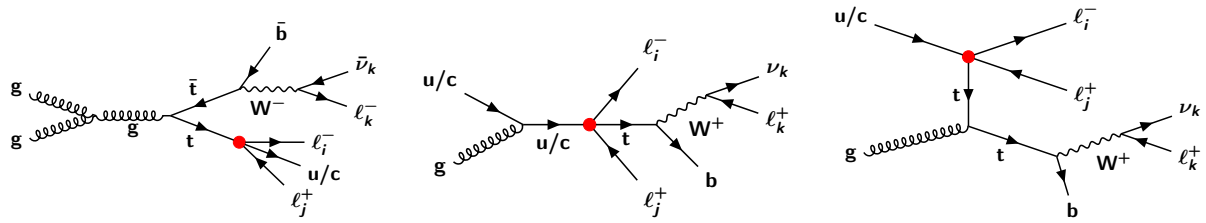

Figure 19.1: Representative Feynman diagrams for the signal processes that are targeted by this analysis. Both top quark decay (left) and production (middle and right) CLFV processes are shown. The indices i, j, and k are lepton-flavor indices that run from 1 to 3 with the following conditions: i) $i \neq j$, ii) one of these three indices is 3, and iii) the other two are smaller than 3.

19.2 Signal Event Generation

In general, the strategy to generate the CLFV signal events for this analysis is very similar to the existing strategy described in Section 12.1. One notable distinction is that all three charged-lepton flavor mixing modes are enabled in samples produced for this analysis. This is achieved by explicitly turning on the $e\tau$ and $\mu\tau$ terms in the EFT operators. For example, the parameterization of the scalar-like operator specified in Equation (12.6) is modified as,

$$\begin{aligned} C_{lequ}^{(1)} &= C_{lequ}^{(1)1213} + C_{lequ}^{(1)2113} + C_{lequ}^{(1)1231} + C_{lequ}^{(1)2131} \\ &+ C_{lequ}^{(1)1313} + C_{lequ}^{(1)3113} + C_{lequ}^{(1)1331} + C_{lequ}^{(1)3131} \\ &+ C_{lequ}^{(1)2313} + C_{lequ}^{(1)3213} + C_{lequ}^{(1)2331} + C_{lequ}^{(1)3231}. \end{aligned} \tag{19.1}$$

This is only done to simplify the MC production procedure as the number of unique samples can be reduced by a factor of three. From a theoretical point of view, each flavor mixing mode corresponds to an independent WC without any presumed correlations with other WCs. The generated signal events from one sample are therefore categorized into three groups using information at the generator level. Since the lepton masses are neglected in the ME calculation, the theoretical cross-section is identical across different flavor mixing modes. Therefore, events from all three groups are normalized to the same cross-section listed in Table 12.2.

The effective Lagrangian is implemented using the SMEFTsim [173] model, which is the common standard agreed by corresponding physics working groups of the ATLAS and CMS Collaborations. Other than the differences in signal cross-sections reported by different models, the CKM and PMNS matrices are also treated differently by SmeftFR [170] and SMEFTsim. More specifically, nonzero off-diagonal terms are added to the entries of the CKM and PMNS matrices by SmeftFR while both matrices are set to identity by SMEFTsim. Effectively, this means SMEFTsim allows no contributions from Flavor-Changing Charged Currents (FCCCs) to the signal processes.

Consequently, this results in a softer kinematic distribution of final-state particles even though the difference is largely negligible, as is shown in Figure 12.1.

Leptons that emerge from the EFT vertex are generally far more energetic in the top quark production events than the top quark decay events. This notable distinction between the two signal modes is exploited to benefit sensitivity, which is discussed in Section 21.2. Representative kinematic distributions of the simulated signal events at the generator level are shown in Figure 19.2.

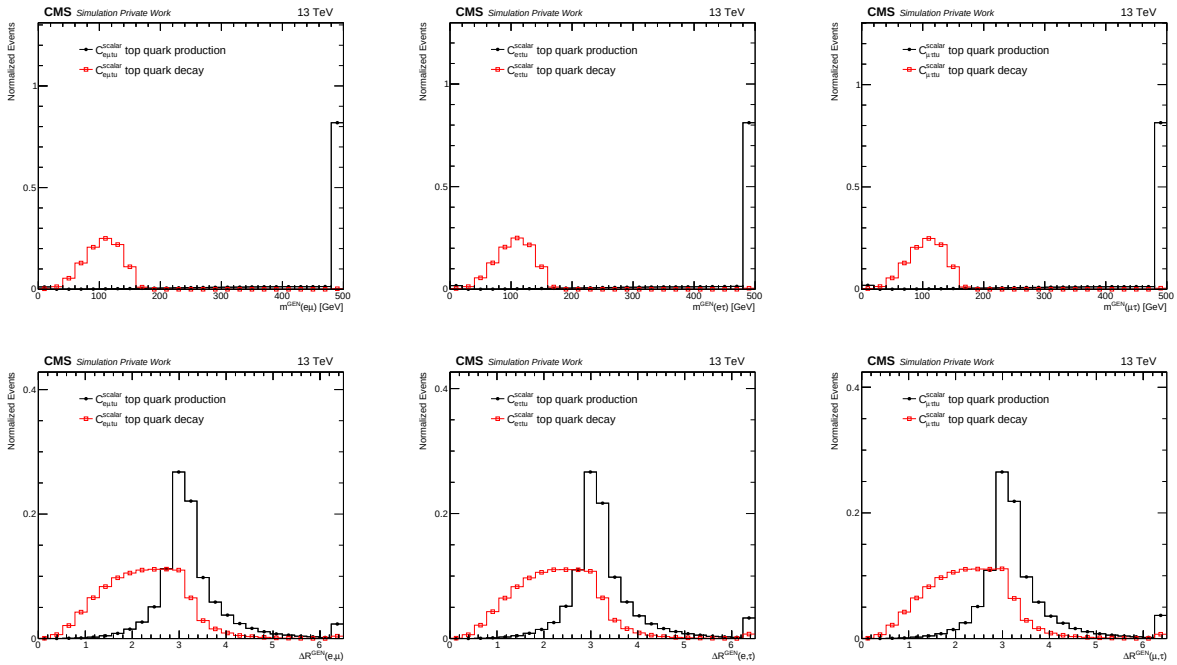

Figure 19.2: Normalized kinematic distributions of the CLFV signal events at the generator level. These events are generated by the scalar-like operator involving an up quark in the EFT vertex. Events from the original samples are categorized into the eμ (left), eτ (middle), and μτ (right) modes. Distributions of the LFV dilepton mass and the opening angle between the two LFV leptons are shown in the top row and the bottom row, respectively. The top quark decay signals are shown in a red line with an open square while the top quark production signals are shown in a black line with a closed circle.

Chapter 20

Object Selection

Similar to the analysis documented in Part III, the three lepton multiplicity requirement removes the vast majority of the $t\bar{t}$ and DY events produced in the collisions. However, these processes, especially DY, still enter and dominate the event selection due to their sheer volumes. In general, $t\bar{t}$ or DY events do not promptly produce three genuine leptons (including hadronic taus), and they can only enter a three-lepton selection if at least one of the light lepton is *nonprompt*, as defined in Chapter 15. Alternatively, jets might also be misidentified as hadronic taus at the reconstruction level, contributing to the so-called "*fake* tau background". One example is the DY+jets events, where the two OSSF light leptons are correctly identified but a jet is misidentified as a hadronic tau. Stringent selection criteria are applied to lepton candidates in order to suppress these backgrounds, which are discussed in Section 20.1 and Section 20.2. Additionally, selection criteria on jets and MET are discussed in Section 20.3.

20.1 Electrons and Muons

An updated version of the TOP LeptonMVA [210] is used to select *prompt* leptons. The same set of features used in the previous version is also used in this new version even though the training set in this new version is constructed solely from simulated $t\bar{t}$ events, as opposed to from $t\bar{t}$, $t\bar{t}W$, $t\bar{t}Z$, and tZq. The previous version of the TOP LeptonMVA was originally designed for a multi-lepton analysis like tZq, which is why samples other than $t\bar{t}$ are included in the training. For this analysis with two leptons (excluding hadronic tau), the new version of the TOP LeptonMVA is better suited. One notable upgrade of this new version is the switch from TMVA [185] to XGBoost [195] in its BDT implementation. This improves the signal efficiency by a few percentage points while keeping the same background efficiency.

Both electron and muon candidates are required to have a minimum TOP LeptonMVA score of 0.64, corresponding to roughly the same background efficiency (1%) that is chosen for the previous analysis. However, this working point corresponds to a signal efficiency of 92%, which is 2% higher than the previous implementation.

On top of the TOP LeptonMVA requirement, a set of selection criteria are added to select electron and muon candidates, which are largely derived from the existing strategy described in

Section 13.1. The minimum p_T requirement is lowered from 38 GeV to 30 GeV for the leading lepton when compared to the previous analysis. This change helps improve the signal acceptance as this analysis faces even lower statistics. The p_T threshold on the sub-leading lepton is kept at 20 GeV. The requirements on η, d_{xy}, d_z, and SIP_3 are kept the same as they come from the same pre-selection requirements used in the BDT training.

The same "mini isolation" variable I^{rel}_{mini} defined in Equation (13.1) is used to create isolated lepton candidates, even though the threshold is loosened from 0.12 to 0.4. Similar to the lowering of the p_T on the leading lepton, this change helps improve the signal acceptance.

Only lepton candidates that pass all the requirements stated above are considered in this analysis. They are referred to as "*tight*" leptons, which does not include hadronic tau.

20.2 Hadronic Taus

A NN-based algorithm called "DeepTau" [211] is used to simultaneously discriminate against jets, electrons, and muons. The core feature of this algorithm is the use of convolutional layers to exploit the translational invariance of the input variables. A combination of lower-level and high-level variables are used as input features to the NN. The lower-level variables are derived from individual particles reconstructed by the PF algorithm while the high-level variables are mostly taken from the previously trained MVA [212]. Two grids are defined in the $\eta - \phi$ plane to encode the positions as well as other low-level inputs from PF candidates. The outer grid and the inner grid consist of 21×21 cells and 11×11 cells, respectively. The total number of input variables is 105703, which consists of 188 low-level variables per grid cell and 47 high-level variables.

When compared to the discriminators from existing algorithms [213, 212], the discriminators against jets and electrons from the DeepTau algorithm provide a 10-30% improvement in signal efficiency while maintaining the same background efficiency. The discriminator against muons from the DeepTau algorithm provides a factor of 3-10 larger background rejection while maintaining the signal efficiency at a very high level (99.1-99.4%).

Tau candidates are required to simultaneously pass "VLoose", "Tight", and "Tight" working points of the discriminators against electrons, muons, and jets, respectively. These working points correspond to over 99% signal efficiency for discriminators against electrons and muons, and 60% for the discriminator against jets. The working point chosen for the discriminator against jets is a lot tighter as the vast majority of *fake* taus in this analysis originate from jets.

In addition to the DeepTau working points, a set of selection criteria is applied to tau candidates, which is mostly derived from the pre-selection requirements of the DeepTau algorithm. Tau candidates are required to have a minimum p_T of 20 GeV with $|\eta| < 2.3$. Similar to the requirements on electron and muon candidates, $|d_{xy}|$ and $|d_z|$ of tau candidates are required to be smaller than 0.05 and 0.1, respectively. Tau candidates reconstructed from decay modes with

missing charged hadrons are excluded.

To enter the event selection of this analysis, tau candidates are required to pass all the requirements stated above. Tau candidates that satisfy all the requirements are referred to as "*tight*" taus in this analysis.

20.3 Jets

The strategy to select jet candidates described in Section 13.2 is largely kept intact. The only notable change is the lowering of the p_T threshold of jets from 30 GeV to 25 GeV. The DeepJet algorithm [191] described in Section 13.3 is also used to tag jets that originate from b quark in this analysis. The "Loose" working point is chosen to tag b jet candidates, which corresponds to roughly 10% improvement in signal efficiency when compared to the "Medium" working point used by the previous analysis.

Chapter 21

Event Selection

Events are required to contain exactly two *tight* leptons and one *tight* tau, described in Chapter 20. A combination of single- and di-lepton HLT triggers are used to select data as well as simulated events. The sum of the electric charges of all three leptons is required to be 1 or -1, which guarantees at least one OSDF pair in every selected event. Depending on the flavors and the charge assignments of the two leptons, events are further categorized into 6 different channels, which are described in Section 21.1. SRs require additional selection criteria to achieve an optimal signal-to-background ratio, which is discussed in Section 21.2. Control regions of the DY background near the Z resonance are also defined to study the accuracy of the MC modeling, which is described in Section 21.3.

21.1 Event Categorization

The two *tight* leptons can come with any flavor- or charge-compositions, which contain 6 possibilities: i) OS-ee, ii) OS-eμ, iii) OS-μμ, iv) SS-ee, v) SS-eμ, and vi) SS-μμ. These subsets of the selected events are referred to as "channels" in this analysis. The OS-eμ and SS-eμ channels are further subdivided into "subchannels" as more than one charged-lepton flavor mixing mode is possible in these channels. For example, due to the requirement on the sum of electric charges, the sign of the selected tau must be different from the signs of the electron and muon in the SS-eμ channel. This means both the eτ and μτ flavor mixing modes are possible under such a scenario. This two-fold ambiguity is resolved by using the existing strategy described in Section 14.3: two SM top quark candidates are reconstructed by combining the MET, the jet with the highest DeepJet score, and two leptons in question. The lepton that gives a top quark mass that is closer to 172.5 GeV is assigned as the standalone lepton while the other lepton is assigned as the LFV lepton that contributes to the flavor mixing. There is only one subchannel for each of the other four channels as there is no ambiguity on how to assign the mixing mode to events residing in these four channels. A total of 9 subchannels are defined, which is illustrated in Figure 21.1.

As is shown in Figure 19.2, the invariant mass of the LFV-dilepton pair of any mixing mode, denoted by m($\ell\ell'$), has a sharp end point at around 150 GeV for top quark decay signals. Such a pattern does not exist in the top quark production signals. Therefore, each subchannel is

further subdivided into two search bins to create regions enriched in different signal modes using a threshold of 150 GeV on m($\ell\ell'$), which leads to a total of 18 search bins. The strategy of creating high (low) mass SRs to target top quark production (decay) signals takes inspiration from the previous analysis.

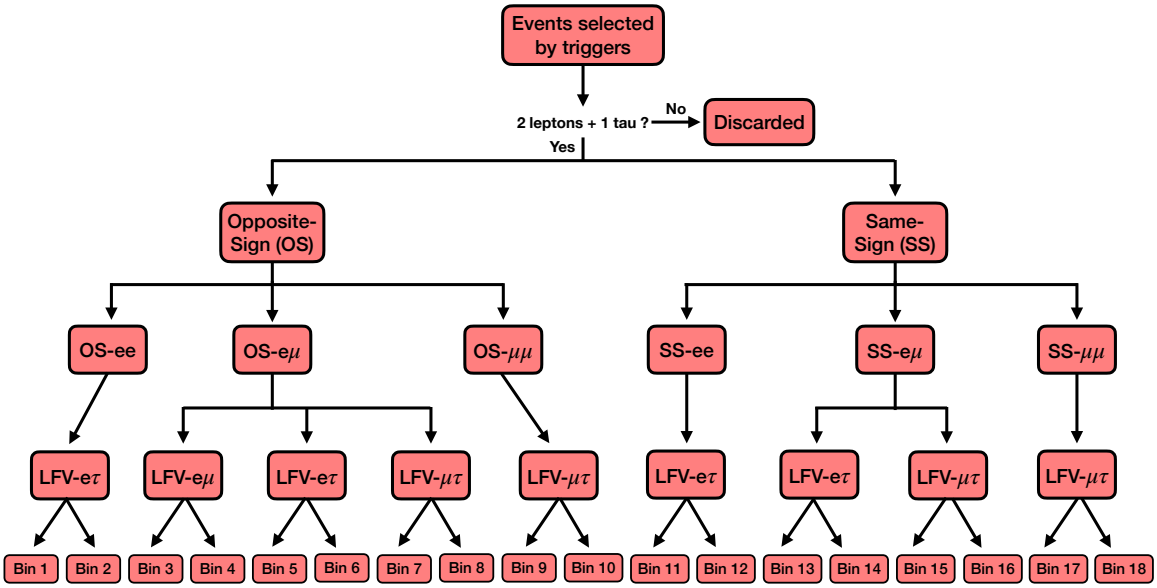

Figure 21.1: Illustration of event categorization scheme used by this analysis. The second to the last row shows 9 exclusive subchannels, where a specific charged-lepton flavor mixing mode is assigned. The odd (even) bins shown in the last row correspond to search bins with the requirement of m($\ell\ell'$) $<$ ($>$) 150 GeV.

The performance of this categorization scheme is evaluated by using simulated signal events that contain all three flavor mixing modes. An incorrect assignment occurs when a signal event is generated in one flavor mixing mode but is categorized into another flavor mixing mode. The rate of occurrences of an incorrect assignment is largely under control, as is shown in Figure 21.2. Further improvement is possible with the assistance of more sophisticated algorithms, such as NNs.

21.2 Signal Region

To further improve the sensitivity of this analysis, additional selection criteria are used to create SRs. More specifically, events are required to contain at least one jet and exactly one b-tagged jet. A minimum MET of 20 GeV is required to account for the presence of neutrinos due to the leptonically decaying top quark. Furthermore, events that contain an OSSF lepton pair with an invariant mass between 58 and 108 GeV are removed to suppress the DY background. A summary of expected signal and background events that enter SRs is shown in Figure 21.3.

Representative distributions of m($\ell\ell'$) and ΔR at reconstruction level are shown in Figure 21.4.

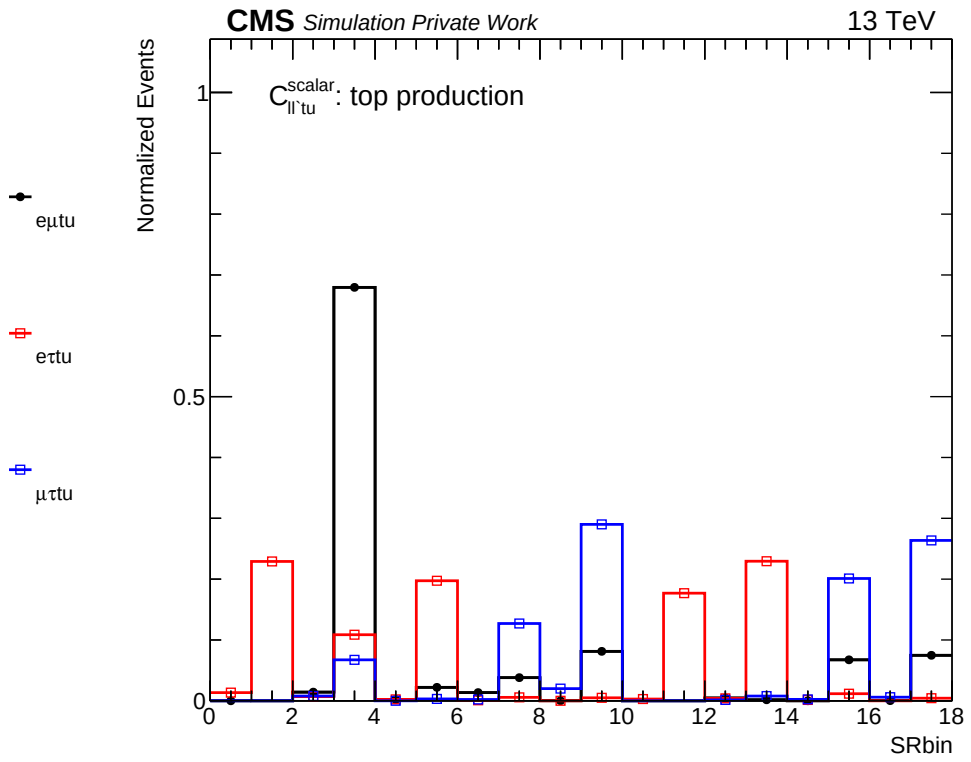

Figure 21.2: Normalized distribution of search bins assigned by the categorization scheme. Signal events generated in eμ, eτ, and μτ modes are shown in black, red, and blue lines respectively. The ordering of the search bins is the same as the one shown in Figure 21.1.

21.3 Drell-Yan Control Region

The Z mass veto used to define SRs is reversed to create regions enriched in DY events. Distributions of the OSSF lepton mass and jet multiplicity in the DY control regions are shown in Figure 21.5.

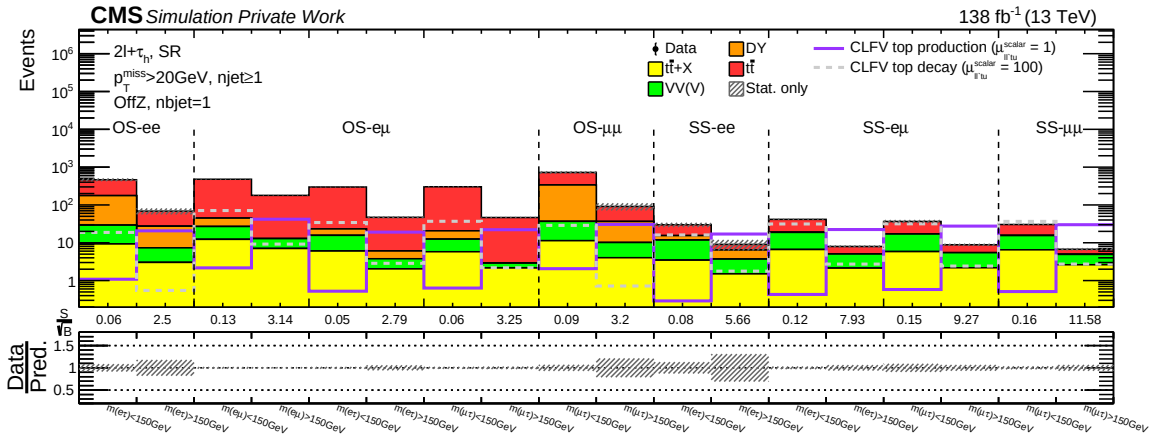

Figure 21.3: Summary of expected signal and background events in SRs. Signal events generated in different flavor mixing modes are not combined. The original signal strength ($\mu^{\text{scalar}}_{\ell\ell'\text{tu}} = 1$), corresponding to $C^{\text{scalar}}_{\ell\ell'\text{tu}}/\Lambda^2 = 1$ TeV^{-2}, is used to normalize the cross-section of top quark production signals. The cross-section of top quark decay signals is scaled up by a factor of 100 for improved visualization. Only statistical uncertainties for the background predictions are included in the hatched bands. The ordering of the search bins is the same as the one shown in Figure 21.1. For each search bin, the number of total signal events divided by the square root of the number of total background events is calculated and shown in the gap between the upper and lower panels.

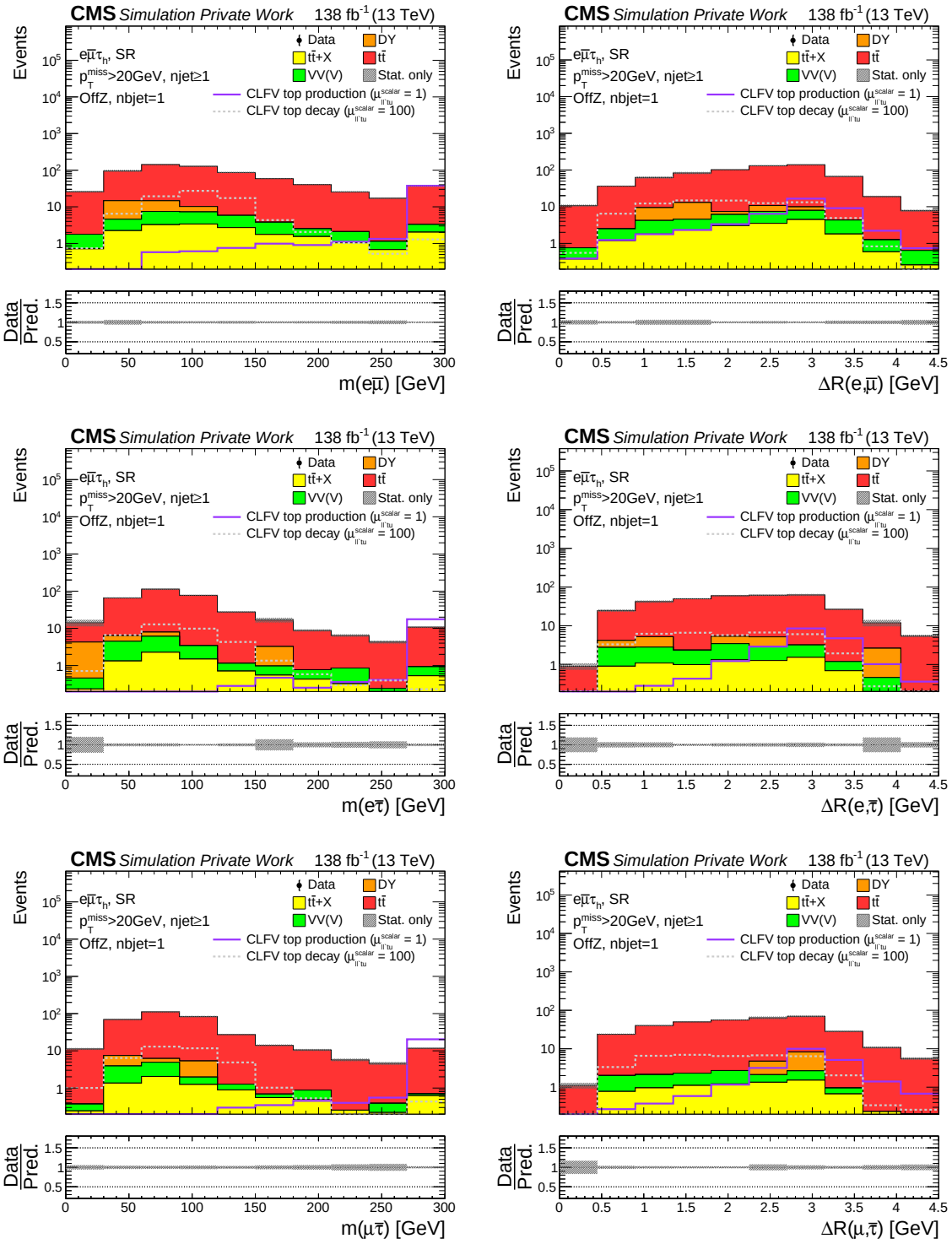

Figure 21.4: Distributions of the LFV-dilepton mass (left column) and opening angle between the two LFV leptons (right column) in the SRs in the OS-eμ channel. Events categorized into the LFV-eμ, LFV-eτ, and LFV-μτ subchannels are shown in the top, middle, and bottom row, respectively. The hatched bands only include statistical uncertainties for the background predictions. The last bin of all histograms includes the overflow events.

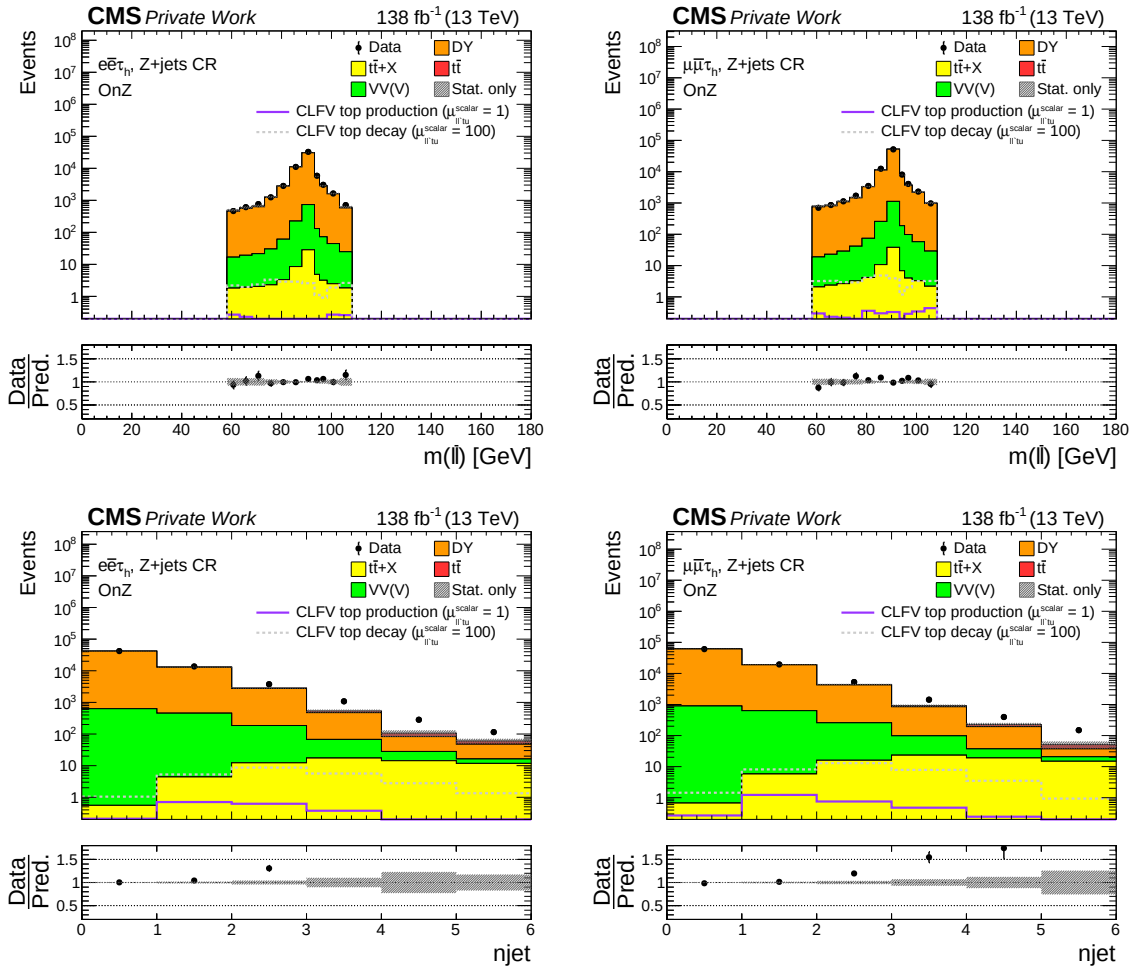

Figure 21.5: Distributions of the OSSF lepton mass (top row) and jet multiplicity (bottom row). Events in the OS-ee, and OS-μμ DY control regions are shown in the left column and right column, respectively. The data are shown as filled points and the background predictions as histograms. The hatched bands only indicate statistical uncertainties for the background predictions. The last bin of the right column histograms includes the overflow events.

Chapter 22

Expected Sensitivity

Data events in the SRs of this analysis are still hidden as strategies are still being finalized. Nevertheless, preliminary studies are performed to understand the overall sensitivity, as well as the sensitivity of each event channel. These studies utilize Asimov datasets to reconstruct the likelihood function, which is then used to perform the profile likelihood fit and calculate the upper limits. The Asimov datasets replace data events with background-only template histograms. The one-dimensional profile likelihood fit and upper limit are discussed in Section 22.1. The two-dimensional likelihood scan is discussed in Section 22.2.

22.1 Upper Limits

The one-dimensional likelihood function $\mathcal{L}(\mu, \theta)$ is very similar to the one described in Section 18.1 with a few notable differences. Firstly, templates are constructed directly from event yields in search bins as BDT is not used in this analysis. Secondly, only statistical uncertainties, luminosity uncertainties, and normalization uncertainties of MC samples are considered as other systematic uncertainties are still being evaluated. A 20% normalization uncertainties are assigned to the normalizations of the $t\bar{t}$ and DY backgrounds as they are considered *fake* tau backgrounds with larger uncertainties. A 10% uncertainty is assigned to the normalizations of signal and other background processes. Lastly, there are three independent signals contained in one sample, and they are used to construct the likelihood functions separately.

The likelihood function is maximized based on the Asimov datasets. Representative impacts of the nuisance parameters on the likelihood fit are shown in Figure 22.1.

Using the same limit setting procedure described in Section 18.2, one-dimensional limits at 95% CL can be calculated for each flavor mixing signal. Expected limits on the scalar-like operator involving an up quark are summarized in Table 18.1.

22.2 Two Dimensional Likelihood Scan

The two-dimensional likelihood function $\mathcal{L}(\mu_1, \mu_2, \theta)$ is constructed by injecting two signals simultaneously. The μ_1 and μ_2 correspond to signal strengths of signals generated in different

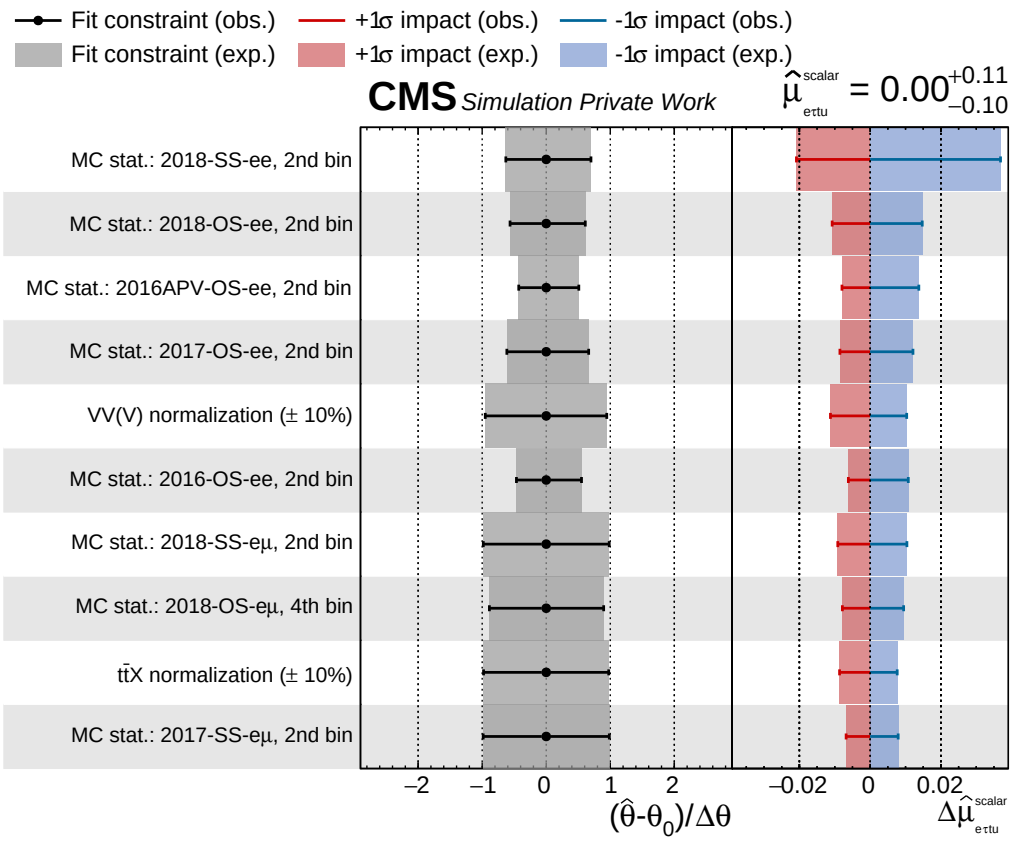

Figure 22.1: The nominal value of the expected signal strength $\hat{\mu}$ and its uncertainty is shown in the top right corner. Ranking of the nuisance parameters according to their expected impacts on $\hat{\mu}$ (represented with error bars) is shown in the right panel. Only the 10 nuisance parameters with the largest observed impacts are shown. The impact of each nuisance parameter, $\Delta\hat{\mu}$, is calculated as the difference between the nominal $\hat{\mu}$ and the value of $\hat{\mu}$ when the corresponding nuisance parameter is fixed to $\hat{\theta} \pm \sigma$, where $\hat{\theta}$ (σ) is its post-fit value (uncertainty).

flavor mixing modes. For a given pair of signal strengths (μ_1, μ_1), nuisance parameters θ are profiled to achieve the maximum likelihood, denoted by $\mathcal{L}(\mu_1, \mu_2, \hat{\theta}_{\mu_1,\mu_2})$. This process is repeated to scan through the μ_1-μ_1 space. The results of the profiled likelihood at each point in μ_1-μ_1 space are then compared with the expected likelihood distribution to locate the boundaries of the 68% and 90% ranges, which are shown in Figure 22.2.

Table 22.1: Preliminary expected upper limits at 95% CL on WCs and the branching fractions. The intervals that contain 68% of the distribution of the expected upper limits are shown in parentheses.

CLFV coupling	Event channel	$C_{\ell\ell' ut}/\Lambda^2$ (TeV^{-2}) Exp. (68% range)	$\mathcal{B}(t \to \ell\ell' u) \times 10^{-6}$ Exp. (68% range)
eμut	SS-eμ	2.23 (1.84–2.74)	5.98 (4.07–9.01)
	SS-μμ	2.02 (1.66–2.50)	4.89 (3.30–7.49)
	OS-eμ	1.09 (0.91–1.30)	1.42 (1.00–2.04)
	Combined	1.04 (0.87–1.24)	1.29 (0.91–1.86)
eτut	OS-ee	1.23 (1.04–1.47)	1.82 (1.30–2.60)
	OS-eμ	0.93 (0.78–1.12)	1.04 (0.73–1.51)
	SS-ee	0.69 (0.57–0.85)	0.58 (0.39–0.87)
	SS-eμ	0.57 (0.48–0.70)	0.40 (0.27–0.59)
	Combined	0.49 (0.41–0.59)	0.29 (0.20–0.42)
μτut	OS-μμ	1.14 (0.97–1.36)	1.56 (1.12–2.22)
	OS-eμ	0.87 (0.73–1.05)	0.91 (0.64–1.33)
	SS-eμ	0.54 (0.45–0.66)	0.36 (0.24–0.53)
	SS-μμ	0.48 (0.40–0.60)	0.28 (0.19–0.43)
	Combined	0.41 (0.34–0.49)	0.20 (0.14–0.29)

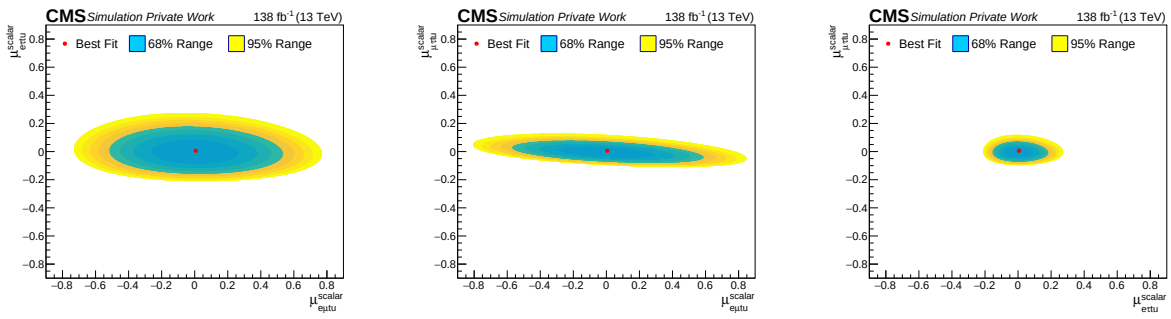

Figure 22.2: Two dimensional likelihood scans performed in the eμ-eτ (left), eμ-μτ (middle), and eτ-μτ (right) spaces.

Chapter 23

Summary and Conclusions

This thesis presents results from a search for charged-lepton flavor violation in both top quark production and decay processes. The data used were collected by the CMS experiment during 2016–2018 and correspond to an integrated luminosity of 138 fb^{-1}. Events were selected for analysis if they contained exactly three charged leptons–one electron and one muon of opposite electric charge as well as one additional electron or muon. Events must also contain at least one jet of which no more than one is associated with a bottom quark. An effective field theory approach is used for parametrizing the charged-lepton flavor-violating interactions. Boosted decision trees are used to distinguish a possible signal from the background. No significant excess is observed over the prediction from the standard model. Upper limits at the 95% confidence level are set on the branching fractions involving up (charm) quarks, $t \to e\mu u$ ($t \to e\mu c$), of $0.032(0.498) \times 10^{-6}$, $0.022(0.369) \times 10^{-6}$, and $0.012(0.216) \times 10^{-6}$ for tensor, vector, and scalar interactions, respectively. These limits constitute the most stringent ones to date on these processes, improving the existing limits by roughly one order of magnitude.

Additionally, the $e\tau qt$ and $\mu\tau qt$ interactions are also being studied currently in a second search. The tau leptons considered in this search undergo hadronic decay and are selected with a NN-based (hadronic tau) identification algorithm. Selected events in this search contain exactly one hadronic tau and two charged leptons (electron or muon) and are divided into 18 search bins. This search is expected to place competitive upper limits on branching fractions of $t\to e\tau q$ and $t\to \mu\tau q$ processes while further improving the upper limits established by the first analysis on $t \to e\mu q$ branching fractions.

Search for CLFV is an active area of research at the LHC experiments, and so far no definitive evidence of CLFV has been reported by the CMS Collaboration. Many of these searches, including the two presented in this thesis, are limited by statistics, where a significant improvement in sensitivity is expected upon the arrival of the HL-LHC dataset. To cope with the harsh environment of the HL-LHC, the CMS Experiment is planning to incorporate tracking information at the Level-1 trigger. This will provide a much-needed handle to reduce data valume and mitigate the effects of pile-up interactions. The Level-1 track-finding algorithm along with one of its applications to electron triggers are also presented in this thesis.

Appendix A

List of Trigger Paths

Table A.1: Triggers used to record events during data taking in 2016.

Dataset	Trigger Path
SingleMuon	HLT_IsoMu22_eta2p1, HLT_IsoTkMu22_eta2p1
	HLT_IsoMu24, HLT_IsoTkMu24
	HLT_Mu50, HLT_TkMu50, HLT_Mu45_eta2p1
SingleElectron	HLT_Ele25_eta2p1_WPTight_Gsf
	HLT_Ele27_WPTight_Gsf
	HLT_Ele27_eta2p1_WPTight_Gsf
	HLT_Ele32_eta2p1_WPTight_Gsf
	HLT_Ele105_CaloIdVT_GsfTrkIdT
	HLT_Ele115_CaloIdVT_GsfTrkIdT
DoubleMuon	HLT_Mu17_TrkIsoVVL_Mu8_TrkIsoVVL
	HLT_Mu17_TrkIsoVVL_TkMu8_TrkIsoVVL
	HLT_TkMu17_TrkIsoVVL_TkMu8_TrkIsoVVL
	HLT_Mu17_TrkIsoVVL_Mu8_TrkIsoVVL_DZ
	HLT_Mu17_TrkIsoVVL_TkMu8_TrkIsoVVL_DZ
	HLT_TkMu17_TrkIsoVVL_TkMu8_TrkIsoVVL_DZ
	HLT_Mu30_TkMu11, HLT_TripleMu_12_10_5
DoubleEG	HLT_Ele23_Ele12_CaloIdL_TrackIdL_IsoVL_DZ
	HLT_Ele16_Ele12_Ele8_CaloIdL_TrackIdL
	HLT_DoubleEle33_CaloIdL_MW
	HLT_DoubleEle33_CaloIdL_GsfTrkIdVL
	HLT_DoubleEle33_CaloIdL_GsfTrkIdVL_MW
MuonEG	HLT_Mu23_TrkIsoVVL_Ele8_CaloIdL_TrackIdL_IsoVL
	HLT_Mu23_TrkIsoVVL_Ele8_CaloIdL_TrackIdL_IsoVL_DZ
	HLT_Mu8_TrkIsoVVL_Ele23_CaloIdL_TrackIdL_IsoVL
	HLT_Mu30_Ele30_CaloIdL_GsfTrkIdVL
	HLT_Mu33_Ele33_CaloIdL_GsfTrkIdVL
	HLT_DiMu9_Ele9_CaloIdL_TrackIdL
	HLT_Mu8_DiEle12_CaloIdL_TrackIdL

Table A.2: Triggers used to record events during data taking in 2017.

Dataset	Trigger Path
SingleMuon	HLT_IsoMu24_eta2p1
	HLT_IsoMu27
	HLT_Mu50
	HLT_OldMu100
	HLT_TkMu100
SingleElectron	HLT_Ele32_WPTight_Gsf_L1DoubleEG
	HLT_Ele35_WPTight_Gsf
	HLT_Ele115_CaloIdVT_GsfTrkIdT
DoubleMuon	HLT_Mu17_TrkIsoVVL_Mu8_TrkIsoVVL
	HLT_Mu17_TrkIsoVVL_Mu8_TrkIsoVVL_DZ
	HLT_Mu17_TrkIsoVVL_Mu8_TrkIsoVVL_DZ_Mass8
	HLT_Mu17_TrkIsoVVL_Mu8_TrkIsoVVL_DZ_Mass3p8
	HLT_Mu19_TrkIsoVVL_Mu9_TrkIsoVVL_DZ_Mass3p8
	HLT_Mu37_TkMu27
	HLT_TripleMu_12_10_5
	HLT_TripleMu_10_5_5_DZ
	HLT_TripleMu_5_3_3_Mass3p8to60_DZ
DoubleEG	HLT_Ele23_Ele12_CaloIdL_TrackIdL_IsoVL
	HLT_Ele16_Ele12_Ele8_CaloIdL_TrackIdL
	HLT_DoubleEle25_CaloIdL_MW
	HLT_DoubleEle33_CaloIdL_MW
	HLT_DiEle27_WPTightCaloOnly_L1DoubleEG
MuonEG	HLT_Mu23_TrkIsoVVL_Ele12_CaloIdL_TrackIdL_IsoVL
	HLT_Mu23_TrkIsoVVL_Ele12_CaloIdL_TrackIdL_IsoVL_DZ
	HLT_Mu8_TrkIsoVVL_Ele23_CaloIdL_TrackIdL_IsoVL_DZ
	HLT_Mu12_TrkIsoVVL_Ele23_CaloIdL_TrackIdL_IsoVL_DZ
	HLT_Mu27_Ele37_CaloIdL_MV
	HLT_Mu37_Ele27_CaloIdL_MV
	HLT_DiMu9_Ele9_CaloIdL_TrackIdL
	HLT_DiMu9_Ele9_CaloIdL_TrackIdL_DZ
	HLT_Mu8_DiEle12_CaloIdL_TrackIdL

Table A.3: Triggers used to record events during data taking in 2018.

Dataset	Trigger Path
SingleMuon	HLT_IsoMu24
	HLT_IsoMu27
	HLT_Mu50
	HLT_OldMu100
	HLT_TkMu100
EGamma	HLT_Ele32_WPTight_Gsf
	HLT_Ele115_CaloIdVT_GsfTrkIdT
	HLT_Ele23_Ele12_CaloIdL_TrackIdL_IsoVL
	HLT_Ele16_Ele12_Ele8_CaloIdL_TrackIdL
	HLT_DoubleEle25_CaloIdL_MW
	HLT_DiEle27_WPTightCaloOnly_L1DoubleEG
DoubleMuon	HLT_Mu17_TrkIsoVVL_Mu8_TrkIsoVVL_DZ_Mass3p8
	HLT_Mu37_TkMu27
	HLT_TripleMu_12_10_5
	HLT_TripleMu_10_5_5_DZ
	HLT_TripleMu_5_3_3_Mass3p8to60_DZ
MuonEG	HLT_Mu23_TrkIsoVVL_Ele12_CaloIdL_TrackIdL_IsoVL
	HLT_Mu23_TrkIsoVVL_Ele12_CaloIdL_TrackIdL_IsoVL_DZ
	HLT_Mu8_TrkIsoVVL_Ele23_CaloIdL_TrackIdL_IsoVL_DZ
	HLT_Mu12_TrkIsoVVL_Ele23_CaloIdL_TrackIdL_IsoVL_DZ
	HLT_Mu27_Ele37_CaloIdL_MV
	HLT_Mu37_Ele27_CaloIdL_MV
	HLT_DiMu9_Ele9_CaloIdL_TrackIdL_DZ
	HLT_Mu8_DiEle12_CaloIdL_TrackIdL

Appendix B

Signal Region Distributions with MC Simulation

Distributions of various variables in SR, which are used in the BDT training. More details on these input features are described in Section 16.2. The data are shown as filled points and the SM background predictions as histograms. The VV(V) background includes ZZ and triboson production, while the $t\bar{t}$ + X(X) component includes $t\bar{t}W$, $t\bar{t}Z$, $t\bar{t}H$, tZq, and smaller backgrounds containing one or two top quarks plus a boson or quark. All backgrounds are estimated using MC simulation. The hatched bands indicate statistical and systematic uncertainties for the SM background predictions. The normalisation of the signal processes is chosen arbitrarily for improved visualisation.

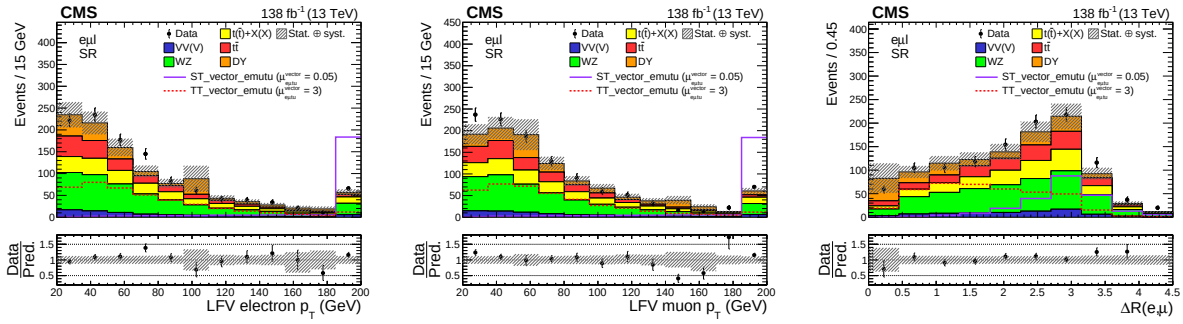

Figure B.1: Distributions of LFV electron p_T (left), LFV muon p_T (middle), and the opening angle between LFV electron and LFV muon (right).

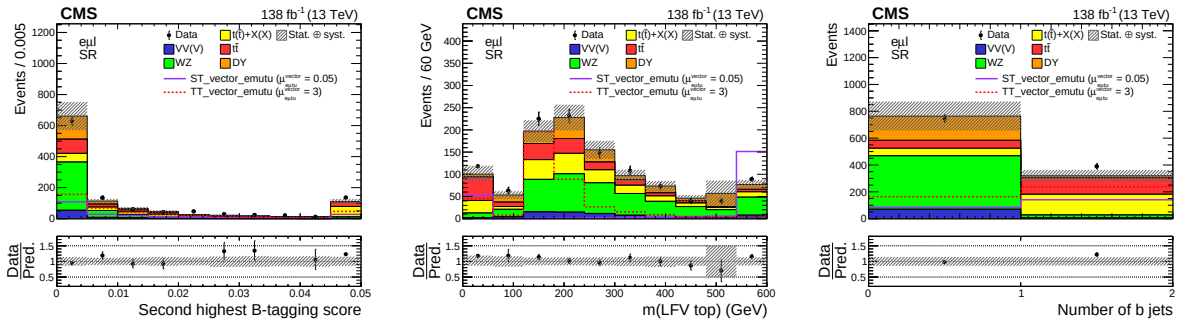

Figure B.2: Distributions of the second highest DeepJet score (left), LFV top mass (middle), b jet multiplicity (right).

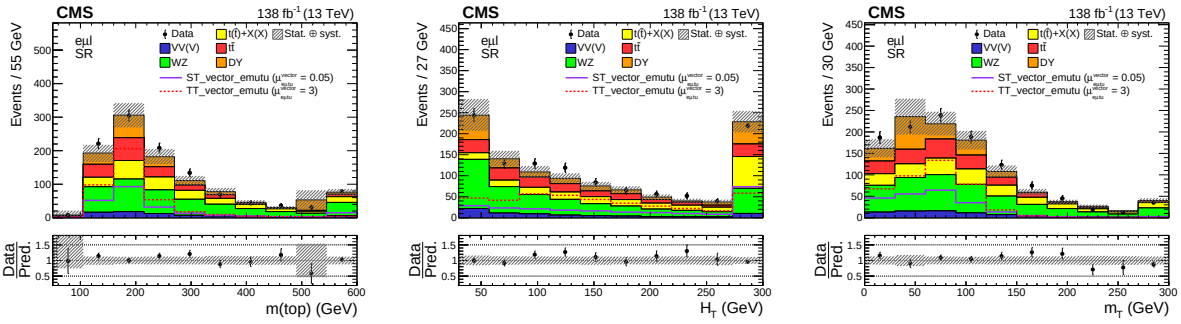

Figure B.3: Distributions of SM top quark mass (left), scalar sum of p_T of all jets (middle), and transverse mass of the W boson (right).

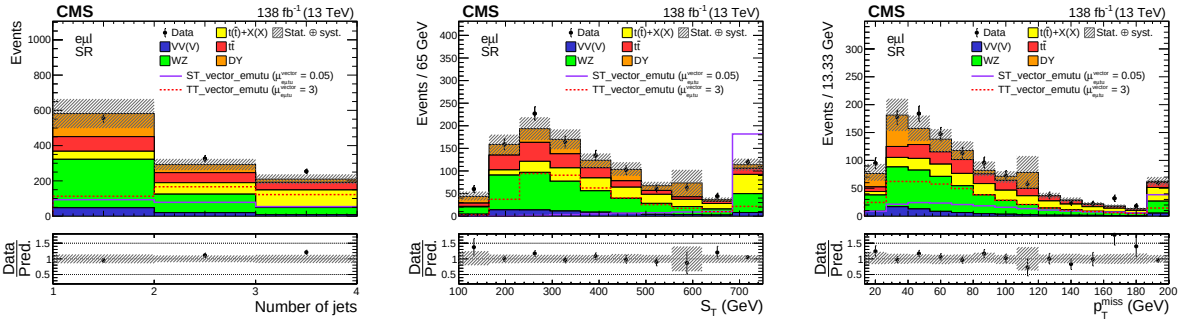

Figure B.4: Distributions of jet multiplicity (left), scalar sum of p_T of all jets and leptons (middle), and MET (right).

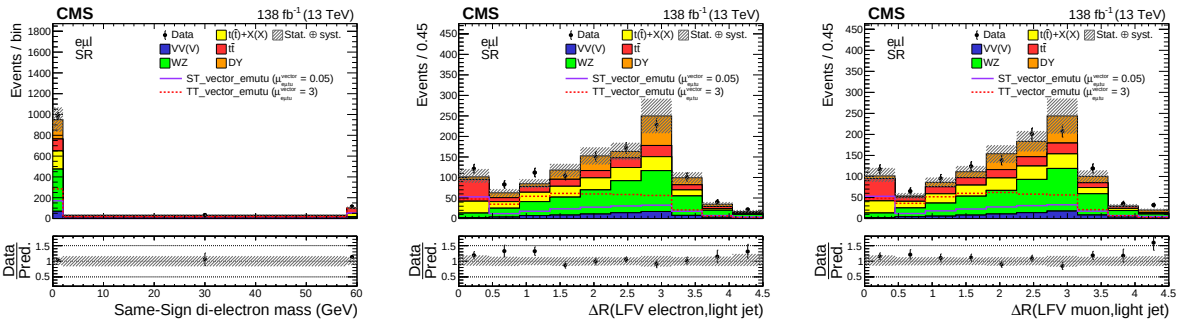

Figure B.5: Distributions of the SS di-electron mass (left), the opening angle between LFV electron and a light flavor jet (middle), and the opening angle between LFV muon and a light flavor jet (right).

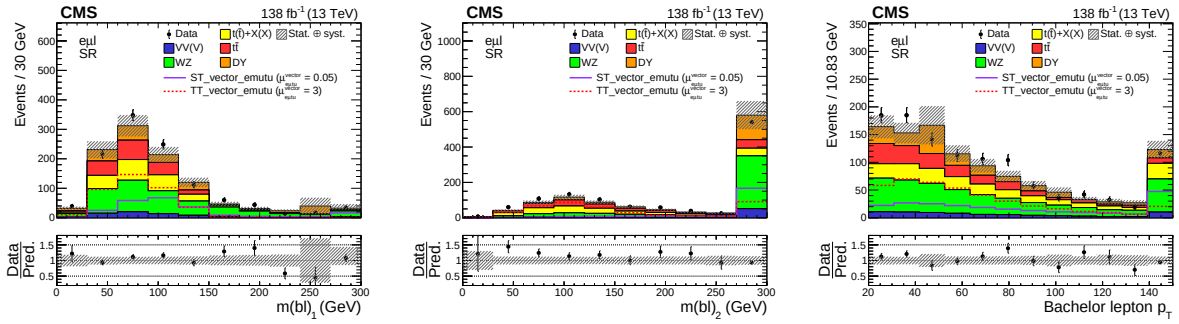

Figure B.6: Distributions of the mass of the first $m_{b\ell}$ system (left), the mass of the second $m_{b\ell}$ system (middle), and standalone lepton p_T (right).

Appendix C

Nuisance Parameter Impact

The observed and expected (μ_{exp} =0) impacts of the nuisance parameters on the profile likelihood fit are shown in Figure C.1-C.2. They were computed using the following commands and plotted below for full run 2.

The expected (μ_{exp} =1) impacts of the nuisance parameters on the profile likelihood fit are shown in Figure C.3.

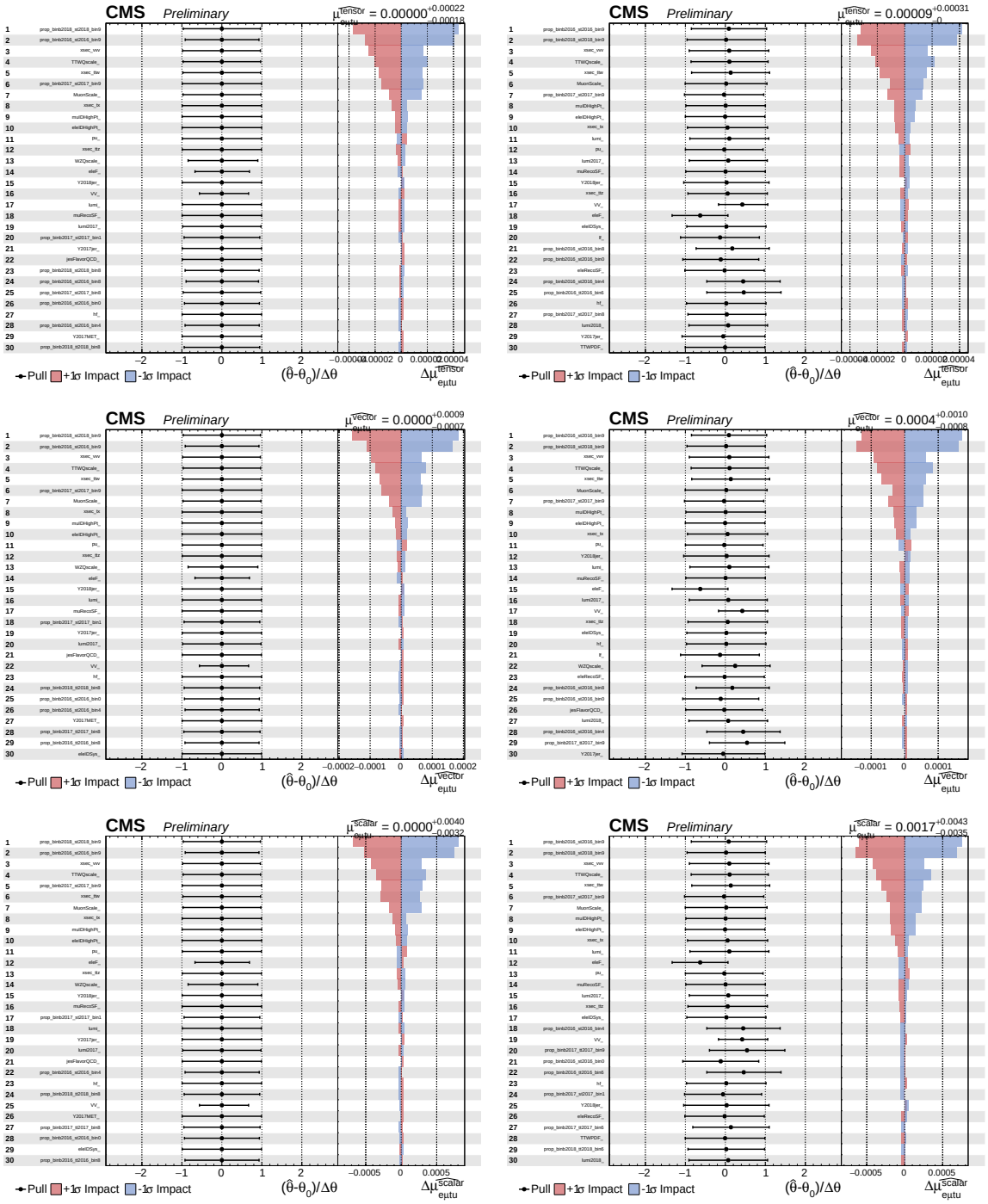

Figure C.1: Impacts of nuissance parameters for run II limit setting. From top to bottom: eμut-tensor, eμut-vector, eμut-scalar. From left to right: expected impact (expected signal strength at 0), observed impact.

Figure C.2: Impacts of nuissance parameters for run II limit setting. From top to bottom: eμct-tensor, eμct-vector, eμct-scalar. From left to right: expected impact (expected signal strength at 0), observed impact.

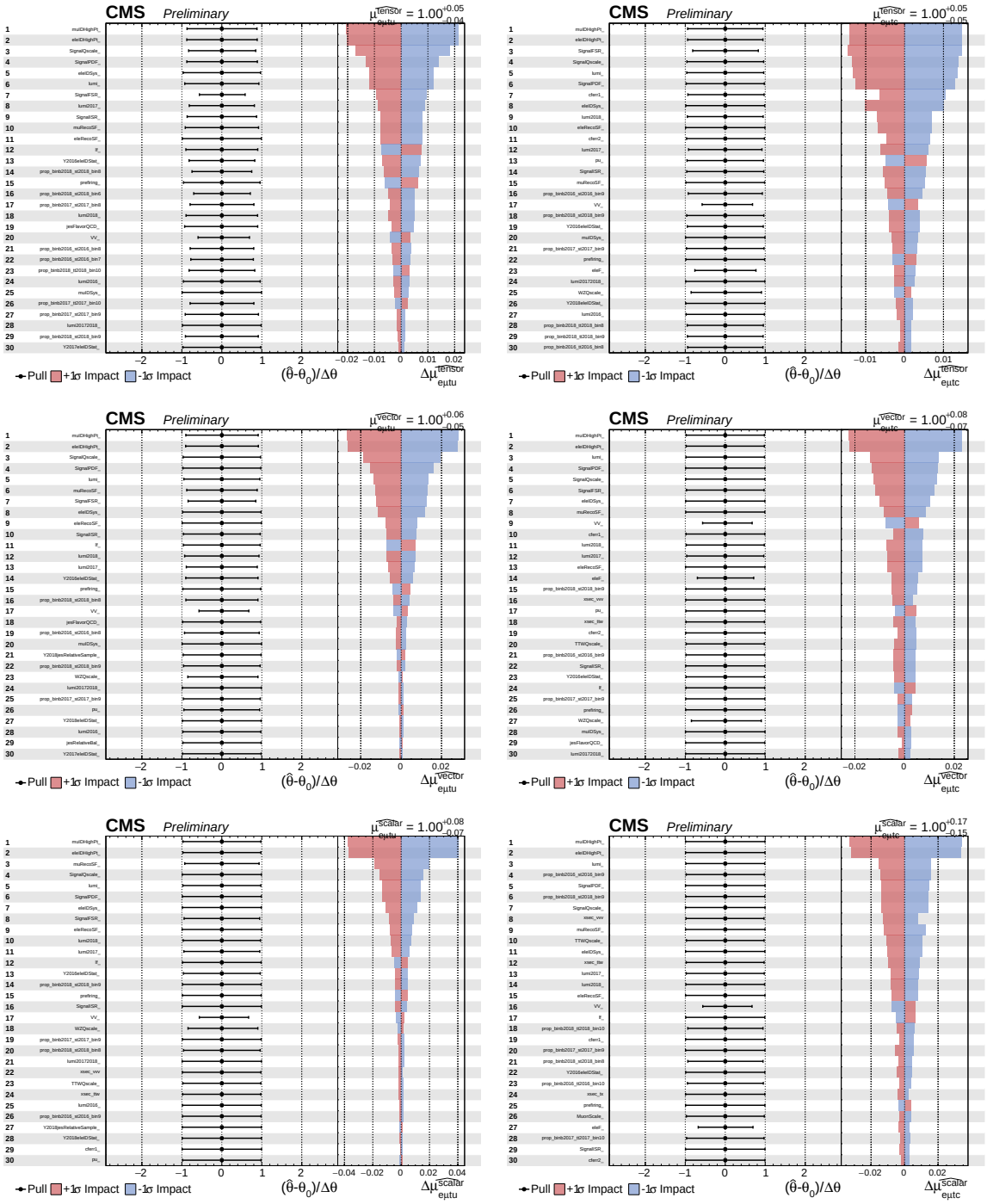

Figure C.3: Expected impact with an expected signal strength at 1. From top to bottom: tensor, vector, scalar. From left to right: eμut, eμct.

References

[1] David Galbraith and Carsten Burgard. *Example: Standard model of physics*. (2016). URL: https://texample.net/tikz/examples/model-physics/. (Cited on pages ix and 4.)

[2] Carl D. Anderson. *The positive electron*. Phys. Rev. **43**, 491–494 (1933). URL: https://link.aps.org/doi/10.1103/PhysRev.43.491, doi:10.1103/PhysRev.43.491. (Cited on pages ix, 6, and 7.)

[3] **Mark I** Colloboration. *Discovery of a Narrow Resonance in e^+e^- Annihilation*. Phys. Rev. Lett. **33**, 1406–1408 (1974). doi:10.1103/PhysRevLett.33.1406. (Cited on pages ix, 7, and 8.)

[4] **ATLAS** Colloboration. *Observation of a new particle in the search for the Standard Model Higgs boson with the ATLAS detector at the LHC*. Phys. Lett. B **716**, 1–29 (2012). arXiv:1207.7214, doi:10.1016/j.physletb.2012.08.020. (Cited on pages ix, 10, and 44.)

[5] **CMS** Colloboration. *Observation of a New Boson at a Mass of 125 GeV with the CMS Experiment at the LHC*. Phys. Lett. B **716**, 30–61 (2012). arXiv:1207.7235, doi:10.1016/j.physletb.2012.08.021. (Cited on pages ix, 10, and 44.)

[6] Lei Wang, Jin Min Yang, Yang Zhang, Pengxuan Zhu, and Rui Zhu. *A concise review on some higgs-related new physics models in light of current experiments*. Universe **9(4)** (2023). URL: https://www.mdpi.com/2218-1997/9/4/178. (Cited on pages ix and 15.)

[7] **CMS** Colloboration. *Running of alpha*. (2023). URL: https://twiki.cern.ch/twiki/pub/CMSPublic/PhysicsResultsCombined/alpha_s-running.pdf. (Cited on pages ix and 23.)

[8] Johan Messchendorp. *Physics with Charmonium – A few recent highlights of BESIII*. PoS **Bormio2013**, 043 (2013). arXiv:1306.6611, doi:10.22323/1.184.0043. (Cited on pages x and 24.)

[9] Joey Huston. *Introduction to QCD from an LHC perspective*. (2018). URL: https://indico.cern.ch/event/680421/contributions/3096162/. (Cited on pages x and 25.)

[10] **NNPDF** Collaboration. *Parton distributions from high-precision collider data*. Eur. Phys. J. C **77(10)**, 663 (2017). arXiv:1706.00428, doi:10.1140/epjc/s10052-017-5199-5. (Cited on pages x, 25, 26, 84, and 116.)

[11] **Super-Kamiokande** Colloboration. *Evidence for oscillation of atmospheric neutrinos*. Phys. Rev. Lett. **81**, 1562–1567 (1998). arXiv:hep-ex/9807003, doi:10.1103/PhysRevLett.81.1562. (Cited on pages x, 2, 29, and 30.)

[12] **HFLAV** Group. *Preliminary average of $\mathcal{R}(D)$ and $\mathcal{R}(D^*)$ for Summer 2023*. (2023). URL: https://hflav-eos.web.cern.ch/hflav-eos/semi/summer23/html/RDsDsstar/RDRDs.html. (Cited on pages x, 31, and 32.)

[13] Ewa Lopienska. *The CERN accelerator complex, layout in 2022*. **CERN-GRAPHICS-2022-001** (2022). URL: https://cds.cern.ch/record/2800984. (Cited on pages xi and 41.)

[14] **CMS** Collaboration. *CMS Luminosity Public Results*. (2023). URL: https://twiki.cern.ch/twiki/bin/view/CMSPublic/LumiPublicResults. (Cited on pages xi, xii, 42, and 60.)

[15] *Longer term LHC schedule*. (2022). URL: https://lhc-commissioning.web.cern.ch/schedule/LHC-long-term.htm. (Cited on pages xi, xii, 43, and 65.)

[16] Tai Sakuma and Thomas McCauley. *Detector and Event Visualization with SketchUp at the CMS Experiment*. J. Phys. Conf. Ser. **513**, 022032 (2014). arXiv:1311.4942, doi:10.1088/1742-6596/513/2/022032. (Cited on pages xi and 44.)

[17] Izaak Neutelings. *CMS coordinate system*. (2022). URL: https://tikz.net/axis3d_cms/. (Cited on pages xi and 45.)

[18] Izaak Neutelings. *Pseudorapidity*. (2022). URL: https://tikz.net/axis2d_pseudorapidity/. (Cited on pages xi and 46.)

[19] **CMS** Collaboration. *Alignment of the CMS Silicon Tracker during Commissioning with Cosmic Rays*. JINST **5**, T03009 (2010). arXiv:0910.2505, doi:10.1088/1748-0221/5/03/T03009. (Cited on pages xi and 47.)

[20] **CMS** Collaboration. *The CMS Phase-1 Pixel Detector Upgrade*. JINST **16(02)**, P02027 (2021). arXiv:2012.14304, doi:10.1088/1748-0221/16/02/P02027. (Cited on pages xi, 46, and 47.)

[21] A. Benaglia. *The CMS ECAL performance with examples*. JINST **9**, C02008 (2014). doi:10.1088/1748-0221/9/02/C02008. (Cited on pages xi and 48.)

[22] **CMS** Collaboration. *Performance of CMS Hadron Calorimeter Timing and Synchronization using Test Beam, Cosmic Ray, and LHC Beam Data*. JINST **5**, T03013 (2010). arXiv:0911.4877, doi:10.1088/1748-0221/5/03/T03013. (Cited on pages xi and 49.)

[23] **CMS** Collaboration. *Precise Mapping of the Magnetic Field in the CMS Barrel Yoke using Cosmic Rays*. JINST **5**, T03021 (2010). arXiv:0910.5530, doi:10.1088/1748-0221/5/03/T03021. (Cited on pages xi and 50.)

[24] **CMS** Collaboration. *CMS Technical Design Report for the Muon Endcap GEM Upgrade*. **CMS-TDR-013** (2015). URL: https://cds.cern.ch/record/2021453. (Cited on pages xi, 50, and 51.)

[25] **CMS** Colloboration. *Performance of the CMS Level-1 trigger in proton-proton collisions at $\sqrt{s} = 13$ TeV*. JINST **15(10)**, P10017 (2020). arXiv:2006.10165, doi:10.1088/1748-0221/15/10/P10017. (Cited on pages xi, 52, and 123.)

[26] David Barney. *CMS Slice*. **CMS-OUTREACH-2018-017** (2018). URL: https://cds.cern.ch/record/2628641. (Cited on pages xi and 53.)

[27] Piergiulio Lenzi, Chiara Genta, and Boris Mangano. *Track reconstruction of real cosmic muon events with CMS tracker detector*. J. Phys. Conf. Ser. **119**, 032030 (2008). doi:10.1088/1742-6596/119/3/032030. (Cited on pages xii and 54.)

[28] **CMS** and TOTal Elastic and diffractive cross section Measurement (TOTEM) Collaborations. *CMS-TOTEM Precision Proton Spectrometer*. **CMS-TDR-013** (2014). URL: https://cds.cern.ch/record/1753795/. (Cited on pages xii and 62.)

[29] **CMS** Collaboration. *The CMS Experiment at the CERN LHC*. JINST **3**, S08004 (2008). doi:10.1088/1748-0221/3/08/S08004. (Cited on pages xii, 40, 44, and 62.)

[30] **CMS** Collaboration. *CMS Software Components (CMSSW)*. URL: https://github.com/cms-sw/cmssw. (Cited on pages xii and 68.)

[31] **CMS** Collaboration. *The Phase-2 Upgrade of the CMS Tracker*. **CMS-TDR-014** (2017). doi:10.17181/CERN.QZ28.FLHW. (Cited on pages xiii, 66, 68, and 69.)

[32] **ATLAS** Colloboration. *Search for charged lepton-flavour violation in top-quark decays at the LHC with the ATLAS detector*. **ATLAS-CONF-2018-044** (2018). URL: https://cds.cern.ch/record/2638305. (Cited on pages xiii, 76, 78, 79, and 131.)

[33] **ATLAS** Colloboration. *Search for charged-lepton-flavour violating $\mu\tau qt$ interactions in top-quark production and decay with the ATLAS detector at the LHC*. **ATLAS-CONF-2023-001** (2023). URL: https://cds.cern.ch/record/2845451. (Cited on pages xiii, 77, and 131.)

[34] **CMS** Collaboration. *Search for charged-lepton flavor violation in top quark production and decay in pp collisions at $\sqrt{s} = 13$ TeV*. JHEP **06**, 082 (2022). arXiv:2201.07859, doi:10.1007/JHEP06(2022)082. (Cited on pages xiv, 78, 79, 82, and 131.)

[35] I. Doršner, S. Fajfer, A. Greljo, J. F. Kamenik, and N. Košnik. *Physics of leptoquarks in precision experiments and at particle colliders*. Phys. Rept. **641**, 1–68 (2016). arXiv:1603.04993, doi:10.1016/j.physrep.2016.06.001. (Cited on pages xxi, 31, and 33.)

[36] **SNO** Colloboration. *Direct evidence for neutrino flavor transformation from neutral current interactions in the Sudbury Neutrino Observatory*. Phys. Rev. Lett. **89**, 011301 (2002). arXiv:nucl-ex/0204008, doi:10.1103/PhysRevLett.89.011301. (Cited on pages 2 and 29.)

[37] **MEG II** Collaboration. *The design of the MEG II experiment*. Eur. Phys. J. C **78(5)**, 380 (2018). arXiv:1801.04688, doi:10.1140/epjc/s10052-018-5845-6. (Cited on page 2.)

[38] **Mu3e** Collaboration. *Technical design of the phase I Mu3e experiment*. Nucl. Instrum. Meth. A **1014**, 165679 (2021). arXiv:2009.11690, doi:10.1016/j.nima.2021.165679. (Cited on page 2.)

[39] Lyndon Evans and Philip Bryant. *LHC Machine*. JINST **3**, S08001 (2008). doi:10.1088/1748-0221/3/08/S08001. (Cited on pages 2 and 40.)

[40] Sacha Davidson, Sylvain Lacroix, and Patrice Verdier. *LHC sensitivity to lepton flavour violating Z boson decays*. JHEP **09**, 092 (2012). arXiv:1207.4894, doi:10.1007/JHEP09(2012)092. (Cited on page 2.)

[41] Anthony Zee. *Group theory in a nutshell for physicists*. (2016). (Cited on page 5.)

[42] Paul A. M. Dirac. *The quantum theory of the electron*. Proc. Roy. Soc. Lond. A **117**, 610–624 (1928). doi:10.1098/rspa.1928.0023. (Cited on page 6.)

[43] **LHCb** Colloboration. *Observation of $J/\psi p$ Resonances Consistent with Pentaquark States in $\Lambda_b^0 \to J/\psi K^- p$ Decays*. Phys. Rev. Lett. **115**, 072001 (2015). arXiv:1507.03414, doi:10.1103/PhysRevLett.115.072001. (Cited on page 7.)

[44] **E598** Colloboration. *Experimental Observation of a Heavy Particle J*. Phys. Rev. Lett. **33**, 1404–1406 (1974). doi:10.1103/PhysRevLett.33.1404. (Cited on page 7.)

[45] **CDF** Colloboration. *Observation of top quark production in $\bar{p}p$ collisions*. Phys. Rev. Lett. **74**, 2626–2631 (1995). arXiv:hep-ex/9503002, doi:10.1103/PhysRevLett.74.2626. (Cited on page 7.)

[46] **D0** Colloboration. *Observation of the top quark*. Phys. Rev. Lett. **74**, 2632–2637 (1995). arXiv:hep-ex/9503003, doi:10.1103/PhysRevLett.74.2632. (Cited on page 7.)

[47] **Mark I** Colloboration. *Evidence for Anomalous Lepton Production in e+ - e- Annihilation*. Phys. Rev. Lett. **35**, 1489–1492 (1975). doi:10.1103/PhysRevLett.35.1489. (Cited on page 8.)

[48] **DONUT** Colloboration. *Observation of tau neutrino interactions*. Phys. Lett. B **504**, 218–224 (2001). arXiv:hep-ex/0012035, doi:10.1016/S0370-2693(01)00307-0. (Cited on page 8.)

[49] Arthur H. Compton. *A quantum theory of the scattering of x-rays by light elements*. Phys. Rev. **21**, 483–502 (1923). URL: https://link.aps.org/doi/10.1103/PhysRev.21.483, doi:10.1103/PhysRev.21.483. (Cited on page 9.)

[50] S. Tomonaga. *On a relativistically invariant formulation of the quantum theory of wave fields*. Prog. Theor. Phys. **1**, 27–42 (1946). doi:10.1143/PTP.1.27. (Cited on page 9.)

[51] Julian S. Schwinger. *On Quantum electrodynamics and the magnetic moment of the electron*. Phys. Rev. **73**, 416–417 (1948). doi:10.1103/PhysRev.73.416. (Cited on page 9.)

[52] R. P. Feynman. *Mathematical formulation of the quantum theory of electromagnetic interaction*. Phys. Rev. **80**, 440–457 (1950). doi:10.1103/PhysRev.80.440. (Cited on page 9.)

[53] F. J. Dyson. *The Radiation theories of Tomonaga, Schwinger, and Feynman*. Phys. Rev. **75**, 486–502 (1949). doi:10.1103/PhysRev.75.486. (Cited on page 9.)

[54] **TASSO** Colloboration. *Evidence for Planar Events in e+ e- Annihilation at High-Energies*. Phys. Lett. B **86**, 243–249 (1979). doi:10.1016/0370-2693(79)90830-X. (Cited on page 9.)

[55] **UA1** Colloboration. *Experimental Observation of Isolated Large Transverse Energy Electrons with Associated Missing Energy at* $\sqrt{s} = 540$ *GeV*. Phys. Lett. B **122**, 103–116 (1983). doi:10.1016/0370-2693(83)91177-2. (Cited on page 10.)

[56] **UA2** Colloboration. *Observation of Single Isolated Electrons of High Transverse Momentum in Events with Missing Transverse Energy at the CERN anti-p p Collider*. Phys. Lett. B **122**, 476–485 (1983). doi:10.1016/0370-2693(83)91605-2. (Cited on page 10.)

[57] **UA1** Colloboration. *Experimental Observation of Lepton Pairs of Invariant Mass Around 95-GeV/c**2 at the CERN SPS Collider*. Phys. Lett. B **126**, 398–410 (1983). doi:10.1016/0370-2693(83)90188-0. (Cited on page 10.)

[58] **UA2** Colloboration. *Evidence for* $Z^0 \to e^+e^-$ *at the CERN* $\bar{p}p$ *Collider*. Phys. Lett. B **129**, 130–140 (1983). doi:10.1016/0370-2693(83)90744-X. (Cited on page 10.)

[59] F. Englert and R. Brout. *Broken symmetry and the mass of gauge vector mesons*. Phys. Rev. Lett. **13**, 321–323 (1964). URL: https://link.aps.org/doi/10.1103/PhysRevLett.13.321, doi:10.1103/PhysRevLett.13.321. (Cited on pages 10 and 15.)

[60] Peter W. Higgs. *Broken symmetries and the masses of gauge bosons*. Phys. Rev. Lett. **13**, 508–509 (1964). URL: https://link.aps.org/doi/10.1103/PhysRevLett.13.508, doi:10.1103/PhysRevLett.13.508. (Cited on pages 10 and 15.)

[61] G. S. Guralnik, C. R. Hagen, and T. W. B. Kibble. *Global conservation laws and massless particles*. Phys. Rev. Lett. **13**, 585–587 (1964). URL: https://link.aps.org/doi/10.1103/PhysRevLett.13.585, doi:10.1103/PhysRevLett.13.585. (Cited on pages 10 and 15.)

[62] E. Noether. *Invariante variationsprobleme*. Nachrichten von der Gesellschaft der Wissenschaften zu Göttingen, Mathematisch-Physikalische Klasse **1918**, 235–257 (1918). URL: http://eudml.org/doc/59024. (Cited on page 12.)

[63] Mattew D. Schwartz. *Quantum Field Theory and the Standard Model*. (2014). (Cited on page 12.)

[64] Chen-Ning Yang and Robert L. Mills. *Conservation of Isotopic Spin and Isotopic Gauge Invariance*. Phys. Rev. **96**, 191–195 (1954). doi:10.1103/PhysRev.96.191. (Cited on page 12.)

[65] T. D. Lee and Chen-Ning Yang. *Question of Parity Conservation in Weak Interactions*. Phys. Rev. **104**, 254–258 (1956). doi:10.1103/PhysRev.104.254. (Cited on page 12.)

[66] C. S. Wu, E. Ambler, R. W. Hayward, D. D. Hoppes, and R. P. Hudson. *Experimental Test of Parity Conservation in β Decay*. Phys. Rev. **105**, 1413–1414 (1957). doi:10.1103/PhysRev.105.1413. (Cited on page 12.)

[67] S. L. Glashow. *Partial Symmetries of Weak Interactions*. Nucl. Phys. **22**, 579–588 (1961). doi:10.1016/0029-5582(61)90469-2. (Cited on page 13.)

[68] T. Nakano and K. Nishijima. *Charge Independence for V-particles*. Prog. Theor. Phys. **10**, 581–582 (1953). doi:10.1143/PTP.10.581. (Cited on page 14.)

[69] M. Gell-Mann. *The interpretation of the new particles as displaced charge multiplets*. Nuovo Cim. **4(S2)**, 848–866 (1956). doi:10.1007/BF02748000. (Cited on page 14.)

[70] Philip W. Anderson. *Plasmons, Gauge Invariance, and Mass*. Phys. Rev. **130**, 439–442 (1963). doi:10.1103/PhysRev.130.439. (Cited on page 14.)

[71] Abdus Salam and John Clive Ward. *Electromagnetic and weak interactions*. Phys. Lett. **13**, 168–171 (1964). doi:10.1016/0031-9163(64)90711-5. (Cited on page 15.)

[72] Steven Weinberg. *A Model of Leptons*. Phys. Rev. Lett. **19**, 1264–1266 (1967). doi:10.1103/PhysRevLett.19.1264. (Cited on pages 15, 17, and 29.)

[73] N. Cabibbo, L. Maiani, G. Parisi, and R. Petronzio. *Bounds on the Fermions and Higgs Boson Masses in Grand Unified Theories*. Nucl. Phys. B **158**, 295–305 (1979). doi:10.1016/0550-3213(79)90167-6. (Cited on page 15.)

[74] R. L. Workman et al. *Review of Particle Physics*. PTEP **2022**, 083C01 (2022). doi:10.1093/ptep/ptac097. (Cited on pages 16 and 28.)

[75] Jeffrey Goldstone, Abdus Salam, and Steven Weinberg. *Broken Symmetries*. Phys. Rev. **127**, 965–970 (1962). doi:10.1103/PhysRev.127.965. (Cited on page 16.)

[76] Steven Weinberg. *Physical Processes in a Convergent Theory of the Weak and Electromagnetic Interactions*. Phys. Rev. Lett. **27**, 1688–1691 (1971). doi:10.1103/PhysRevLett.27.1688. (Cited on page 16.)

[77] **CDF** Colloboration. *High-precision measurement of the W boson mass with the CDF II detector*. Science **376(6589)**, 170–176 (2022). doi:10.1126/science.abk1781. (Cited on page 16.)

[78] Nicola Cabibbo. *Unitary Symmetry and Leptonic Decays*. Phys. Rev. Lett. **10**, 531–533 (1963). doi:10.1103/PhysRevLett.10.531. (Cited on page 18.)

[79] Makoto Kobayashi and Toshihide Maskawa. *CP Violation in the Renormalizable Theory of Weak Interaction*. Prog. Theor. Phys. **49**, 652–657 (1973). doi:10.1143/PTP.49.652. (Cited on page 18.)

[80] B. Pontecorvo. *Mesonium and anti-mesonium*. Sov. Phys. JETP **6**, 429 (1957). (Cited on page 18.)

[81] Ziro Maki, Masami Nakagawa, and Shoichi Sakata. *Remarks on the unified model of elementary particles*. Prog. Theor. Phys. **28**, 870–880 (1962). doi:10.1143/PTP.28.870. (Cited on page 18.)

[82] G. Zweig. *An SU(3) model for strong interaction symmetry and its breaking. Version 1* **CERN-TH-401** (1964). (Cited on page 20.)

[83] Murray Gell-Mann. *A Schematic Model of Baryons and Mesons*. Phys. Lett. **8**, 214–215 (1964). doi:10.1016/S0031-9163(64)92001-3. (Cited on page 20.)

[84] H. Fritzsch, Murray Gell-Mann, and H. Leutwyler. *Advantages of the Color Octet Gluon Picture*. Phys. Lett. B **47**, 365–368 (1973). doi:10.1016/0370-2693(73)90625-4. (Cited on page 20.)

[85] R. P. Feynman. *The behavior of hadron collisions at extreme energies*. Conf. Proc. C **690905**, 237–258 (1969). (Cited on page 21.)

[86] Louis Victor Pierre Raymond de Broglie. *Recherches sur la théorie des quanta*. Annals Phys. **2**, 22–128 (1925). (Cited on page 21.)

[87] J. D. Bjorken and Emmanuel A. Paschos. *Inelastic Electron Proton and gamma Proton Scattering, and the Structure of the Nucleon*. Phys. Rev. **185**, 1975–1982 (1969). doi:10.1103/PhysRev.185.1975. (Cited on page 22.)

[88] Gerard 't Hooft. *Renormalization of Massless Yang-Mills Fields*. Nucl. Phys. B **33**, 173–199 (1971). doi:10.1016/0550-3213(71)90395-6. (Cited on page 22.)

[89] David J. Gross and Frank Wilczek. *Ultraviolet Behavior of Nonabelian Gauge Theories*. Phys. Rev. Lett. **30**, 1343–1346 (1973). doi:10.1103/PhysRevLett.30.1343. (Cited on page 22.)

[90] H. David Politzer. *Reliable Perturbative Results for Strong Interactions?* Phys. Rev. Lett. **30**, 1346–1349 (1973). doi:10.1103/PhysRevLett.30.1346. (Cited on page 22.)

[91] Alexandre Deur, Stanley J. Brodsky, and Guy F. de Teramond. *The QCD Running Coupling*. Nucl. Phys. **90**, 1 (2016). arXiv:1604.08082, doi:10.1016/j.ppnp.2016.04.003. (Cited on page 23.)

[92] John C. Collins, Davison E. Soper, and George F. Sterman. *Factorization of Hard Processes in QCD*. Adv. Ser. Direct. High Energy Phys. **5**, 1–91 (1989). arXiv:hep-ph/0409313, doi:10.1142/9789814503266_0001. (Cited on page 24.)

[93] **NNPDF** Collaboration. *Parton distributions for the LHC Run II*. JHEP **04**, 040 (2015). arXiv:1410.8849, doi:10.1007/JHEP04(2015)040. (Cited on pages 25, 84, and 116.)

[94] V. N. Gribov and L. N. Lipatov. *Deep inelastic electron scattering in perturbation theory*. Phys. Lett. B **37**, 78–80 (1971). doi:10.1016/0370-2693(71)90576-4. (Cited on page 25.)

[95] Guido Altarelli and G. Parisi. *Asymptotic Freedom in Parton Language*. Nucl. Phys. B **126**, 298–318 (1977). doi:10.1016/0550-3213(77)90384-4. (Cited on page 25.)

[96] Yuri L. Dokshitzer. *Calculation of the Structure Functions for Deep Inelastic Scattering and e+ e- Annihilation by Perturbation Theory in Quantum Chromodynamics.* Sov. Phys. JETP **46**, 641–653 (1977). (Cited on page 25.)

[97] R. D. Field and R. P. Feynman. *Quark Elastic Scattering as a Source of High Transverse Momentum Mesons*. Phys. Rev. D **15**, 2590–2616 (1977). doi:10.1103/PhysRevD.15.2590. (Cited on page 26.)

[98] J. Alwall, R. Frederix, S. Frixione, V. Hirschi, F. Maltoni, O. Mattelaer, H. S. Shao, T. Stelzer, P. Torrielli, and M. Zaro. *The automated computation of tree-level and next-to-leading order differential cross sections, and their matching to parton shower simulations*. JHEP **07**, 079 (2014). arXiv:1405.0301, doi:10.1007/JHEP07(2014)079. (Cited on pages 27 and 82.)

[99] Stefano Frixione, Paolo Nason, and Carlo Oleari. *Matching NLO QCD computations with Parton Shower simulations: the POWHEG method*. JHEP **11**, 070 (2007). arXiv:0709.2092, doi:10.1088/1126-6708/2007/11/070. (Cited on pages 27 and 84.)

[100] Andy Buckley et al. *General-purpose event generators for LHC physics*. Phys. Rept. **504**, 145–233 (2011). arXiv:1101.2599, doi:10.1016/j.physrep.2011.03.005. (Cited on page 27.)

[101] Torbjörn Sjöstrand, Stefan Ask, Jesper R. Christiansen, Richard Corke, Nishita Desai, Philip Ilten, Stephen Mrenna, Stefan Prestel, Christine O. Rasmussen, and Peter Z. Skands. *An introduction to PYTHIA 8.2*. Comput. Phys. Commun. **191**, 159–177 (2015). arXiv:1410.3012, doi:10.1016/j.cpc.2015.01.024. (Cited on pages 27 and 84.)

[102] Bo Andersson, G. Gustafson, G. Ingelman, and T. Sjostrand. *Parton Fragmentation and String Dynamics*. Phys. Rept. **97**, 31–145 (1983). doi:10.1016/0370-1573(83)90080-7. (Cited on page 28.)

[103] D. J. Lange. *The EvtGen particle decay simulation package*. Nucl. Instrum. Meth. A **462**, 152–155 (2001). doi:10.1016/S0168-9002(01)00089-4. (Cited on page 28.)

[104] Steven Weinberg. *Baryon and Lepton Nonconserving Processes*. Phys. Rev. Lett. **43**, 1566–1570 (1979). doi:10.1103/PhysRevLett.43.1566. (Cited on pages 29 and 37.)

[105] **LHCb** Collaboration. *Measurement of the ratios of branching fractions $\mathcal{R}(D^*)$ and $\mathcal{R}(D^0)$*. Phys. Rev. Lett. **131**, 111802 (2023). arXiv:2302.02886, doi:10.1103/PhysRevLett.131.111802. (Cited on page 30.)

[106] Sheldon L. Glashow, Diego Guadagnoli, and Kenneth Lane. *Lepton Flavor Violation in B Decays?* Phys. Rev. Lett. **114**, 091801 (2015). arXiv:1411.0565, doi:10.1103/PhysRevLett.114.091801. (Cited on page 31.)

[107] Jogesh C. Pati and Abdus Salam. *Unified Lepton-Hadron Symmetry and a Gauge Theory of the Basic Interactions*. Phys. Rev. D **8**, 1240–1251 (1973). doi:10.1103/PhysRevD.8.1240. (Cited on page 31.)

[108] Claudia Cornella, Darius A. Faroughy, Javier Fuentes-Martin, Gino Isidori, and Matthias Neubert. *Reading the footprints of the B-meson flavor anomalies*. JHEP **08**, 050 (2021). arXiv:2103.16558, doi:10.1007/JHEP08(2021)050. (Cited on page 33.)

[109] **ATLAS** Collaboration. *Search for pair production of third-generation leptoquarks decaying into a bottom quark and a τ-lepton with the ATLAS detector*. Eur. Phys. J. C **83(11)**, 1075 (2023). arXiv:2303.01294, doi:10.1140/epjc/s10052-023-12104-7. (Cited on page 33.)

[110] **ATLAS** Collaboration. *Search for leptoquarks decaying into the $b\tau$ final state in pp collisions at $\sqrt{s} = 13$ TeV with the ATLAS detector*. JHEP **10**, 001 (2023). arXiv:2305.15962, doi:10.1007/JHEP10(2023)001. (Cited on page 33.)

[111] **CMS** Collaboration. *Search for a singly produced third-generation scalar leptoquark decaying to a τ lepton and a bottom quark in proton-proton collisions at $\sqrt{s} = 13$ TeV*.

JHEP **07**, 115 (2018). arXiv:1806.03472, doi:10.1007/JHEP07(2018)115. (Cited on page 33.)

[112] Aram Hayrapetyan et al. *Search for a third-generation leptoquark coupled to a τ lepton and a b quark through single, pair, and nonresonant production in proton-proton collisions at $\sqrt{s}$ = 13 TeV.* (2023). arXiv:2308.07826. (Cited on page 33.)

[113] Tae Jeong Kim, Pyungwon Ko, Jinmian Li, Jiwon Park, and Peiwen Wu. *Correlation between $R_{D^{(*)}}$ and top quark FCNC decays in leptoquark models.* JHEP **07**, 025 (2019). arXiv:1812.08484, doi:10.1007/JHEP07(2019)025. (Cited on page 34.)

[114] Sacha Davidson, Michelangelo L. Mangano, Stephane Perries, and Viola Sordini. *Lepton Flavour Violating top decays at the LHC.* Eur. Phys. J. C **75(9)**, 450 (2015). arXiv:1507.07163, doi:10.1140/epjc/s10052-015-3649-5. (Cited on pages 34 and 77.)

[115] Enrico Fermi. *Tentativo di una teoria dell'emissione dei raggi beta.* Ric. Sci. **4**, 491–495 (1933). (Cited on page 35.)

[116] B. Grzadkowski, M. Iskrzynski, M. Misiak, and J. Rosiek. *Dimension-Six Terms in the Standard Model Lagrangian.* JHEP **10**, 085 (2010). arXiv:1008.4884, doi:10.1007/JHEP10(2010)085. (Cited on pages 38 and 80.)

[117] **ALICE** Collaboration. *The ALICE experiment at the CERN LHC.* JINST **3**, S08002 (2008). doi:10.1088/1748-0221/3/08/S08002. (Cited on page 40.)

[118] **ATLAS** Collaboration. *The ATLAS Experiment at the CERN Large Hadron Collider.* JINST **3**, S08003 (2008). doi:10.1088/1748-0221/3/08/S08003. (Cited on page 40.)

[119] **LHCb** Collaboration. *The LHCb Detector at the LHC.* JINST **3**, S08005 (2008). doi:10.1088/1748-0221/3/08/S08005. (Cited on page 40.)

[120] *LEP Design Report: Vol.2. The LEP Main Ring.* **CERN-LEP-84-01** (1984). URL: https://cds.cern.ch/record/102083. (Cited on page 40.)

[121] E. Boltezar, H. Haseroth, W. Pirkl, G. Plass, T. Sherwood, U. Tallgren, P. Tetu, D. Warner, and M. Weiss. *The New CERN 50-MeV LINAC.* 10th International Linear Accelerator Conference, pages S2–2 (1980). URL: https://accelconf.web.cern.ch/l79/papers/s2-2.pdf. (Cited on page 40.)

[122] J. Vollaire et al. *Linac4 design report.* **6/2020** (2020). doi:10.23731/CYRM-2020-006. (Cited on page 40.)

[123] K. H. Reich. *The CERN Proton Synchrotron Booster.* IEEE Trans. Nucl. Sci. **16**, 959–961 (1969). doi:10.1109/TNS.1969.4325414. (Cited on page 40.)

[124] **CERN** Proton Synchrotron Group. *Lectures on the Theory and Design of an Alternating-Gradient Proton Synchrotron.* (1953). URL: https://cds.cern.ch/record/1097613/files/cm-p00051825-OCR.pdf. (Cited on page 40.)

[125] E. D. Courant, M. S. Livingston, and H. S. Snyder. *The strong-focusing synchrotron: A new high-energy accelerator*. Phys. Rev. **88**, 1190–1196 (1952). doi:10.1103/PhysRev.88.1190. (Cited on page 40.)

[126] J. P. Blewett. *Radial focusing in the linear accelerator*. Phys. Rev. **88**, 1197–1199 (1952). URL: https://link.aps.org/doi/10.1103/PhysRev.88.1197, doi:10.1103/PhysRev.88.1197. (Cited on page 40.)

[127] J. B. Adams and E. J. N. Wilson. *Design studies for a large proton synchrotron and its laboratory*. Nucl. Instrum. Meth. **87**, 157–179 (1970). doi:10.1016/0029-554X(70)90199-0. (Cited on page 40.)

[128] *High-Luminosity Large Hadron Collider (HL-LHC): Technical Design Report V. 0.1.* **4/2017** (2017). doi:10.23731/CYRM-2017-004. (Cited on pages 42 and 65.)

[129] **CMS** Collaboration. *The CMS tracker system project: Technical Design Report*. **CMS-TDR-5** (1997). URL: https://cds.cern.ch/record/368412. (Cited on page 46.)

[130] **CMS** Collaboration. *Description and performance of track and primary-vertex reconstruction with the CMS tracker*. JINST **9(10)**, P10009 (2014). arXiv:1405.6569, doi:10.1088/1748-0221/9/10/P10009. (Cited on page 46.)

[131] **CMS** Collaboration. *The CMS electromagnetic calorimeter project: Technical Design Report*. **CMS-TDR-4** (1997). URL: https://cds.cern.ch/record/349375. (Cited on page 48.)

[132] **CMS** Collaboration. *The CMS hadron calorimeter project: Technical Design Report*. **CMS-TDR-2** (1997). URL: https://cds.cern.ch/record/357153. (Cited on page 48.)

[133] **CMS** Collaboration. *The CMS magnet project : Technical Design Report*. **CMS-TDR-1** (1997). URL: https://cds.cern.ch/record/331056. (Cited on page 49.)

[134] **CMS** Collaboration. *The CMS muon project: Technical Design Report*. **CMS-TDR-3** (1997). URL: https://cds.cern.ch/record/343814. (Cited on page 50.)

[135] **CMS** Collaboration. *The CMS trigger system*. JINST **12(01)**, P01020 (2017). arXiv:1609.02366, doi:10.1088/1748-0221/12/01/P01020. (Cited on page 51.)

[136] **CMS** Collaboration. *CMS Technical Design Report for the Level-1 Trigger Upgrade*. **CMS-TDR-012** (2013). URL: https://cds.cern.ch/record/1556311. (Cited on page 52.)

[137] **CMS** Collaboration. *Particle-flow reconstruction and global event description with the CMS detector*. JINST **12(10)**, P10003 (2017). arXiv:1706.04965, doi:10.1088/1748-0221/12/10/P10003. (Cited on pages 53 and 66.)

[138] T. Speer, W. Adam, R. Fruhwirth, A. Strandlie, T. Todorov, and M. Winkler. *Track reconstruction in the CMS tracker*. Nucl. Instrum. Meth. A **559**, 143–147 (2006). doi:10.1016/j.nima.2005.11.207. (Cited on page 54.)

[139] R. Fruhwirth. *Application of Kalman filtering to track and vertex fitting*. Nucl. Instrum. Meth. A **262**, 444–450 (1987). doi:10.1016/0168-9002(87)90887-4. (Cited on page 54.)

[140] K. Rose. *Deterministic annealing for clustering, compression, classification, regression, and related optimization problems*. IEEE Proc. **86(11)**, 2210–2239 (1998). doi:10.1109/5.726788. (Cited on page 55.)

[141] R. Fruhwirth, W. Waltenberger, and P. Vanlaer. *Adaptive vertex fitting*. J. Phys. G **34**, N343 (2007). doi:10.1088/0954-3899/34/12/N01. (Cited on page 55.)

[142] Wolfgang Adam, R. Fruhwirth, Are Strandlie, and T. Todor. *Reconstruction of electrons with the gaussian-sum filter in the CMS tracker at the LHC*. J. Phys. G **31(9)**, N9–N20 (2005). arXiv:physics/0306087, doi:10.1088/0954-3899/31/9/n01. (Cited on page 55.)

[143] S. Baffioni, C. Charlot, F. Ferri, D. Futyan, P. Meridiani, I. Puljak, C. Rovelli, R. Salerno, and Y. Sirois. *Electron reconstruction in CMS*. Eur. Phys. J. C **49**, 1099–1116 (2007). doi:10.1140/epjc/s10052-006-0175-5. (Cited on page 55.)

[144] **CMS** Colloboration. *Performance of the CMS muon detector and muon reconstruction with proton-proton collisions at $\sqrt{s} = 13$ TeV*. JINST **13(06)**, P06015 (2018). arXiv:1804.04528, doi:10.1088/1748-0221/13/06/P06015. (Cited on pages 55, 56, and 122.)

[145] Matteo Cacciari, Gavin P. Salam, and Gregory Soyez. *The anti-k_t jet clustering algorithm*. JHEP **04**, 063 (2008). arXiv:0802.1189, doi:10.1088/1126-6708/2008/04/063. (Cited on pages 56 and 88.)

[146] Stephen D. Ellis and Davison E. Soper. *Successive combination jet algorithm for hadron collisions*. Phys. Rev. D **48**, 3160–3166 (1993). arXiv:hep-ph/9305266, doi:10.1103/PhysRevD.48.3160. (Cited on page 56.)

[147] Matteo Cacciari, Gavin P. Salam, and Gregory Soyez. *FastJet User Manual*. Eur. Phys. J. C **72**, 1896 (2012). arXiv:1111.6097, doi:10.1140/epjc/s10052-012-1896-2. (Cited on page 57.)

[148] **CMS** Collaboration. *Determination of Jet Energy Calibration and Transverse Momentum Resolution in CMS*. JINST **6**, P11002 (2011). arXiv:1107.4277, doi:10.1088/1748-0221/6/11/P11002. (Cited on page 57.)

[149] Serguei Chatrchyan et al. *Performance of tau-lepton reconstruction and identification in CMS*. JINST **7**, P01001 (2012). arXiv:1109.6034, doi:10.1088/1748-0221/7/01/P01001. (Cited on page 57.)

[150] **CMS** Colloboration. *Performance of missing transverse momentum reconstruction in proton-proton collisions at $\sqrt{s}$ = 13 TeV using the CMS detector*. JINST **14(07)**, P07004 (2019). arXiv:1903.06078, doi:10.1088/1748-0221/14/07/P07004. (Cited on pages 58 and 123.)

[151] S. Yousaf Shah, Andromachi Tsirou, Piero Giorgio Verdini, Frank Hartmann, Lorenzo Masetti, Guido H. Dirkes, Robert Stringer, and Manuel Fahrer. *The CMS Tracker Detector Control System*. Nucl. Instrum. Meth. A **604**, 281–283 (2009). doi:10.1016/j.nima.2009.01.093. (Cited on page 64.)

[152] Wassef Karimeh, Maroun Chammoun, Ivan Shvetsov, Andromachi Tsirou, and Piero Giorgio Verdini. *Status and Future of the CMS Tracker DCS*. EPJ Web Conf. **245**, 01005 (2020). doi:10.1051/epjconf/202024501005. (Cited on page 64.)

[153] **CMS** Collaboration. *Technical Proposal for the Phase-II Upgrade of the CMS Detector*. (2015). doi:10.17181/CERN.VU8I.D59J. (Cited on pages 65 and 73.)

[154] **CMS** Collaboration. *The Phase-2 Upgrade of the CMS Level-1 Trigger*. **CMS-TDR-021** (2020). URL: https://cds.cern.ch/record/2714892/. (Cited on pages 66, 69, and 71.)

[155] Daniele Bertolini, Philip Harris, Matthew Low, and Nhan Tran. *Pileup Per Particle Identification*. JHEP **10**, 059 (2014). arXiv:1407.6013, doi:10.1007/JHEP10(2014)059. (Cited on page 66.)

[156] **CMS** Collaboration. *The Phase-2 Upgrade of the CMS Barrel Calorimeters*. **CMS-TDR-015** (2017). URL: https://cds.cern.ch/record/2283187/. (Cited on page 66.)

[157] **CMS** Collaboration. *The Phase-2 Upgrade of the CMS Endcap Calorimeter*. **CMS-TDR-019** (2017). URL: https://cds.cern.ch/record/2293646/. (Cited on page 66.)

[158] **CALICE** Collaboration. *Response of the CALICE Si-W electromagnetic calorimeter physics prototype to electrons*. Nucl. Instrum. Meth. A **608**, 372–383 (2009). arXiv:0811.2354, doi:10.1016/j.nima.2009.07.026. (Cited on page 66.)

[159] **CMS** Collaboration. *A MIP Timing Detector for the CMS Phase-2 Upgrade*. **CMS-TDR-020** (2019). URL: https://cds.cern.ch/record/2667167/. (Cited on page 66.)

[160] **CMS** Collaboration. *The Phase-2 Upgrade of the CMS Muon Detectors*. **CMS-TDR-016** (2017). URL: https://cds.cern.ch/record/2283189/. (Cited on page 67.)

[161] **CMS** Collaboration. *The Phase-2 Upgrade of the CMS Data Acquisition and High Level Trigger*. **CMS-TDR-022** (2021). URL: https://cds.cern.ch/record/2759072/. (Cited on page 67.)

[162] **CMS** Collaboration. *The Phase-2 Upgrade of the CMS Beam Radiation Instrumentation and Luminosity Detectors*. **CMS-TDR-023** (2021). URL: https://cds.cern.ch/record/2759074/. (Cited on page 67.)

[163] C. Foudas, A. Rose, J. Jones, and G. Hall. *A Study for a tracking trigger at first level for CMS at SLHC*. 11th Workshop on Electronics for LHC and Future Experiments page 90 (2005). arXiv:physics/0510227. (Cited on page 67.)

[164] M. Raymond, D. Braga, W. Ferguson, J. Fulcher, G. Hall, J. Jacob, L. Jones, M. Pesaresi, and M. Prydderch. *The CMS binary chip for microstrip tracker readout at the SLHC*. JINST **7**, C01033 (2012). doi:10.1088/1748-0221/7/01/C01033. (Cited on page 69.)

[165] D. Ceresa, J. Kaplon, R. Francisco, A. Caratelli, K. Kloukinas, and A. Marchioro. *A 65 nm pixel readout ASIC with quick transverse momentum discrimination capabilities for the CMS Tracker at HL-LHC*. JINST **11(01)**, C01054 (2016). doi:10.1088/1748-0221/11/01/C01054. (Cited on page 69.)

[166] **CMS** Colloboration. *Search for charged-lepton flavor violation in the production and decay of top quarks using trilepton final states in proton-proton collisions at $\sqrt{s} = 13$ TeV*. (2023). arXiv:2312.03199. (Cited on pages 75 and 131.)

[167] Alexander Read. *Presentation of search results: The CL_s technique*. J. Phys. G **28**, 2693 (2002). doi:10.1088/0954-3899/28/10/313. (Cited on pages 77 and 127.)

[168] Mikael Chala, Jose Santiago, and Michael Spannowsky. *Constraining four-fermion operators using rare top decays*. JHEP **04**, 014 (2019). arXiv:1809.09624, doi:10.1007/JHEP04(2019)014. (Cited on page 77.)

[169] D. Barducci et al. *Interpreting top-quark LHC measurements in the standard-model effective field theory*. **CERN-LPCC-2018-01** (2018). arXiv:1802.07237. (Cited on page 80.)

[170] A. Dedes, M. Paraskevas, J. Rosiek, K. Suxho, and L. Trifyllis. *SmeftFR – Feynman rules generator for the Standard Model Effective Field Theory*. Comput. Phys. Commun. **247**, 106931 (2020). arXiv:1904.03204, doi:10.1016/j.cpc.2019.106931. (Cited on pages 81 and 132.)

[171] Celine Degrande, Claude Duhr, Benjamin Fuks, David Grellscheid, Olivier Mattelaer, and Thomas Reiter. *UFO - The Universal FeynRules Output*. Comput. Phys. Commun. **183**, 1201–1214 (2012). arXiv:1108.2040, doi:10.1016/j.cpc.2012.01.022. (Cited on page 81.)

[172] Neil D. Christensen and Claude Duhr. *FeynRules - Feynman rules made easy*. Comput. Phys. Commun. **180**, 1614–1641 (2009). arXiv:0806.4194, doi:10.1016/j.cpc.2009.02.018. (Cited on page 81.)

[173] Ilaria Brivio, Yun Jiang, and Michael Trott. *The SMEFTsim package, theory and tools*. JHEP **12**, 070 (2017). arXiv:1709.06492, doi:10.1007/JHEP12(2017)070. (Cited on pages 82 and 132.)

[174] Michal Czakon and Alexander Mitov. *Top++: A Program for the Calculation of the Top-Pair Cross-Section at Hadron Colliders*. Comput. Phys. Commun. **185**, 2930 (2014). arXiv:1112.5675, doi:10.1016/j.cpc.2014.06.021. (Cited on pages 83 and 85.)

[175] Jennifer Kile and Amarjit Soni. *Model-Independent Constraints on Lepton-Flavor-Violating Decays of the Top Quark*. Phys. Rev. D **78**, 094008 (2008). arXiv:0807.4199, doi:10.1103/PhysRevD.78.094008. (Cited on pages 83 and 127.)

[176] **CMS** Colloboration. *Event generator tunes obtained from underlying event and multiparton scattering measurements*. Eur. Phys. J. C **76(3)**, 155 (2016). arXiv:1512.00815, doi:10.1140/epjc/s10052-016-3988-x. (Cited on page 84.)

[177] **CMS** Colloboration. *Extraction and validation of a new set of CMS PYTHIA8 tunes from underlying-event measurements*. Eur. Phys. J. C **80(1)**, 4 (2020). arXiv:1903.12179, doi:10.1140/epjc/s10052-019-7499-4. (Cited on page 84.)

[178] John M. Campbell, R. Keith Ellis, and Ciaran Williams. *Vector boson pair production at the LHC*. JHEP **07**, 018 (2011). arXiv:1105.0020, doi:10.1007/JHEP07(2011)018. (Cited on pages 85 and 116.)

[179] Rikkert Frederix and Ioannis Tsinikos. *On improving NLO merging for* $t\bar{t}W$ *production*. JHEP **11**, 029 (2021). arXiv:2108.07826, doi:10.1007/JHEP11(2021)029. (Cited on pages 85 and 116.)

[180] Anna Kulesza, Leszek Motyka, Daniel Schwartländer, Tomasz Stebel, and Vincent Theeuwes. *Associated top quark pair production with a heavy boson: differential cross sections at NLO+NNLL accuracy*. Eur. Phys. J. C **80(5)**, 428 (2020). arXiv:2001.03031, doi:10.1140/epjc/s10052-020-7987-6. (Cited on pages 85 and 116.)

[181] Ye Li and Frank Petriello. *Combining QCD and electroweak corrections to dilepton production in FEWZ*. Phys. Rev. D **86**, 094034 (2012). arXiv:1208.5967, doi:10.1103/PhysRevD.86.094034. (Cited on page 85.)

[182] GEANT4 Colloboration. *GEANT4–a simulation toolkit*. Nucl. Instrum. Meth. A **506**, 250–303 (2003). doi:10.1016/S0168-9002(03)01368-8. (Cited on page 84.)

[183] **CMS** Colloboration. *Observation of Single Top Quark Production in Association with a Z Boson in Proton-Proton Collisions at* $\sqrt{s}$ *=13 TeV*. Phys. Rev. Lett. **122(13)**, 132003 (2019). arXiv:1812.05900, doi:10.1103/PhysRevLett.122.132003. (Cited on pages 86 and 119.)

[184] **CMS** Colloboration. *Inclusive and differential cross section measurements of single top quark production in association with a Z boson in proton-proton collisions at* $\sqrt{s} = 13$ *TeV*.

JHEP **02**, 107 (2022). arXiv:2111.02860, doi:10.1007/JHEP02(2022)107. (Cited on page 86.)

[185] **TMVA** Colloboration. *TMVA - Toolkit for Multivariate Data Analysis*. **CERN-OPEN-2007-007** (2007). arXiv:physics/0703039. (Cited on pages 86 and 134.)

[186] Matteo Cacciari and Gavin P. Salam. *Pileup subtraction using jet areas*. Phys. Lett. B **659**, 119–126 (2008). arXiv:0707.1378, doi:10.1016/j.physletb.2007.09.077. (Cited on page 87.)

[187] **CMS** Collaboration. *Pileup Removal Algorithms*. **CMS-PAS-JME-14-001** (2014). URL: https://cds.cern.ch/record/1751454. (Cited on page 88.)

[188] **CMS** Collaboration. *Jet algorithms performance in 13 TeV data*. **CMS-PAS-JME-16-003** (2017). URL: https://cds.cern.ch/record/2256875. (Cited on page 88.)

[189] **CMS** Collaboration. *Pileup Jet Identification*. **CMS-PAS-JME-13-005** (2013). URL: https://cds.cern.ch/record/1581583. (Cited on page 88.)

[190] **CMS** Collaboration. *Performance of the pile up jet identification in CMS for Run 2*. **CMS-DP-2020-020** (2020). URL: https://cds.cern.ch/record/2715906. (Cited on page 88.)

[191] Emil Bols, Jan Kieseler, Mauro Verzetti, Markus Stoye, and Anna Stakia. *Jet Flavour Classification Using DeepJet*. JINST **15(12)**, P12012 (2020). arXiv:2008.10519, doi:10.1088/1748-0221/15/12/P12012. (Cited on pages 89 and 136.)

[192] **CMS** Colloboration. *Identification of heavy-flavour jets with the CMS detector in pp collisions at 13 TeV*. JINST **13(05)**, P05011 (2018). arXiv:1712.07158, doi:10.1088/1748-0221/13/05/P05011. (Cited on page 89.)

[193] **CMS** Colloboration. *Performance of the DeepJet b tagging algorithm using 41.9 fb^{-1} of data from proton-proton collisions at 13 TeV with Phase 1 CMS detector*. **CMS-DP-2018-058** (2018). URL: http://cds.cern.ch/record/2646773. (Cited on page 89.)

[194] Thomas P. S. Gillam and Christopher G. Lester. *Improving estimates of the number of 'fake' leptons and other mis-reconstructed objects in hadron collider events: BoB's your UNCLE*. JHEP **11**, 031 (2014). arXiv:1407.5624, doi:10.1007/JHEP11(2014)031. (Cited on page 97.)

[195] Tianqi Chen and Carlos Guestrin. *XGBoost: A scalable tree boosting system*. Proceedings of the 22nd ACM SIGKDD International Conference on Knowledge Discovery and Data Mining. page 785 (2016). arXiv:1603.02754, doi:10.1145/2939672.2939785. (Cited on pages 108, 110, and 134.)

[196] **CMS** Colloboration. *Performance of CMS Muon Reconstruction in pp Collision Events at $\sqrt{s} = 7$ TeV*. JINST **7**, P10002 (2012). arXiv:1206.4071, doi:10.1088/1748-0221/7/10/P10002. (Cited on page 116.)

[197] **CMS** Colloboration. *Measurement of the Higgs boson production rate in association with top quarks in final states with electrons, muons, and hadronically decaying tau leptons at $\sqrt{s} = 13$ TeV*. Eur. Phys. J. C **81(4)**, 378 (2021). arXiv:2011.03652, doi:10.1140/epjc/s10052-021-09014-x. (Cited on page 119.)

[198] **CMS** Colloboration. *Precision luminosity measurement in proton-proton collisions at $\sqrt{s} = 13$ TeV in 2015 and 2016 at CMS*. Eur. Phys. J. C **81(9)**, 800 (2021). arXiv:2104.01927, doi:10.1140/epjc/s10052-021-09538-2. (Cited on page 121.)

[199] **CMS** Colloboration. *CMS luminosity measurement for the 2017 data-taking period at $\sqrt{s} = 13$ TeV*. **CMS-PAS-LUM-17-004** (2018). URL: https://cds.cern.ch/record/2621960/. (Cited on page 121.)

[200] **CMS** Colloboration. *CMS luminosity measurement for the 2018 data-taking period at $\sqrt{s} = 13$ TeV*. **CMS-PAS-LUM-18-002** (2019). URL: https://cds.cern.ch/record/2676164/. (Cited on page 121.)

[201] **CMS** Colloboration. *Measurement of the inelastic proton-proton cross section at $\sqrt{s} =$ 13 TeV*. JHEP **07**, 161 (2018). arXiv:1802.02613, doi:10.1007/JHEP07(2018)161. (Cited on page 121.)

[202] **CMS** Colloboration. *Measurements of Inclusive W and Z Cross Sections in pp Collisions at $\sqrt{s} = 7$ TeV*. JHEP **01**, 080 (2011). arXiv:1012.2466, doi:10.1007/JHEP01(2011)080. (Cited on page 121.)

[203] **CMS** Colloboration. *Energy Calibration and Resolution of the CMS Electromagnetic Calorimeter in pp Collisions at $\sqrt{s} = 7$ TeV*. JINST **8**, P09009 (2013). arXiv:1306.2016, doi:10.1088/1748-0221/8/09/P09009. (Cited on page 122.)

[204] A. Bodek, A. van Dyne, J. Y. Han, W. Sakumoto, and A. Strelnikov. *Extracting Muon Momentum Scale Corrections for Hadron Collider Experiments*. Eur. Phys. J. C **72**, 2194 (2012). arXiv:1208.3710, doi:10.1140/epjc/s10052-012-2194-8. (Cited on page 122.)

[205] **CMS** Colloboration. *Jet energy scale and resolution in the CMS experiment in pp collisions at 8 TeV*. JINST **12(02)**, P02014 (2017). arXiv:1607.03663, doi:10.1088/1748-0221/12/02/P02014. (Cited on page 122.)

[206] Roger J. Barlow and Christine Beeston. *Fitting using finite Monte Carlo samples*. Comput. Phys. Commun. **77**, 219 (1993). doi:10.1016/0010-4655(93)90005-W. (Cited on page 126.)

[207] Thomas Junk. *Confidence level computation for combining searches with small statistics*. Nucl. Instrum. Meth. A **434**, 435 (1999). arXiv:hep-ex/9902006, doi:10.1016/S0168-9002(99)00498-2. (Cited on page 127.)

[208] Glen Cowan, Kyle Cranmer, Eilam Gross, and Ofer Vitells. *Asymptotic formulae for likelihood-based tests of new physics*. Eur. Phys. J. C **71**, 1554 (2011). arXiv:1007.1727, doi:10.1140/epjc/s10052-011-1554-0. (Cited on page 127.)

[209] **CMS** Collaboration. *HEPData record for CMS-TOP-22-005*. (2023). doi:10.17182/hepdata.135831. (Cited on page 127.)

[210] **CMS** Colloboration. *Observation of four top quark production in proton-proton collisions at $\sqrt{s} = 13$ TeV*. (2023). arXiv:2305.13439. (Cited on page 134.)

[211] **CMS** Colloboration. *Identification of hadronic tau lepton decays using a deep neural network*. JINST **17**, P07023 (2022). arXiv:2201.08458, doi:10.1088/1748-0221/17/07/P07023. (Cited on page 135.)

[212] **CMS** Colloboration. *Reconstruction and identification of τ lepton decays to hadrons and ν_τ at CMS*. JINST **11(01)**, P01019 (2016). arXiv:1510.07488, doi:10.1088/1748-0221/11/01/P01019. (Cited on page 135.)

[213] **CMS** Colloboration. *Performance of reconstruction and identification of τ leptons decaying to hadrons and ν_τ in pp collisions at $\sqrt{s} = 13$ TeV*. JINST **13(10)**, P10005 (2018). arXiv:1809.02816, doi:10.1088/1748-0221/13/10/P10005. (Cited on page 135.)